Physical modeling of cell motility and morphodynamics

Ido Lavi

SORBONNE UNIVERSITÉ
CRÉATEURS DE FUTURS DEPUIS 1257

LABORATOIRE Jean Perrin

THÈSE DE DOCTORAT
DE LA SORBONNE UNIVERSITÉ

Spécialité : Physique

École doctorale n°564: Physique en Île-de-France

réalisée

au Laboratoire Jean Perrin

sous la direction de Raphaël VOITURIEZ

et co-supervisé par Matthieu PIEL et Jaume CASADEMUNT

présentée par

Ido LAVI

pour obtenir le grade de :

DOCTEUR DE LA SORBONNE UNIVERSITÉ

Sujet de la thèse :

Physical Modeling of Cell Motility and Morphodynamics

soutenue le 15 novembre 2019

devant le jury composé de :

Mme.	Rhoda HAWKINS	Rapporteur
M.	Karsten KRUSE	Rapporteur
M.	Jean-François JOANNY	Examinateur
M.	Pierre RECHO	Examinateur
M.	Benoit LADOUX	Examinateur
M.	Raphaël VOITURIEZ	Directeur de thèse
M.	Matthieu PIEL	Invité
M.	Jaume CASADEMUNT	Invité

Contents

Résumé

Les cellules vivantes constituent un exemple frappant de système microscopique loin de l'équilibre thermodynamique et hautement déformable. Au cours de nombreux processus biologiques comme le développement embryonnaire, la réponse immunitaire ou encore certaines maladies comme le cancer, les cellules subissent des modifications morphologiques importantes. C'est notamment le cas durant les processus de division et de migration cellulaire, deux fonctions vitales resultant d'un ensemble coordonné de processus mécano-chimiques. Cette thèse a pour but de fournir une description physique minimale de ces phénomènes, pouvant donner lieu à un traitement analytique et numérique explicite du problème.

Concrètement, nous introduisons un modèle hydrodynamique minimal de polarisation, migration et déformation d'une cellule vivante confinée entre deux surfaces parallèles. Dans notre modèle, le cytoplasme cellulaire est un système hors d'équilibre du fait des forces actives générées dans le cytosquelette. Le cytoplasme est décrit comme une gouttelette visqueuse passive dans le régime d'écoulement de Hele-Shaw. Il contient un soluté diffusif qui contrôle la force active induite par le cytosquelette. Bien que relativement simple, ce modèle à deux dimensions prédit une gamme de comportements dynamiques très riche. Une analyse linéaire de la stabilité du système, effectuée analytiquement, révèle que l'activité du soluté déstabilise d'abord un mode global de polarisation et de translation, induisant une motilité cellulaire par rupture spontanée de symétrie. À une activité plus élevée, le système traverse une série de bifurcations de Hopf conduisant à des oscillations couplées de la forme des gouttelettes et de la concentration en soluté. Au niveau non linéaire, nous trouvons des solutions de type onde progressive associées à des formes polarisées non triviales ressemblant à des observations expérimentales.

En plus des techniques analytiques, nous avons développé une simulation numérique de notre problème basée sur la méthode des éléments finis. Cet outil numérique a été conçu pour explorer la dynamique de ce modèle de cellule déformable dans des régimes de paramètres arbitraires et dans des situations impliquant des interactions mécaniques avec l'environnement extérieur. L'étude numérique a mis en évidence la stabilité des solutions de type onde progressive, l'existence d'attracteurs oscillants et l'apparition d'une singularité topologique à temps fini (point de pincement), qui conduit probablement à la fragmentation des cellules. En ce qui concerne les interactions mécaniques, nous nous sommes concentrés sur la diffusion cellulaire en présence de parois et d'obstacles stationnaires, la migration à travers des micro-géométries imposées et les collisions cellule-cellule. Les résultats de ces études démontrent des comportements non triviaux résultant d'une combinaison de mémoire intrinsèque et de déformabilité cellulaire.

Globalement, le modèle présenté ici fournit un paradigme mathématique de systèmes

actifs déformables dans lequel l'hydrodynamique de Stokes est couplée à des transducteurs de force diffusifs. L'outil numérique, en particulier, fournit un cadre très utile et versatile pour simuler la dynamique de gouttelettes visqueuses actives dans la géométrie de Hele-Shaw. Les extensions possibles incluent: (i) l'étude systématique des problèmes de diffusion cellulaire en fonction de paramètres intrinsèques, (ii) la caractérisation des effets du bruit et / ou l'augmentation de la complexité biochimique sur la vitesse et la forme des cellules, et (iii) l'extension du modèle unicellulaire à une description numérique des tissus morphodynamiques, composée de plusieurs cellules qui interagissent les unes avec les autres tant mécaniquement que chimiquement.

Abstract

Biological cells provide a striking example of far-from-equilibrium, highly deformable microscopic systems. During embryonic development, immunity, or disease, cells undergo vital functions involving morphological changes. These include cell division and cell migration, two hallmarks of life that are driven by a perplexing array of coordinated mechanochemical processes. This thesis focuses on the challenge of providing a succinct physical description of such phenomena, that is, to offer a plausible and easily understandable mechanism of cell motility and morphodynamics.

More specifically, we introduce a minimal hydrodynamic model of polarization, migration, and deformation of a biological cell confined between two parallel surfaces. In our model, the cell cytoplasm is driven out of equilibrium by active forces generated in the cytoskeleton. The cytoplasm is described as a passive viscous droplet in the Hele-Shaw flow regime. It contains a diffusive solute that actively transduces the applied cytoskeleton force. While fairly simple, this quasi-2D model predicts a range of compelling dynamic behaviours. A linear stability analysis of the system, performed analytically, reveals that solute activity first destabilizes a global polarization-translation mode, prompting cell motility through spontaneous-symmetry-breaking. At higher activity, the system crosses a series of Hopf bifurcations leading to coupled oscillations of droplet shape and solute concentration profiles. At the nonlinear level, we find traveling-wave solutions associated with unique polarized shapes that resemble experimental observations.

In addition to analytical techniques, we developed a numerical simulation of our problem based on the finite element method. This computational tool was constructed in order to explore the dynamics of our free-boundary system in arbitrary parametric regimes, and in situations involving external mechanical interactions on the cell surface. The simulation served to demonstrate the stability of our traveling-wave solutions, the existence of sustained oscillatory attractors, and the emergence of a finite-time topological singularity (pinch-off point), which plausibly leads to cell fragmentation. As for mechanical interactions, we focused on cell scattering from stationary walls and obstacles, migration through imposed micro-geometries, and cell-cell collisions. The results of these exercises demonstrate nontrivial behaviors arising from a combination of the intrinsic memory and deformability of the cell.

Altogether, the model presented here offers a mathematical paradigm of active deformable systems in which Stokes hydrodynamics are coupled to diffusive force-transducers. The numerical tool, in particular, provides a useful modular framework for simulating arbitrary dynamics of active viscous droplets in the Hele-Shaw geometry. Possible extensions include: (i) the systematic study of cell scattering problems as a function of intrinsic parameters, (ii) characterizing the effects of noise and/or augmented biochemical complexity

on cell speeds and shapes, and (iii) expanding the single cell model to a computational description of morphodynamic tissues, comprised of multiple cells that interact with each other both mechanically and chemically.

Acknowledgements

This thesis is one of the requirements towards obtaining the PhD degree at the Sorbonne University. It was made possible by the 'Interface Pour le Vivant' (IPV) program at UPMC, from which I was awarded a three-year scholarship. I am grateful for the opportunity I was given, and I would like to extend my appreciation to the selecting committee.

My sincere gratitude goes out to my PhD advisors, Raphaël Voituriez, Matthieu Piel, and Jaume Casademunt. I have been very fortunate, both at the professional and personal levels, to have worked alongside all of three of you. Looking back, I cannot imagine having better advisors for this PhD study.

To Raphaël, who has been a mentor of mine ever since my MSc studies, and whose elegant ideas have inspired my work both back then and during this PhD. I am very grateful for your thoughtful guidance, for your support and encouragement, and for allowing me the freedom to explore my own directions and collaborations. I appreciate in particular the friendly, accessible manner in which you communicated your immense knowledge. Through the five years that we have known each other, our working relationship has been relaxed, inspiring, and fun—with healthy doses of enthusiasm and perspective. Thank you for providing me with the tools that I needed in order to begin and complete this PhD (both scientifically and logistically), and thank you, Raphaël, for making this challenging long-term race into the enriching experience that it was. I look forward to our continued friendship.

To Jaume, who has been my advisor through the extended stays I had in Barcelona, and whose input to my PhD work has been invaluable. I learned a lot from your unique expertise and perspective on both classical and active hydrodynamic problems. I appreciate the fact that you were always approachable and easy to talk with, and I particularly enjoyed your willingness to explore some very specific questions that arose through the various analyses of our model. Most importantly, thank you for challenging me and teaching me. I sincerely hope that we will have opportunities to collaborate in the future, and I really look forward to a copy of your book.

To Matthieu, who has accepted me, a young physics student with little to no prior knowledge in biology, to his remarkable lab. It has been a true pleasure to work with you and the excellent people in your team. Thank you for believing in my ability to contribute in various ways and for enthusiastically exchanging ideas with me for experiments, analyses, and models. As you know, the theoretical work of this PhD study is directly inspired by the methods developed, and the discoveries obtained, in your lab. While we did not have the time to do everything that we planned together, I hope that we will have the chance to complete our projects moving forward.

I would also like to thank my collaborators,

Nicolas Meunier, who is a mathematician, has made several contributions to this study. The most crucial one has been the design of the implicit curvature scheme in our numerical simulation. In fact, Nicolas has taught me everything I know today about solving PDEs with the finite element method. We have worked closely together for the past three years and have exchanged countless ideas about various models and techniques. I believe that this collaboration has been very fruitful, and that what we have built together has the potential of opening new and exciting directions of research.

Nir S. Gov, who was my MSc supervisor, introduced me to this field of research in the first place. Thank for you starting the collaboration on the blebbing project (and some others, not included in this thesis), for all your scientific input, and—most importantly—for jump-starting my PhD. I am lucky to have you as a close friend and collaborator.

Pierre Sens, who served as scientific tutor on my PhD monitoring committee, was also the lead source of knowledge in the membrane blebbing and tubulation project. I am really grateful for your crucial input and patient style. I remember our discussions very fondly from the very first sketches.

Mohammad Goudarzi and Erez Raz, who designed and performed the experiments in the blebbing project. Thanks for all the input and efforts.

Pablo Vargas, Pablo Sáez, Bianca Cali, and Lucie Barbier, thank you for sharing your inspiring work with me and for all the stimulating and friendly conversations we had about the meaning of your observations. I am glad we got to collaborate closely, and that we managed to capture a pattern in complex cell trajectories that is very interesting from both the biological and physical viewpoints.

Jean-Léon Maître and Özge Özgüç, with whom we started a collaboration aimed at interpreting the pulsating behaviors exhibited by cells in the early stages of the mouse embryo. I appreciate the exchanges we had so far and I sincerely hope that we will manage to put the pieces together in the future.

To all my labmates,

At the Piel-Vargas team; Pablo Sáez, Bianca, Lucie, Nico, Juanma, Larisa, Matthieu Deygas, Nishit, Aastha, Alice, Damien, Guilherme, Valentin, Zahraa, Aditya, Rafaele, Clotilde, Yanjun, and Aleksey. It was important to have your feedback and a lot of fun to be around you.

At the Laboratoire Jean Perrin, and specifically members of the theory group; Annne-Florence Bitbol, Thibault Bertrand, Loïc Marrec, Ananyo Maitra, and Claude Loverdo, who served as mentor on my PhD monitoring committee. Thank you for making me feel welcomed and for all the conversations we had.

In addition, I thank the members of the Curie theory group for welcoming me in their seminars, and specifically Pierre Sens, Jacques Prost, Jean-François Joanny, Amit Singh Vishen, and Carles Blanch-Mercader. Advice given by Carles was very helpful in the complex analysis of the droplet geometric moments.

The PhD experience would have been very different if it weren't for my close friends in Paris and Barcelona; Dan Levy, Jean-Charles Quine, Kotryna Vaidžiulytė, Anna Sawicka, Jacopo Marchi, Adriaan Ludl, and Ricard Alert. It was very nice, and crucial at times, to have you all on board.

My special thanks extends to my parents for their ultimate support. The same goes for all my family and friends in Israel, and my in-laws in Spain and Mexico. I appreciate you a lot and I am grateful for the times we shared during this period.

Saving the best for last, I would like to thank my loving wife, Andrea. This PhD thesis would not have been possible without her support, patience, and encouragement—which she conveyed in English, Spanish, Hebrew, and French. Andrea has also helped me reduce some of the very entangled ideas I had into plain English, and has offered me a healthy perspective overall that, in my opinion, has truly benefited this study.

Publications

My MSc study leading to this PhD work is published here:

- Lavi, I., Piel, M., Lennon-Duménil, A. M., Voituriez, R., & Gov, N. S. (2016). Deterministic patterns in cell motility. *Nature Physics*, 12(12), 1146

The work discussed in this thesis is partly accepted for publication, partly in revision, and partly in redaction:

- Lavi, I., Goudarzi, M., Raz, E., Gov, N. S., Voituriez, R., & Sens, P. (2019). Cellular Blebs and Membrane Invaginations Are Coupled through Membrane Tension Buffering. *Biophysical journal*.
- Lavi, I., Meunier, N., Voituriez, R., & Casademunt, J., (2019). Motility and morphodynamics of confined cells. In revision.
- Lavi, I., Meunier, N., Casademunt, J., & Voituriez, R., (2019). Computational study of cell motility in confined microenvironments. In redaction.
- Lavi, I., Meunier, N., & Pantz, O. (2019). A mathematical model for cell crawling migration. In redaction.

My work on the analysis of experiments (performed during my PhD, but not discussed in thesis) is included in:

- Barbier, L., Sáez, P. J., Attia, R., Lennon-Duménil, A. M., Lavi, I., Piel, M., & Vargas, P. (2019). Myosin II activity is selectively needed for migration in highly confined microenvironments in mature dendritic cells. *Frontiers in Immunology*, 10, 747.
- Sáez P. J., Cali, B., Deygas, M., Lavi, I., Barbier, L., Voituriez, R., Piel, M., & Vargas, P. (2019). Trapping effects limit directional cell migration in complex microenvironments. In redaction.

Chapter I

Introduction

I.1 General context

The physical approach to biological systems is a particularly broad and interdisciplinary area of research that has been developing exceedingly over the past few decades. The underlying purpose motivating this science is to understand physical processes that govern living matter at all scales; from molecules to cells, from cells to tissues and organisms, and from organisms to populations.

In the eyes of a student trained in physics, the biological cell is a fascinating but frighteningly complex system. Indeed, this basic unit of life contains numerous molecules that interact with each other through thousands of chemical reactions, producing far-from-equilibrium physics. The various functions performed by cells, and in particular cell locomotion, rely on the emergent spatio-temporal coordination of the underlying molecular processes.

When venturing into the approach of physicists into cell biology problems, we learned that by focusing on the mechanical properties of cell components, it is possible to select a reduced number of relevant ones that can serve as a basis of constructing relatively simple theoretical descriptions. The objective of studying such models is two-fold. The straightforward 'end-game' goal is to provide quantitative predictions of the cell behaviour. The less obvious, but equally valuable goal is to provide opportunities for inferring new physical insights and ideas for new experiments (whether inside or outside the context of biology).

In practice, not every simplified physical representation of the biological reality provides an easy mathematical problem to solve. Often times, in order to obtain insights and theoretical solutions, one must take a deep excursion in the realm of mathematical analysis. This enriches the scope of truly interdisciplinary knowledge that traverses traditionally separate areas of science. At the intersection of disciplines, and stemming from a very concrete problem, new challenging physical questions are put forward. Our hope is that the work presented in this thesis will constitute a useful stepping stone in this hard but worthwhile endeavour.

I.2 Overview of cell motility

Cell motility refers to the ability of biological cells to perform directional locomotion. In animals, this ability plays a key role in a range of life processes, such as embryogenesis, immune responses, wound healing, and cancer metastasis. From the biomedical point of view, defects in motility are known to induce a multitude of life threatening situations. Examples include congenital diseases that follow from motility failures during embryogenesis, chronic inflammatory diseases and autoimmune disorders caused by immune cell migration to wrong places, as well as the spreading of cancerous tumors (metastasis). As cell motility conditions our lives from conception to death, the importance of understanding the apparatus driving this phenomenon cannot be overstated.

Depending on the biological process, cells move either as individuals or in groups, as cohesive units, in a phenomenon known as 'collective cell migration'. Migration in groups, which is instrumental in morphogenesis, tissue regeneration, and metastasis, differs from single cell migration in the sense that it involves cell-cell coordination and communication (see Friedl and Gilmour (2009); Ladoux and Mège (2017) for reviews). Although mechanical cell-cell interactions will be discussed by the end of this study, we stress at this stage that our work focuses on individual cell migration, itself a highly intricate phenomenon.

From the physics viewpoint, motility presents a remarkable example of nonequilibirium self-organization, involving: (i) chemical and mechanical component processes which are connected through feedback interactions, and (ii) integration over a wide range of spatial and temporal scales. At the scale of the cell, motility takes various forms depending on the cell type and the environment in which the cell is migrating. The specifics of crawling motility are influenced by factors such as adhesion strength, the type of substratum (tissues/gels), external migratory cues (both chemical and mechanical), and the organization of the cellular cytoskeleton Friedl and Wolf (2010). The cytoskeleton, a dynamic network of interlinking protein filaments, is responsible for generating the molecular forces necessary for active (ATP-fueled) translocation. By interacting with the external environment, the cortical cytoskeleton produces cell movements and deformations that correlate with internal flows and shifting distributions of intracellular biomolecules Alberts et al (2002). The key force-generating components in the cytoskeleton (regulators of the actomyosin system) have long been identified. However, it remains unclear how their transport mechanisms and active function are dynamically coupled to the cell morphology. It is this broadly defined puzzle that has motivated the main study of this thesis.

I.2.1 Cell structures

A basic familiarity with the main cellular structures at play is essential for expanding our discussion on the motile cell system. Here, we provide brief definitions of the cytoplasm, cytoskeleton, actomyosin cortex and the cell plasma membrane.

The cytoplasm of a cell refers to all of the material enclosed by the cell membrane, with the exception of the cell nucleus. The main components of the cytoplasm are the cytosol (a highly viscous gel-like substance), the organelles (the internal sub-structures of the cell), and various cytoplasmic inclusions. It is composed mostly of water (about 80%), proteins (10 to 15%), lipids (2 to 4%), nucleic acids, inorganic salts and polysaccharides in smaller amounts Shepherd (2006); Bibbo and Wilbur (2014). The cytoplasm is a

dynamic environment through which intracellular components are moved and mixed. In rapidly deforming motile cells, such as human neutrophils, bulk cytoplasmic flow couples cell deformation to the transport and dispersion of cytoplasmic particles Koslover et al (2017).

The cytoskeleton of eukaryotic animal cells is a viscoelastic protein structure (contained in the cytoplasm) that supports the cell shape and anchors the organelles within the cell Alberts et al (2002). It is comprised of semiflexible protein polymers including actin, microtubules, intermediate filaments and septins Fischer and Fowler (2015).

The actomyosin cortex (or cortical cytoskeleton) is a thin (100 to 1000 nanometers thick) crosslinked F-actin network that lies beneath the cell membrane. The constituents of the cortex undergo rapid turnover, making it both rigid and plastic-like Salbreux et al (2012). Actin filaments are nucleated mainly by formin or the Arp2/3 complex Blanchoin et al (2014), and myosin motors exert contractile forces in this meshwork, inducing actin flows and cell shape changes Howard et al (2001). The cortex filaments are also crosslinked with the cell plasma membrane by proteins such as ezrin, radixin and moesin (ERM) Tsukita et al (1997).

The cell plasma membrane (PM) is a thin ($\sim$5 nm thick) sheet that encloses the cell cytoplasm. It contains many carbohydrates and proteins, which are important to a large variety of biological functions. The structural basis of the PM is a lipid bilayer formed by phospholipid molecules, which self-assemble into the bilayer configuration owing to their amphiphatic nature (having a hydrophobic tail and a hydrophilic head). In the bilayer, the phospholipid heads point towards the water both inside and outside of the enclosed cell Alberts et al (2002). Membranes comprised of lipid bilayers are unique in that they have both fluid and elastic material properties Singer and Nicolson (1972); Helfrich (1973). In both layers, the lipids encounter very low resistance in their lateral (in-plane) motion. This means that shear strains are met with little to no resistance in the membrane. Conversely, by stretching or bending a flat membrane, the hydrophobic tails become more exposed to water. The free energy cost associated with this exposure produces an effective tension and bending rigidity. That said, biological cell membranes are typically not flattened along the cell periphery. Since the PM is practically inextensible, cells accommodate shape changes by storing membrane area in fluctuations, ruffles, small vesicles, and various invaginations Kosmalska et al (2015). As the cell membrane plays the role of a physical barrier, it is considered a master regulator of all biological processes involving cell morphodynamics. In particular, through their linkage to the active actomyosin cortex, cell membranes are also directly involved in cell motility Sens and Plastino (2015).

I.2.2 Active forces in the cytoskeleton

Several actin-binding molecules are capable of converting chemical energy to mechanical work through the hydrolysis of adenosine triphosphate (ATP) into adenosine diphosphate (ADP) Alberts et al (2002); Howard et al (2001). Such reactions produce active forces in the cytoskeleton by two main processes: (i) the polymerisation and depolymerization of actin filaments (Fig. I.1a), and (ii) the contraction of filaments by the power-stoke cycle of myosin (Fig. I.1b).

The polymerization at the plus "barbed" end of F-actin is promoted, in part, by the ATP that binds to G-actin monomers Alberts et al (2002). The hydrolysis of ATP along

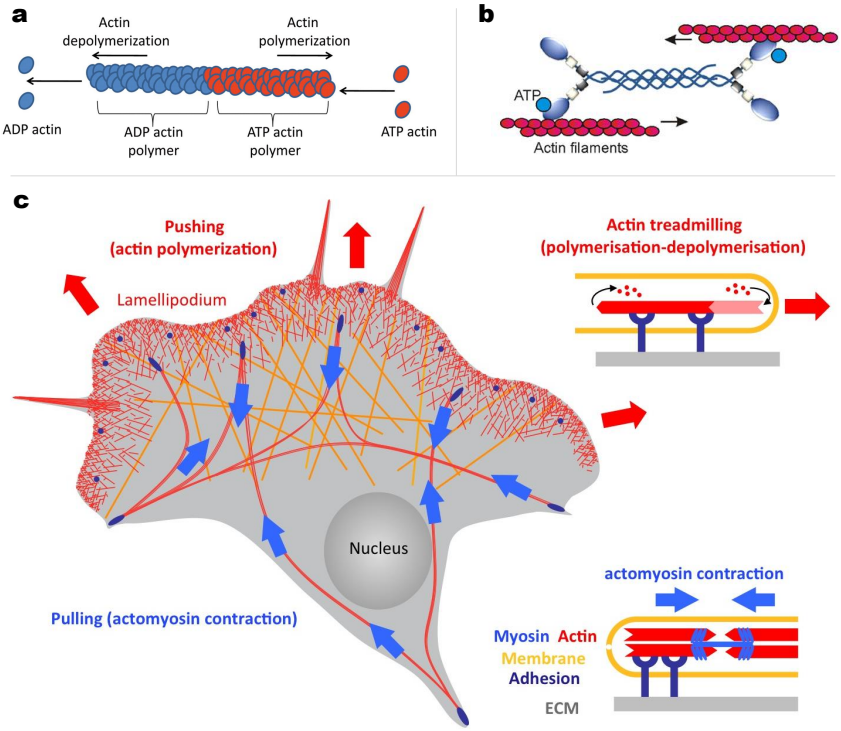

Fig. I.1 ***Active forces in the cytoskeleton***. *a) Individual subunits of ATP-bound G-actin assemble into long F-actin polymers, creating a double helix structure. Hydrolysis of the ATP destabilizes the polymer, causing dissolution of F-actin into G-actin monomers (adapted from Street and Bryan (2011)). b) The activated myosin II molecule (blue) associates with anti-parallel F-actin filaments (red) to generate contractile forces using cellular ATP (adapted from Betapudi (2014)). c) Forces are produced by the growth (red arrows) and the contraction (blue arrows) of the actin cytoskeleton. The generation of such forces depends on the linkage (or anchoring) of the actin networks to the extracellular matrix (taken from Le Clainche home page, adapted from Le Clainche and Carlier (2008)).*

the filament itself then promotes the disassembly of monomers, inducing depolymerization at the minus end (see Fig. I.1a). This process generates a phenomenon known as actin treadmilling. By linkage of filaments to the external substratum, the actin treadmilling applies a protrusive force that acts against the cell membrane (see Fig. I.1c). This force is known to play an important role in cell motility as it generates leading-edge protrusions such as lamellipodia and filopodia Pollard and Borisy (2003). The formation of one type of structure or another depends on which actin nucleator is involved, and the specifics of the actin closslinkers Pollard and Borisy (2003).

F-actin filaments also act as tracks for actin-binding myosin molecules, which can crosslink filaments and also move along them Alberts et al (2002). The directional motion of myosin, which is fueled by ATP to ADP hydrolysis, generates microscopic forces that produce a macroscopic active stress Kruse et al (2004). An illustration of how myosin II produces a pulling force on anti-parallel actin filaments is shown in Fig. I.1b. This

phenomenon, called actomyosin contraction, plays a crucial role in cell motility since (i) cell rear retraction requires the contraction of the actin cytoskeleton, and (ii) the ripping of cell-substrate adhesions at the trailing edge of the cell is promoted, in part, by these contractile forces, see Fig. I.1c. In addition, myosin II can induce cell polarity by establishing the cell rear, where it generates large actomyosin filament bundles Mseka et al (2009).

I.2.3 Integration challenges

The motile cell system integrates the dynamics of the membrane, cortex, cytoskeleton and cytoplasm. From the physics perspective, this problem becomes very complicated very quickly for several reasons.

First, the dynamics of the cytoskeleton alone (in isolation) are extremely nontrivial. In addition to passive processes, the polar actin filaments are subject to active forces driven by treadmilling and actomyosin contraction (see Fig. I.1). In fact, the intricacy of the cytoskeleton has inspired the development of a highly influential generic theory of active polar gels, based on symmetry considerations and irreversible thermodynamics Kruse et al (2004, 2005); Joanny and Prost (2009); Marchetti et al (2013); Prost et al (2015). To this day, the active gel theory was shown to support a large variety of patterns Voituriez et al (2006); Marchetti et al (2013); Prost et al (2015) and continues to be a very active field of research (recent realizations for particular systems include Doostmohammadi et al (2018); Pérez-González et al (2019); Mietke et al (2019); Farutin et al (2019)).

Second, the presence of an internal cytoplasmic fluid—which typically constitutes the bulk of the cell mass—inflicts important mechanical constraints on the overall dynamics: (i) in certain situations, the viscosity of this fluid could be a considerable source of kinetic energy dissipation, (ii) the interaction of the fluid with the external substratum may lead to a marked transfer of momentum, and (iii) the incompressibility of the internal fluid means that cell volume is controlled by water fluxes at the cell membrane. The latter are induced by differences in the osmotic concentrations of the cytoplasmic and extracellular fluids Lodish et al (2000).

Third, the cortex is mechanically linked to the cell cytoplasm. At the scale of the cell, the cortex activity is known to induce shape changes by means of actomyosin contraction and/or F-actin polymerization. In turn, such deformations naturally produce internal cytoplasmic flows Keren et al (2009); Lewis et al (2015); Koslover et al (2017); Klughammer et al (2018). Moreover, it has been shown that cytoplasmic flows (induced externally by optical means) can shift the distribution of proteins that regulate cortex activity Mittasch et al (2018). In the context of cell motility, such flows are thought to play an important role due to the hydrodynamic forces they apply, as well as to their influence on the transport of cytoskeleton components Keren et al (2009).

Fourth, the cortex is mechanically attached to the cell plasma membrane, a fact that has several important ramifications (reviewed in Sens and Plastino (2015)). The plasma membrane tension is capable of suppressing protrusions driven by actin polymerization. By doing so, the tension favors the formation of a single protrusion rather than multiple competing ones in different directions Houk et al (2012). Moreover, in many cell types and situations, the membrane can locally detach from the cortical cytoskeleton. Such events produce bleb-type protrusions (transient membrane bulges extending from the cell

surface) that have been directly implicated in cell motility Charras and Paluch (2008); Maugis et al (2010); Ruprecht et al (2015).

Lastly, in dimensions greater than 1, cell motility as a mathematical physics problem falls into the class of dynamic curved fronts. Such free boundary problems are notoriously difficult to solve (both analytically and numerically), particularly when finite capillary forces are considered.

I.2.4 Polarization and translocation

It is well established that the directional locomotion of cells is based on the development and maintenance of functional asymmetry (polarity) between a 'cell front' and a 'cell rear' Verkhovsky et al (1999); Ladoux et al (2016). Intrinsic markers for front-rear cell polarity include elements such as the concentration and organization of actin filaments, the levels of myo-II molecular motors, the distribution of microtubules, the localization of cellular organelles, and the asymmetric shape of the cell, see Fig. I.2a. The polarization of motile cells may be induced by external gradient signals or spontaneously, through an intrinsic mechanism that produces and sustains directional persistence, see Fig I.2b. The precise mechanism by which cells obtain polarity remains an open question. In theoretical descriptions, this question is typically addressed by incorporating advection-diffusion-reaction equations for actin and myosin, and/or generic signaling proteins (see, e.g., Kruse et al (2006); Kozlov and Mogilner (2007); Mori et al (2008); Shao et al (2012); Camley et al (2013); Maiuri et al (2015)).

The classical view of the component processes driving the crawling motion of a single cell (as summarised in Ananthakrishnan and Ehrlicher (2007)), are illustrated in Fig. I.2c. These include: (i) actin-based protrusion of the leading edge, (ii) adhesion to the substratum at the cell front and de-adhesion at the cell rear, and (iii) translocation of the cell body by contraction of the actomyosin cortex at the rear. Sustained mesenchymal motility is thought to be achieved by a cycle of these processes, as first suggested in Abercrombie et al (1971). It is therefore a highly complex mechano-chemical phenomenon that must be coordinated spatio-temporally.

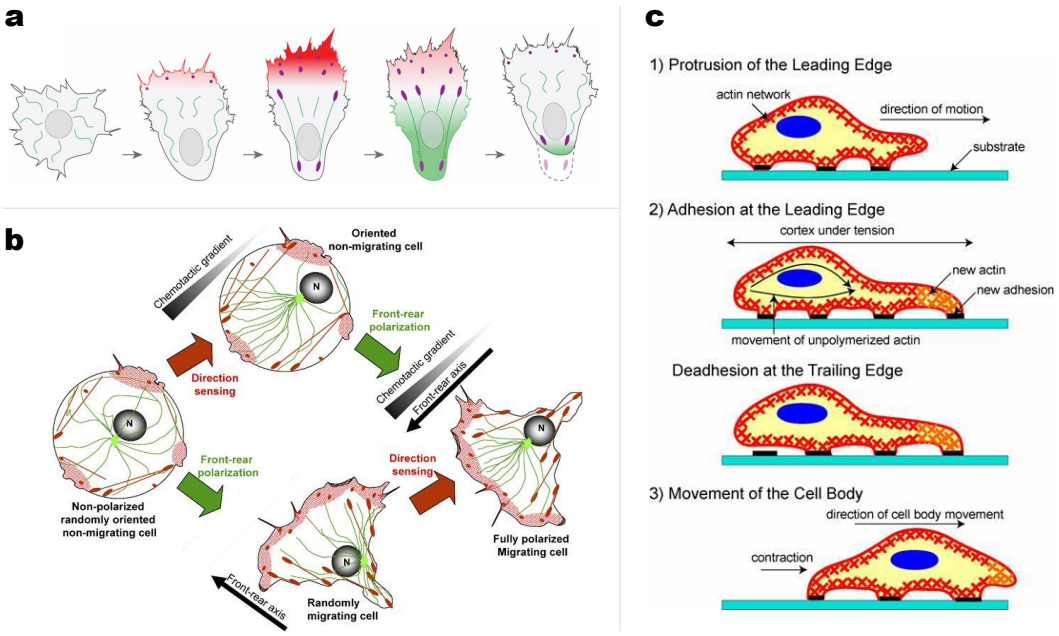

Fig. I.2 ***Polarization and translocation of crawling cells***. *a) Illustration of cell polarization: from a symmetric (non-motile) state on the left to a polarized (motile) state on the right (adapted from Reig et al (2014)). This image highlights typical polarity markers, e.g., actin polymerisation-dependent processes (red), cell-substrate adhesive structures (purple) and myosin II-dependent events (green). b) Schematic of cell polarization in the presence or absence of external guidance cues (adapted from Etienne-Manneville (2008)). c) Illustration of the stages in typical (mesenchymal) motility (taken from Ananthakrishnan and Ehrlicher (2007)). The polarized cell extends a forward protrusion by actin polymerization at the leading edge. This edge then adheres to the surface on which the cell is moving. Finally, the cell body is pulled forward by de-adhesion and contraction of the cell rear.*

I.2.5 Amoeboid vs. mesenchymal motility

Cell migration phenotypes have been broadly classified into two main modes: (i) the mesenchymal mode, which is characterised by strong specific adhesion to the surrounding environment and critically powered by actin polymerisation, and (ii) the amoeboid mode, which in extreme cases involves only weak non-specific interactions with the environment and is characterised by high contractility levels of the actomyosin cortex (see Paňková et al (2010); Friedl and Wolf (2010); Paluch et al (2016) for reviews, Fig. I.3 for examples and Fig. I.4 for a schematic).

In mesenchymal migration (Fig. I.3 (left) and Fig. I.4a), cells typically exhibit a highly organized cytoskeleton with actin-rich protrusions at the leading edge of the cell, known as filopodia and lamellipodia Paňková et al (2010). Directional locomotion is achieved by actin polymerization at the cell front, the generation of cell-substrate adhesions, and myosin-based contractility at the cell rear (see Fig. I.2c). This mode of migration is

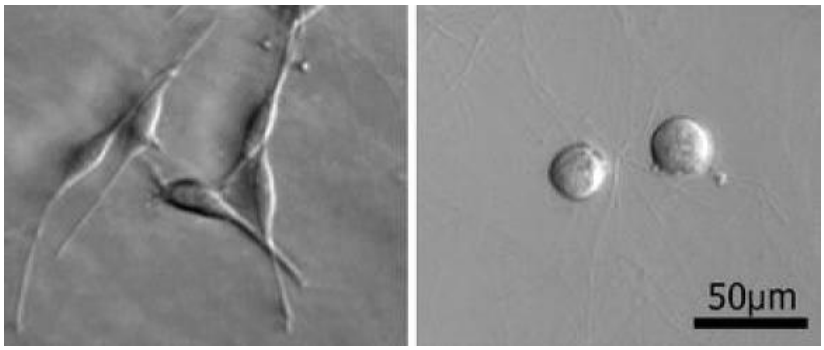

Fig. I.3 ***Examples of mesenchymal and amoeboid motility phenotypes in cancer cells***. *Left: mesenchymal morphology of K4 sarcoma cells. Right: amoeboid morphology of A3 sarcoma cells. Figure taken from Paňková et al (2010)).*

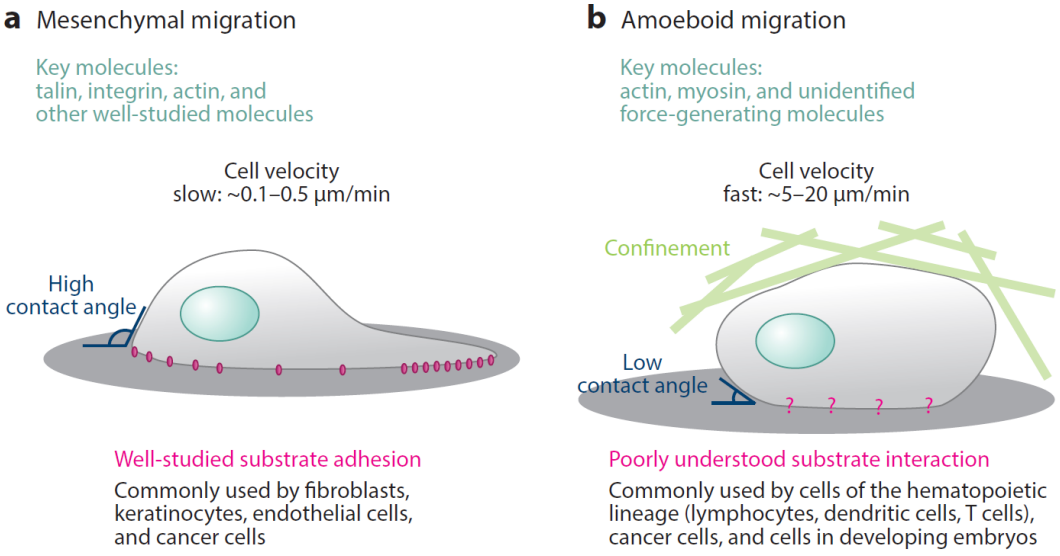

Fig. I.4 ***Overview of mesenchymal and amoeboid migration***. *Key characteristics of the two modes, highlighting (i) the important molecules involved, (ii) typical speeds, (iii) typical shapes, (iv) environments which facilitate each mode (with pink dots denoting cell-substrate linkage), and (v) typical cell lines classified in each mode. Figure taken from Paluch et al (2016).*

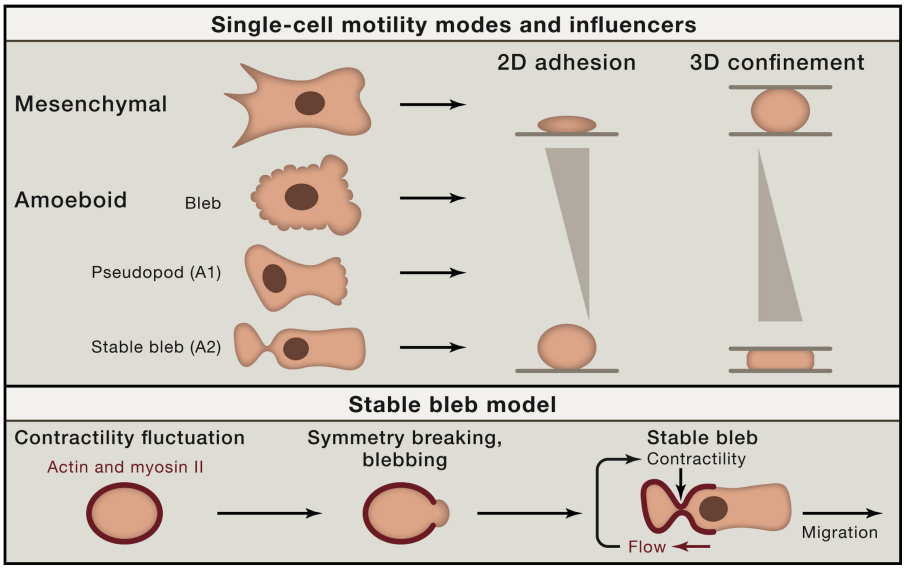

Fig. I.5 ***Motility modes and their influencers.*** *Cells can switch between mesenchymal motility and various forms of amoeboid motility, depending on cell-substrate adhesiveness and the degree of 3D confinement. Figure taken from Welch (2015).*

characterized by fairly low speeds ($\sim$ 0.1–0.5 μm/min) owing the low turnover of integrin-mediated focal adhesions Palecek et al (1997). Given that new attachments must form at the cell front while old attachments must break at the cell rear, the migration speed is highly dependent on the specifics of the cell-substrate adhesiveness. Indeed, the maximal speed in mesenchymal motility is both predicted DiMilla et al (1991) and observed Palecek et al (1997) to occur at an intermediate ratio of adhesion strength to contractile forces. Mesenchymal cell types include fibroblasts, keratinocytes, endothelial cells, and various cancer cells Paňková et al (2010); Friedl and Wolf (2010); Paluch et al (2016).

In amoeboid migration, cells typically have a less organized cytoskeleton and exhibit a smoother, more rounded morphology, akin to the *Dictyostelium* amoeba Paňková et al (2010). Protrusions in this mode include pseudopods, which are transient arm like projections, and blebs, which are membrane bulges arising from membrane-cortex detachments. Force transmission by the substratum is generally achieved through friction rather than adhesion sites Paluch et al (2016) and studies have suggested that this mode is powered by cortical contractility and actin retrograde flows (see, e.g., Bergert et al (2015); Ruprecht et al (2015); Liu et al (2015)). Compared to mesenchymal motility, amoeboid cells can reach much faster speeds, in the range 2–25 μm/min, depending on the cell type and the external environment Paňková et al (2010). Amoeboid cell types include lymphocytes, dendritic cells, T cells, cells in developing embryos, and some cancer cells Paňková et al (2010); Friedl and Wolf (2010); Paluch et al (2016).

The qualitative mesenchymal-amoeboid classification is somewhat arbitrary, as migrating cells do not necessarily fall under one mode or the other Friedl and Wolf (2010). In fact, it was shown over the last decade that environmental cues could trigger dramatic phenotypic changes and induce prototypical 'amoeboid' motility in several 'mesenchymal'

cell types Lämmermann et al (2008); Balzer et al (2012); Liu et al (2015); Ruprecht et al (2015); Bergert et al (2015). For instance, it was shown in Liu et al (2015) that low adhesion and geometric confinement can prompt ameoboid-like motility in fibroblasts, the canonical example of mesenchymal motility. Many cell types tested in confinement have produced various amoeboid morphologies, including extensive blebbing, pseudopods, as well as a new amoeboid submode characterized by a large stable bleb at the cell front Liu et al (2015); Ruprecht et al (2015), see Fig. I.5.

Generally, the key molecular components driving amoeboid motility (i.e., cortical actomyosin and the cell plasma membrane) are thought to be conserved across cell types. However, a puzzling array of amoeboid shapes has been observed in various environments, including quasi-2D confinement Bergert et al (2012); Liu et al (2015); Ruprecht et al (2015); Yang et al (2019). One wonders if this morphological heterogeneity is controlled by the same key parameters that underlie the motility apparatus. In this thesis, we attempt to shed light on this question by studying a simplified physical model of confined cell motility and morphodynamics.

I.3 Theoretical models

Historically, most *in-vitro* studies of motility have concentrated on mesenchymal cell migration on flat 2D surfaces. Following this trend, physical models of the problem, aimed at deciphering the minimal building blocks of motility, have focused primarily on the mesenchymal (adhesion and polymerization-based) mode, see, e.g., Lauffenburger (1989); DiMilla et al (1991); Mogilner and Oster (1996); Mogilner et al (2001); Dawes et al (2006); Kruse et al (2006); Kozlov and Mogilner (2007); Callan-Jones et al (2008); Doubrovinski and Kruse (2011); Ziebert et al (2012); Shao et al (2012); Blanch-Mercader and Casademunt (2013); Camley et al (2013); Löber et al (2014), with fewer descriptions of the amoeboid (contractility or friction-based) mode Gracheva and Othmer (2004); Hawkins et al (2009, 2011); Callan-Jones and Voituriez (2013); Recho et al (2013); Farutin et al (2013); Dreher et al (2014); Bergert et al (2015); Lewis et al (2015); Wu et al (2015). In all, the extensive modeling efforts have made use of several theoretical tools, such as reaction-diffusion equations (as in Gracheva and Othmer (2004); Mori et al (2008); Doubrovinski and Kruse (2011); Shao et al (2010); Camley et al (2017)), active gel hydrodynamics (as in Callan-Jones et al (2008); Hawkins et al (2009, 2011); Tjhung et al (2012); Marchetti et al (2013); Blanch-Mercader and Casademunt (2013); Recho et al (2013); Prost et al (2015); Tjhung et al (2015)), and phenomenological equations based on symmetry considerations (as in Ohta et al (2016)). Analytical treatments were mostly limited to 1D Mogilner et al (2001); Dawes et al (2006); Hawkins et al (2009); Carlsson (2011); Recho et al (2013); Maiuri et al (2015); Lavi et al (2016), while 2D and 3D models typically required numerical simulations. Further discussion on the numerical approaches is given in the foreword to Chapter III.

Here, we will outline two 1D models and one 2D model of particular relevance to our own formulation. For more comprehensive reviews on the theoretical literature, see Holmes and Edelstein-Keshet (2012); Danuser et al (2013); Ziebert and Aranson (2016).

I.3.1 Rigid 1D models

Universal coupling of cell speed and cell persistence (UCSP)

Let us first comment on the significance of this model, originally proposed in Maiuri et al (2015), to our previous (MSc) study Lavi et al (2016), and to the main topic of this PhD thesis. In Lavi et al (2016), we describe a coupling between the UCSP motility mechanism (a deterministic version) and the antigen capture function of dendritic cells (DCs), see Fig. I.6. The model focuses on immature DCs, which are known to scan tissues for pathogens (viruses and bacteria) and capture them by means of a vesicle-based 'drinking' process called macropinocytosis. It was observed in Chabaud et al (2015) that the motility and macropincytosis functions of DCs were competing for the myo-II molecular motor. Our work in Lavi et al (2016) links the generic UCSP motility model with the macropinocytosis that takes place at leading edge of the DC. The coupled model predicts both persistent and oscillatory migration patterns, akin to those exhibited by DCs in linear micro-fabricated channels Chabaud et al (2015). As for this thesis, the work presented in Chapter II, which was not aimed specifically at extending the UCSP model, can in fact be interpreted as a deterministic 2D analogue. For these reasons, this introductory part is somewhat extended and goes into the important details.

For context, the model proposed in Maiuri et al (2015) was aimed at explaining the observed positive correlation between the mean cell speed and mean persistence time in non-directed 'random' motility experiments performed in the "First World Cell Race" Maiuri et al (2012). The idea was to offer a conserved universal principle that would apply to all motile cell types. Hence, it was suggested that the speed-persistence coupling is mediated by the commonly-observed retrograde flow of actin from the front to the rear of the cell. This actin flow is powered by the combined forces of actin polymerization at the leading edge and actomyosin contraction at the trailing edge. Retrograde flow can also reinforce these processes by rearwards advection of actin-binding molecules such as myosins or inhibitors of actin polymerization (e.g., arpin) Svitkina et al (1997). Indeed, it was found experimentally that myo-II light chain (MLC, the molecule that comprises the actin-binding head of myosin) responds to an increase of actin retrograde flow by a strong rearward localization (see Fig. I.7a,b). In addition, the actomyosin cortex is known to couple to the substratum via friction and/or adhesion sites. Hence, the actin retrograde flow applies traction forces that could induce forward cell motion Mogilner and Oster (1996); Svitkina et al (1997); Jurado et al (2005).

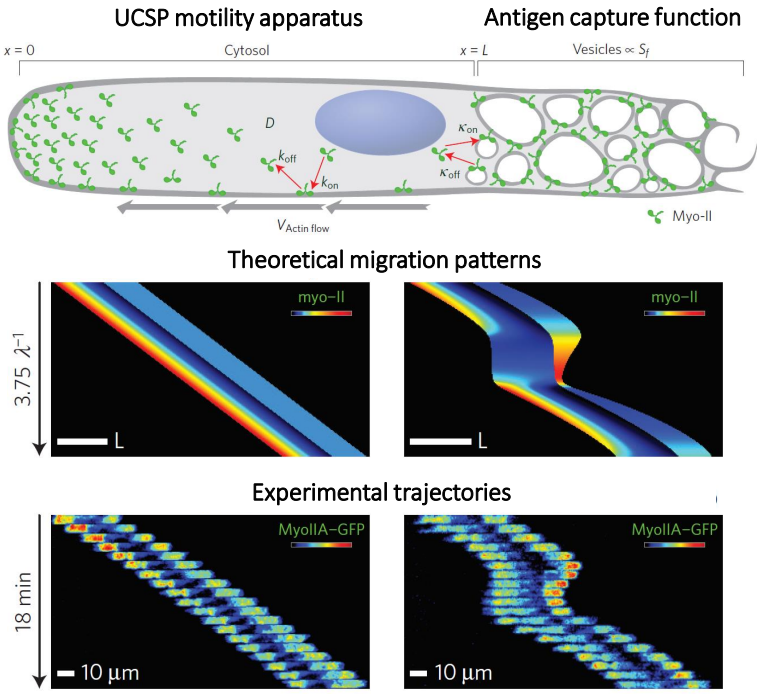

Fig. I.6 ***The dendritic cell model: UCSP motility and antigen capture compete for myo-II.*** *Top: schematic of the coupled 1D model for immature dendritic cell migration in microchannels. In the UCSP mechanism, actin retrograde flow advects myo-II motors to the rear, thereby enforcing the flow and producing locomotion (towards the right). At the leading edge, the cell produces actin-based vesicles that recruit myo-II. Bottom: comparison between theoretical and experimental kymographs, showing the myo-II density in the moving cell as a function of time (y-axis). These panels demonstrate both persistent and oscillatory 'stop-and-go' patterns. Figure adapted from Lavi et al (2016). Experiments are from Chabaud et al (2015).*

The model in Maiuri et al (2015) assumes an established polarity axis of the cell, which allows to conceptually reduce the problem to one spatial dimension (disregarding morphological aspects). It describes a rigid linear cell (of length L) containing a diffusive back-polarity marker (of concentration $c(x,t)$), which binds to actin filaments that are subject to retrograde flow (of mean amplitude $V(t)$), see Fig. I.7c. Note that V refers to the average velocity of actin in the reference frame of the cell, which moves forward in the lab frame with the velocity v. By the assumption of constant friction, v is linearly proportional to V. The basic idea behind the speed-persistence coupling is that $c(x,t)$ is advected by $V(t)$, which is itself driven by a front-rear inbalance in $c(x,t)$.

Assuming fast equilibration of the marker (with respect to the actin flow), the mean concentration is approximated by the quasi-stationary state:

$$\bar{c}_V(x) = Ce^{-\tilde{V}x/\tilde{D}} \tag{I.1}$$

where $\tilde{V} = Vk_{\text{on}}/(k_{\text{on}}+k_{\text{off}})$ and $\tilde{D} = Dk_{\text{off}}/(k_{\text{on}}+k_{\text{off}})$ (with D representing the diffusion coefficient of unbound molecules and k_{on}, k_{off} denoting the on/off binding rates to actin,

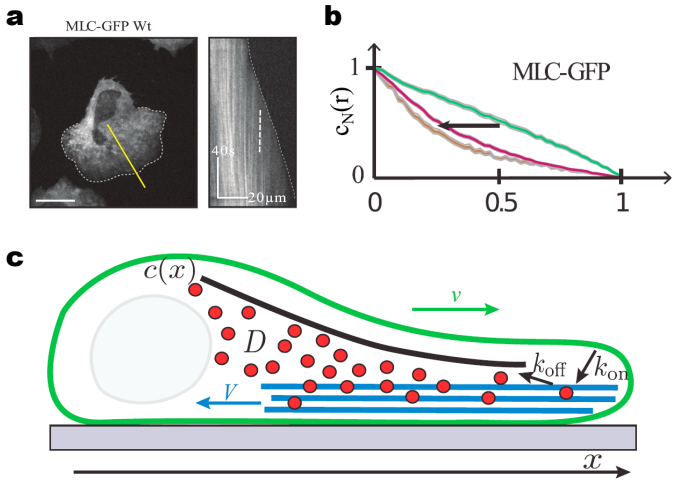

Fig. I.7 ***The UCSP model***. *(a) Left: fluorescence image of MLC-GFP localization in migrating wild-type (Wt) dendritic cell under 2D confinement. Dashed line marks the cell border. Scale bar in µm. Right: kymograph performed along the yellow line. White dashed line indicates retrograde myosin flow in the lab reference frame. (b) Normalized concentration profile of MLC as a function of normalized position x along the cell polarity axis. Colors indicate different cell-substrate adhesion strengths. Arrow shows the shift of MLC concentration toward the cell rear with increasing actin retrograde flow. (c) Schematic of the UCSP model. Polarity factors are shown as red dots, actin filaments are in blue, cell outline is green, and external substrate is gray. Figure adapted from Maiuri et al (2015).*

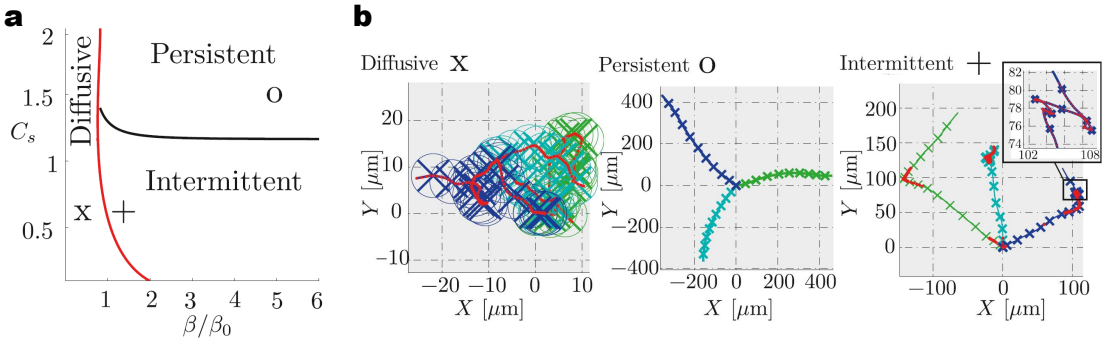

Fig. I.8 ***UCSP motility phases***. *(a) Motility phase diagram in the β–C_s plane. Symbols (X,O,+) mark the parameters used for the simulated trajectories in (b). Colored crosses in (b) indicate cell positions at regular time intervals. Circles in the diffusive case mark the cell length L. Figure adapted from Maiuri et al (2015).*

see Fig. I.7c). In addition, C is a normalization factor that depends on V and L. Note that the exponential profile in Eq. (I.1) represents the stationary solution to an effective 1D convection-diffusion equation with no-flux boundary conditions (assuming uniform stationary V). Due to noise in the transport equation, the marker concentration also fluctuates about $\bar{c}_V(x)$.

The dynamics of actin flow V and the polarity orientation angle ϕ are defined by

$$\begin{aligned} \dot{V} &= \gamma(V - V^*) + \frac{K}{2V} + \sqrt{K}\zeta_V, \quad \textit{with } V^* := \beta\left(\frac{c^n(0,t)}{C_s^n + c^n(o,t)} - \frac{c^n(L,t)}{C_s^n + c^n(L,t)}\right) \\ \dot{\phi} &= \frac{K}{V}\zeta_\phi \end{aligned} \tag{I.2}$$

where γ^{-1} is a relaxation time scale associated with acin flow fluctuations, β is a parameter controlling the intensity of the coupling (also corresponding to the maximal actin speed), C_s is a saturation parameter for the marker concentration (meaning the maximal concentration of 'activated' molecules), K controls the amplitude of fluctuations, and ζ_V, ζ_ϕ represent Gaussian white noise of variance unity. We emphasize that the driving force in Eq. (I.2) is formulated as a Hill-type response function of index n. A simple default choice is $n = 1$ as all moderate values produce qualitatively similar results.

Remark I.3.1. *The authors in Maiuri et al (2015) justify V^* by considering an active gel-like description of non-uniform (and hence compressible) actin velocity $V(x)$ subject to either (i) actin depolymerization induced by c at the edges, or (ii) contractile stress induced by c in the bulk. For both options, they obtain the model above by calculating the mean of $V(x)$. Note that similar 1D descriptions in which $V(x)$ is compressible were proposed in Carlsson (2011); Recho et al (2013).*

The stochastic model (with noise in both c and V) predicts a rich motility phase diagram in the parameters β and C_s, see Fig. I.8. The phases are: (i) 'diffusive' cell migration, whereby the speed-persistence coupling β is too weak to overcome the combined effects of friction and marker diffusion, (ii) 'persistent' migration, in which β is strong and the cell obtains steady motility (with fluctuations due to noise), and (iii) 'intermittent' migration (corresponding to the low C_s regime), whereby the cell stochastically switches between 'diffusive' and 'persistent' motility. Theoretical trajectories in each phase are demonstrated in Fig. I.8b. It was also shown in Maiuri et al (2015) that experimental cell trajectories could be broadly classified into these three phases.

The main result in Maiuri et al (2015), obtained by statistical analysis of the stochastic equations of motion, was a monotonic (exponential) relationship between the mean persistence time τ and mean speed V, i.e., $\tau = Ae^{\lambda V}$ (with A and λ depending on parameters). It was demonstrated that such a relationship can fit the experimental data very well, at the level of all cell lines studied in Maiuri et al (2012).

Pushing off the walls: cell migration in quasi-1D confinement

This model was proposed in Hawkins et al (2009) to explain confinement-induced motility observed in pioneering *in-vitro* experiments of dendritic cell migration though linear micro-fabricated channels (see Fig. I.9a). Note that, compared with the UCSP, this

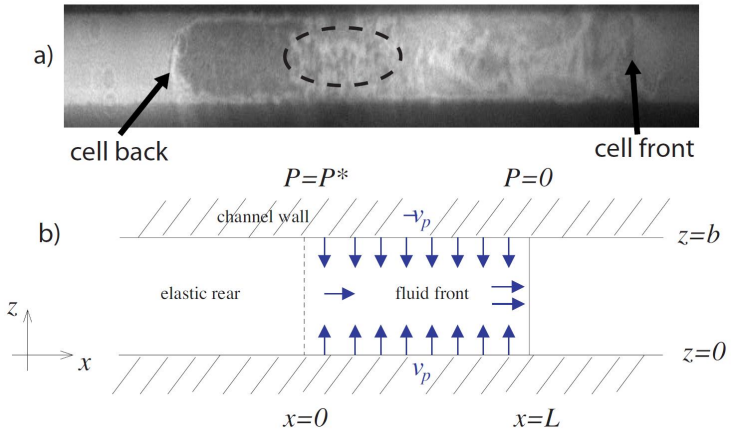

Fig. I.9 ***Pushing off the walls: a mechanism of cell motility in 1D confinement***. *a) RICM image of a dendritic cell moving to the right in a channel of 4μm width. The dark zone at the back of the cell (left) indicates a strong contact of the membrane with the channel wall (independent of the nucleus, dotted line), compared to the cell front (right). The typical observed velocity reaches 12 - 15μm/min in channels. b) Channel geometry and model schematic. The gel is fluid at the front ($0 < x < L$) and elastic at the rear ($x \leq 0$). In the fluid phase, the gel polymerizes against the channel walls with speed v_p. Arrows show the flow direction. Figure taken from Hawkins et al (2009).*

model is considerably more complex as it integrates active-gel hydrodynamics with phenomenological friction and polymerization dynamics. Here, we describe the assumptions and main result, and also comment on the connection to our own formulation.

The model considers an incompressible viscoelastic active-gel confined in a bidimensional channel of width b (along the z axis, see Fig. I.9b). The gel is assumed to behave as a viscous fluid with velocity (v_x, v_z), extending from $x = 0$ to the leading edge ($x = L$). For $x \leq 0$, the gel is assumed to behave as an elastic medium, and hence the liquid velocity goes to zero at $x = 0$. This qualitative change in the material property is linked to the cytoskeleton of dendritic cells, which has a significantly denser concentration of linkers in a trailing edge structure called the uropod Serrador et al (1999). In addition, the model assumes that the liquid gel polymerizes against the confining walls (in the $\hat{z}$ direction) with speed $v_p \equiv v_z(x, z = 0) = -v_z(x, z = b)$, and depolymerizes in the bulk with rate k_d. The constitutive relation for the liquid is given by $\sigma_{ij} = \eta(\partial_i v_j + \partial_j v_i)$, where σ is the deviatoric stress tensor and η is the shear viscosity.

In the lubrication approximation ($b \ll L$), the gap-averaged flow v of the fluid in the $\hat{x}$ direction is determined by an effective Darcy's law:

$$v(x) = -\frac{b^2}{12\eta}\left(1 + \frac{6\eta}{b}\xi^{-1}\right)\frac{\mathrm{d}P}{\mathrm{d}x} \tag{I.3}$$

where ξ represents friction between the gel and the walls. In principle, ξ depends on P and σ_{zz} (the normal deviatoric stress component on $z = 0$ and $z = b$). According to Eq.

(I.3), finite velocity is achieved if the system sustains a decreasing pressure profile from the rear to the front of the cell.

Remark I.3.2. *In our description of a cell in 2D confinement, the internal viscous flow also relies on the classical lubrication approximation, which we provide in Appendix A.1. Note that, if the fluid-substrate friction ξ is constant (which is not the case here), the relation in Eq. (I.3) does not change qualitatively at the limit $\xi \to \infty$. In this limit, which corresponds to no-slip conditions, the gap-averaged flow v is still associated with an effectively finite friction.*

The mass balance equation, which reads $\frac{\mathrm{d}v}{\mathrm{d}x} = 2v_p/b - k_d$, defines an ODE problem for $P(x)$ that should be solved with two boundary conditions. By neglecting friction with the surrounding fluid, one has $P(x = L) = 0$, and since $v(x = 0) = 0$, one has $P'(x = 0) = 0$. The main challenge is to solve this equation with the particular choices for $\xi(P, \sigma_{zz})$ and $v_p(P, \sigma_{zz})$. By incorporating (i) a theoretical relation for the dependence of gel-substrate friction on the total normal stress applied, and (ii) a standard ratchet-based result for the rate of polymerization, it is assumed that (i) $\frac{b}{6\eta}\xi = \tilde{\xi}_0 e^{\beta(P-\sigma_{zz})}$, and (ii) $v_p = v_p^0 e^{-\alpha(P-\sigma_{zz})}$. As this problem for $P(x)$ could not be solved analytically, the authors employ a semi-analytical iterative scheme that efficiently converges on the solution. Indeed, the solution of $P(x)$ is monotonically decreasing. It was also demonstrated that the pressure gradient increases with β and decreases with α. With $P(x)$ resolved, the idea is that the forward velocity V of the fluid front is determined by $v(L) + v_p(L)$ (with $v(L)$ obtained through Eq. (I.3)). Then, to conserve the cell mass, it is further assumed that the gel at the trailing edge (the uropod) depolymerizes with the speed V. Hence, L is kept constant and V defines the cell speed.

At the crux of the proposed mechanism, the pressure $P(x)$ is built up towards the cell rear owing to the exponential dependence of the friction ξ on the pressure itself. Hence, the mechanism is largely independent on specific adhesion properties. By also incorporating actin polarization and myosin contractility, as prescribed in active gel theory Kruse et al (2004), the model predicts an increased velocity, which is known experimentally. Nevertheless, myosin is not essential to achieve locomotion in this model.

The significance of this work is that, to best of our knowledge, it offered the first physical mechanism of cell motility that relates directly to geometric confinement. The model highlights the fact that, unlike the classical picture of cell crawling on substrates, confined motility could be achieved through an intrinsic adhesion-less process that sustains pressure build up towards the cell rear. Such a process is also described in our 2D model, albeit through a different mechanism that is, in fact, more similar to the UCSP.

Remark I.3.3. *Two limitations of this effective 1D motility model should be mentioned. First, the model is rather complicated, involving (i) many assumptions, and (ii) many parameters. From a minimalistic point of view, these factors make the model quite difficult to solve and thus hard to interpret analytically. Second, the model does not account for the symmetry-breaking phenomenon (the cell polarization) that must precede the assumed front-rear organization of the gel.*

I.3.2 Deformable 2D model

Actin-based fragment that polymerizes on a free boundary

This model was originally proposed in Callan-Jones et al (2008) and further analyzed in Blanch-Mercader and Casademunt (2013). Much like our own study, the aim here was to construct a mathematical description of reduced complexity to elucidate the underlying mechanisms connecting cell motion to cell shape. Similarly to the work discussed in the previous subsection Hawkins et al (2009), the equations in Callan-Jones et al (2008) are based on active gel hydrodynamics and Darcy's Law. The main differences are that this model (i) considers a quasi-2D problem with free boundaries and surface tension, and (ii) assumes that the material is homogeneous. It was shown in the original paper Callan-Jones et al (2008) that the model captures a viscous fingering-like morphological instability Bensimon et al (1986); Casademunt (2004). However, it was not clear if it also supports sustained directional motion (motility). The analysis provided five years later in Blanch-Mercader and Casademunt (2013) has extended the understanding of the governing equations and demonstrated that spontaneous motility is indeed supported.

The model describes a thin layer of active polar gel with a sharp deformable interface, depicting the actin cytoskeleton bounded by a membrane, see Fig. I.10. It is assumed that the relevant dynamics are sufficiently slow as to adopt a viscous fluid description that neglects elastic effects in the gel. By disregarding the dynamics of the actin polarization field $\mathbf{p}$, and assuming that no myosin motors are present, the constitutive law reduces to that of an isotropic viscous fluid with shear viscosity η. Assuming either strong friction ξ with the substratum or, alternatively, that the fluid is confined between two parallel plates (a Hele-Shaw geometry), it follows that the 2D flow $\mathbf{v}$ is governed by Darcy's law, see Eq. (I.4). Activity enters the model through actin polymerization on the boundary with constant velocity v_p, and depolymerization in the fragment interior at constant rate k_d. The depolymerization introduces negative divergence of the flow, see Eq. (I.5). As in classical Hele-Shaw problems, the fluid pressure $P(x, y)$ is determined on the boundary by the Young-Laplace condition, see Eq. (I.6). Finally, the polymerization of the gel enters by modification of the kinematic condition, see Eq. (I.7).

$$\mathbf{v} = -M\nabla P \qquad \text{in } \Omega(t) \tag{I.4}$$

$$\nabla \cdot \mathbf{v} = -k_d \qquad \text{in } \Omega(t) \tag{I.5}$$

$$P = \gamma\kappa \qquad \text{on } \partial\Omega(t) \tag{I.6}$$

$$V_\mathrm{n} = \mathbf{v} \cdot \mathbf{n} + v_p \qquad \text{on } \partial\Omega(t) \tag{I.7}$$

where $M = 1/\xi$ if friction dominates or $M = \frac{b^2}{12\eta}\left(1 + \frac{6\eta}{b\xi}\right)$ in confinement (see also Eq. (I.3)). The parameter γ is the surface tension and V_n represents the velocity of the sharp interface in the normal direction ($\mathbf{n}$).

The model given by Eqs. (I.4) – (I.7) has a stationary solution defined by a circle of radius $R_0 = 2v_p/k_d$ (representing global mass balance). The authors in Callan-Jones et al (2008) performed a linear stability analysis of the steady state by taking $R(\theta, t) = R_0 + \sum_m \delta R_m(t)\cos(m\theta)$, where m are integers and $\delta R_m(t) \ll R_0$. This analysis shows that $\delta\dot{R}_m = \lambda(m)\delta R_m$, with the dispersion relation given by $\lambda(m) = -R_0^{-3}M\gamma m(m^2 - 1) + k_d(m-1)/2$. It follows that: (i) the mode $m = 0$, which represents a uniform

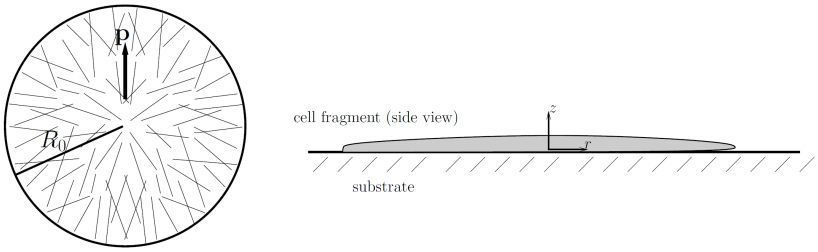

Fig. I.10 ***Thin fragment of actin-based polar gel***. *Left: schematic drawing of actin cytoskeleton in the unperturbed, radial state (note that* **p** *refers to actin polarization, neglected in the case presented here). Right: side view of the fragment. Figure taken from Callan-Jones et al (2008).*

perturbation of the radius, is strictly stable ($\lambda(0) = -k_d/2$), (ii) the mode $m = 1$, which represents infinitesimal translation, is marginally-stable ($\lambda(m) = 0$), meaning that self-propulsion is not supported at the linear level, and (iii) for each $m \geq 2$ (the morphological modes), a bifurcation occurs at $k_d R_0^3 \geq 2M\gamma m(m+1)$. In words, the combined effects of active polymerization and depolymerization destabilize the fragment shape by acting against the stabilizing surface tension force.

The authors in Blanch-Mercader and Casademunt (2013) have used a simple mapping of the coordinate $(x,\, y)$ to the complex number $(z = x+iy)$ to derive by standard calculus the following exact relations:

$$\dot{A} = v_p L - k_d A, \qquad \dot{R}_A = \frac{v_p L}{A}(R_L - R_A) \tag{I.8}$$

where $A(t)$, $L(t)$ are, respectively, the fragment area and the perimeter (the length of $\partial\Omega(t)$), and $R_A(t)$, $R_L(t)$ are, respectively, the center of mass coordinates of the fragment and the boundary (both defined in the complex plane).

The results in Eq. (I.8) are quite intuitive. The equation for the fragment area $A(t)$ simply describes the uniform injection of mass on the perimeter (at rate v_p) and the uniform suction of mass in the bulk (at rate k_d). The center of mass velocity $\dot{R}_A(t)$ is given by flow from a point source (centered at R_L) to a point sink (centered at R_A). This equation reveals that net motion is achieved whenever the shape is asymmetric (meaning $R_A \neq R_L$). In particular, steady velocity is obtained if there exist asymmetric steady states. To explore this question, the authors track the evolution of the shape by means of conformal mapping techniques Bensimon et al (1986). Without going into technical details, we note that this analysis provides several important insights. First, it proves the nonlinear instability of the center of mass translation. Second, it allows to trace the multiple (asymmetric) stationary solution branches emerging from the bifurcation of each shape mode $m \geq 2$ (demonstrated in Fig. I.11a). Note here that all bifurcations were found to be subcritical. Lastly, the conformal mapping framework is used to build a numerical simulation of the moving-boundary dynamics. This simulation demonstrates the morphological instability of the circle, the onset of translation, and the stability of the resolved steady-states (see example in Fig. I.11b).

Remark I.3.4. *In this model, the inner fluid is identified as polymerized actin, while the actin monomers in solution and the cytosol are ignored. Accordingly, mass is continuously*

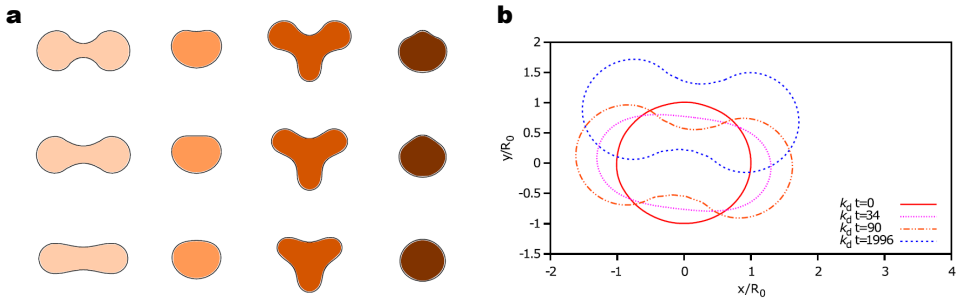

Fig. I.11 ***Steady moving states and numerical simulation***. *a) Examples of stationary propagating shapes. The first two columns correspond to two distinct solution branches bifurcating at the $m = 2$ critical point. The last two columns correspond to branches bifurcating the $m = 3$ point. Tension increases from top to bottom and speed increases from bottom to top. b) Example of numerical time evolution of a randomly perturbed circular interface with finite surface tension. Figure adapted from Blanch-Mercader and Casademunt (2013).*

added on the boundary and eliminated in the bulk. This is in contrast with our model, which deals with a passive viscous fluid (the cytosol) whose mass is locally conserved. Hence, the two models describe physical systems that are quite different from each other. Nevertheless, both formulations share clear mathematical similarities and fall under the same class of dynamic boundary-value problems. For this reason, we adopt in our study some of the illuminating analysis tools that were used here.

I.4 Overview of this thesis

This thesis focuses on a minimal moving-boundary model of both mesenchymal and amoeboid motility under quasi-2D confinement. The main objective behind this study was to characterize the dynamics of the most basic cell components required for sustained directional locomotion and cell shape changes (in the spirit of Callan-Jones et al (2008); Blanch-Mercader and Casademunt (2013)). At the same time, we were aiming for a physically-sound description that would conserve cytoplasmic mass while adhering to the geometric constraint imposed by vertical confinement (as in Hawkins et al (2009)). In terms of complexity, the idea was to work with a mathematical model that is sufficiently simple (with a small number of phenomenological parameters), as to provide analytical insights, and yet sufficiently rich, as to capture a range of patterns that could be linked to experimental observations (as in Maiuri et al (2015)). In constructing and analysing our model, we incorporated ideas from the works outlined in the previous section Callan-Jones et al (2008); Blanch-Mercader and Casademunt (2013); Hawkins et al (2009); Maiuri et al (2015).

The thesis is organized into two main parts. The first part (Chapter II) introduces the formulation of our model and provides many explicit results and insights by mathematical analyses of the problem. The second part (Chapter III) introduces a finite-element simulation of our equations of motion. This computational tool was constructed in order to explore the limit behaviours of our isolated cell system and also for introducing

various model extensions (motivated by experimental studies). Both parts are concluded and discussed at the end of each chapter. In Chapter IV, we propose avenues for future research. Appendices A and B provide preliminaries, extended mathematical derivations and technical details for Chapters II and III, respectively.

In Appendix C, we attach an additional study that deals with the interplay between cellular blebbing and plasma membrane tubulation. We provide the preprint of our article along with its supplementary information. This study also falls under the theme of amoeboid motility. However, we chose to keep it separate from the principal subject matter of this thesis as it deals more specifically with the plasma membrane physics underlying the expansion mechanisms of bleb-type protrusions. The modeling approach is also quite different as it relies on equilibrium thermodynamics rather than partial differential equations.

Chapter II

Analytical moving-boundary model

In this chapter, we introduce and analyze our model for the motility and morphodynamics of biological cells confined between two parallel surfaces. Unlike most previous works, we tackle the problem from the perspective of the passive cytoplasmic fluid (the cytosol) rather than the active cytoskeleton. That is, we model the cytoplasm as a confined viscous droplet that is driven on its boundary (the cell membrane) by an active, cytoskeleton-induced force. Conceivably, such a force can be generated in cells either by actin polymerisation against the membrane or by actomyosin contraction of cortical filaments, which adhere to the membrane. In our minimal model, the active force is controlled by a diffusive chemical (solute) that (i) has some affinity to the confining surfaces, and (ii) is advected by the internal cytoplasmic flow.

This part of the thesis is structured as follows. Section II.1 introduces the formulation of our model in terms of physical units. Section II.2 gives initial insights into the supported theoretical behaviours by providing the dynamic evolution laws for geometric moments. Section II.3 outlines a reduced dimensionless representation of our equations of motion, replacing the dimensional equations for the remainder of this thesis. Section II.4 provides a rigorous linear stability analysis characterizing the rest-state solution. This analysis shows that a global polarization-translation (motility) mode becomes unstable beyond a critical threshold of solute activity. Upon increasing activity further, the system crosses a series of Hopf bifurcations of multipolar modes, destabilizing coupled shape-concentration waves. Section II.5 provides a semi-analytical method for computing nonlinear steadily-moving solutions. The results obtained in this section reveal how the steady-state speed and shape of traveling cells vary as functions of model parameters. In Section II.6, we discuss the significance of our findings in light of experimental observations *in-vitro* and point to some unsettled questions pertaining the limit behaviours of our system.

II.1 Formulation

We consider a fluid droplet of viscosity μ confined between two parallel plates separated by a gap h (a Hele-Shaw cell), as illustrated in Fig. II.1. Let $\mathbf{u}$ be the gap-averaged planar flow and $p = p(t, x, y)$ be the fluid pressure. The 2D moving-boundary-value problem for

the droplet is given by

$$\mathbf{u} = -M\nabla p \qquad \text{in } \Omega(t) \qquad \text{(II.1)}$$
$$\nabla \cdot \mathbf{u} = 0 \qquad \text{in } \Omega(t) \qquad \text{(II.2)}$$
$$p + F_{\text{act}}(c)/h = \sigma\kappa \qquad \text{on } \partial\Omega(t) \qquad \text{(II.3)}$$
$$V_{\text{n}} = \mathbf{u} \cdot \mathbf{n} \qquad \text{on } \partial\Omega(t) \qquad \text{(II.4)}$$

In Eq. (II.1), we present the effective Darcy's law for the flow $\mathbf{u}$, where $M = h^2/12\mu$ is the mobility. Note that $\mathbf{u}$ averages the parabolic Hele-Shaw flow profile, which approximates the solution to the Stokes momentum-balance equation in thin films, see Appendix A.1.

In Eq. (II.2), we give the fluid mas-balance equation (incompressibility condition). Note that Eqs. (II.1) – (II.2) impose that the pressure is Laplacian in the droplet domain, i.e., $\Delta p = 0$ in $\Omega(t)$.

In Eq. (II.3), we present the normal force balance on the droplet boundary $\partial\Omega(t)$. Here, σ denotes the surface tension and κ denotes the curvature. The Young-Laplace condition is perturbed in our model by an active traction force, $F_{\text{act}}(c)\mathbf{n}$, where $\mathbf{n}$ is the unit normal pointing outward (see Fig. II.1). This force is defined per unit length and is controlled locally by the gap-integrated concentration of an internal solute, $c = c(t, x, y)$. We stress that $F_{\text{act}}(c)$ can be either positive (pushing outwards) or negative (pulling inwards). In this regard, any uniform term $F_0 \in \mathbb{R}$ added to $F_{\text{act}}(c)$ would merely offset the pressure p by a constant $(-F_0/h)$ and thus be irrelevant to the dynamics. For the sake of generality, we do not specify an explicit form of $F_{\text{act}}(c)$ at this stage.

In Eq. (II.4), we present the kinematic condition, stating that the normal velocity of the sharp interface, V_{n}, is given by the normal velocity of the fluid on $\partial\Omega(t)$.

Remark II.1.1. *As we focus on the hydrodynamics of the passive cytoplasmic fluid, we do not describe directly the active cortex layer that generates F_{act}. We postulate that this force is driven either by actin polymerization against the membrane, or by the contraction of actomyosin filaments. In order to transmit the external force on the boundary, the filaments must also interact mechanically with the substrate, e.g., via cortex-substrate adhesion.*

To close our system, we formulate the internal solute transport problem. In the bulk, we assume fast adsorption on the top and bottom plates (or onto an adhered cortex), as shown in Fig. II.1. With rapid on and off rates (k_{on} and k_{off}), the quasi-2D transport dynamics are given by

$$\partial_t c + (1-a)\mathbf{u} \cdot \nabla c - D\Delta c = 0 \qquad \text{in } \Omega(t) \qquad \text{(II.5)}$$
$$D\nabla c \cdot \mathbf{n} + aV_{\text{n}}c = 0 \qquad \text{on } \partial\Omega(t) \qquad \text{(II.6)}$$

where $a = k_{\text{on}}/(k_{\text{on}} + k_{\text{off}})$ is the steady fraction of adsorbed molecules not convected by the average flow and D is an effective diffusion coefficient, see derivation in Appendix A.1.

In Eq. (II.5), we present the effective convection-diffusion dynamics. Note here that the total (convective + diffusive) solute flux is $\mathbf{j} = (1-a)\mathbf{u}c - D\nabla c$.

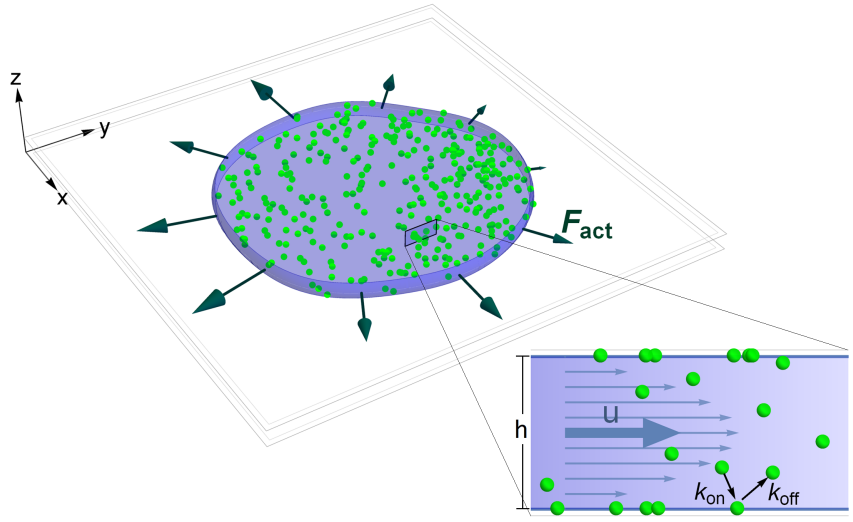

Fig. II.1 **Model illustration.** *An active actomyosin force (dark arrows) drives the motility and morphodynamics of the confined cytoplasmic droplet (blue). This force acts on the droplet free-boundary in the normal direction and is modulated locally by a diffusive solute (green). Inset: cross-section highlighting the fluid flow and solute transport within the droplet. Thin arrows mark the parabolic flow profile, induced by the pressure gradient (blue-level background). The gap-averaged flow is denoted by* $\mathbf{u}$ *(thick blue arrow). The solute binds on and off the plates with rates* k_{on}, k_{off} *and is advected by the fluid flow only in the unbound state.*

In Eq. (II.6), we impose zero solute flux on the moving boundary, i.e., $\mathbf{j}\cdot\mathbf{n} - V_{\mathrm{n}}c = 0$, where we insert the kinematic condition, Eq. (II.4). Simply put, the solute is effectively convected at a slower velocity than that of the fluid. Hence, its concentration decreases (increases) towards an advancing (retracting) front.

Remark II.1.2. *The transport problem in Eqs.* (II.5) – (II.6) *conserves the total solute* $C_{tot} := \int_\Omega c\,\mathrm{d}a$. *This follows from (i) the fact that the flow* $\mathbf{u}$ *is incompressible and there are no unbalanced reactions (sources/sinks) in* Ω *(see Eq.* (II.5)*), and (ii) the no-flux condition on* $\partial\Omega$ *(see Eq.* (II.6)*). Formally,*

$$\frac{d}{dt}\int_{\Omega(t)} c\,\mathrm{d}a = -\int_{\Omega(t)} \nabla\cdot\mathbf{j}\,\mathrm{d}a + \oint_{\partial\Omega(t)} V_n c\,\mathrm{d}l = \oint_{\partial\Omega(t)} (-\mathbf{j}\cdot\mathbf{n} + V_n c)\,\mathrm{d}l = 0$$

To this end, the solute can be any cytoplasmic protein controlling the active force-generation/adhesion machinery. In our model, we assume that the concentration c either induces an inwards pulling force or inhibits an outwards pushing force (see Fig.(II.1)). In line with this principal assumption, we define the negative linear response of $F_{\mathrm{act}}(c)$ to solute deviations about the mean planar concentration c_0:

$$F'_{\mathrm{act}}(c_0) := -\chi \tag{II.7}$$

where $\chi > 0$.

II.1.1 Perspective on the degrees of freedom

Our deterministic equations of motion (Eqs. (II.1) – (II.6)) describe the evolution of trajectories in an open shape-concentration phase space. In other words, at any point in time, the coupled PDE problem is fully determined by (i) the droplet shape and (ii) the internal solute concentration. This can be seen more clearly by first isolating the boundary-value problem for the pressure field p. Recall that $\Delta p = 0$ in $\Omega(t)$ (Eqs. (II.1) – (II.2)) and that $p = \sigma\kappa - F_{\mathrm{act}}(c)$ on $\partial\Omega(t)$ (Eq. (II.3)). In this Dirichlet problem for the Laplace equation, p is determined by the geometry Ω (which defines the curvature κ) and the solute profile c (which defines $F_{\mathrm{act}}(c)$). Once p is resolved, the flow $\mathbf{u}$ is decided via Eq. (II.1). Then, $\mathbf{u}$ defines both the shape evolution, via Eq. (II.4), and the solute transport dynamics, via Eqs. (II.5) – (II.6).

Note that the allowed shape-concentration configurations are only those that are consistent with the boundary conditions, Eqs. (II.3) – (II.4) and (II.6). Indeed, this fact constrains the phase space to a certain extent. Nevertheless, the degrees of freedom in our problem are still particularly broad; for any sufficiently smooth shape, one can imagine any arbitrary concentration field c in Ω, with a constrained profile in the vicinity of $\partial\Omega$ that will take care of the no-flux condition.

II.2 Dynamics of moments

In this section, we gain initial insights into the behaviours of our coupled moving-boundary system by deriving the dynamic laws governing the geometric moments associated with $\Omega(t)$. Similarly to Blanch-Mercader and Casademunt (2013), we use the simple mathematical trick of mapping the (x, y) coordinate to the complex number $z = x + iy$ and define the k-th order moment as

$$\mathcal{M}_k(t) = \int_{\Omega(t)} z^k \,\mathrm{d}a$$

It is easy to recognize that $\mathcal{M}_0 = A$ and $\mathcal{M}_1 = AR_A$, where A is the droplet area and R_A is the center of mass coordinate over the complex plane. We compute the time derivative of $\mathcal{M}_k(t)$,

$$\begin{aligned}
\dot{\mathcal{M}}_k(t) &= \oint_{\partial\Omega(t)} z^k V_{\mathrm{n}} \,\mathrm{d}l = \oint_{\partial\Omega(t)} z^k \mathbf{u}\cdot\mathbf{n} \,\mathrm{d}l = \int_{\Omega(t)} \nabla\cdot(z^k\mathbf{u})\,\mathrm{d}a \\
&= \int_{\Omega(t)} \mathbf{u}\cdot\nabla z^k \,\mathrm{d}a = -M\int_{\Omega(t)} \nabla p\cdot\nabla z^k \,\mathrm{d}a = -M\int_{\Omega(t)} \nabla\cdot(p\nabla z^k)\,\mathrm{d}a \\
&= -M\oint_{\partial\Omega(t)} (p\nabla z^k)\cdot\mathbf{n}\,\mathrm{d}l = M\oint_{\partial\Omega(t)} (F_{\mathrm{act}}(c)/h - \sigma\kappa)\nabla z^k\cdot\mathbf{n}\,\mathrm{d}l
\end{aligned} \tag{II.8}$$

where, in the first line, we expressed the flux of z^k through the moving boundary $\partial\Omega(t)$, substituted the kinematic condition, Eq. (II.4), and used the Divergence theorem. In the second line, we substituted incompressibility, Eq. (II.2), the effective Darcy law, Eq. (II.1), and used the harmonicity of analytic functions ($\Delta z^k = 0$). Finally, in the third line, we used the Divergence theorem again and substituted the normal force balance on the boundary, Eq. (II.3).

II.2.1 Area conservation

Substituting $k = 0$ in Eq. (II.8) gives

$$\dot{\mathcal{M}}_0(t) = \dot{A} = 0 \tag{II.9}$$

Note that this result is a straightforward consequence of fluid volume conservation, imposed in our model by incompressibility, Eq.(II.2), and the kinematic condition, Eq. (II.4).

II.2.2 External force balance

Substituting $k = 1$ in Eq. (II.8) and using Eq. (II.9), we obtain

$$\dot{\mathcal{M}}_1 = A\dot{R}_A = M \oint_{\partial\Omega(t)} (F_{\text{act}}(c)/h - \sigma\kappa)\nabla z \cdot \mathbf{n}\, \mathrm{d}l \tag{II.10}$$

Over $\mathbb{C}$, $\dot{R}_A$ represents the center of mass velocity and $\nabla z \cdot \mathbf{n} = n_x + in_y$ is the unit normal pointing outwards on $\partial\Omega(t)$. Multiplying Eq. (II.10) by h/M, and going back to $\mathbb{R}^2$, we may restate Eq. (II.10) as follows

$$-hM^{-1}A\mathbf{u}_{\text{cm}} + \oint_{\partial\Omega(t)} F_{\text{act}}(c)\mathbf{n}\, \mathrm{d}l = 0 \tag{II.11}$$

where $\mathbf{u}_{\text{cm}}$ denotes the droplet center of mass velocity over $\mathbb{R}^2$. Here, we used the fact that, over a simple closed curve, the line integral of the curvature vector vanishes: $\oint \kappa\mathbf{n}\, \mathrm{d}l = 0$.

We recognize that Eq. (II.11) represents the external force balance on the droplet. The second term on the LHS equals the net active traction force acting on the droplet boundary in the normal direction. We will now show that the first term equals the net viscous shearing force applied externally on the two fluid layers in contact with the no-slip plates. This dissipative force is given by

$$F_{\text{diss}} = \int_{\Omega(t)} \left(\tau|_{z=0}\,(-\hat{\mathrm{z}}) + \tau|_{z=h}\,\hat{\mathrm{z}}\right)\, \mathrm{d}a$$

where $\tau = \mu\left(\nabla\underline{\mathrm{u}} + (\nabla\underline{\mathrm{u}})^{\mathrm{T}}\right)$ is the 3D viscous shear stress tensor and $\underline{\mathrm{u}}$ is the 3D flow field. Given the parabolic profile of the flow, $\underline{\mathrm{u}}(x, y, z) = (u, v, 0) = -\frac{z(h-z)}{2\mu}\nabla p(x, y)$ (see Appendix A.1), we obtain $\tau\,\hat{\mathrm{z}} = \mu(\partial_z u, \partial_z v, 0) = \frac{2z-h}{2}\nabla p(x, y)$, and thus

$$F_{\text{diss}} = \int_{\Omega(t)} (h\nabla p)da = -hM^{-1}\int_{\Omega(t)} \mathbf{u}da = -hM^{-1}A\mathbf{u}_{\text{cm}}$$

Note that F_{diss} is akin to an effective friction with coefficient $h/2M$ on each plate.

II.3 Nondimensionalization

In this section, we reduce the number of independent model parameters by formulating our physical equations in terms of rescaled dimensionless variables.

We consider length in units of $R_0 = \sqrt{A/\pi}$ (the droplet radius), time in units of R_0^2/D (solute diffusion time over the droplet), solute concentration in units of $c_0 = C_{\mathrm{tot}}/A$, and pressure in units of D/M. Accordingly, the curvature (κ) will be given in units of $1/R_0$ and velocities ($\mathbf{u}$, V_{n}) in units of D/R_0. In addition, F_{act} will be given in units of Dh/M. We then make the transformation $F_{\mathrm{act}} \to F_{\mathrm{act}}/h$ to simplify the notation in Eq. (II.3).

The reduced dimensionless form of Eqs. (II.1) – (II.6) is given by

$$\mathbf{u} = -\nabla p \qquad \text{in } \Omega(t) \tag{II.12}$$

$$\nabla \cdot \mathbf{u} = 0 \qquad \text{in } \Omega(t) \tag{II.13}$$

$$p + F_{\mathrm{act}}(c) = \sigma' \kappa \qquad \text{on } \partial\Omega(t) \tag{II.14}$$

$$V_{\mathrm{n}} = \mathbf{u} \cdot \mathbf{n} \qquad \text{on } \partial\Omega(t) \tag{II.15}$$

$$\partial_t c + (1-a)\mathbf{u} \cdot \nabla c - \Delta c = 0 \qquad \text{in } \Omega(t) \tag{II.16}$$

$$\nabla c \cdot \mathbf{n} + a V_{\mathrm{n}} c = 0 \qquad \text{on } \partial\Omega(t) \tag{II.17}$$

with Eq. (II.7) translating to:

$$F'_{\mathrm{act}}(1) = -\chi' \tag{II.18}$$

The system of Eqs. (II.12) – (II.18) is defined by three dimensionless parameters:

$$a = \frac{k_{\mathrm{on}}}{k_{\mathrm{on}} + k_{\mathrm{off}}}, \quad \sigma' = \frac{M\sigma}{DR_0}, \quad \chi' = \frac{MC_{\mathrm{tot}}\chi}{DAh} \tag{II.19}$$

The dimensionless droplet area A and the total solute C_{tot} are then:

$$A = \int_{\Omega(t)} \mathrm{d}a = \pi, \quad C_{\mathrm{tot}} = \int_{\Omega(t)} c \, \mathrm{d}a = \pi \tag{II.20}$$

and the dimensionless form of the external force balance, Eq. (II.11), is

$$\mathbf{u}_{\mathrm{cm}} = \frac{1}{\pi} \oint_{\partial\Omega} F_{\mathrm{act}}(c)\mathbf{n} \, \mathrm{d}l \tag{II.21}$$

For the sake of brevity, we shall omit the primes in Eq. (II.19) hereinafter, meaning that σ, χ will denote the dimensionless parameters throughout this thesis unless stated otherwise.

II.4 Linear stability analysis

In this section, we examine the shape-concentration dynamics close to the circular homogeneous rest-state, which is a straightforward solution to our problem for all parameter values. In this state, the shape is defined by $R = 1$ and the internal solute concentration is $c = 1$. It follows that $\kappa = 1$ on $\partial\Omega$ and the resulting pressure is constant: $p = \sigma - F_{\mathrm{act}}(1)$ in Ω, meaning that $\mathbf{u} = -\nabla p = 0$. We now perturb both the shape of the droplet and the solute concentration such that $R = 1 + \delta R(t, \theta)$ and $c = 1 + \delta c(t, r, \theta)$, where $\delta R \ll 1$ and $\delta c \ll 1$. In a classical manner, our goal is to characterize the linear dynamical system in the coupled perturbations, $\delta R(t, \theta)$ and $\delta c(t, r, \theta)$.

II.4.1 Linearized equations and the characteristic function

Let us first expand the small perturbations in normal Fourier modes (in the spirit of Callan-Jones et al (2008)),

$$\delta R(t,\theta) = \sum_m \left(\delta R_{\mathrm{c}m}(t)\cos(m\theta) + \delta R_{\mathrm{s}m}\sin(m\theta)\right) \tag{II.22}$$

$$\delta c(t,r,\theta) = \sum_m \left(\delta c_{\mathrm{c}m}(t,r)\cos(m\theta) + \delta c_{\mathrm{s}m}(t,r)\sin(m\theta)\right) \tag{II.23}$$

where $m = 0, 1, 2, \cdots$, and $\delta R_m \ll 1$, $\delta c_m \ll 1$.

Similarly to Eqs. (II.22) – (II.23), we expand the resulting variation in pressure. From incompressibility, Eq. (II.13), it follows that $\Delta\delta p = 0$, and thus

$$\delta p(t,r,\theta) = \sum_m \left(A_m(t) r^m \cos(m\theta) + B_m(t) r^m \sin(m\theta)\right)$$

where we discarded Laplacian solutions that diverge at $r = 0$ (proportional to r^{-m}).

From the normal force balance, Eq. (II.14), it follows that $\delta p = \sigma\delta\kappa - \delta F_{\mathrm{act}}(c)$ on $\partial\Omega$, where $\delta F_{\mathrm{act}}(c) = F'_{\mathrm{act}}(1)\delta c = -\chi\delta c$ is the deviation in the applied active force. On the boundary, the linear deviations in the fluid pressure and solute concentration are

$$\delta p \simeq \delta p(r=1) = \sum_m \left(A_m(t)\cos(m\theta) + B_m(t)\sin(m\theta)\right) \tag{II.24}$$

$$\delta c \simeq \delta c(r=1) = \sum_m \left(\delta c_{\mathrm{c}m}(t,1)\cos(m\theta) + \delta c_{\mathrm{s}m}(t,1)\sin(m\theta)\right) \tag{II.25}$$

The curvature on $R(t,\theta) = 1 + \delta R(t,\theta)$ is

$$\kappa = \frac{R^2 + 2(\partial_\theta R)^2 - R\partial_{\theta\theta}R}{\left(R^2 + (\partial_\theta R)^2\right)^{3/2}} \simeq 1 - \delta R(t,\theta) - \partial_{\theta\theta}\delta R(t,\theta)$$

and thus

$$\delta\kappa \simeq \sum_m (m^2-1)\left(\delta R_{\mathrm{c}m}(t)\cos(m\theta) + \delta R_{\mathrm{s}m}\sin(m\theta)\right) \tag{II.26}$$

Substituting Eqs. (II.24), (II.25), and (II.26) in the force balance, we obtain the pressure amplitudes

$$A_m(t) = \sigma(m^2-1)\delta R_{\mathrm{c}m}(t) + \chi\delta c_{\mathrm{c}m}(t,1) \tag{II.27}$$

$$B_m(t) = \sigma(m^2-1)\delta R_{\mathrm{s}m}(t) + \chi\delta c_{\mathrm{s}m}(t,1) \tag{II.28}$$

We proceed by expressing a linearized version of the kinematic condition, Eq. (II.15). This task consists of finding the flow $\mathbf{u}$, the normal $\mathbf{n}$, and the velocity of the sharp interface V_{n} in terms of of the linear perturbations.

The flow is given by $\mathbf{u} = -\nabla\delta p$, and thus

$$\begin{aligned} u_r &= -\partial_r\delta p = -\sum_m mr^{m-1}\left(A_m(t)\cos(m\theta) + B_m\sin(m\theta)\right) \\ u_\theta &= -\frac{1}{r}\partial_\theta\delta p = \sum_m mr^{m-1}\left(A_m(t)\sin(m\theta) - B_m\cos(m\theta)\right) \end{aligned} \tag{II.29}$$

The normal pointing outwards on the boundary is given by

$$\mathbf{n} = \frac{\nabla\left(r - R(t,\theta)\right)}{|\nabla\left(r - R(t,\theta)\right)|}$$

Hence,

$$n_r \simeq 1\,, \quad n_\theta \simeq \sum_m m\left(\delta R_{\mathrm{c}m}(t)\sin(m\theta) - \delta R_{\mathrm{s}m}(t)\cos(m\theta)\right) \tag{II.30}$$

Using Eqs. (II.29) – (II.30), we compute the normal fluid velocity to linear order

$$\mathbf{u}\cdot\mathbf{n} \simeq u_r(r=1) = -\sum_m m\left(A_m(t)\cos(m\theta) + B_m\sin(m\theta)\right) \tag{II.31}$$

where we neglected the quadratic term $u_\theta n_\theta$ coming from the LHS.

To express the absolute velocity of the interface V_n, let us consider its $\hat{r}$ projection

$$V_\mathrm{n} n_r = \frac{dR(t,\theta)}{dt} = \lim_{\Delta t\to 0}\frac{R(t+\Delta t, \theta + \frac{V_\mathrm{n} n_\theta}{R(t,\theta)}\Delta t) - R(t,\theta)}{\Delta t} = \partial_t R(t,\theta) + \frac{V_\mathrm{n} n_\theta}{R(t,\theta)}\partial_\theta R(t,\theta)$$

and thus

$$V_\mathrm{n} = \frac{\partial_t \delta R(t,\theta)}{n_r - \frac{\partial_\theta \delta R(t,\theta)}{1+\delta R(t,\theta)} n_\theta} \simeq \partial_t \delta R(t,\theta) = \sum_m \left(\delta\dot{R}_{\mathrm{c}m}(t)\cos(m\theta) + \delta\dot{R}_{\mathrm{s}m}(t)\sin(m\theta)\right) \tag{II.32}$$

where we neglected the quadratic term $(\partial_\theta \delta R) n_\theta$ in the denominator.

By substituting Eqs. (II.31) and (II.32) in the kinematic condition, Eq. (II.15), we obtain $\delta\dot{R}_{\mathrm{c}m}(t) = -mA_m(t)$ and $\delta\dot{R}_{\mathrm{s}m}(t) = -mB_m(t)$. Inserting the pressure amplitudes, Eqs. (II.27) – (II.28), we find the linearized dynamic equations for the shape perturbations

$$\delta\dot{R}_{\mathrm{c}m}(t) = -\sigma m(m^2-1)\delta R_{\mathrm{c}m}(t) - \chi m \delta c_{\mathrm{c}m}(t,1) \tag{II.33}$$

$$\delta\dot{R}_{\mathrm{s}m}(t) = -\sigma m(m^2-1)\delta R_{\mathrm{s}m}(t) - \chi m \delta c_{\mathrm{s}m}(t,1) \tag{II.34}$$

We stress here that all orthogonal shape-concentration perturbations are uncoupled (i.e., no mixing of $\cos(m\theta)$ and $\sin(m\theta)$ modes). Note that for $\chi = 0$ we recover the cubic dispersion relation characterizing the morphological stability of the passive viscous droplet.

Next, we wish to linearize the solute transport problem. By neglecting the quadratic convection term ($\mathbf{u}\cdot\nabla c = -\nabla\delta p\cdot\nabla\delta c$) in the convection-diffusion equation, Eq. (II.16), we obtain the heat equation for δc (i.e., $\partial_t \delta c - \Delta\delta c = 0$). Substituting the Fourier series expansion, Eq. (II.23), we obtain

$$\partial_t \delta c_{\mathrm{c}m}(t,r) = \left[\partial_{rr} + r^{-1}\partial_r - r^{-2}m^2\right]\delta c_{\mathrm{c}m}(t,r) \tag{II.35}$$

$$\partial_t \delta c_{\mathrm{s}m}(t,r) = \left[\partial_{rr} + r^{-1}\partial_r - r^{-2}m^2\right]\delta c_{\mathrm{s}m}(t,r) \tag{II.36}$$

From the no-flux condition, Eq. (II.17), it follows that

$$\partial_r \delta c \simeq -aV_\mathrm{n}$$

where on the LHS we neglected the quadratic term $\left(\frac{1}{r}\partial_\theta \delta c\right) n_\theta$ coming from $\nabla c \cdot \mathbf{n}$ and on the RHS we neglected the quadratic term $-a\delta c V_\mathrm{n}$ coming from $-acV_\mathrm{n}$. Using $\partial_r \delta c \simeq \partial_r \delta c(r=1)$ and inserting the linearized V_n, Eq. (II.32), we obtain

$$\partial_r \delta c_{cm}(r=1,t) = -a\delta \dot{R}_{cm}(t) \tag{II.37}$$

$$\partial_r \delta c_{sm}(r=1,t) = -a\delta \dot{R}_{sm}(t) \tag{II.38}$$

Like Eqs. (II.33) – (II.34), our linearized solute transport equations, Eqs. (II.35) – (II.38), do not mix any orthogonal perturbations. In other words, Eqs. (II.33), (II.35), and (II.37) describe a closed dynamical system for the pair of shape-concentration cosine perturbations ($\delta R_{cm}(t)\cos(m\theta)$ and $\delta c_{cm}(t,r)\cos(m\theta)$), and Eqs. (II.34), (II.36), and (II.38) describe the equivalent system for the pair of sine perturbations. Without loss of generality, we will consider only the cosine system hereinafter.

The kernels of Eq. (II.35) are known and can be expressed as $J_m(-i\sqrt{s}r)e^{st}$, where J_m is the Bessel function of the first kind of order m and s is the eigenvalue (constrained by the boundary condition and normally real-negative for pure diffusion problems). Note that we discard the Bessel functions of the second kind, $Y_m(-i\sqrt{s}r)$, which diverge at $r=0$. We look for coupled shape-concentration eigenmodes by imposing a shared growth-rate (the eigenvalue s) for both degrees of freedom, i.e.,

$$\delta R_{cm}(t) = \alpha_{ms} e^{st}, \quad \delta c_{cm}(t,r) = \beta_{ms} J_m(-i\sqrt{s}r)e^{st} \tag{II.39}$$

where generally $s, \alpha_{ms}, \beta_{ms} \in \mathbb{C}$, and δc_{cm} is chosen to solve Eq. (II.35).

Substituting the ansatz, Eq. (II.39), back in Eqs. (II.33) and (II.37) constitutes the final reduction of our linearized system

$$\left(s + \sigma m(m^2-1)\right)\alpha_{ms} = -\chi m J_m(-i\sqrt{s})\beta_{ms} \tag{II.40}$$

$$-\frac{i\sqrt{s}}{2}\left(J_{m-1}(-i\sqrt{s}) - J_{m+1}(-i\sqrt{s})\right)\beta_{ms} = -as\alpha_{ms} \tag{II.41}$$

Note that the mode $m=0$ is independent of all three parameters (where the independence on a in Eq. (II.41) follows from Eq. (II.40) that gives $s\alpha_{0s}=0$). In addition, the mode $m=1$ is independent of σ.

The eigenvalues of our contracted linear system in Eqs. (II.40) – (II.41) are then computed as the roots of the following characteristic function

$$\begin{aligned} G_m(s) &= -\frac{i\sqrt{s}}{2}\left(J_{m-1}(-i\sqrt{s}) - J_{m+1}(-i\sqrt{s})\right)\left(s+\sigma m(m^2-1)\right) - a\chi m s J_m(-i\sqrt{s}) \\ &= \left(-\frac{i\sqrt{s}}{2}\right)^m \sum_{n=0}^{\infty}\left(\frac{s}{4}\right)^n \frac{4n(m+n)\left(2(n-1)+m(1-a\chi)\right)+\sigma m(m^2-1)(m+2n)}{n!(m+n)!} \end{aligned} \tag{II.42}$$

We stress that, for each m, $G_m(s)$ has an infinite set of roots. Each root, s, is an eigenvalue that is associated with an eigenmode,

$$v_{ms}(r,\theta) = \begin{pmatrix} \alpha_{ms} \\ \beta_{ms} J_m(-i\sqrt{s}r) \end{pmatrix} \cos(m\theta), \tag{II.43}$$

where α_{ms}, β_{ms} represent a solution to Eqs. (II.40) – (II.41) for a given s.

To clarify, $v_{ms}(r,\theta)$ represents a coupled shape-concentration perturbation of the circular homogeneous rest-state that evolves with the growth rate s. Hence, if the real part of s is negative (or positive) then the associated eigenmode is stable (or unstable). We find that Eq. (II.42), which determines s and thus governs stability, depends only two control parameters: σ and $a\chi$, where $a\chi$ represents the closed shape-concentration coupling. Note that $a\chi$ also has the meaning of a Pe number, as it represents the ratio between the driven advection rate of the solute (relative to the fluid) over its diffusive transport rate. Also note that unlike s, the eigenmode $v_{ms}(r,\theta)$ will depend on all three independent parameters.

To help verify the physical viability of our reduced equations, Eqs. (II.40) – (II.42), we square the liner stability results with a straightforward interpretation of the special cases: $a = 0$, $\chi = 0$, and $\sigma = 0$ (see Appendix A.2). In the following subsections, we analyse each mode $m \geq 0$ in the general case ($a, \chi, \sigma \neq 0$).

II.4.2 Mass modes: marginal stability

Here, we consider only the azimuthally symmetric perturbations of droplet shape and solute concentration. Substituting $m = 0$ in Eq. (II.42) gives

$$G_0(s) = i\sqrt{s}J_1(-i\sqrt{s})s$$

This characteristic function, which is independent of both σ and $a\chi$, has only real-negative roots; $s = 0$ and $s_{0,n} = -j_{1,n}^2$, where $j_{1,n}$ is the n^{th} zero of $J_1(x)$ (the Bessel-J function of order 1).

Substituting $m = 0$ back in Eqs. (II.40) – (II.41), we find that the root $s = 0$ is associated with two non-trivial eigenmodes

$$v_{00}^R(r,\theta) = \begin{pmatrix} 1 \\ 0 \end{pmatrix}, \quad v_{00}^c(r,\theta) = \begin{pmatrix} 0 \\ J_0(0) \end{pmatrix} = \begin{pmatrix} 0 \\ 1 \end{pmatrix}$$

where v_{00}^R represents a uniform change in the droplet radius and v_{00}^c represents a uniform elevation in the solute concentration. Due to the conservation of total fluid and total solute, these mass perturbations are both marginally-stable (and hence $s = 0$).

Each real-negative root, $s_{0,n} = -j_{1,n}^2$, is associated with an $m = 0$ decaying diffusion mode, given by

$$v_{0,n}(r,\theta) = \begin{pmatrix} 0 \\ J_0(j_{1,n}r) \end{pmatrix}$$

II.4.3 Polarization-translation mode: motility via symmetry breaking

Substituting $m = 1$ in Eq. (II.42) gives the characteristic function

$$G_1(s) = -\frac{i\sqrt{s}}{2}\left(J_0(-i\sqrt{s}) - J_2(-i\sqrt{s})\right)s - a\chi s J_1(-i\sqrt{s}) \tag{II.44}$$

It is easy to see that $s = 0$ is a root of $G_1(s)$ for all parameter values. Substituting $m = 1$ in Eqs. (II.40) – (II.41), and given that $J_1(0) = 0$, we find that $s = 0$ is associated with

a single non-trivial eigenmode

$$v_{10}(r,\theta) = \begin{pmatrix} 1 \\ 0 \end{pmatrix} \cos\theta$$

This mode merely describes the infinitesimal translation of the droplet. At the linear level, the shape remains circular and c remains uniform, as in the circular homogeneous rest-state. Due to translational invariance, this perturbation is marginally-stable (and hence $s = 0$).

Since $G_1(s)$ is highly nonlinear, we cannot find its additional roots analytically. As we are interested in instabilities, we expand Eq. (II.44) about $s = 0$ in order to find those roots that continuously cross zero as a function of $a\chi$.

$$G_1(s) \simeq -s\frac{i\sqrt{s}}{2}\left(1 - a\chi + \frac{1}{8}(3 - a\chi)s\right)$$

In addition to $s = 0$, this function has the real root $s_1 = \frac{8(a\chi-1)}{3-a\chi}$, which changes sign from negative to positive as $a\chi$ exceeds the value of 1. Note that s_1 approximates a true root of $G_1(s)$, Eq. (II.44), so long as it is small, that is, for $a\chi \approx 1$. In which case, we may write $s_1 \approx 4(a\chi - 1)$. The associated eigenmode to s_1 is then given by

$$v_{1s_1}(r,\theta) = \begin{pmatrix} -\chi J_1(-i\sqrt{s_1}) \\ s_1 J_1(-i\sqrt{s_1}r) \end{pmatrix} \cos\theta \approx \frac{i\sqrt{s_1}}{2}\begin{pmatrix} \chi \\ -s_1 r \end{pmatrix}\cos\theta \sim \begin{pmatrix} \chi \\ 4(1-a\chi)r \end{pmatrix}\cos\theta$$

where we expanded the Bessel functions for small s_1 and omitted prefactors. This mode shows that the global translation of the droplet is coupled to an internal solute polarity, as suggested already by Eq. (II.21). It is instructive to note that as $a\chi$ passes 1, and thus s_1 changes sign (v_{1s_1} becomes unstable), the solute gradient component in $v_{1s_1}(r,\theta)$ also changes sign.

The physics of mode $v_{1s_1}(r,\theta)$ are understood as follows. Given an infinitesimal solute gradient such as $\delta c = \varepsilon r\cos(\theta) = \varepsilon x$, the circular droplet is driven in the direction $-\text{sign}[\varepsilon]\hat{x}$. In the stable case ($a\chi < 0$, visualized in Fig. II.2a), the solute diffusion dominates over its relative drift with respect to the fluid. Consequently, the solute spreads out over the droplet domain ($\delta c \to 0$) at a typical relaxation time $\tau_1 = |s_1|^{-1}$. As the driving force loses polarity, the droplet slows down and stalls ($\mathbf{u} \to 0$) after translating a total distance $\Delta x \simeq -\tau_1\chi\varepsilon$. As expected, $\Delta x \propto -\epsilon$ has the opposite sign to the initial solute gradient. In the unstable case ($a\chi > 1$, Fig. II.2b), the solute drift with respect to the fluid dominates over diffusion. As the solute accumulates at the rear, it amplifies the forward flow (proportional to $-\chi\nabla c$, see Eqs. (II.18) and (II.21)). In turn, this flow increases the rearward solute accumulation (proportional to $-a\mathbf{u}$, see Eq. (II.17)). This positive feedback loop, factored by $a\chi$, destabilizes the polarization-translation mode which breaks the front-rear symmetry and leads to motility.

II.4.4 Coupled multipolar modes: begetting shape-concentration waves

We now examine the roots of $G_m(s)$, Eq. (II.42), for $m \geq 2$ with $a\chi > 0$ and $\sigma > 0$. Note that the special cases $a = 0$, $\chi = 0$, and $\sigma = 0$ are discussed separately in Appendix A.2.

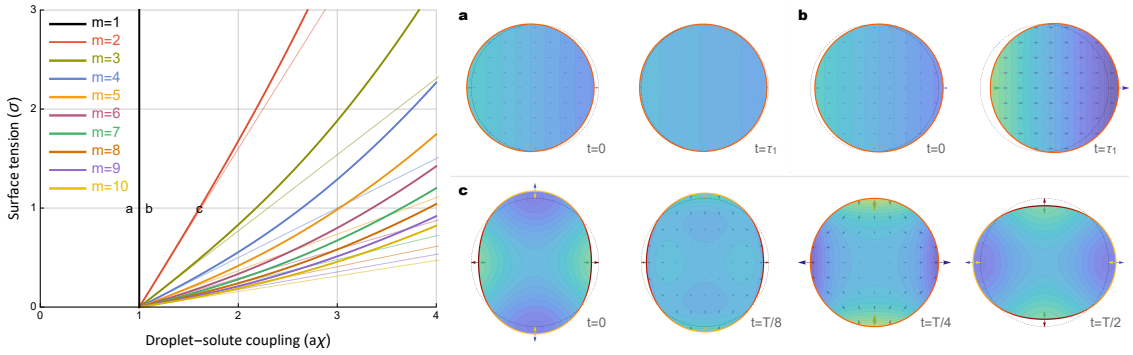

Fig. II.2 **The droplet-solute coupling destabilizes shape-concentration modes.** *Linear stability phase diagram (left): To the right of the black line ($a\chi > 1$), the coupled polarization-translation (motility) mode is unstable. To the right of the colored lines, the multipolar shape-concentration waves (respective to each $m \geq 2$) are unstable. These critical lines are found computationally by tracing the Hopf-bifurcations over the parameter space. The thin translucent lines mark their analytic low-σ approximation, Eq. (II.46). a) & b)–Visualizations of the polarization-translation mode in the stable case (a), where $a\chi = 0.9$, and the unstable case (b), where $a\chi = 1.1$. Both are evolving from left to right following the characteristic time $\tau_1 = |s_1|^{-1}$. c)–Standing shape-concentration waves corresponding to mode $m = 2$, evolving from left to right at the marked time stamps, where $T = 2\pi/\mathrm{Im}[s_2]$ denotes the oscillation period. Parameters are set on the Hopf bifurcation point, such that $Re[s_2] = 0$ (matching in this case to $\sigma = 1$ and $a\chi \simeq 1.61$). The color density map in the bulk represents δc (negative in blue to positive in light green), and the color coded boundary represents $\delta\kappa$ (negative in dark red to positive in yellow). On the boundary, these perturbations give rise to deviations in the active force, $-\chi\delta c\mathbf{n}$, and the restoring capillary force, $-\sigma\delta\kappa\mathbf{n}$ (both marked with matching arrows). The blue vector field in the bulk represent the instantaneous fluid flow, $\mathbf{u} = -\nabla\delta p$.*

It is easy to see that $s = 0$ is always a root of Eq. (II.42) for all m. However, it is not necessarily associated with a physically meaningful eigenmode. Substituting $s = 0$ in Eqs. (II.40) – (II.41), and considering $m \geq 2$ and $\sigma > 0$, it follows from Eq. (II.40) that $\alpha_{m0} = 0$, i.e., the shape component in the associated eigenmode vanishes. In addition, since $J_m(0) = 0$ for any $m \geq 1$, the solute component also vanishes, see Eq. (II.43). In sum, for $m \geq 2$ and $\sigma > 0$, the eigenvalue $s = 0$ is associated only with the trivial eigenmode ($v_{m0} = 0$).

As we are interested in instabilities, we look for an eigenvalue s^* (complex root of $G_m(s)$) whose real part changes sign from negative to positive as a function of the destabilizing control parameter $a\chi$. At the critical point, denoted $a\chi^c$, the real part of s^* is zero and thus $s^*(a\chi^c) = i\omega$ (where $\omega \in \mathbb{R}$ represents an oscillation frequency of the associated eigenmode). By solving $\Re[G_k(i\omega)] = \Im[G_k(i\omega)] = 0$, we may compute both ω and $a\chi^c$ as functions of m and σ.

Assuming small (yet nonzero) frequency ω, let us expand $G_m(i\omega)$, Eq. (II.42), to up to the power $(m/2+3)$

$$\begin{aligned} G_m(i\omega) &= \left(-\frac{i\sqrt{i\omega}}{2}\right)^m \sum_{n=0}^{\infty} \left(\frac{i\omega}{4}\right)^n \frac{4n(m+n)\left(2(n-1)+m(1-a\chi)\right)+\sigma m(m^2-1)(m+2n)}{n!(m+n)!} \\ &\simeq \left(-\frac{i\sqrt{i\omega}}{2}\right)^m \left(F_m(\omega^2)+\left(\frac{i\omega}{4}\right)H_m(\omega^2)+O(\omega^4)\right) \end{aligned} \tag{II.45}$$

where $F_m(\omega^2)$, $H_m(\omega^2)$ are the real-valued functions

$$\begin{aligned} F_m(\omega^2) =& \frac{\sigma m^2\left(m^2-1\right)}{m!} - \left(\frac{\omega}{4}\right)^2 \frac{8(m+2)(2+m(1-a\chi))+\sigma m\left(m^2-1\right)(m+4)}{2(m+2)!} \\ H_m(\omega^2) =& \frac{4(m+1)\left(m(1-a\chi)\right)+\sigma m(m^2-1)(m+2)}{(m+1)!} \\ & - \left(\frac{\omega}{4}\right)^2 \frac{12(m+3)\left(4+m(1-a\chi)\right)+\sigma m(m^2-1)(m+6)}{6(m+3)!} \end{aligned}$$

Since we need to solve $G_m(i\omega)=0$, it follows that $F_m(\omega^2)\simeq 0$ and $H_m(\omega^2)\simeq 0$. This system of two implicit equations can be solved in the variables ω^2 and $a\chi$. Using Mathematica, we find one explicit solution that gives $\omega\to 0$ and $a\chi^{\mathrm{c}}\to 1$ at the limit $\sigma\to 0$, agreeing with our result for zero surface tension (see Appendix A.2). We stress that this explicit solution can be considered a valid approximation of the bifurcation point so long as ω is small. Hence, we expand it here up to leading order in σ

$$a\chi^{\mathrm{c}} \simeq 1+\frac{\left(3m^2+m-4\right)\sigma}{4(m+2)} \tag{II.46}$$

$$\omega_{\pm} \simeq \pm m(m+1)\sqrt{2\sigma(m-1)} \tag{II.47}$$

To recapitulate, we find a pair of complex-conjugate eigenvalues whose real part crosses 0 as $a\chi$ exceeds the critical point $a\chi^{\mathrm{c}}$, approximated by Eq. (II.46). At this Hopf-bifurcation point, the frequency ω is approximated by Eq. (II.47). Using Eq. (II.40), we can express the coupled eigenmode associated with the eigenvalue $s^*=i\omega$. This eigenmode represents a shape-concentration standing wave,

$$\begin{aligned} v_{ms^*}(r,\theta) &= \begin{pmatrix} -\chi m J_m(-i\sqrt{i\omega}) \\ \left(i\omega+\sigma m(m^2-1)\right)J_m(-i\sqrt{i\omega}r) \end{pmatrix}\cos(m\theta) \\ &\sim \begin{pmatrix} \chi \\ (m+1)\left(\mp i\sqrt{2\sigma(m-1)}-\sigma(m-1)\right)r^m \end{pmatrix}\cos(m\theta) \end{aligned} \tag{II.48}$$

where we expanded the Bessel functions near $\omega=0$, used Eq. (II.47), and omitted global prefactors. Using Eq. (II.48), we find that $\Delta\phi_{\pm}\approx\pi\pm\arctan(\sqrt{2/(\sigma(m-1))})$ approximates the phase-shift between the shape and solute components in the standing wave. For low σ, we obtain $\Delta\phi_{\pm}\approx\mp\pi/2$.

Remark II.4.1. *To gain insight, we use Eq. (II.47) to infer the dimensional frequency ω_{dim} in terms of the physical parameters. In the dimensionless representation, we work with the time unit $\tau_{solute} = R_0^2/D$ (the solute diffusion time over the droplet), and thus $\omega_{dim} = \tau_{solute}^{-1}\omega$. Substituting the dimensionless tension, $\sigma \to \frac{M\sigma}{DR_0}$ (see Eq. (II.19)), back in Eq. (II.47), we obtain*

$$\omega_{dim} \simeq \frac{D}{R_0^2} m(m+1)\sqrt{2\frac{M\sigma}{DR_0}(m-1)} = m(m+1)\sqrt{2(m-1)}\sqrt{\frac{DM\sigma}{R_0^5}}$$

The oscillation period is then

$$T = 2\pi/\omega_{dim} \simeq \frac{2\pi\sqrt{\tau_{solute}\tau_{droplet}}}{m(m+2)\sqrt{2(m-1)}}$$

where $\tau_{droplet} = R_0^3/(M\sigma)$ is the characteristic shape relaxation time of the viscous droplet. The fact that T is proportional to the geometric mean of the two distinct relaxation times in our system demonstrates that both processes (i.e., solute diffusion and the tension-driven viscous relaxation) play an essential role in the oscillatory cycle.

From a physical standpoint, the standing waves result from a dynamic interplay between the active driving force and the restoring surface tension. Consider an initial state in which finite solute and curvature gradients produce force variations on the boundary that directly balance each other (Fig. II.2c, t=0). At this instant, the resultant pressure is uniform and thus $\mathbf{u} = 0$. The solute then spreads out via diffusion while the tension persists in countering the curvature gradients (t=T/8). As the free boundary is driven by tension, retracting edges amass solute while advancing edges disperse with solute (see Eq. (II.17)). By the time the circular shape is recovered (t=T/4), a residual solute gradient on the boundary induces a nonuniform active force that pulls in the retracting edges further. Essentially, this overshoot is due to the lag associated with the diffusive transport of the solute. As the droplet is deformed in the transverse direction by $F_{\text{act}}(c)\mathbf{n}$, the tension counters the new deformation until the fluid stalls again (t=T/2). The same mechanism then drives the droplet back to the initial state (as seen in Movie II.1.a). We stress that such oscillations can be stable (damped) or unstable (amplified), depending on the strength of the shape-concentration coupling (see diagram in Fig. II.2).

Remark II.4.2. *Traveling shape-concentration waves are also supported by the model at the linear level. Such waves can be constructed in a straight-forward manner by superimposing two orthogonal standing waves ($\cos(m\theta)$ and $\sin(m\theta)$) evolving at the same amplitude and frequency with a temporal phase-shift of a quarter period (see supplemental Movies II.1 and II.2). Interestingly, in these traveling waves, the fluid pathlines circulate locally over time while the instantaneous streamlines remain irrotational by-definition (being that $\mathbf{u} = -\nabla p$). Our model sustains such intriguing flow patterns because the external force $F_{act}(c)$ continuously drives the droplet out of mechanical equilibrium in a time-dependent manner.*

II.4.5 Recap

In sum, in this section we have determined the stability of the circular homogeneous rest-state with respect to coupled shape-concentration perturbations in each normal mode

m. For the radially symmetric mode $m = 0$, we found the exact eigenvalues with their associated eigenmodes. These include the (infinitely many) decaying diffusion modes as well as two marginally-stable modes corresponding to perturbations of fluid mass and solute mass. To find closed explicit results for modes $m \geq 1$, we worked with low-order Taylor expansions of the complex characteristic function $G_m(s)$ (Eq. (II.42)). To complement our analytic efforts, we performed a computational root-finding analysis of the exact $G_m(s)$ (see Appendix A.3). This exercise supports our main conclusions in this section (summarized in Fig. II.2), namely that

- The mode $m = 1$ is destabilized once through a steady bifurcation (with zero imaginary part of s_1) at $a\chi = 1$. In other words, the polarization-translation mode, which breaks the front-symmetry and leads to motility, is unstable for $a\chi \geq 1$ (see Fig. A.1).

- Each $m \geq 2$ is destabilized once through a Hopf bifurcation. That is, for any $\sigma > 0$ (including large values of σ) there exist a critical $a\chi^{\mathrm{c}}$ at which two complex-conjugate eigenmodes are destabilized with non-vanishing frequency (see Fig. A.1).

- Our low-σ approximation for $a\chi^{\mathrm{c}}$, Eq. (II.46), is tangent to the computational $a\chi^{\mathrm{c}}$ at the critical parametric point $(a\chi, \sigma) = (1, 0)$ (see Fig. II.2).

- In the case of zero surface tension ($\sigma = 0$), the multipolar modes are analogous to mode $m = 1$ (see Fig. A.1).

- Aside from the eigenvalues of interest highlighted here, there exist for each $m \geq 1$ a series of infinitely many real-negative eigenvalues that originate from the solute diffusion problem (as in $m = 0$). While these eigenvalues may vary as a function of $a\chi$, they remain real and negative for all parameter values (see Fig. A.1).

The Hopf bifurcations leading to the shape-concentration oscillations reveal a robust physical instability enabling 'active-capillary' waves. To support this finding, we show that the Hopf instability is not specific to the closed circular geometry considered here. In Appendix A.4, we place our system in rectangular chamber geometry (of dimensions $L \times 1$) and follow the same linearization procedure performed here. For coupled perturbations of the (flat) free surface, and the (uniform) internal solute concentration, the complex characteristic function associated with the wavenumber $k_m := 2\pi m/L$ is

$$G_{k_m}(s) = \left(\coth(k_m)s + \sigma k_m^3\right) i\sqrt{s + k_m^2} \sin\left(-i\sqrt{s + k_m^2}\right) - a\chi s k_m \cos\left(-i\sqrt{s + k_m^2}\right)$$

where s is the eigenvalue and σ, a, χ are the dimensionless parameters—as in Eq. (II.42).

With the exception of $m = 1$, which is here qualitatively indistinct from $m \geq 2$, this characteristic function has the same properties as Eq. (II.42). That is, for $\sigma > 0$, each $m > 0$ is destabilized once through a Hopf Bifurcation at some critical $a\chi^{\mathrm{c}}$ with a

frequency $\omega_{\pm}$, approximated by

$$a\chi^{\mathrm{c}} \simeq 1 + \left(\frac{k^3}{\sinh(2k) + 2k} + \frac{3}{4} k \tanh(k) \right) \sigma$$
$$\omega_{\pm} \simeq \pm 2k^2 \sinh(k) \sqrt{\frac{\sigma k}{(\sinh(2k) + 2k)}}$$

for small σ.

The associated eigenmode to $s_{\pm}^{*} = i\omega_{\pm}$ then represents a standing shape-concentration wave. In addition, the orthogonal cosine and sine waves in each m can be superimposed to produce a traveling wave. Note that the absence of a 'polarization-translation' mode in this geometry has to with the fact that our rectangular system is bound by a no fluid flux condition at a fixed boundary (located at $y = 0$). For more details on the rectangular model, see Appendix A.4.

II.5 Nonlinear steadily-moving states

In this section, we step beyond the linear regime and look for self-consistent stationary solutions to our droplet-solute problem.

II.5.1 Force saturation

To account for the plausible physical saturation of the active traction force, we introduce a Hill-type formulation of $F_{\mathrm{act}}(c)$ (with Hill coefficient $n = 1$, as adopted in previous 1D models Maiuri et al (2015); Lavi et al (2016)).

$$F_{\mathrm{act}}(c) = -\frac{\beta c}{c_{\mathrm{s}} + c} \tag{II.49}$$

where $\beta > 0$ is the maximal pulling force and $c_{\mathrm{s}} > 0$ is a saturation parameter. In the dimensionless model, β and c_{s} are defined as $\frac{M\beta}{Dh}$ and $\frac{Ac_{\mathrm{s}}}{C_{\mathrm{tot}}}$, respectively (in terms of the dimensional parameters).

For convenience, let us also rephrase Eq. (II.49) in terms of our dimensionless linear-response parameter ($\chi = -F'_{\mathrm{act}}(1) = \beta c_{\mathrm{s}}/(c_{\mathrm{s}} + 1)^2$),

$$F_{\mathrm{act}}(c) = -\chi \frac{(c_{\mathrm{s}} + 1)^2 c}{c_{\mathrm{s}}(c_{\mathrm{s}} + c)} \tag{II.50}$$

Note that this equivalent definition makes it easier to connect the nonlinear picture with our linear stability analysis performed in the previous section.

Remark II.5.1. *We have some freedom in how we define the nonlinear form of $F_{act}(c)$. The important point is that this function reaches saturation. The idea here is to contain the polarization-translation feedback loop at the nonlinear level in order to prevent nonphysical solution 'blow-ups'.*

II.5.2 Reverse-engineering problem

We search for solutions to our model that are characterized by a fixed stationary shape, i.e.,

$$0 = V_{\rm n} - \mathbf{u}_{\rm cm}\cdot\mathbf{n} = (\mathbf{u}-\mathbf{u}_{\rm cm})\cdot\mathbf{n} \quad \text{on } \partial\Omega(t) \tag{II.51}$$

where we used the kinematic condition, Eq. (II.15).

Remarkably, for a closed-surface Hele-Shaw problem (such as ours), the condition above mandates that the entire fluid bulk flows at a uniform speed, meaning $\mathbf{u} = \mathbf{u}_{\rm cm}$ in $\Omega(t)$. Let us define and prove this generic result more formally.

Lemma II.5.2. *Let* $\mathbf{u}$ *be an incompressible and irrotational flow field in* $\Omega(t)$*, such that*

$$\nabla\cdot\mathbf{u} = 0\,, \quad \nabla\times\mathbf{u} = 0 \quad \textit{in } \Omega(t)$$

Given the kinematic and fixed shape conditions on $\partial\Omega(t)$*, which give Eq.* (II.51)*, the internal flow* $\mathbf{u}$ *is uniform, and given by*

$$\mathbf{u} = \mathbf{u}_{cm} \quad \textit{in } \Omega(t)$$

where $\mathbf{u}_{cm}$ *is a constant in* $\mathbb{R}^2$ *defined as* $\mathbf{u}_{cm} = A^{-1}\oint_{\partial\Omega(t)}\mathbf{x}(\mathbf{u}\cdot\mathbf{n})\,\mathrm{d}l$*.*

Proof. We define the flow field in the moving frame of reference as $\tilde{\mathbf{u}} = \mathbf{u} - \mathbf{u}_{\rm cm}$. Since $\mathbf{u}_{\rm cm}$ is a constant and $\mathbf{u}$ is both incompressible and irrotational, it follows that $\nabla\cdot\tilde{\mathbf{u}} = 0$ and $\nabla\times\tilde{\mathbf{u}} = 0$. Thus, we may define Φ as a Laplacian flow potential for $\tilde{\mathbf{u}}$:

$$\tilde{\mathbf{u}} = \nabla\Phi\,, \quad \Delta\Phi = 0 \quad \text{in } \Omega$$

Note that, for Hele-Shaw flow, one has $\Phi = -\nabla p - \mathbf{u}_{\rm cm}\cdot\mathbf{x}$.

In the moving frame, Ω is stationary due to the fixed shape assumption, Eq. (II.51). In terms of Φ, this assumption translates to

$$\nabla\Phi\cdot\mathbf{n} = 0 \quad \text{on } \partial\Omega$$

Using Green's identity, one obtains

$$-\int_\Omega(\Delta\Phi)\Phi\,\mathrm{d}a = \int_\Omega\nabla\Phi\cdot\nabla\Phi\,\mathrm{d}a - \oint_{\partial\Omega}(\partial_{\rm n}\Phi)\Phi\,\mathrm{d}l$$

It is easy to see that both the LHS and the boundary integral on the RHS vanish (due to incrompressibility and the fixed shape condition). Therefore,

$$0 = \int_\Omega\tilde{\mathbf{u}}^2\,\mathrm{d}a$$

It follows that $\tilde{\mathbf{u}} = 0$ in Ω and thus $\mathbf{u} = \mathbf{u}_{\rm cm}$ in $\Omega(t)$. □

Without loss of generality, let us define $\mathbf{u}_{\rm cm} = u_1\hat{x}$. Our reverse-engineering problem is now the following: find a self-consistent solution to the nonlinear dimensionless model, Eqs. (II.12) – (II.17) and Eq. (II.49), such that $\mathbf{u}(t,x,y) = u_1\hat{x}$ for some $u_1 \neq 0$. At this steadily-moving state, the fluid pressure p and the solute concentration c are stationary in the moving frame of reference. In other words, p and c are traveling-wave solutions:

$p(t,x,y) = p(\tilde{x},y)$ and $c(t,x,y) = c(\tilde{x},y)$, where $\tilde{x} = x - u_1 t$ represents the x-coordinate in the moving frame.

Given that $-\nabla p = u_1 \hat{x}$, Eq. (II.12), the pressure is of the form

$$p = p_1 - u_1 \tilde{x} \qquad \text{in } \Omega \tag{II.52}$$

where p_1 is a normalization constant for the droplet area.

Let us now resolve the solute transport problem. Substituting $\mathbf{u} = u_1 \hat{x}$ and $c = (\tilde{x}, t)$ in Eqs. (II.16) – (II.17), one obtains

$$-\left[\partial_x(au_1 + \partial_x) + \partial_y^2\right] c(\tilde{x},y) = 0 \qquad \text{in } \Omega \tag{II.53}$$

$$\left[n_x\left(au_1 + \partial_x\right) + n_y\partial_y\right] c(\tilde{x},y) = 0 \qquad \text{on } \partial\Omega \tag{II.54}$$

where we used the fact that $\partial_t c(\tilde{x},y) = -u_1 \partial_x c(\tilde{x},y)$.

Lemma II.5.3. *For any smooth open subset $\Omega \subset \mathbb{R}^2$ (with $\mathbf{n} = (n_x, n_y)$ being the outward normal on $\partial\Omega$), the solution to the boundary-value problem in Eqs. (II.53) – (II.54) is unique and given in the following y-independent form:*

$$c = c_1 e^{-au_1\tilde{x}} \qquad \text{in } \Omega \tag{II.55}$$

where c_1 is a normalization constant for the total solute.

Proof. Without loss of generality, let us substitute $c(\tilde{x},y) = f(\tilde{x},y)e^{-au_1\tilde{x}}$ back in Eqs. (II.53) – (II.54). One obtains the following boundary-value problem for f

$$\left[au_1\partial_x - \partial_{xx} - \partial_{yy}\right] f(\tilde{x},y) = 0 \qquad \text{in } \Omega \tag{II.56}$$

$$\left[n_x\partial_x + n_y\partial_y\right] f(\tilde{x},y) = 0 \qquad \text{on } \partial\Omega \tag{II.57}$$

This elliptic Neumann problem is clearly solved by any constant $f = c_1$. All that is left is to is show that non-constant solutions do not exist.

Assume that $f \in \mathcal{C}^2(\Omega) \cap \mathcal{C}^0(\bar{\Omega})$ is a non constant solution to Eq. (II.56), we denote its maximum by $M = \max_{\bar{\Omega}} f > 0$. The fact that the operator in Eq. (II.56) is uniformly elliptic (being that the Laplacian is positive semidefinite) means that the strong maximum principle holds. If there exists a point $\mathbf{x} \in \Omega$ such that $f(\mathbf{x}) = M$ then by strong maximum principle f is constant. It follows that $f < M$ in Ω and there exists a point $\mathbf{y}$ on $\partial\Omega$ for which $f(\mathbf{y}) = M$. This means that $\partial_{\mathrm{n}} f(\mathbf{y}) > 0$, in contradiction with the Neumann condition, Eq. (II.57). For a more generic proof of this class of problems see lecture notes by A. Cesaroni. □

To recapitulate, the Eqs. (II.52) and (II.55) significantly reduce the degrees of freedom in our reverse-engineering problem. Indeed, if a nonlinear steadily-moving solution exists for a given set of parameters, it is fully determined by the three constant numbers (u_1, p_1, c_1). The remaining challenge is to find those combinations of numbers that produce a self-consistent shape; sustaining the normal force balance, Eq. (II.14), and the conservation laws, Eq. (II.20).

II.5.3 Rigid cell solutions

We first work under the crude assumption that the steadily-moving shape is the rigid unit disk (as in the rest-state). This simplifying assumption is physically valid at the limit of high tension and low steady-state velocity, $\sigma/(\chi a^2 u_1^2) \to \infty$.

Since the unit disk Ω is physically-viable and dimensionless, there is no need to explicitly resolve the constant p_1.

We find the solute normalization constant c_1 analytically (in terms of u_1) by imposing the dimensionless conservation of solute, $\pi = \int_\Omega c\,\mathrm{d}a$, see Eq. (II.20). We consider the unit disk geometry and substitute the steady-state form of the concentration, Eq. (II.55), in polar coordinates, $c(r,\theta) = c_1 e^{-au_1 r\cos\theta}$,

$$\pi = \int_0^1 r dr \int_0^{2\pi} c(r,\theta) d\theta = \frac{c_1 2\pi I_1(au_1)}{au_1} \quad \Rightarrow \quad c_1 = \frac{au_1}{2\mathrm{I}_1(au_1)} \tag{II.58}$$

where I_1 denotes the modified Bessel function of the first kind of order 1.

To find u_1, we substitute $\mathbf{u}_{\mathrm{cm}} = u_1\hat{x}$ and $c(r,\theta) = \frac{au_1}{2I_1(au_1)} e^{-au_1 r\cos\theta}$ back in the external force balance, Eq. (II.21). Taking the $\hat{x}$ component of the net external force F_{ext}, we obtain

$$0 = F_{\mathrm{ext}}\cdot\hat{x} = -\pi u_1 + \oint_{\partial\Omega} F_{\mathrm{act}}(c) n_x dl = -\pi u_1 + \int_0^{2\pi} F_{\mathrm{act}}(c(1,\theta))\cos(\theta) d\theta \tag{II.59}$$

where we consider the Hill-type formulation of $F_{\mathrm{act}}(c)$, Eq. (II.50). Note that this implicit equation in u_1 is defined with three parameters: a, χ, and c_{s}. However, one can simplify this further by multiplying Eq. (II.59) by $a \neq 0$. This gives an implicit equation for the variable au_1 in two control parameters: $a\chi$ and c_{s}. Hence, one could set $a = 1$ without loss of generality.

Unfortunately, we are unable to perform the integration on the RHS of Eq. (II.59) analytically. Nevertheless, the integral can be done systematically by first expanding the integrand in powers of au_1. We do this up to 6^{th} order and obtain

$$0 \simeq (a\chi - 1)au_1 + \frac{a\chi(1-2c_{\mathrm{s}})}{4(c_{\mathrm{s}}+1)^2} a^3 u_1^3 + \frac{a\chi(c_{\mathrm{s}}(c_{\mathrm{s}}(2c_{\mathrm{s}}+57)-60)+5)}{192(c_{\mathrm{s}}+1)^4} a^5 u_1^5 + O\left(a^7 u_1^7\right) \tag{II.60}$$

where we also multiplied Eq. (II.59) by a/π.

Let us briefly note the meaning of each term in this expansion. The sign of the first term determines the stability of the trivial solution $u_1 = 0$ (corresponding to the circular homogeneous rest-state). Clearly, this term is negative for $a\chi < 1$ and positive for $a\chi > 1$ —in agreement with our linear stability analysis, see Section II.4. The second term determines the 2nd-order nature of the bifurcation from $u_1 = 0$ into traveling solutions. This term changes sign at $c_{\mathrm{s}} = 0.5$. The saturation of the active Hill-type force, Eq. (II.50), is expected to ultimately dampen the steady-state velocity u_1. This nonlinear effect is manifest in our expansion so long as the last term is negative (that is, for $0.091273 < c_{\mathrm{s}} < 0.927885$). Outside of this parametric range, Eq. (II.60) does not capture the essential physics and thus Eq. (II.59) is best solved numerically.

Explicit low-speed solutions

We obtain three branches of symmetric solutions to Eq. (II.60),

$$u_1 = 0$$

$$u_{1\mathrm{S}\pm} = \pm\frac{2(c_\mathrm{s}+1)}{a}\sqrt{\frac{6}{g}\left(2c_\mathrm{s}-1-\sqrt{(2c_\mathrm{s}-1)^2-\frac{(a\chi-1)g}{3a\chi}}\right)} \qquad \in \mathbb{R} \text{ over } \Lambda_1 \text{ (II.61)}$$

$$u_{1\mathrm{U}\pm} = \pm\frac{2(c_\mathrm{s}+1)}{a}\sqrt{\frac{6}{g}\left(2c_\mathrm{s}-1+\sqrt{(2c_\mathrm{s}-1)^2-\frac{(a\chi-1)g}{3a\chi}}\right)} \qquad \in \mathbb{R} \text{ over } \Lambda_2 \text{ (II.62)}$$

where $g = c_\mathrm{s}(c_\mathrm{s}(2c_\mathrm{s}+57)-60)+5$ (strictly negative in the regimes of interest), and

$$\Lambda_1 = \{c_\mathrm{s} \in (0.091273, 0.927885) \cap a\chi \in [1,\infty)\} \cup \Lambda_2$$

$$\Lambda_2 = \left\{c_\mathrm{s} \in (0.091273, 0.5] \cap a\chi \in \left(1-\frac{3(1-2c_\mathrm{s})^2}{c_\mathrm{s}(48-c_\mathrm{s}(45+2c_\mathrm{s}))-2}, 1\right]\right\} \qquad \text{(II.63)}$$

We reiterate that the steadily-moving branch $u_{1\mathrm{S}\pm}$, Eq. (II.61)), is valid (real-valued) over the parametric regime Λ_1 (which includes Λ_2), while the branch $u_{1\mathrm{U}\pm}$, Eq. (II.62), is valid only over Λ_2.

The challenge now is to address the linear stability of the traveling solutions, Eqs. (II.61) – (II.62). The response of the center of mass velocity to a small perturbation δu_1 about the steady-state speed u_1 (meaning a perturbation in $c(x)$) is proportional to $F'_\mathrm{ext}(u_1)\delta u_1$. Hence, we may determine the linear stability of the states $u_{1\mathrm{S}\pm}$ and $u_{1\mathrm{U}\pm}$ by computing the sign of $\Delta F'_\mathrm{ext}(u_1)$ on each branch. Using Eq. (II.60), we obtain

$$F'_\mathrm{ext}(u_{1\mathrm{S}\pm}) = \frac{4\pi a\chi f}{g}\left(\sqrt{3}(1-2c_\mathrm{s})+f\right) \propto -\left(\sqrt{3}(1-2c_\mathrm{s})+f\right) < 0 \qquad \text{over } \Lambda_1 \text{ (II.64)}$$

$$F'_\mathrm{ext}(u_{1\mathrm{U}\pm}) = \frac{4\pi a\chi f}{g}\left(\sqrt{3}(2c_\mathrm{s}-1)+f\right) \propto -\left(\sqrt{3}(2c_\mathrm{s}-1)+f\right) > 0 \qquad \text{over } \Lambda_2 \text{ (II.65)}$$

where $f = \sqrt{-(2+c_\mathrm{s}(c_\mathrm{s}(2c_\mathrm{s}+45)-48))+g/a\chi}$. It follows from Eqs. (II.64) – (II.65) that the branch $u_{1\mathrm{S}\pm}$ is linearly stable while $u_{1\mathrm{U}\pm}$ is linearly unstable.

To conclude, at $a\chi = 1$ we find a transition from the trivial solution $u_1 = 0$ into steadily-moving states (with $u_1 \neq 0$). This transition takes the form of either a super- or subcritical pitchfork bifurcation. In the supercritical case ($c_\mathrm{s} \geq 0.5$) the stable traveling states $u_{1\mathrm{S}\pm}$ branch out continuously from the stable rest-state as $a\chi$ exceeds 1. In the subcritical case ($c_\mathrm{s} < 0.5$) the unstable states $u_{1\mathrm{U}\pm}$ branch out continuously from the unstable rest-state as $a\chi$ falls behind 1. The latter scenario typically implies entrance into a bi-stable parametric regime. Indeed, over Λ_2, Eq. (II.63), we find co-existence of both the stable rest-state $u_1 = 0$ and the stable traveling states $u_{1\mathrm{S}\pm}$. In this regime, $|u_{1\mathrm{S}\pm}| \geq |u_{1\mathrm{U}\pm}|$ and $u_{1\mathrm{S}\pm} = u_{1\mathrm{U}\pm} = \pm\frac{2(c_\mathrm{s}+1)}{a}\sqrt{6(2c_\mathrm{s}-1)/g}$ on a saddle-node bifurcation, occurring at $a\chi^* = 1-\frac{3(1-2c_\mathrm{s})^2}{c_\mathrm{s}(48-c_\mathrm{s}(45+2c_\mathrm{s}))-2}$ (see limit of Λ_2 in Eq. (II.63)).

Computational solutions

While the explicit Eqs. (II.61) – (II.62) provide important insight, they are strictly low u_1 approximations of the true solutions to the exact Eq. (II.59). To complete the nonlinear

bifurcation picture, we solve Eq. (II.59) numerically. As stated below this equation, we may set $a = 1$ without loss of generality. The idea is to trace the stable/unstable solution branches starting from the bifurcation point at $\chi = 1$. To do so, we employ a continuous-extension procedure in which we vary χ incrementally. Working in Mathematica (TM), we use the NIntegrate function to compute the integral in Eq. (II.59) and employ the FindRoot function to obtain a numerical root of this equation about an initial guess u_1^{g}. To facilitate convergence and to ensure continuity of the solution branch, we define u_1^{g} as the numerical root u_1 obtained in the preceding parametric iteration.

Remark II.5.4. *About the bifurcation point ($\chi = 1$), the true u_1 is small and so we use Eqs.* (II.61) – (II.62) *to define the initial guess. Specifically, we take $u^g = u_{1\,S+}$ for $c_s \geq 0.5$ and $u^g = u_{1\,U+}$ for $c_s < 0.5$.*

In Fig. II.3 we compare the results of our numerical continuous-extension procedure (full lines) to the approximations given in Eqs. (II.61) – (II.62) (dashed lines). It is evident that the numerical bifurcation structure behaves as expected in both the low and high c_{s} regimes—including ranges over which the analytical approximations are no longer valid. Due to the transition from a super- to a subcritical bifurcation at $c_{\mathrm{s}} = 0.5$, and the emergence of a saddle node in the subcritical regime, it is clear that Eq. (II.59) admits three motility phases (as shown in Fig. II.4): 1. Rest phase, where only the stable rest-state exists ($a\chi < 1$ & $c_{\mathrm{s}} \geq 0.5$ or $a\chi < a\chi^{*\mathrm{N}}$ & $c_{\mathrm{s}} < 0.5$, where $a\chi^{*\mathrm{N}}$ denotes the numerical saddle-node bifurcation point), 2. Traveling phase, where the rest-state is unstable and there exists a stable traveling state ($a\chi > 1$), 3. Bistable phase, where both the rest-state and a high-speed traveling state are stable ($a\chi^{*\mathrm{N}} < a\chi < 1$ & $c_{\mathrm{s}} < 0.5$). In this phase, we find an additional low-speed steady state which is unstable. Far from critical points, the speed u_1 (on the stable branch in blue) tends to scale linearly with the maximal pulling force $\beta = \chi(c_{\mathrm{s}} + 1)^2/c_{\mathrm{s}}$.

In Fig. II.4 we show different representations of the motility phase diagram. In particular, Fig. II.4a shows the χ – c_{s} diagram (essentially a top view of the 3D bifurcation diagram in Fig. II.3). Fig. II.4b shows the motility phases in terms of β – c_{s}, which are the original parameters defining the Hill-type force, Eq. (II.49). Note here the close correspondence with the analogous 1D model Maiuri et al (2015) (with its deterministic version analysed in the supplementary information of Lavi et al (2016)). Since the pitchfork bifurcation occurs at $\beta = (c_{\mathrm{s}} + 1)^2/c_{\mathrm{s}} = 2(1 + \cosh(\log c_{\mathrm{s}}))$, we found it useful to also present the phase diagrams in terms of $\log c_{\mathrm{s}}$ (Figs. II.4c,d). Interestingly, Fig. II.4d reveals that $\beta^{*\mathrm{N}}$ (the numerical saddle node bifurcation) is closely approximated by the tangent to the critical line $\beta = (c_{\mathrm{s}} + 1)^2/c_{\mathrm{s}} = 2(1 + \cosh(\log c_{\mathrm{s}}))$ at $c_{\mathrm{s}} = 0.5$.

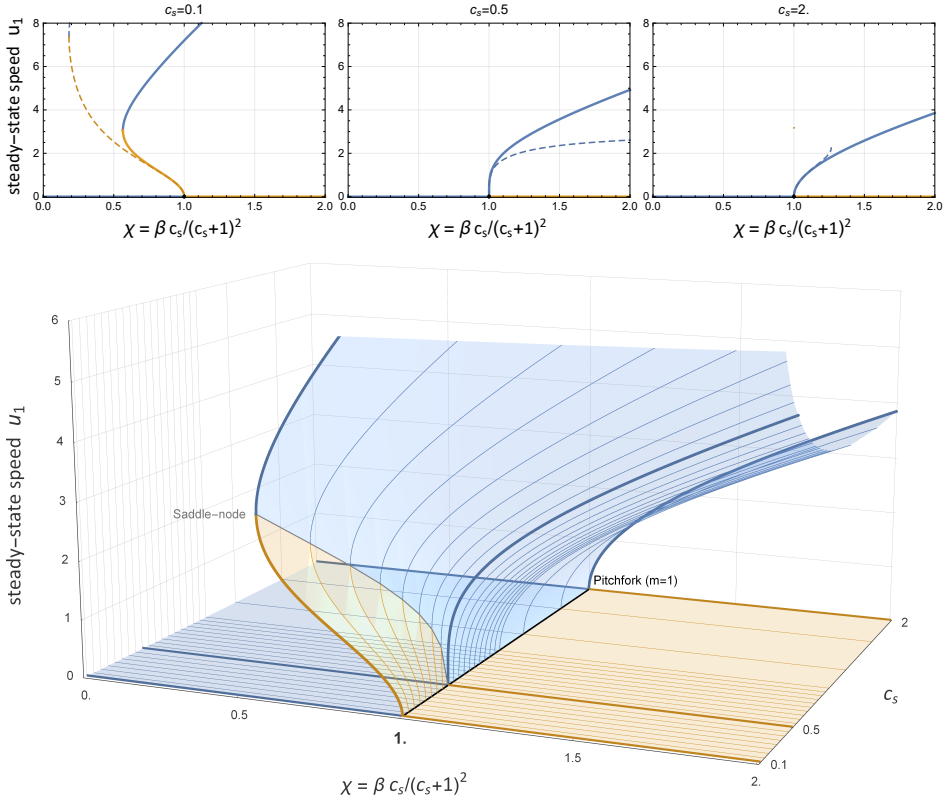

Fig. II.3 **Steadily-moving states (rigid cell bifurcation diagram)**. *Shown at the top are plots of the steady-state speed u_1 as a function of the linear response parameter χ for varying values of c_s. The blue (orange) lines represent the stable (unstable) solution branches. We compare the analytical low-speed approximations (dashed lines, Eqs. (II.61) – (II.62)) with the computational solutions to the exact Eq. (II.59) (full lines). Note the agreement between the curves about the bifurcation point $\chi = 1$. Below, we present the complete computational bifurcation diagram prescribed by Eq. (II.59). The steady-state velocity u_1 is plotted as a function of the two force parameters: χ and c_s. Blue (orange) contours/surfaces mark the stable (unstable) branch of the steadily-moving rigid cell solutions. The homogeneous rest-state is represented by the plane $u_1 = 0$. On this plane, the black line marks the linear instability of the motility mode ($m = 1$). The branching of traveling states at $\chi = 1$ takes the form of a pitchfork bifurcation, which is supercritical if $c_s \geq 0.5$, and subcritical if $c_s < 0.5$. The gray line marks the motility saddle-node bifurcation occurring in the subcritical regime.*

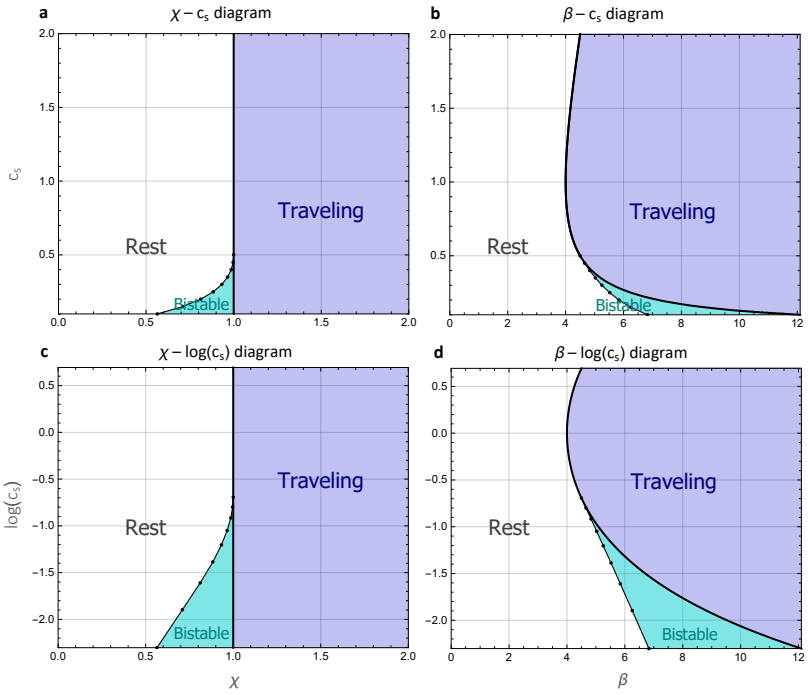

Fig. II.4 **Motility phase diagrams (rigid cell)**. *Shown are different parametric representations of the motility phases sustained by Eq. (II.59). In each plot, the thick black line marks the motility pitchfork bifurcation occurring at* $\chi = \beta c_s/(c_s+1)^2 = 1$. *To the right of this line, we find the traveling phase (blue region), in which the rest-state is unstable and there exists a stable traveling state. The rest-state is always stable to the left of this line. For* $c_s < 0.5$ *and* $a\chi^{*N} < \chi < 1$ *(bistable phase, cyan region) there exists in addition a stable (high-speed) traveling state and an unstable (low-speed) traveling state. The left-most limit of this phase corresponds to the numerical saddle-node bifurcation. The rest phase (white region) spans the parametric regime over which there are no steadily-moving solutions.*

II.5.4 Deformable cell solutions

We wish to obtain the steadily-moving states for a deformable droplet of arbitrary surface tension σ. This problem consists of finding both the speed and the shape of the steady-state in a self-consistent manner. It is therefore far more complicated than the rigid circular case, which amounted to one nonlinear equation in one variable (u_1). To deal with this challenge, we must first derive three necessary and sufficient equations for resolving the three numbers that make up our reverse-engineered solution (u_1, p_1, c_1).

Let us work in the reference frame of the moving cell and omit the tilde in $\tilde{x}$ for brevity. Substituting Eqs. (II.52) and (II.55) back in the normal force balance, Eq. (II.14), we obtain the x-dependent curvature:

$$\sigma\kappa(x) = p_1 - u_1 x - \frac{\beta c_1 e^{-a u_1 x}}{c_\mathrm{s} + c_1 e^{-a u_1 x}} \quad \text{on } \partial\Omega \tag{II.66}$$

where, for simplicity, we used the definition of $F_{\text{act}}(c)$ in Eq. (II.49). Note that $\kappa(x)$, which determines the shape, depends on the three solution variables (u_1, p_1, c_1) and the four dimensionless parameters (σ, a, β, c_s). This can be simplified further by multiplying the equation by $a \neq 0$. It is then easy to see that the same $\kappa(x)$ depends on three variables (au_1, ap_1, c_1) and only three contracted parameters ($a\sigma$, $a\beta$, c_s, where $a\beta$ can be replaced by $a\chi(c_\text{s}+1)^2/c_\text{s}$). Hence, we can set $a = 1$ without loss of generality.

The fact that the steady-state curvature is strictly a single-valued function of x implies reflection symmetry of $\partial\Omega$ about the polarity axis $\hat{x}$. It is therefore natural to define the boundary line via a curve $\pm y(x)$, where $+y(x) \geq 0$ represents the top half of $\partial\Omega$ and $-y(x)$ represents the mirrored bottom half. The curvature on $y(x)$ is given by $\kappa = \frac{-y''}{(1+y'^2)^{3/2}}$. Changing variables to $Y = -\sigma y'/\sqrt{1+y'^2}$, such that $Y' = \sigma\kappa$, reduces Eq. (II.66) to a first-order ODE in Y. We solve this equation analytically along with the condition $Y(0) = 0$, which corresponds to $y'(0) = 0$.

$$Y(x) = p_1 x - \frac{1}{2}u_1 x^2 + \frac{\beta}{u_1}\log\left(\frac{c_\text{s} + c_1 e^{-u_1 x}}{c_\text{s} + c_1}\right) \tag{II.67}$$

Remark II.5.5. *The condition $y'(0) = 0$ is chosen arbitrarily for convenience. It essentially aligns the top and bottom poles (those that are transverse to the direction of motion) at $x = 0$. Although p_1 and c_1 are sensitive to shifts along the axis of motion (due to the x-dependence of p and c), the translational invariance of the problem implies that the shape itself and the speed u_1 will be unaffected by this choice (so long as the solution is self-consistent).*

Next, we find the left-most and right-most limits of the curve $y(x)$. Strictly speaking, these are the singular points $x_\text{L} < 0$ and $x_\text{R} > 0$ at which $y'(x_\text{L}) = +\infty$ and $y'(x_\text{R}) = -\infty$. We may use Eq. (II.67) to compute x_L and x_R numerically, substituting $Y(x_\text{L}) = -\sigma$ and $Y(x_\text{R}) = +\sigma$.

Finally, we find the curve $y(x)$ over the domain $x \in (x_\text{L}, x_\text{R})$ by integrating numerically the first-order ODE

$$y'(x) = -\frac{Y(x)}{\sqrt{\sigma^2 - Y^2(x)}}; \quad y(x_\text{R}) = 0 \tag{II.68}$$

Here, the boundary condition $y(x_\text{R}) = 0$ ensures that the curves $\pm y(x)$ join continuously at the front end (the point $(x_\text{R}, 0)$) without forming a cusp. In other words, this condition, along with the fact that $y'(x_\text{R}) = -\infty$, guaranties the smoothness of $\partial\Omega$ at the front. For $\partial\Omega$ to be physically viable, an equivalent condition must hold at the rear. The freedom to impose this additional boundary condition is implicit in our choice of (u_1, p_1, c_1).

For a given set of dimensionless model parameters, we look for solutions to Eq. (II.68) that satisfy the following three constraints:

1. The boundary defined by $\pm y(x)$ represents a simple (non-intersecting) closed contour without cusps. To exclude intersections, we must take care that $y(x) \geq 0$ for $x \in (x_\text{L}, x_\text{R})$. To unsure the smoothness of $\partial\Omega$ at the rear, we look for a solution that satisfies

$$y(x_\text{L}) = 0.$$

2. The dimensionless area is conserved, such that

$$A := 2\int_{x_{\rm L}}^{x_{\rm R}} y(x)dx = \pi.$$

3. The dimensionless total solute is conserved, such that

$$C_{\rm tot} := 2\int_{x_{\rm L}}^{x_{\rm R}} y(x)c_1 e^{-u_1 x}dx = \pi.$$

Together, these constraints describe a system of three implicit nonlinear equations in the three variables (u_1, p_1, c_1). If a dimensionless steadily-moving solution exists for a given set of parameters, it can in principle be found by varying those three numbers while re-integrating Eq. (II.68). Rather than resorting to an exhaustive 3-dimensional grid-search, we employ a more sophisticated computational optimization procedure, which greatly facilitates convergence.

Computational optimization procedure

1. For a new set of dimensionless model parameters, we begin by finding a good quantitative guess of the solution $(u_1^{\rm g}, p_1^{\rm g}, c_1^{\rm g})$. Normally, the computation of $(u_1^{\rm g}, p_1^{\rm g}, c_1^{\rm g})$ relies on polynomial interpolations of (u_1, p_1, c_1) as functions of the varied parameter. Technically, these interpolation functions are constructed using the registered numerical solutions obtained in preceding parametric iterations.

2. We define a dense matrix of phase-space coordinates $\{(p_1, c_1)\}$ about $(p_1^{\rm g}, c_1^{\rm g})$. For each such coordinate, we run the following computational element.

3. With fixed (p_1, c_1), we resolve constraint #1 (minimization of $|y(x_{\rm L})|$) by varying u_1 about $u_1^{\rm g}$ while re-integrating Eq. (II.68). This automated shooting-solution method converges rapidly on a velocity $u_1 > 0$ that grants an acceptable error of $|y(x_{\rm L})| < 10^{-7}$. The resultant contours $\pm y(x)$ then bound a shape Ω which is physically-viable ($\partial\Omega$ is closed without cusps), but generally not consistent with the dimensionless normalization conditions: constraints #2 and #3. We compute the area A and the total solute $C_{\rm tot}$ associated with the physically-viable solution.

4. We use the registered numerical data from steps 2–3 to generate the polynomial interpolation functions, $A(p_1, c_1)$ and $C_{\rm tot}(p_1, c_1)$. We then solve two implicit functions in two variables, namely: $A(p_1, c_1) - \pi = 0$ and $C_{\rm tot}(p_1, c_1) - \pi = 0$. The solution, (p_1^*, c_1^*), is then substituted back in element 3, giving a speed $u_1^* > 0$ and a corresponding curve $y^*(x)$ that resolve constraint #1.

5. We check if $y^*(x)$ actually satisfies constraints #2 and #3. In practice, if we find an acceptable error of both $|A - \pi| < 10^{-5}$ and $|C_{\rm tot} - \pi| < 10^{-5}$, we output and register (u_1^*, p_1^*, c_1^*). Else, we substitute (u_1^*, p_1^*, c_1^*) as a new updated guess in step 2, and repeat this process while possibly changing the extent and the density of our $\{(p_1, c_1)\}$ grid.

By using this powerful continuation + minimization procedure we are able to converge with high precision on the coveted steady-states. Difficulties in convergence arise in highly nonlinear regimes (e.g., close to bifurcations), where the speed and/or the shape vary strongly as functions of the parameters or as functions of (p_1, c_1). Hence, in these regimes we work with smaller parametric iterations and denser $\{(p_1, c_1)\}$ grids. While these practices are generally time-consuming, they tend to improve the accuracy of both the initial guess and the interpolation functions, which together promote convergence.

Remark II.5.6. *As we span the parameter space, we fix σ and c_s arbitrarily and perform incremental iterations of χ (substituting $\beta = \chi(c_s+1)^2/c_s$ in Eq. (II.67)). We always begin at $\chi = 1$ (the motility-mode instability), where the steadily-moving states are known to branch out from the circular rest-state via a super- or subcritical pitchfork bifurcation. About this critical point, both the speed u_1 and the shape deviation from the circle are small, so we can use our rigid-droplet results to compute the initial guess. In more detail, Eqs. (II.61) – (II.62) are used for computing u_1^g. Then, u_1^g is substituted in Eq. (II.58) for computing c_1^g. Finally, c_1^g is used to compute $p_1^g = \sigma - F_{act}(c_1^g)$.*

Remark II.5.7. *Any physically-viable solution (u_1, p_1, c_1), which resolves constraint #1 but is not consistent with constraints #2 and #3 (obtained, e.g., via step 3 in our procedure), can be mapped directly to a self-consistent dimensionless solution. To perform this mapping correctly, one must rescale both the parameters and the solution variables in accordance with our nondimensionalization scheme,*

$$(\sigma, \beta, c_s) \to \left(\frac{1}{R_0}\sigma, \beta, \frac{A}{C_{tot}}c_s\right); \quad (u_1, p_1, c_1) \to \left(R_0 u_1, p_1, \frac{A}{C_{tot}}c_1\right)$$

where $R_0 = \sqrt{A/\pi}$. Note that when working with χ instead of β, i.e., with Eq. (II.50), one should rescale χ like $\chi \to \frac{C_{tot}(c_s+1)^2}{A(c_s+C_{tot}/A)^2}\chi$.

For the new set of 3 dimensionless parameters, the rescaled solution automatically satisfies all three constraints (discussed above) and is therefore a dimensionless steadily-moving state. We stress that, in this appealing shortcut to constraints #2 and #3, the dimensionless parameters (σ and c_s specifically) may be not fixed a priori. Hence, unlike our complete optimization procedure, this rescaling 'trick' is not well-suited for spanning the parameter space in a controlled, structured manner.

Computational solutions

In Fig. II.5, we fix a moderate finite tension ($\sigma = 1$) and trace the dimensionless steadily-moving states as they branch out from the rest-state ($u_1 = 0$) at $\chi = 1$ (the motility-mode instability). As in the rigid case, the pitchfork bifurcation is supercritical if $c_s \geq 0.5$ and subcritical if $c_s < 0.5$. Moreover, in the subcritical regime we also find the saddle-node bifurcation of finite velocity occurring at some $\chi^{*N} < 1$. Thus, at a qualitative level, we obtain the same bifurcation structure and consequent motility phases as in the rigid case. Indeed, we find that this picture is very robust for sufficiently high tension. That being said, our results for the deformable droplet do not merely reconstitute a force-speed relationship. Using our computational optimization method for resolving the self-consistent traveling states, we also capture their shapes (Figs. II.5a-c). This acquisition allows

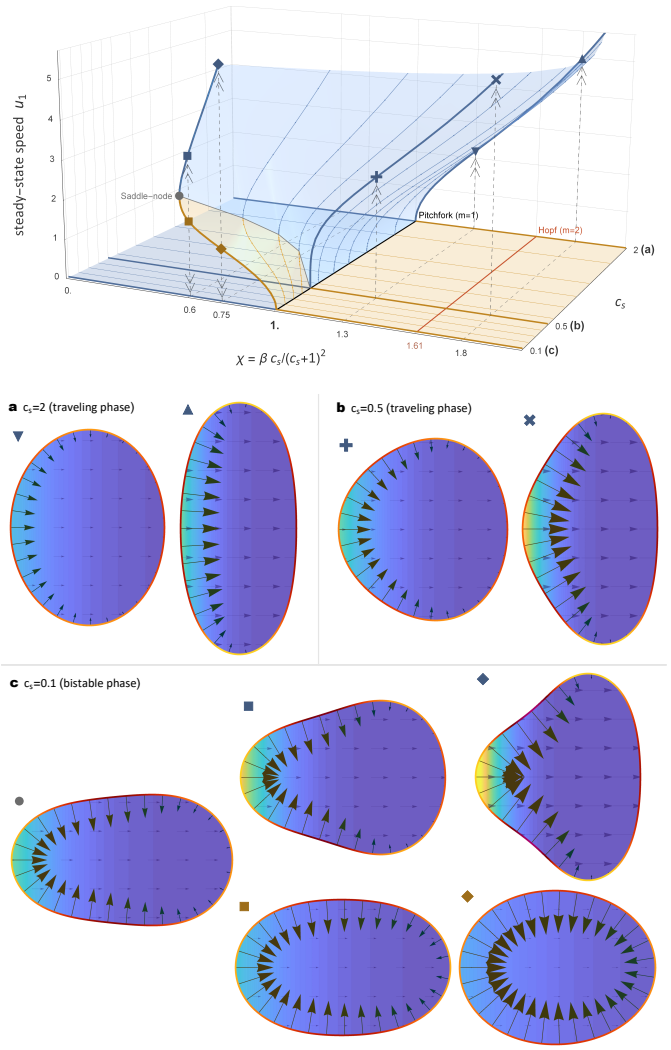

Fig. II.5 **Steadily-moving states (moderate tension)**. *Motility bifurcation diagram (top): with $\sigma = 1$, $a = 1$ fixed, we plot the steady-state velocity u_1 as a function of the force parameters; χ and c_s. Blue (orange) contours/surfaces mark the stable (unstable) branch of the steady traveling solutions. The circular homogeneous rest-state is represented by the plane $u_1 = 0$. On this plane, the black line marks the linear instability of the motility mode ($m = 1$), and the red line marks the $m = 2$ Hopf bifurcation. The branching of traveling states at $\chi = 1$ takes the form of a pitchfork bifurcation, which is supercritical if $c_s > 0.5$ and subcritical if $c_s < 0.5$. The gray line marks the motility saddle-node bifurcation occurring in the subcritical regime. Large symbols mark the representative solutions visualized in panels (a)–(c). In these panels, the color density map in the bulk represents the solute profile, $c(x) = c_1 e^{-a u_1 x}$. The color coded boundary represents the curvature, $\kappa = \sigma^{-1}\left(p + F_{act}\left(c\right)\right)$. The blue vector field in the bulk represents the fluid velocity, $\mathbf{u} = u_1 \hat{x}$. The dark arrows on the boundary represent $F_{act}(c)\mathbf{n}$, Eq. (II.50). In panel (c), the saddle-node state on the left corresponds to $\chi \simeq 0.558$. Parameters matching all other states can be inferred from the diagram.*

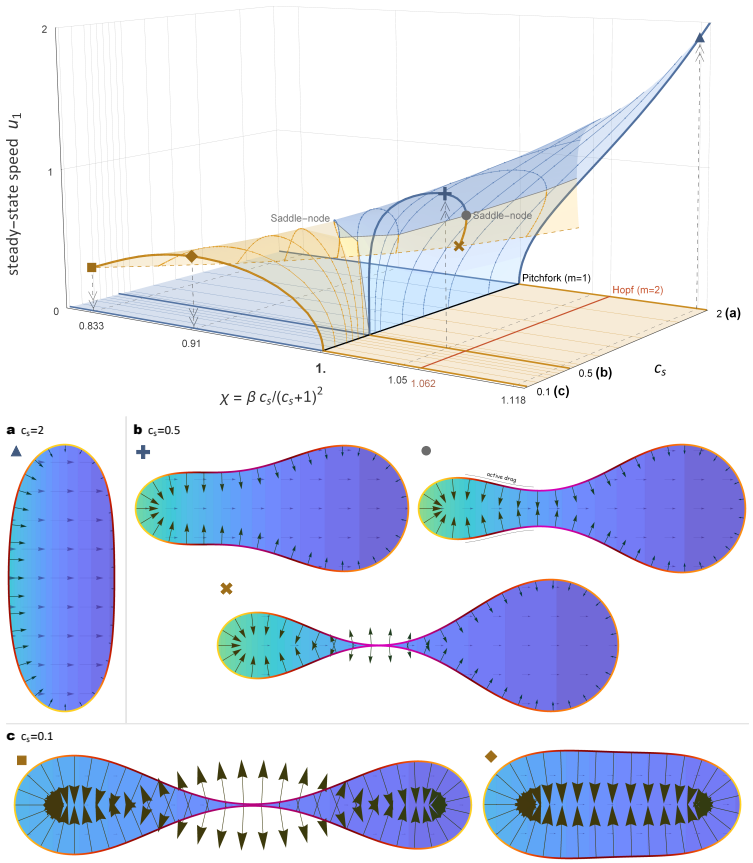

Fig. II.6 **Steadily-moving states (low tension)**. *Motility bifurcation diagram (top): with $\sigma = 0.1$, $a = 1$ fixed, we plot the steady-state velocity u_1 as a function of the force parameters: χ and c_s. All graphics objects and colors have the same meaning as in Fig. II.5. Note here the additional saddle-node bifurcation occurring at high χ (gray line). This bifurcation annihilates the stable branch and gives rise to a new unstable branch beneath it. The latter is itself cut off at a pinched state, traced on the diagram by the dashed orange curve. As the two saddle-node bifurcations disappear simultaneously for low c_s, the unstable subrcitical branch merges with the unstable pinching branch. Large symbols mark the representative solutions visualized in panels (a)–(c). In these panels, graphics objects and color codes have the same meaning as in Figs. II.5a-c. In panel (b), the second (saddle-node) and third (pinched) states correspond to $\chi \simeq 1.063$ and $\chi \simeq 1.058$ respectively. All other parameters can inferred from the diagram.*

us to explore the force-shape (or speed-shape) relationship efficiently—at the nonlinear level—without having to simulate the complex moving-boundary dynamics.

In Fig. II.6, we fix a low tension ($\sigma = 0.1$) and trace the steadily-moving solutions in the same manner. Here, the bifurcation diagram exhibits a distinct qualitative change in the force-speed dependence. Strikingly, we find a parametric regime (about $c_s = 0.5$), for which the steady-state speed u_1 (on the stable branch in blue) becomes a non-monotonic function of the force amplitude β. Moreover, the drop in speed ends at an inverted saddle-node bifurcation (occurring at some $\chi^{**} > \min[\chi^*, 1]$, depending on c_s). This unexpected critical point essentially annihilates the stable branch for higher force amplitudes. It also gives birth to a new unstable branch that terminates at some $\chi < \chi^{**}$, where a pinching point occurs, implying a topological singularity (visualized in Fig. II.6b). This singularity is traced on the diagram by the dashed orange line. Note that the phenomenon of an unstable solution branch terminating at a topological singularity has been found previousely in the classical viscous fingering problem Álvarez-Lacalle et al (2004). In addition, there exists a critical c_s (smaller than 0.5), below which the two saddle-nodes (corresponding to χ^* and χ^{**}) are annihilated simultaneously and the stable branch completely disappears. At this stage, the unstable pinching branch merges with the unstable subcritical branch, which originates at $\chi = 1$. The recovered shapes basically reveal that this intricate bifurcation structure is caused by a particular deformation tendency that takes hold in the low c_s (and low σ) regime. This provides a unique opportunity to gain insights into the nonlinear physics underlying the force-shape-speed dependence.

II.5.5 Interpretation of the steady morphology

We may infer the qualitative makeup of the steady-state shape (as defined by $\pm y(x)$) from an overview of the curvature extrema points.

Due to reflection symmetry about the axis motion $\hat{x}$, the front and rear limits, x_R and x_L, are themselves local curvature extrema. As explained previously, both coordinates are determined implicitly by the constraints which grant a self-consistent solution.

Deriving Eq. (II.66) (with $a = 1$), we also obtain a maximum (x_+) and minimum (x_-) of $\kappa(x)$:

$$x_\pm = \frac{1}{u_1} \log\left(\frac{c_1}{2c_s}\left(\beta - 2 \pm \sqrt{\beta\,(\beta-4)}\right)\right)$$

where here we recall that u_1, c_1 are themselves nonlinear functions of all dimensionless parameters—including σ. Note that $x_\pm$ are necessarily real numbers since the minimal $a\beta$ for which steady traveling states exist is 4.

From a physics viewpoint, the extrema $x_\pm$ have the meaning of crossover points in the normal force balance, Eq. (II.66). For $x > x_+$, the curvature decreases with x because the pressure, Eq. (II.52), dominates the equation ($F_{\text{act}}(c)$ is negligible at high x due to the exponential drop of $c(x)$, Eq. (II.55)). For $x \in (x_-, x_+)$, the curvature increases with x due to the nonlinear rearwards amplification of the active pulling force (in this regime, $\partial_x F_{\text{act}}(c(x)) > 0$ dominates over $p'(x) = -u_1$). For $x < x_-$, the curvature again decreases with x due to the saturation of $F_{\text{act}}(c)$.

For high c_s, we generally find that $x_- < x_L < x_+ < x_R$. This means that x_- is irrelevant (out of bounds) and both x_L, x_R are local curvature minima. The resulting shape is thus elliptical—shortened along the polarity axis—as seen Fig. II.5a and Fig.

II.6a. A decrease in c_s prompts the saturation of F_{act} as a function of x, giving $x_L < x_- < x_+ < x_R$. In this case, the front is still a curvature minimum but the rear is now a curvature maximum. The shape is thus triangulated with a bulged rear, as seen in Fig. II.5b. Note that, about x_-, the curvature can also be negative, as seen in Fig. II.5c (high speed stable state on the right) and Fig. II.6b. For slow traveling states at low c_s, we typically find that $x_L < x_- < x_R < x_+$. In this arrangement, x_+ is irrelevant and both x_L, x_R are curvature maxima. The corresponding shape is then necessarily elongated in the direction of motion, as seen in Fig. II.5c (left-most steady-state) and Fig. II.6c. At low tension and low c_s, the force amplitude β amplifies the negative curvature deformation along the stable branch, leading to a peanut-like (or cat-tongue) shape, as evident in the saddle-node state (second image in Fig. II.6b). This introduces a boundary section, just prior to the rear (where $F_{act}(c)$ is saturated), on which $n_x > 0$ and hence $F_{act}(c)n_x < 0$. Given the external force balance, Eq. (II.21), the speed u_1 ultimately decreases as a consequence of this deformation-induced 'active drag' effect. The same effect also leads to the morphological pinching point which terminates the newly formed unstable branch (see bottom image in Fig. II.6b).

II.6 Conclusion and discussion

In sum, our coupled moving-boundary model offers a concise physical description of symmetry-breaking, active-capillary waves, and steady motility of confined cells. While such phenomena usually entail significantly more complex and analytically intractable modeling, our simple equations of motion give rise to (i) two types of physical instabilities, and (ii) a rich landscape of stationary patterns that connect motion with shape. Despite their intricacy, these results are accordant with the constraints imposed by the external geometry and the internal cytoplasmic fluid.

The model provides both quantitative predictions (i.e., particular speeds and shapes for given parameters) and physical insights, meaning an understanding of the mechano-chemical mechanisms governing the self-organisation of our system. Indeed, the main value of our work is in these physical insights. Given the simplicity of our formulation, and since $F_{act}(c)$ is defined phenomenologically, realistic quantitative predictions for actual cell behaviors remain beyond the scope of the present study.

Notwithstanding, the theoretical patterns obtained here do bear some strong qualitative similarities to a number of experimental observations. Specifically, the elongated traveling shape solutions, found in the low tension regime, are reminiscent of *in-vitro* ameoboid cell migration in quasi-2D confinement Liu et al (2015); Ruprecht et al (2015); Bergert et al (2015). Note the distinct similarity between the polarized progenitor cells in Ruprecht et al (2015) and the predicted pear-like shape in Fig. II.6b (first steady-state). Our model also captures the formation of a uropod-like structure at the cell rear, which is typical to various motile cell types, particularly under confinement Liu et al (2015); Bergert et al (2015). The high aspect-ratio shapes, represented in Figs. II.5a,b, and Fig. II.5c (specifically the high speed steady state), bear more resemblance to confined dendritic cell migration Maiuri et al (2015) or 'mesenchymal' keratocyte migration on substrates Verkhovsky et al (1999); Keren et al (2008).

In addition to motility patterns, standing and traveling normal waves have been ob-

served in various systems, including *Dictyostelium* cells Driscoll et al (2012), suspended fibroblasts Pullarkat (2006) (which have been modeled in Salbreux et al (2007)), developing embryonic cells Maître et al (2015), migrating micogrlia cells Yang et al (2019), and synthetic membrane vesicles containing the Min protein system Litschel et al (2018). Although these experiments were not set in 2D confinement, the similarity to our coupled multipolar oscillations suggest the involvement of a similar mechanism, meaning a viscous fluid-mediated interplay between the restoring surface tension force and an active pushing (pulling) force that is controlled by a diffusive inhibitor (activator).

To this end, there are still open questions pertaining to the nonlinear dynamics and limit behaviors in our system. Notably, the global stability of the resolved steadily-moving states is not guaranteed. Such states may have only a limited basin of attraction within the vast shape-concentration phase space. To contemplate this point, imagine a randomly perturbed rest-state that is linearly unstable with respect to numerous normal modes. In this scenario, the growing multipolar waves would ultimately couple to each other and to the transnational symmetry-breaking mode at the nonlinear level. Plausible additional attractors such as shape-concentration limit-cycles could conceivably compete with the steadily-moving state for selection. Furthermore, the low tension regime presents a particularly puzzling conundrum: when the rest-state is unstable and our branch of stable traveling solutions no longer exists, the dynamic attractor of the motility mode is completely unknown. The possibility of incurring asymmetric fragmentation via a finite-time topological singularity (pinch-off) is in itself an exciting avenue for further investigation. Such unsettled questions may be answered with an appropriate numerical simulation of the problem. Indeed, this will be the objective of the following chapter.

Chapter III

Finite element simulation

In this chapter, we build a numerical simulation of our coupled moving-boundary model. This computational extension of our study has two main objectives. First, we wish to answer some of the unsettled questions pertaining to the limit behaviours of our system as posed in the previous chapter. Second, we aim to expand the scope of the isolated cell model to encompass more biologically-relevant situations. These include the scattering of crawling cells from walls and stationary obstacles, migration through channels and constrictions, and collisions between deformable motile cells.

Broadly speaking, there are many possible ways to discretize free boundary equations. In the context of cell motility, previous computational works have made use of (i) Lagrangian interface representation methods, among which the immersed boundary method Bottino and Fauci (1998); Whitfield and Hawkins (2016) that was originally developed to simulate fluid-structure interaction Peskin (2002), and (ii) Eulerian interface representations such as the Volume-Of-Fluid (VOF) Hirt and Nichols (1981), level-set Maitre et al (2012) and phase-field Shao et al (2010, 2012); Ziebert et al (2011); Camley et al (2013); Tjhung et al (2015); Camley et al (2017) methods (see Ziebert and Aranson (2016) for a review). In free boundary problems, representations of interface and bulk fields are coupled through: (i) interface kinematics: the transport of the Lagrangian or Eulerian interface description by the Eulerian velocity field, or (ii) interface dynamics: problems with boundary (or jump) conditions associated with the sharp interface. The solution of the interface kinematic problem has seen major progress in the past twenty years. However, the situation for interface dynamics, and surface tension in particular, is more complex and a wide range of methods or their combinations have been proposed, see, e.g., Gallinato et al (2017).

Typically, Hele-Shaw flow problems with a sharp moving interface are solved numerically (if not analytically) by taking advantage of elegant meshless techniques such as conformal mapping and the vortex-sheet method (see Bensimon et al (1986); Dallaston (2013) for reviews). However, to simulate our type of problem, in which the fluid flow ($\mathbf{u}$) is coupled to the bulk dynamics of some concentration field (c), it is crucial to determine, at each time step, the deformed geometry on which c and $\mathbf{u}$ are defined. In principle, one could avoid explicitly tracing the interface by using a phase-field (or level-set) method, but this entails formulating a new model that would only approximate our equations of motion at a computationally-expensive limit. In our attempt to maximize precision at efficient computation costs, we chose to build a dynamic-interface simulation based on

the finite element method (FEM), which is known as one of the most powerful numerical techniques for solving PDEs on arbitrary domains.

Our particular method features a high order fully-implicit time integration scheme that overcomes stability issues related to the explicit discretization of the nonlinear curvature vector that determines the surface tension force Lavi et al (2019b). At each time step, the implicit nonlinear problem is solved by a Newton-Raphson method. We address in detail the main features of the proposed method and we present several numerical experiments with the aim of demonstrating its accuracy and efficiency. Quantitative comparisons are performed with respect to the analytic results obtained in the previous chapter. Note that comparative investigations with respect to fully explicit and semi-implicit schemes will be done in future work.

Readers who are generally unfamiliar with variational formulations and boundary discretizations are advised that Section III.1 (the formulation of our method) is technically and mathematically involved. On the other hand, the simulation results shown in Sections III.2 – III.4 are presented in a manner that is more accessible for all readers who are already familiar with our results in Chapter II.

III.1 Formulation

In this section, we present a new numerical methodology for solving the coupled Hele-Shaw and convection-diffusion equations on a moving cell domain. This approach avoids the usual stability conditions and time step restrictions that hold for fully explicit schemes Lavi et al (2019b). Our goal is to convert our continuous time PDE problems into a time discrete variational formulation, which is a standard form of calculus allowing the use of FEM (see preliminary Appendix B.1). Note that our implicit scheme will be based on a Newton method for solving the nonlinear minimization problem associated with the variational formulation. For the sake of clarity and modularity, we first provide the complete treatment of the classical 2D problem of the confined passive droplet. Afterwards, we will couple this problem to the solute force-generation and convection-diffusion dynamics (also formulated in the variational framework). At the end of this section, we explain the spatial discretization into finite elements.

III.1.1 Time discretization

We first recall the continuous time moving-boundary-value problem associated with the confined passive droplet. Let $\Omega_0 = \Omega(t=0)$ be a given smooth (convex and bounded) domain of $\mathbb{R}^2$. For all $t > 0$, the velocity $\mathbf{u}(t,\mathbf{x})$, the pressure $p(t,\mathbf{x})$ and the domain describing the cell $\Omega(t)$ satisfy

$$\begin{cases} \mathbf{u} + \nabla p = 0 & \text{in } \Omega(t) \\ \nabla \cdot \mathbf{u} = 0 & \text{in } \Omega(t) \\ p\mathbf{n} = \sigma\kappa\mathbf{n} & \text{on } \partial\Omega(t) \end{cases} \tag{III.1}$$

together with the kinematic condition, stating that the normal velocity of the sharp interface V_n is given by

$$V_\mathrm{n} = \mathbf{u}\cdot\mathbf{n} \quad \text{on } \partial\Omega(t) \tag{III.2}$$

where $\mathbf{n}$ is the unit vector pointing outward.

We express the time-discrete version of Eqs. (III.1) – (III.2) by taking a time step Δt. Let Ω^i and Γ^i be the cell domain and its interface at time $t_i = i\Delta t$, where i is an integer. The implicit time-discrete version of Eq. (III.1) is

$$\begin{cases} \mathbf{u}^{i+1} + \nabla p^{i+1} = 0 & \text{in } \Omega^i \\ \nabla \cdot \mathbf{u}^{i+1} = 0 & \text{in } \Omega^i \\ p^{i+1}\mathbf{n}^i = \sigma \tilde{\mathbf{H}}^{i+1} & \text{on } \Gamma^i \end{cases} \tag{III.3}$$

where $\mathbf{u}^i$ and $\mathbf{n}^i$ are respectively the known velocity and the outward pointing normal from Γ^i at time t_i. In Eq. (III.3), the solution variables ($\mathbf{u}^{i+1}$, p^{i+1}) are implicit, meaning that their computation requires the knowledge of the future geometry in the next time iteration (Ω^{i+1}), itself determined by $\mathbf{u}^{i+1}$ as explained below. The implicit nature of the problem is embedded in the term $\tilde{\mathbf{H}}^{i+1}$, which represents an approximation of the vector curvature of Γ^{i+1} expressed back in Γ^i.

According to the kinematic condition, Eq. (III.2), the time-varying set of points $\Gamma(t)$ should depend only on the normal component of the velocity ($\mathbf{u} \cdot \mathbf{n}$). This is because any movement along the tangent $\mathbf{t}$ serves merely to re-parameterize Γ. In other words, the shape of the deformed interface is determined by the normal velocity alone. Hence, the tangential flow component on the boundary ($\mathbf{u} \cdot \mathbf{t}$) is completely irrelevant for the continuous problem. In fact, one can define the new (deformed) domain by

$$\Omega^{i+1} = (\mathrm{Id} + \Delta t\, \mathbf{u}^{i+1})(\Omega^i) := \varphi^{i+1}(\Omega^i) \tag{III.4}$$

where $\mathbf{u}^{i+1}$ is the velocity in the next time iteration defined in Ω^i (the solution to Eq. (III.3)). Importantly, the discrete propagation via Eq. (III.4) also means that any point $\mathbf{x}^i$ on Γ^i evolves as

$$\mathbf{x}^{i+1} = \mathbf{x}^i + \Delta t\, \mathbf{u}^{i+1}(\mathbf{x}^i) = \varphi^{i+1}(\mathbf{x}^i) \tag{III.5}$$

where $\mathbf{x}^{i+1}$ is the corresponding point on Γ^{i+1}. It is easy to recognize that the normal component of this equation represents the time discrete version of the kinematic condition, Eq. (III.2).

Implicit treatment of the curvature

Let $\mathbf{t}^i$ and $\mathbf{t}^{i+1}$ denote the tangent vectors along Γ^i and Γ^{i+1} respectively, and let T^{i+1} represent the tangent vector on Γ^{i+1} "pulled back" on Γ^i. In other words, the input of T^{i+1} is any $\mathbf{x}^i$ on Γ^i and the output is $\mathbf{t}^{i+1}(\mathbf{x}^{i+1})$ where $\mathbf{x}^{i+1}$ is given by Eq. (III.5). It follows from Eq. (III.5) that

$$T^{i+1} := \mathbf{t}^{i+1} \circ (\mathrm{Id} + \Delta t\, \mathbf{u}^{i+1}) = \frac{(\mathrm{I} + \Delta t \nabla \mathbf{u}^{i+1})\mathbf{t}^i}{|(\mathrm{I} + \Delta t \nabla \mathbf{u}^{i+1})\mathbf{t}^i|} \tag{III.6}$$

where $\nabla \mathbf{u}^{i+1}$ denotes the gradient matrix of $\mathbf{u}^{i+1}$ (defined in Ω^i) and I represents the 2×2 identity matrix.

Let $\mathbf{X}^i(s)$ for $s \in I$ be a parameterization of Γ^i. We use Eq. (III.5) to build a parameterization $\mathbf{X}^{i+1}(s)$ of the interface $\Gamma^{i+1} := \partial\Omega^{i+1}$, such that

$$\mathbf{X}^{i+1}(s) = \mathbf{X}^i(s) + \Delta t\, \mathbf{u}^{i+1}\left(\mathbf{X}^i(s)\right)$$

Note here that $s = (\mathbf{X}^i)^{-1}(\mathbf{x}^i) = (\mathbf{X}^{i+1})^{-1}(\mathbf{x}^{i+1})$ for all $\mathbf{x}^i \in \Gamma^i$ and $\mathbf{x}^{i+1} = \varphi^{i+1}(\mathbf{x}^i)$.

The curvature vectors $\mathbf{H}^i := \kappa^i \mathbf{n}^i$ on Γ^i and $\mathbf{H}^{i+1} := \kappa^{i+1}\mathbf{n}^{i+1}$ on Γ^{i+1} are defined as

$$\mathbf{H}^i = -|\mathbf{X}^{i\prime}(s)|^{-1}\frac{\mathrm{d}}{\mathrm{d}s}\mathbf{t}^i(\mathbf{X}^i(s)) = -\nabla \mathbf{t}^i\,\mathbf{t}^i$$

$$\mathbf{H}^{i+1} = -|\mathbf{X}^{i+1\prime}(s)|^{-1}\frac{\mathrm{d}}{\mathrm{d}s}\mathbf{t}^{i+1}(\mathbf{X}^{i+1}(s)) = -\nabla \mathbf{t}^{i+1}\,\mathbf{t}^{i+1}$$

where we use the notation $\nabla \mathbf{f}\,\mathbf{t} = (\mathbf{t}\cdot\nabla)\mathbf{f}$.

The definition of $\tilde{\mathbf{H}}^{i+1}$ (an approximation of $\mathbf{H}^{i+1}$ pulled back on Γ^i) is

$$\tilde{\mathbf{H}}^{i+1} = -|\mathbf{X}^{i\prime}(s)|^{-1}\frac{\mathrm{d}}{\mathrm{d}s}\left(T^{i+1}(\mathbf{X}^i(s))\right) = -\nabla T^{i+1}\,\mathbf{t}^i \tag{III.7}$$

By plugging the fully implicit Eq. (III.7) in Eq. (III.3) one obtains a nonlinear set of equations in $\mathbf{u}^{i+1}$ at each time-step. We stress that the nonlinearity comes from the fact that the domain Ω^{i+1} is not known a priori. To handle this problem efficiently, we will convert the discrete nonlinear PDE system into a sequence of linear problems. This will be done within the variational framework as to allow the use of the finite element method.

Remark III.1.1. *There is some freedom in how we choose to define the curvature vector in the time discrete problem, Eq. (III.3). Instead of $\tilde{\mathbf{H}}^{i+1}$, which is highly nonlinear and difficult to grasp intuitively, one could have considered the fully explicit $\kappa^i\mathbf{n}^i$, or—preferably—a semi-implicit approximation of $\kappa^{i+1}\mathbf{n}^i$ based solely on Γ^i, i.e.,*

$$\kappa^{i+1}\mathbf{n}^i \simeq \kappa^i\mathbf{n}^i - \Delta t\,|\mathbf{X}^{i\prime}(s)|^{-2}\frac{\mathrm{d}^2}{\mathrm{d}s^2}\mathbf{u}^{i+1}(\mathbf{X}^i(s)),$$

where $|\mathbf{X}^{i\prime}(s)|^{-2}\frac{\mathrm{d}^2}{\mathrm{d}s^2}$ represents the second derivative with respect to the arc length coordinate on the boundary of the current configuration (Γ^i). Note that this approximation is termed 'semi-implicit' because the curvature is implicit while the geometry is explicit. It effectively adds a diffusion term to the curvature vector that helps to regularize the problem by avoiding singularities. With respect to our fully-implicit term ($\tilde{H}^{i+1}$), which is more accurate, the 'semi-implicit' approximation has the advantage of being linear in $\mathbf{u}^{i+1}$ (thereby making Eq. (III.3) strictly linear).

The explicit choice would have required the introduction of a Courant–Friedrichs–Lewy (CFL) condition, which imposes a highly restrictive upper bound for Δt at each time step to ensure the stability of the scheme. By using either the semi-implicit or our fully implicit schemes, we expect to circumvent the source of instability associated with the explicit method.

In this study, we proceed with $\tilde{\mathbf{H}}^{i+1}$ as it allows to conveniently formulate each time iteration as a minimization problem (explained in the following subsection). We expect this formulation to be consistent, meaning that if the solution is smooth, the time discretization introduces a truncature error of order Δt.

III.1.2 Variational formulation and the minimization problem

Here, we derive the variational formulation associated with the time discrete Eqs. (III.3) – (III.4). Note that this part assumes basic preliminary knowledge of Sobolev function spaces and variational formulations, see Appendix B.1 for an introduction.

We multiply the first equation in Eq. (III.3) by an arbitrary smooth vector field test function $\mathbf{v}$ and integrate over the domain Ω^i

$$\int_{\Omega^i} \mathbf{u}^{i+1} \cdot \mathbf{v} \, \mathrm{d}a + \int_{\Omega^i} \nabla p^{i+1} \cdot \mathbf{v} \, \mathrm{d}a = 0$$

Integrating the second term by parts:

$$\int_{\Omega^i} \mathbf{u}^{i+1} \cdot \mathbf{v} \, \mathrm{d}a - \int_{\Omega^i} p^{i+1} (\nabla \cdot \mathbf{v}) \, \mathrm{d}a + \oint_{\Gamma^i} p^{i+1} (\mathbf{v} \cdot \mathbf{n}^i) \, \mathrm{d}l = 0$$

Substituting the Dirichlet condition (third in Eq. (III.3)) in the boundary term:

$$\int_{\Omega^i} \mathbf{u}^{i+1} \cdot \mathbf{v} \, \mathrm{d}a - \int_{\Omega^i} p^{i+1} (\nabla \cdot \mathbf{v}) \, \mathrm{d}a + \sigma \oint_{\Gamma^i} \tilde{\mathbf{H}}^{i+1} \cdot \mathbf{v} \, \mathrm{d}l = 0 \tag{III.8}$$

We also multiply the second equation in Eq. (III.3) by a smooth scalar test function q and integrate over Ω^i:

$$\int_{\Omega^i} (\nabla \cdot \mathbf{u}^{i+1}) q \, \mathrm{d}a = 0 \tag{III.9}$$

The variational formulation of the boundary value problem in Eq. (III.3) is then obtained by combining Eqs. (III.8) – (III.9),

$$\int_{\Omega^i} \mathbf{u}^{i+1} \cdot \mathbf{v} \, \mathrm{d}a - \int_{\Omega^i} p^{i+1} (\nabla \cdot \mathbf{v}) \, \mathrm{d}a - \int_{\Omega^i} (\nabla \cdot \mathbf{u}^{i+1}) q \, \mathrm{d}a + \sigma \oint_{\Gamma^i} \tilde{\mathbf{H}}^{i+1} \cdot \mathbf{v} \, \mathrm{d}l = 0 \tag{III.10}$$

Formally, the problem consists of finding $\mathbf{u}^{i+1} \in H^1(\Omega^i)^2$ and $p^{i+1} \in L^2(\Omega^i)$ such that Eq. (III.10) holds for any arbitrary smooth test functions $\mathbf{v} : \Omega^i \to \mathbb{R}^2$ (for the velocity) and $q : \Omega^i \to \mathbb{R}$ (for the pressure).

Use of the shape derivative of the perimeter

In order to compute the term $\oint_{\Gamma^i} \tilde{\mathbf{H}}^{i+1} \cdot \mathbf{v} \, \mathrm{d}l$ we will rely on the fact that the shape derivative $d\mathcal{P}(\Omega; \mathbf{v})$ of the perimeter $\mathcal{P}(\Omega)$ of Ω is given by

$$d\mathcal{P}(\Omega; \mathbf{v}) = \oint_{\partial\Omega} \kappa \mathbf{n} \cdot \mathbf{v} \, \mathrm{d}l$$

Let $F(\mathbf{u})$ be the perimeter functional in the deformed configuration, i.e.,

$$F(\mathbf{u}) = \mathcal{P}((\mathrm{Id} + \Delta t \, \mathbf{u})(\Omega)) = \int_\Gamma |(\mathrm{I} + \Delta t \nabla \mathbf{u}) \mathbf{t}| \, \mathrm{d}l \tag{III.11}$$

Then,

$$F'(\mathbf{u})(\mathbf{v}) = d\mathcal{P}\left((\mathrm{Id} + \Delta t \, \mathbf{u})(\Omega); \mathbf{v}\right)$$

In Appendix B.2, we prove via a first order expansion of F at $\mathbf{u}$ that

$$\oint_{\Gamma^i} \tilde{\mathbf{H}}^{i+1} \cdot \mathbf{v} \, \mathrm{d}l = \frac{1}{\Delta t} F'(\mathbf{u}^{i+1})(\mathbf{v}) = \oint_{\Gamma^i} \nabla \mathbf{v} \, \mathbf{t}^i \cdot T^{i+1} \, \mathrm{d}l \tag{III.12}$$

Note that the expression on the RHS absolves us from the difficult task of computing $\tilde{\mathbf{H}}^{i+1}$ directly. That being said, our problem is still nonlinear through the dependence of T^{i+1} on $\mathbf{u}^{i+1}$, see Eq. (III.6).

The minimization problem

Here, we give physical intuition of Eq. (III.10) by showing its correspondence to a gradient decent problem derived from an energy functional (with two hydrodynamic constraints).

We first substitute Eq. (III.12) back in Eq. (III.10) and omit the superscript i for brevity,

$$\int_\Omega \mathbf{u}\cdot\mathbf{v}\,\mathrm{d}a - \int_\Omega p(\nabla\cdot\mathbf{v})\,\mathrm{d}a - \int_\Omega (\nabla\cdot\mathbf{u})q\,\mathrm{d}a + \frac{\sigma}{\Delta t}F'(\mathbf{u})(\mathbf{v}) = 0\,, \tag{III.13}$$

where $\mathbf{u}\in H^1(\Omega)^2$ and $p\in L^2(\Omega)$ for any arbitrary smooth test functions $\mathbf{v}:\Omega\to\mathbb{R}^2$ and $q:\Omega\to\mathbb{R}$. We also recall that $F(\mathbf{u})$ is the perimeter functional in the deformed configuration, given by Eq. (III.11).

Before introducing the functional, we remark that by assuming $\nabla\cdot\mathbf{u}=0$, and substituting $\mathbf{v}=\mathbf{u}$ in Eq. (III.13), one obtains $F'(\mathbf{u})(\mathbf{u})\propto -\int_\Omega|\mathbf{u}|^2\,\mathrm{d}a<0$. This means that the droplet perimeter $F(\mathbf{u})$ is minimized by any incompressible solution $\mathbf{u}$ of Eq. (III.13).

Lemma III.1.2. *The variational formulation in Eq.* (III.13) *is the Euler equation for the following minimization problem:*

$$\inf_{\mathbf{u}\in V(\Omega)} J(\mathbf{u})\,,$$

where Ω is a given smooth subset of $\mathbb{R}^2$ and the functional J is defined by

$$J(\mathbf{u}) = \frac{1}{2}\int_\Omega|\mathbf{u}|^2\,\mathrm{d}a + \frac{\sigma}{\Delta t}F(\mathbf{u})\,, \tag{III.14}$$

over the set $V(\Omega)$ defined by

$$V(\Omega) = \left\{\mathbf{u}\in H^1(\Omega)^2 \text{ such that } \nabla\cdot\mathbf{u}=0 \text{ and } \nabla\times\mathbf{u}=0 \text{ in } \Omega\right\}.$$

Proof. We expand $J(\mathbf{u}+\delta\mathbf{u})$ to first order in $\delta\mathbf{u}$,

$$J(\mathbf{u}+\delta\mathbf{u}) = J(\mathbf{u}) + \int_\Omega \mathbf{u}\cdot\delta\mathbf{u}\,\mathrm{d}a + \frac{\sigma}{\Delta t}F'(\mathbf{u})(\delta\mathbf{u}) + O(|\delta\mathbf{u}|^2)\,.$$

Hence, for $\mathbf{u}$ that minimizes $J(\mathbf{u})$ the following equality should hold

$$\delta J(\mathbf{u};\mathbf{v}) = \int_\Omega \mathbf{u}\cdot\mathbf{v}\,\mathrm{d}a + \frac{\sigma}{\Delta t}F'(\mathbf{u})(\mathbf{v}) = 0$$

for any smooth vector field function $\mathbf{v}:\Omega\to\mathbb{R}^2$.

Indeed, this equality reproduces the first and fourth terms on the LHS of Eq. (III.13). The second term in that equation, $-\int_\Omega p(\nabla\cdot\mathbf{v})\,\mathrm{d}a$, imposes Darcy's law, $\mathbf{u}=-\nabla p$, meaning that the flow is irrotational ($\nabla\times\mathbf{u}=0$ in Ω). The third term, $-\int_\Omega(\nabla\cdot\mathbf{u})q\,\mathrm{d}a$, is a Lagrange multiplier imposing the incompressibility condition ($\nabla\cdot\mathbf{u}=0$ in Ω). In other words, the two terms in Eq. (III.13) that are absent in $\delta J(\mathbf{u};\mathbf{v})$ ensure that $\mathbf{u}\in V(\Omega)$. Hence the result. □

From the physics point of view, the minimization of the energy functional in Eq. (III.14) can be understood as follows. In each time iteration, we look for a flow field $\mathbf{u}$ that minimizes the surface energy (proportional the perimeter times the energy density σ of the liquid surface) while taking into account the rate of kinetic energy dissipation that comes from the effective friction in the bulk (exerted on the confined viscous fluid by the no-slip plates).

III.1.3 A Newton algorithm

The main difficulty in solving Eq. (III.13) is to find a method to handle the nonlinear boundary term, Eq. (III.12). To this end, we propose to use a Newton like method for mapping this problem into a sequence of converging linear problems (see Ortega and Rheinboldt (1970) for a comprehensive guide).

Assume that $\mathbf{u}^{\mathrm{g}}$ is a close guess to the true root $\mathbf{u}$ of Eq. (III.13), and that $F''(\mathbf{u}^{\mathrm{g}})$ is a positive definite matrix on Γ. Then, the solution $(\mathbf{u}, p)$ of the linearized system,

$$\begin{aligned}\int_\Omega \mathbf{u}\cdot\mathbf{v}\,\mathrm{d}a - \int_\Omega p(\nabla\cdot\mathbf{v})\,\mathrm{d}a - \int_\Omega (\nabla\cdot\mathbf{u})q\,\mathrm{d}a + \frac{\sigma}{\Delta t}F'(\mathbf{u}^{\mathrm{g}})(\mathbf{v}) \\ + \frac{\sigma}{\Delta t}F''(\mathbf{u}^{\mathrm{g}})\left(\mathbf{u}-\mathbf{u}^{\mathrm{g}},\mathbf{v}\right) = 0\,,\end{aligned} \tag{III.15}$$

gives a flow field $\mathbf{u}$ that is closer than $\mathbf{u}^{\mathrm{g}}$ to the true root of Eq. (III.13).

Remark III.1.3. *The last term in Eq.* (III.15) *is a bilinear form. It is obtained by finding the second order asymptotic expansion of* F *at* $\mathbf{u}$.

Our Newton like method is based on the the notion above. At each time step, it consists of computing a sequence $(u^k)_k$ where $\mathbf{u}^0 = 0$ and $\mathbf{u}^{k+1} \in H^1(\Omega)^2$, $p \in L^2(\Omega)$ are solutions to the following variational problem

$$\begin{aligned}\int_\Omega \mathbf{u}^{k+1}\cdot\mathbf{v}\,\mathrm{d}a - \int_\Omega p(\nabla\cdot\mathbf{v})\,\mathrm{d}a - \int_\Omega (\nabla\cdot\mathbf{u}^{k+1})q\,\mathrm{d}a + \frac{\sigma}{\Delta t}F'(\mathbf{u}^k)(\mathbf{v}) \\ + \frac{\sigma}{\Delta t}F''(\mathbf{u}^k)\left(\mathbf{u}^{k+1}-\mathbf{u}^k,\mathbf{v}\right) = 0\end{aligned} \tag{III.16}$$

for any arbitrary smooth test functions $\mathbf{v}$, q.

Assuming that this method converges, i.e., $\lim_{k\to\infty}|\mathbf{u}^{k+1}-\mathbf{u}^k| \to 0$, we shall denote by $\mathbf{u}$ the limit of $(u^k)_k$ for $k\to\infty$. It follows that $(\mathbf{u}, p)$ will satisfy Eq. (III.13). The remaining challenge is to compute the matrix F''.

Second order expansion of the deformed perimeter

To apply our Newton like method we must first perform an asymptotic expansion of order two of the perimeter functional in the deformed configuration. In Appendix B.3, we prove that

$$\begin{aligned}F(\mathbf{u}+\delta\mathbf{u}) =& F(\mathbf{u}) + \Delta t\oint_\Gamma \nabla\delta\mathbf{u}\,\mathbf{t}\cdot T\,\mathrm{d}s \\ &+ \frac{\Delta t^2}{2}\oint_\Gamma \frac{(\nabla\delta\mathbf{u}\,\mathbf{t}\cdot\mathbf{N})^2}{\mathrm{d}S}\,\mathrm{d}s + O(||\nabla\delta\mathbf{u}||^3)\end{aligned} \tag{III.17}$$

where $\mathrm{d}s$, $\mathbf{t}$ and $\mathbf{n}$ are respectively the unit length, the tangent and the outward pointing unit normal vectors in the current configuration Ω, and $\mathrm{d}S$, T and $\mathbf{N}$ are respectively the unit length, the tangent and the outward pointing unit normal vectors in the deformed configuration $(\mathrm{Id}+\Delta t\mathbf{u})(\Omega)$, "pulled back" in the coordinate system of the current configuration.

First linearized problem

It follows from Eq. (III.17) that

$$F'(\mathbf{u})(\mathbf{v}) = \Delta t \oint_\Gamma \nabla \mathbf{v}\,\mathbf{t} \cdot T \,\mathrm{d}s, \quad F''(\mathbf{u})(\delta\mathbf{u}, \mathbf{v}) = \Delta t^2 \oint_\Gamma \frac{(\nabla \delta\mathbf{u}\,\mathbf{t} \cdot \mathbf{N})\,(\nabla \mathbf{v}\,\mathbf{t} \cdot \mathbf{N})}{\mathrm{d}S} \,\mathrm{d}s$$

Substituting these terms into our Newton like Method, Eq. (III.16), gives

$$\begin{aligned} \int_\Omega \mathbf{u}^{k+1} \cdot \mathbf{v} \,\mathrm{d}a - \int_\Omega p(\nabla \cdot \mathbf{v}) \,\mathrm{d}a - \int_\Omega (\nabla \cdot \mathbf{u}^{k+1}) q \,\mathrm{d}a + \sigma \oint_\Gamma \nabla \mathbf{v}\,\mathbf{t} \cdot T^k \,\mathrm{d}s \\ + \sigma \Delta t \oint_\Gamma \frac{(\nabla \delta\mathbf{u}^{k+1}\,\mathbf{t} \cdot \mathbf{N}^k)(\nabla \mathbf{v}\,\mathbf{t} \cdot \mathbf{N}^k)}{\mathrm{d}S^k} \,\mathrm{d}s = 0 \end{aligned} \tag{III.18}$$

where $\delta\mathbf{u}^{k+1} := (\mathbf{u}^{k+1} - \mathbf{u}^k)$ and

$$\mathrm{d}S^k = |(\mathrm{I} + \Delta t \,\nabla \mathbf{u}^k)\mathbf{t}|, \quad T^k = \frac{(\mathrm{I} + \Delta t \,\nabla \mathbf{u}^k)\mathbf{t}}{|(\mathrm{I} + \Delta t \,\nabla \mathbf{u}^k)\mathbf{t}|}, \quad \mathbf{N}^k = T^{k\perp}$$

We emphasize the fact that Eq. (III.18) does not contain second-order spatial derivatives, meaning that the curvature vector has been transformed into a term involving only the first spatial derivatives (hence less regularity is needed).

This system in the variables $(\mathbf{u}^{k+1}, p)$ does not necessarily admit a solution (let alone unique) due to the possible lack of coercivity of the bilinear form. Moreover, even if solutions to Eq.(III.18) exist, the convergence of our iterative Newton method is not granted. The straightforward remedy is to replace the bilinear term in Eq. (III.18) by a coercive one, which can be done in various ways. The classical scheme is to compute the eigenvectors and eigenvalues of the matrix and to construct the modified term using only the eigenspaces associated with the positive eignevalues. For simplicity and robustness of our algorithm, we prefer to predetermine a closed formula for the modified matrix which is coercive.

Modified problem

The main obstacle in our current method is that the bilinear form in Eq. (III.18) is not positive definite. Hence, we wish to define a modified problem with a positive-definite matrix.

It follows from the majoration $\sqrt{1+x} \le 1 + x/2$ that

$$\begin{aligned} |(\mathrm{I} + \Delta t \,\nabla(\mathbf{u} + \delta\mathbf{u}))\mathbf{t}| &= \sqrt{|(\mathrm{I} + \Delta t \,\nabla \mathbf{u})\mathbf{t}|^2 + 2\Delta t \nabla \delta\mathbf{u}\,\mathbf{t} \cdot (\mathbf{t} + \Delta t \,\nabla \mathbf{u}\,\mathbf{t}) + \Delta t^2 |\nabla \delta\mathbf{u}\,\mathbf{t}|^2} \\ &\le |(\mathrm{I} + \Delta t \,\nabla \mathbf{u})\mathbf{t}| + \Delta t \,\nabla \delta\mathbf{u}\,\mathbf{t} \cdot T + \frac{\Delta t^2 |\nabla \delta\mathbf{u}\,\mathbf{t}|^2}{2\,\mathrm{d}S} \end{aligned}$$

where $\mathrm{d}S$ and T are given below Eq. (III.18).

A substitution of this relation in the functional of the deformed perimeter gives

$$\begin{aligned} F(\mathbf{u} + \delta\mathbf{u}) \quad \le \quad & F(\mathbf{u}) + \Delta t \oint_\Gamma \nabla \delta\mathbf{u}\,\mathbf{t} \cdot T \,\mathrm{d}s \\ & + \frac{\Delta t^2}{2} \oint_\Gamma \frac{(\nabla \delta\mathbf{u}\,\mathbf{t}) \cdot (\nabla \delta\mathbf{u}\,\mathbf{t})}{\mathrm{d}S} \,\mathrm{d}s \end{aligned}$$

We stress that here, unlike Eq. (III.17), the bilinear form on the RHS is positive definite. We choose to adopt this term in our modified Newton like method.

To recapitulate, in each time step we omit the index i and compute a sequence $(u^k)_k$, where $\mathbf{u}^0 = 0$ and $\mathbf{u}^{k+1} \in H^1(\Omega)^2$, $p \in L^2(\Omega)$ are solutions of the following variational problem

$$\begin{aligned}\int_\Omega \mathbf{u}^{k+1} \cdot \mathbf{v}\,\mathrm{d}a - \int_\Omega p(\nabla \cdot \mathbf{v})\,\mathrm{d}a - \int_\Omega (\nabla \cdot \mathbf{u}^{k+1}) q\,\mathrm{d}a + \sigma \oint_\Gamma \nabla \mathbf{v}\,\mathbf{t} \cdot T^k\,\mathrm{d}s \\ + \sigma \Delta t \oint_\Gamma \frac{(\nabla \delta \mathbf{u}^{k+1}\,\mathbf{t}) \cdot (\nabla \mathbf{v}\,\mathbf{t})}{\mathrm{d}S^k}\,\mathrm{d}s = 0\end{aligned} \tag{III.19}$$

for all arbitrary smooth test functions $\mathbf{v} : \Omega \to \mathbb{R}^2$, $q : \Omega \to \mathbb{R}$, and where

$$\mathrm{d}S^k = |(\mathrm{I} + \Delta t\,\nabla \mathbf{u}^k)\mathbf{t}|, \quad T^k = \frac{(\mathrm{I} + \Delta t\,\nabla \mathbf{u}^k)\mathbf{t}}{|(\mathrm{I} + \Delta t\,\nabla \mathbf{u}^k)\mathbf{t}|}$$

In our algorithm, the method is applied recursively until the stopping criteria based on the computation of the global residual is satisfied. We set the the Newton tolerance to 10^{-5} in our computations, i.e.,

$$\int_\Omega \left|\delta \mathbf{u}^{k+1}\right|^2 = \int_\Omega \left|\mathbf{u}^{k+1} - \mathbf{u}^k\right|^2 < 10^{-5}$$

When this condition is satisfied, we take $(\mathbf{u}^{k+1}, p)$ as the approximate solution for $(\mathbf{u}^{i+1}, p^{i+1})$ in the time-discrete PDE problem, Eq. (III.3). All that is left is to propagate the domain via Eq. (III.4).

III.1.4 Coupling the convection-diffusion problem

We introduce a solute concentration function $c^i \in H^1(\Omega^i)$ which transduces the active boundary force, see Eq. (II.14). In the time-discrete problem, Eq. (III.3), c^i modulates the Dirichlet condition for the pressure p^{i+1}:

$$p^{i+1}\mathbf{n}^i + F_{\mathrm{act}}(c^i)\mathbf{n}^i = \sigma \tilde{\mathbf{H}}^{i+1} \quad \text{on } \Gamma^i \tag{III.20}$$

where we will normally use the Hill-type force defined in Eq. (II.50).

Due to the high degree of complexity associated with solving multiple coupled nonlinear PDEs simultaneously on a moving domain, we do not introduce the implicit c^{i+1} at this stage. That is, c^i in Eq. (III.20) represents a solution of the solute transport problem obtained in the previous time iteration (with c^0 denoting the initial condition).

In the variational formulation of the droplet problem, the active force $F_{\mathrm{act}}(c^i)\mathbf{n}^i$ in Eq. (III.20) merely introduces an added linear term in $\mathbf{v}$, such that Eq. (III.10) will now be given by

$$\begin{aligned}\int_{\Omega^i} \mathbf{u}^{i+1} \cdot \mathbf{v}\,\mathrm{d}a - \int_{\Omega^i} p^{i+1}(\nabla \cdot \mathbf{v})\,\mathrm{d}a - \int_{\Omega^i} (\nabla \cdot \mathbf{u}^{i+1}) q\,\mathrm{d}a \\ + \sigma \oint_{\Gamma^i} \tilde{H}^{i+1} \cdot \mathbf{v}\,\mathrm{d}l - \oint_{\Gamma^i} F_{\mathrm{act}}(c^i)\mathbf{n}^i \cdot \mathbf{v}\,\mathrm{d}l = 0\end{aligned}$$

This added term remains present in our modified Newton like method. It follows that Eq. (III.19) is now given by

$$\begin{aligned}\int_\Omega \mathbf{u}^{k+1}\cdot\mathbf{v}\,\mathrm{d}a - \int_\Omega p(\nabla\cdot\mathbf{v})\,\mathrm{d}a - \int_\Omega(\nabla\cdot\mathbf{u}^{k+1})q\,\mathrm{d}a + \sigma\oint_\Gamma \nabla\mathbf{v}\,\mathbf{t}\cdot T^k\,\mathrm{d}s \\ + \sigma\Delta t\oint_\Gamma \frac{(\nabla\delta\mathbf{u}^{k+1}\,\mathbf{t})\cdot(\nabla\mathbf{v}\,\mathbf{t})}{\mathrm{d}S^k}\,\mathrm{d}s - \oint_\Gamma F_{\mathrm{act}}(c^i)\mathbf{n}\cdot\mathbf{v}\,\mathrm{d}s = 0\end{aligned} \tag{III.21}$$

After solving for $(\mathbf{u}^{i+1},\ p^{i+1})$ in each time step i (i.e., once our Newton method converges), and before we propagate the domain via Eq. (III.4), we wish to solve the solute convection-diffusion dynamics in Ω^i for the time period Δt.

Let us recall the continuous time boundary-value problem for the solute, Eqs. (II.16) – (II.17),

$$\begin{cases}\partial_t c + (1-a)\mathbf{u}\cdot\nabla c - \Delta c = 0 & \text{in } \Omega(t)\\ \nabla c\cdot\mathbf{n} + ac\mathbf{u}\cdot\mathbf{n} = 0 & \text{on } \partial\Omega(t)\end{cases} \tag{III.22}$$

As a first step, we solve the following time discrete problem for c^{i+1} in the fixed domain Ω^i:

$$\begin{cases}(c^{i+1}-c^i)/\Delta t - \mathrm{div}\ \left(a\mathbf{u}^{i+1}c^{i+1} + \nabla c^{i+1}\right) = 0 & \text{in } \Omega^i\\ \left(a\mathbf{u}^{i+1}c^{i+1} + \nabla c^{i+1}\right)\cdot\mathbf{n}^i = 0 & \text{on } \Gamma^i\end{cases} \tag{III.23}$$

where here we stress the fact that the bulk convection speed is defined by $-a\mathbf{u}$ rather than $(1-a)\mathbf{u}$ (as in Eq. (III.22)). As explained in more detail later, the discrete propagation of the domain via $\varphi^{i+1}(\Omega^i)$ will automatically take care of the material convective term $1\mathbf{u}\cdot\nabla c^{i+1}$.

Variational formulation

Multiplying the first equation in Eq. (III.23) by a test function ϕ and integrating over Ω^i:

$$\int_{\Omega^i}(c^{i+1}-c^i)\phi/\Delta t\,\mathrm{d}a - \int_{\Omega^i}\mathrm{div}\ \left(a\mathbf{u}^{i+1}c^{i+1} + \nabla c^{i+1}\right)\phi\,\mathrm{d}a = 0$$

Integrating the second term by parts:

$$\int_{\Omega^i}(c^{i+1}-c^i)\phi/\Delta t\,\mathrm{d}a + \int_{\Omega^i}\left(a\mathbf{u}^{i+1}c^{i+1} + \nabla c^{i+1}\right)\cdot\nabla\phi\,\mathrm{d}a = 0 \tag{III.24}$$

where we used the fact that

$$-\oint_{\Gamma^i}\left(\left(a\mathbf{u}^{i+1}c^{i+1} + \nabla c^{i+1}\right)\cdot\mathbf{n}^i\right)\phi\,\mathrm{d}l = 0$$

due to the no-flux condition (second in Eq. (III.23)).

The variational formulation in Eq. (III.24) consists in finding a solution $c^{i+1}\in H^1(\Omega^i)$ for any arbitrary smooth test function $\phi:\Omega^i\to\mathbb{R}$.

Material convection

After finding a solution to Eq. (III.24), we apply the discrete propagation of the domain via $\Omega^{i+1} = \varphi^{i+1}(\Omega^i)$, Eq. (III.4). This propagation automatically imposes a Lagrangian advection of all fields defined on the moved finite-elements. In Eulerian terms, c^{i+1} essentially follows the transformation

$$c^{i+1} \to c^{i+1} + \Delta t\, \mathbf{u}^{i+1} \cdot \nabla c^{i+1}$$

where, on the RHS, c^{i+1} represents our solution to Eq. (III.23) defined in Ω^i. Importantly, this operation effectively takes care of the term $1\mathbf{u} \cdot \nabla c^{i+1}$ which was missing in in Eq. (III.23).

III.1.5 Space discretization

Each subdomain is covered by a regular triangulation $\mathcal{T}_h$, with maximum mesh size h, and such that it is globally a conforming triangulation of Ω, i.e., $\mathcal{T}_h$ contains a piecewise affine approximation Γ_h of the interface Γ.

In a classical manner, we approximate each component of the velocity in each element $K \in \mathcal{T}_h$ by a polynomial of degree one enriched with a "bubble" function (a polynomial of degree 3 defined as the product of the barycentric coordinates in K and vanishing on the faces of K) and the pressure in each element by a polynomial of degree one. Both approximations are continuous across the element faces except for the pressure at the interface Γ_h. Hence, we consider the following discretizations of the spaces $X := H^1(\Omega)^2$ and $M := L^2(\Omega)$:

$$X_h = \{v_h \in \mathcal{C}^0(\bar{\Omega})^2\,;\ \forall K \in \mathcal{T}_h\,,\ v_{h|K} \in (\mathbb{P}_1 + b_K)^2\} \cap X\,,$$

and

$$M_h = \{q_h \in \mathcal{C}^0(\bar{\Omega})\,;\ \forall K \in \mathcal{T}_h\,,\ q_{h|K} \in \mathbb{P}_1\} \cap M\,,$$

The discrete problem relies on the variational formulations, Eqs. (III.21) and (III.24).

The numerical experiments presented in the following sections were conducted using the package FreeFem++ Hecht et al (2008). The saved data was then analyzed and visualized using our dedicated post-processing tool (written in Mathematica (TM)).

III.2 Verification: simulation-theory comparisons

In this section, we validate our FEM simulation by comparing numerical experiments with theoretical predictions. A good quantitative agreement between simulation and theory in distinct aspect of the model will allow us to proceed with confidence to a FEM-based investigation of the full system dynamics. Note that this section also introduces some important technical details such as meshing schemes and post-processing analyses that will be adopted later on.

We divide this section into two parts. In the first part, we run simulations of the passive Hele-Shaw droplet, without incorporating the convection-diffusion problem. In the second part, we simulate the full droplet-solute dynamics. We define a series of performance tests for the numerical data motivated by our theoretical results in Chapter

II. In more detail, we demonstrate that the FEM tool is quantitatively consistent with global analytical properties of the model (mass conservation laws, external force balance), our linear stability analysis, and our predicted steadily-moving solutions.

III.2.1 Passive Hele-Shaw droplet

To simulate the passive droplet problem (using our code in FreeFem++) one must specify the tension σ, the numerical time step Δt and the initial finite element domain (meaning the triangulation mesh $\mathcal{T}_h$).

Let us first comment on the choice of the time step size. The convergence of the Newton algorithm is indeed quite sensitive to Δt. Values that are too large may lead to starting iterations in our recursive method that would be are far from the expected solutions. There exist several strategies for improving the choice of Δt, but we leave this topic beyond the scope of the present study. In practice, for each numerical experiment, we choose a value of Δt that is 2–4 orders of magnitude smaller than the physical timescale.

Building the finite element domain is done by inputting an explicit counter-clockwise parameterization of the closed interface. Here, we use the polar parameterization $\{x(\theta), y(\theta)\} = \{R^0(\theta)\cos(\theta), R^0(\theta)\sin(\theta)\}$ for $\theta \in (0, 2\pi)$. We define $R^0(\theta) = 1 + \delta R^0(\theta)$, where we write $\delta R^0(\theta)$ in terms of Fourier modes, as in Eq. (II.22),

$$\delta R^0(\theta) = \sum_m \Big(\delta R^0_{cm} \cos(m\theta) + \delta R^0_{sm} \sin(m\theta) \Big) \tag{III.25}$$

Then, by specifying the number (or density) of vertices along the parameterized boundary, FreeFem++ automatically generates the internal triangulation mesh (see Fig. III.1a,b). Note that one could also define an adaptive (non-uniform) mesh, as in Fig. III.1c, which is designed to have a finer definition of vertices along the boundary. The motivation behind such a mesh is to improve the resolution of the shape itself while not 'hyper-meshing' the bulk and thereby drastically increasing computation time (of order h^{-2}).

In each time step, we follow the algorithm outlined at the end of Section III.1.3 (Eq. (III.19)). The simulation data is saved at some fixed interval of time iterations (of order 10-100, depending on Δt and the duration of the simulation) and then imported into our post-processing tool using Mathematica (TM). In each imported frame, we are able to reconstruct the finite-element domain and the interpolation functions for $\mathbf{u}$ and p. In addition, we use the interface vertices to construct a polar piece-wise interpolation function of the boundary, $R^{\rm sim}(\theta)$.

Our objective is to square the simulation results with known characteristics of the passive droplet, namely:

- Conservation of the droplet area, $\dot{A} = 0$.
- External force balance, $\mathbf{u}_{\rm cm} = 0$.
- Morphological relaxation dynamics of linear shape perturbations.

Remark III.2.1. *There are several ways of computing* $\mathbf{u}_{cm}$*. In our post-processing tool, we define* $\mathbf{u}_{cm} = A^{-1} \int_{\partial\Omega} \mathbf{x}(\mathbf{u}\cdot\mathbf{n})\,\mathrm{d}l$*.*

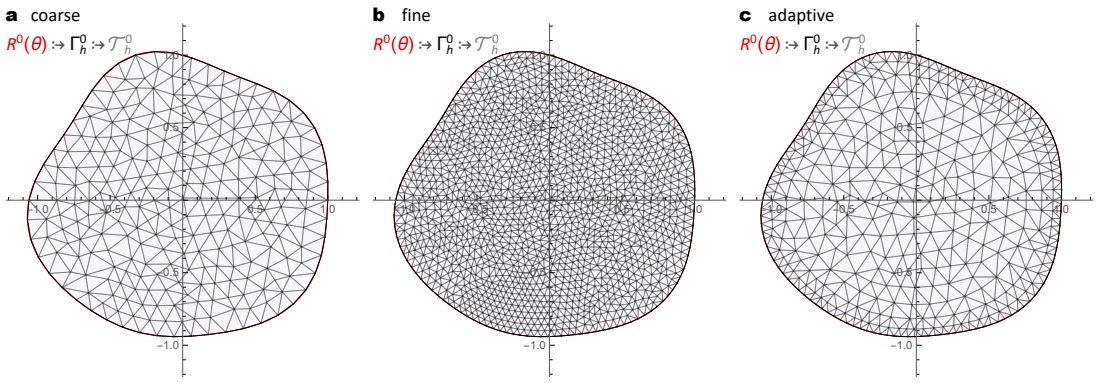

Fig. III.1 ***Building different finite element domains for the same interface.*** *The parameterization $R^0(\theta) = 1 + \delta R^0(\theta)$ (red, Eq. (III.25)) is used to define the affine approximation of the initial interface, Γ_h^0 (black). In turn, FreeFem++ uses Γ_h^0 to generate the internal tiangulation mesh $\mathcal{T}_h^0$ (gray). The density of the mesh is controlled by specifying the number of vertices on the interface. This number is increased from (a) to (b). The adaptive mesh (c) is constructed with two starting interfaces: one (dense) interface on the boundary and another (coarse) interface in the bulk. These define two triangulation meshes (a "disk" and a "ring") which are then joined to form a single connected mesh.*

Remark III.2.2. *To find the numerical growth rate of each normal mode, we first decompose $R^{sim}(\theta)$ into Fourier components,*

$$\begin{aligned} \delta R_{cm}^{sim} &= \frac{1}{\pi}\int_0^{2\pi}\Big(R^{sim}(\theta)-1\Big)\cos(m\theta)d\theta \\ \delta R_{sm}^{sim} &= \frac{1}{\pi}\int_0^{2\pi}\Big(R^{sim}(\theta)-1\Big)\sin(m\theta)d\theta \end{aligned} \tag{III.26}$$

The growth rate of each such component is then obtained by fitting $\delta R_{cm}^{sim}(t)$ and $\delta R_{sm}^{sim}(t)$ to an exponential function $\varepsilon e^{s_m^N t}$. The idea is to compare the fitted s_m^N with the classical cubic dispersion relation, $s_m = -\sigma m(m^2-1)$.

Results of three simulations are represented in Figs. III.2 – III.4. In Figs. III.2 and III.3 we introduced an initial shape perturbation strictly in one Fourier mode ($m = 2$ and $m = 3$, respectively), whereas in Fig. III.4 we introduced a superposition of small perturbations in $m = 2$–5. For the time step and mesh density chosen, we find numerical deviations in $A(t)$ and $|\mathbf{u}_{\rm cm}(t)|$ as low as order 10^{-7}. Moreover, the fitted numerical growth rates of the perturbed Fourier modes are also in good quantitative agreement with the classical dispersion relation s_m (see details in figure captions). We stress that small deviations in the fitted growth rates may also arise from nonlinear effects that have been neglected in the calculation of s_m. As expected, we found through further experimentation with the numerical tool that precision is gained by decreasing Δt, increasing the overall mesh density and/or decreasing the initial perturbation amplitudes.

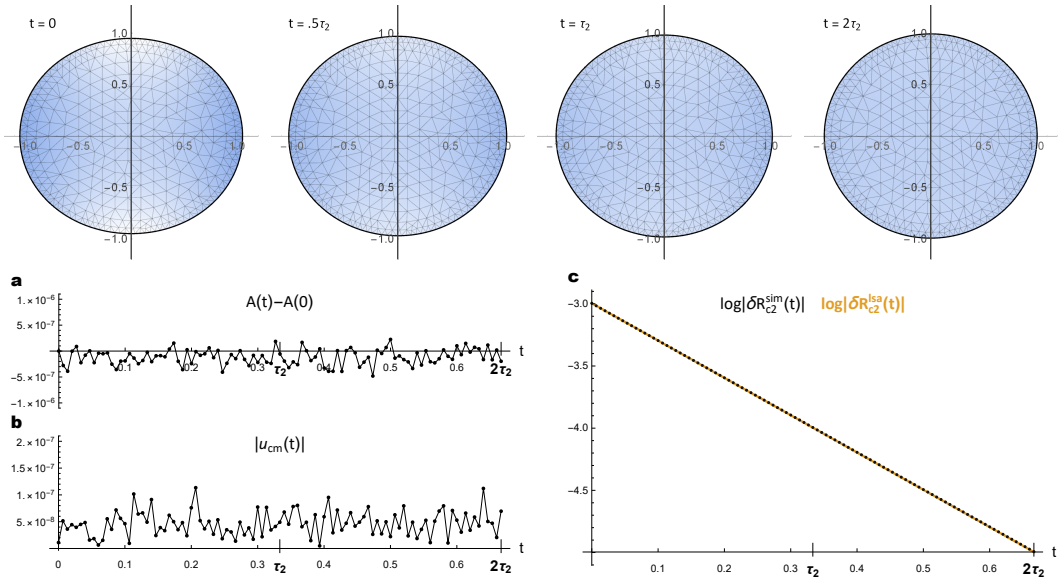

Fig. III.2 ***Decaying shape perturbation (mode*** $m = 2$***):*** *We set* $\delta R^0_{c2} = .05$ *in Eq.* (III.25)*, fixed* $\sigma = 0.5$*, and chose* $\Delta t = 0.0005\tau_2$*, where* $\tau_2 = |s_2|^{-1} = 1/3$*. At the top we present simulation snapshots demonstrating the decay of the shape perturbation. The density plot in the bulk represents the pressure* p *(from low in white to high in blue). a) Time series for the domain area* $A(t)$*. b) Time series for the absolute center of mass velocity* $|\mathbf{u}_{cm}(t)|$*. c) The predicted linear behaviour of the perturbed mode,* $\log|\delta R^{lsa}_{c2}(t)| = \log|\delta R^0_{c2}| - 3t$ *(continuous orange line) vs. the simulation time series,* $\log|\delta R^{sim}_{c2}(t)|$ *(black, computed via Eq.* (III.26)*). We find that the fitted growth rate,* $s_2^N \simeq -2.995$*, compares well with the classical linear-stability growth rate,* $s_2 = -3$ *(giving a deviation of* $(s_2^N - s_2)/s_2 \sim 2 \times 10^{-3}$*).*

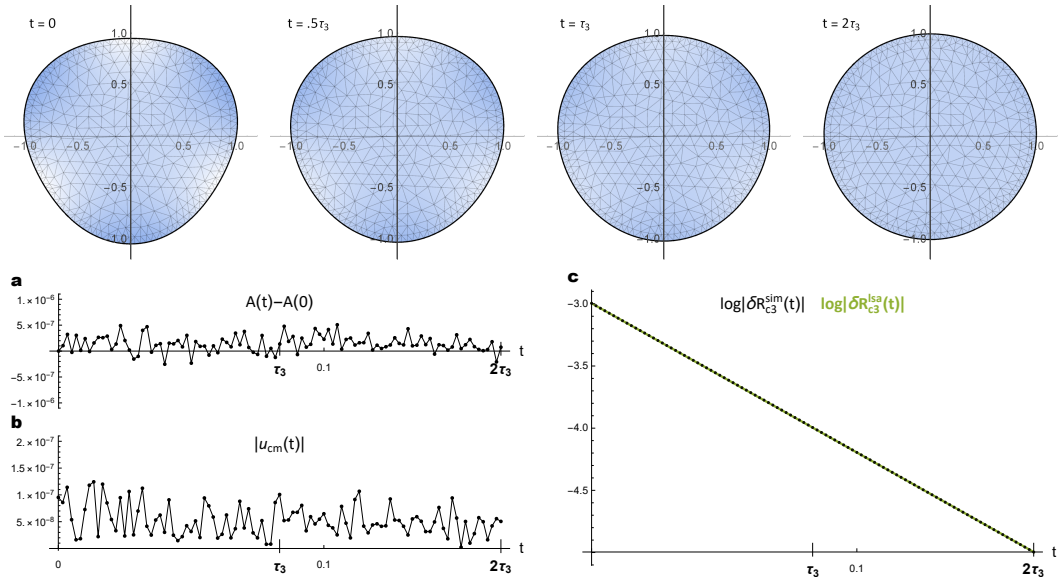

Fig. III.3 ***Decaying shape perturbation (mode*** $m = 3$***):*** *We set* $\delta R^0_{c3} = .05$ *in Eq.* (III.25)*, fixed* $\sigma = 0.5$*, and chose* $\Delta t = 0.0005\tau_3$*, where* $\tau_3 = |s_3|^{-1} = 1/12$*. At the top we present simulation snapshots demonstrating the decay of the shape perturbation. The density plot in the bulk represents the pressure* p *(from low in white to high in blue). a) Time series for the domain area* $A(t)$*. b) Time series for the absolute center of mass velocity* $|\mathbf{u}_{cm}(t)|$*. c) The predicted linear behaviour of the perturbed mode,* $\log|\delta R^{lsa}_{c3}(t)| = \log|\delta R^0_{c3}| - 12t$ *(continuous green line) vs. the simulation time series,* $\log|\delta R^{sim}_{c3}(t)|$ *(black, computed via Eq.* (III.26)*). We find that the fitted growth rate,* $s^N_3 \simeq -11.996$*, compares well with the classical linear-stability growth rate,* $s_3 = -12$ *(giving a deviation of* $(s^N_2 - s_2)/s_2 \sim 4 \times 10^{-4}$*).*

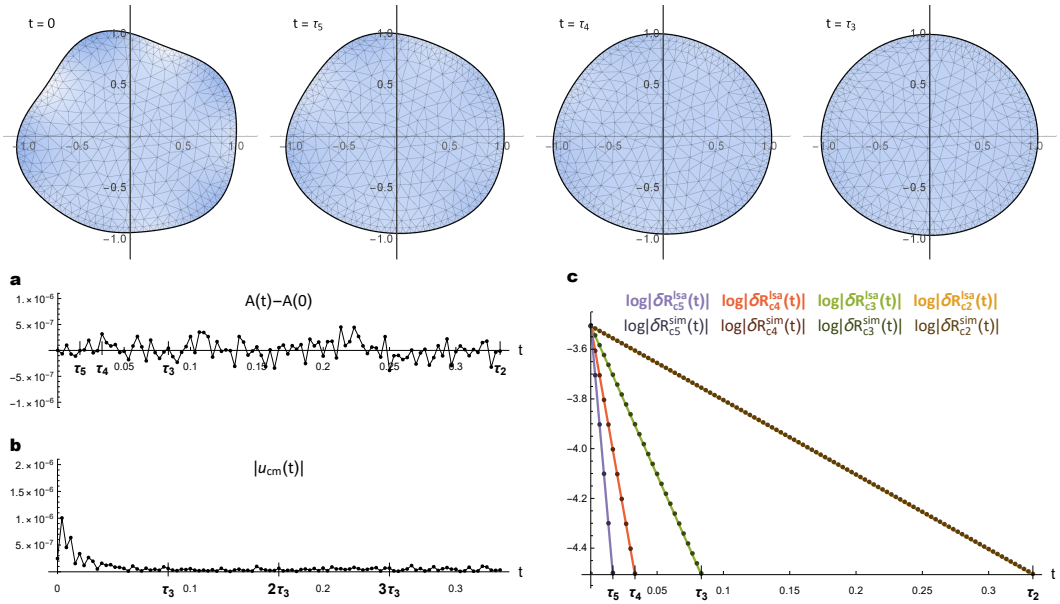

Fig. III.4 ***Decaying shape perturbations (mixed modes*** $m = 2$–5***):*** *We set* $\delta R_{c2} = .03$, $\delta R^0_{s3} = -.03$, $\delta R_{s4} = .03$, *and* $\delta R_{c5} = -.03$ *in Eq.* (III.25), *fixed* $\sigma = 0.5$, *and chose* $\Delta t = 0.005\tau_5$, *where* $\tau_5 = |s_5|^{-1} = 1/120$. *At the top we present simulation snapshots demonstrating the sequential decay of the perturbed shape modes. The density plot in the bulk represents the pressure* p *(from low in white to high in blue). a) Time series for the droplet area* $A(t)$. *b) Time series for the absolute center of mass velocity* $|\mathbf{u}_{cm}(t)|$. *c) The predicted linear behaviour of each perturbed mode,* $\log|\delta R^{lsa}_{c,sm}(t)| = \log|R^0_{c,sm}| - s_m t$ *(continuous colored lines) vs. the simulation time series,* $\log|\delta R^{sim}_{c,sm}(t)|$ *(darker colors, computed via Eq.* (III.26)*). We find that the fitted growth rates,* ($s^N_2 \simeq -2.99$, $s^N_3 \simeq -11.91$, $s^N_4 \simeq -29.83$, $s^N_5 \simeq -59.50$) *are all in good quantitative agreement with the classical linear-stability growth rates* ($s_2 = -3$, $s_3 = -12$, $s_4 = -30$, $s_5 = -60$).

III.2.2 Coupled droplet-solute system

To simulate the coupled model, one must specify all four dimensionless parameters (σ, a, χ, c_s), the time step Δt, the initial finite element domain, and the initial solute concentration c^0. Like in the pure droplet simulation, the finite-element domain is generated via an explicit counter-clockwise parameterization of the closed interface.

In each time step, we implement the algorithm outlined in Section III.1.4. The simulation data is saved at some fixed interval of time iterations and then analysed using our post-processing tool in Mathematica (TM). For each imported time frame, we reconstruct the finite-element domain and the interpolation functions for $\mathbf{u}$, p and c. For linear perturbation experiments, we use the interfacial vertices to build the interpolation function $R^{\text{sim}}(\theta)$ (as in the passive droplet case).

Our aim is to square the simulation results with our theoretical predictions outlined in Chapter II, namely:

- Conservation of the droplet area ($\dot{A} = 0$) and the total solute ($\dot{C}_{\text{tot}} = 0$).
- External force balance, $\mathbf{u}_{\text{cm}} = A^{-1} \int_{\partial\Omega} F_{\text{act}}(c)\mathbf{n}\, \mathrm{d}l$.
- Linear growth dynamics of coupled shape-concentration perturbations.
- Stationary of our reverse-engineered steadily-moving solutions.

Remark III.2.3. *The computations of $\mathbf{u}_{cm}$ and the shape Fourier components (δR^{sim}_{cm}, δR^{sim}_{sm}) are done as outlined in the previous subsection.*

Linear eigenmode perturbations

We begin by examining the temporal evolution of small coupled perturbations about the circular homogeneous rest-state. The idea is to test for a quantitative correspondence between the coupled FEM dynamics and our linear stability analysis performed in Section II.4.

To start with, we select parameters in some regime of interest and compute eigenvalues with their associated eigenmodes. Let us recall that for a given s (a root of $G_m(s)$, Eq. (II.42)), the calculation of $v_{ms}(r,\theta)$, Eq. (II.43), consists of finding a straightforward solution (α_{ms}, β_{ms}) to the linear Eqs. (II.40) – (II.41). In the simulation, we set the same parameter values and use α_{ms}, β_{ms} to define the initial state. We introduce initial perturbations such that $R^0(\theta) = 1 + \delta R^0(\theta)$ and $c^0(r,\theta) = 1 + \delta c^0(r,\theta)$, where $\delta R^0(\theta)$, $\delta c^0(r,\theta)$ are written in the basis of the coupled eigenmodes.

Let $\delta R^0_{cm}, \delta R^0_{sm} \in \mathbb{C}$ be arbitrary scaling factors for the initial amplitudes and phases of the shape components in the perturbed eigenmodes. It follows that

$$\delta R^0(\theta) = \sum_m \left(\Re\left[\delta R^0_{\text{cm}}\right] \cos(m\theta) + \Re\left[\delta R^0_{\text{sm}}\right] \sin(m\theta) \right) \tag{III.27}$$

$$\delta c^0(r,\theta) = \sum_m \left(\Re\left[\delta c^0_{\text{cm}}(r)\right] \cos(m\theta) + \Re\left[\delta c^0_{\text{sm}}(r)\right] \sin(m\theta) \right) \tag{III.28}$$

where $\delta c^0_{cm}(r) := \frac{\beta_{ms}\delta R^0_{cm}}{\alpha_{ms}} J_m(-i\sqrt{s}r)$, $\delta c^0_{sm}(r) := \frac{\beta_{ms}\delta R^0_{sm}}{\alpha_{ms}} J_m(-i\sqrt{s}r)$.

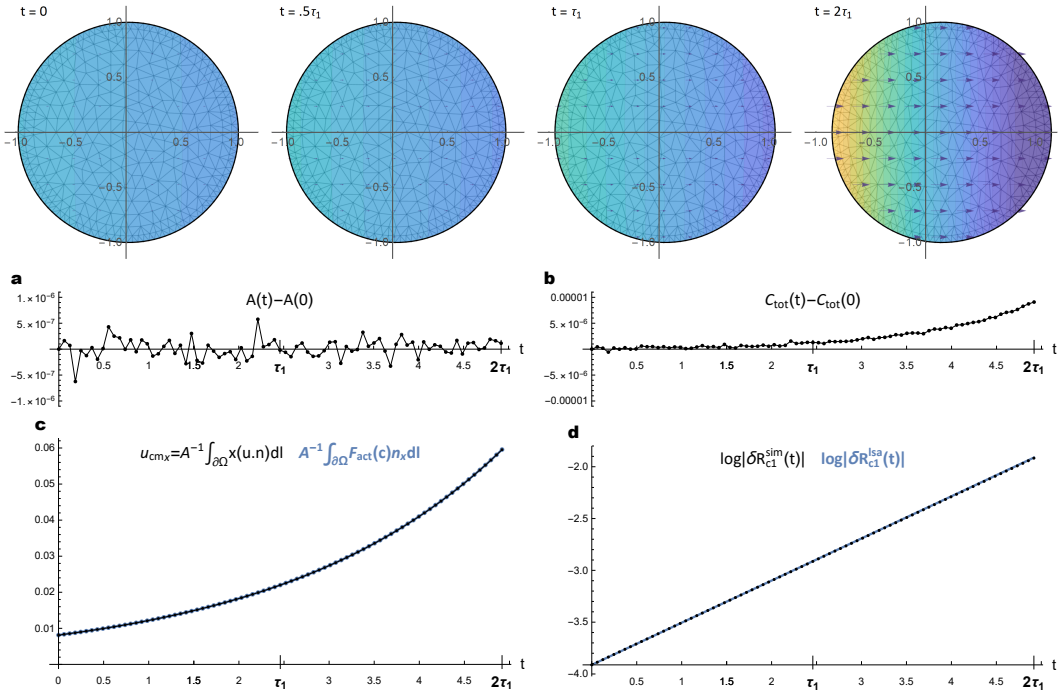

Fig. III.5 ***Symmetry breaking and motility (mode*** $m = 1$***):*** *We fixed* $\sigma = 1$, $a = 1$, $\chi = 1.1$, *set* $\delta R_{c1} = 0.02$ *in Eqs.* (III.27) – (III.28), *and chose* $\Delta t = 0.001\tau_1$, *where* $\tau_1 = 1/s_1 \simeq 2.4587$. *At the top we present simulation snapshots capturing the exponential growth of the polarization-translation mode. The density plot in the bulk represents the solute concentration field* c *(from low in blue to high in yellow) and the vector field represents the fluid flow* $\mathbf{u}$. *a) Time series for the domain area* $A(t)$. *b) Time series for the total solute* $C_{tot}(t)$. *c) Test of the external force-balance, Eq.* (II.14) *(showing the* x*-component). This graph demonstrates that the simulation upholds the expectation for the center of mass velocity (black) as a function of the net active force (blue). d) The predicted linear behaviour of the perturbed mode,* $\log|\delta R^{lsa}_{c1}(t)| = \log|\delta R^{0}_{c1}| + s_1 t$ *(blue line) vs. the simulation time series,* $\log|\delta R^{sim}_{c1}(t)|$ *(black, computed via Eq.* (III.26)*). We find that the fitted growth rate,* $s_1^N \simeq 0.4058$, *compares well with the predicted linear-stability growth rate,* $s_1 \simeq 0.4067$ *(giving a deviation of* $(s_1^N - s_1)/s_1 \simeq -2 \times 10^{-3}$*).*

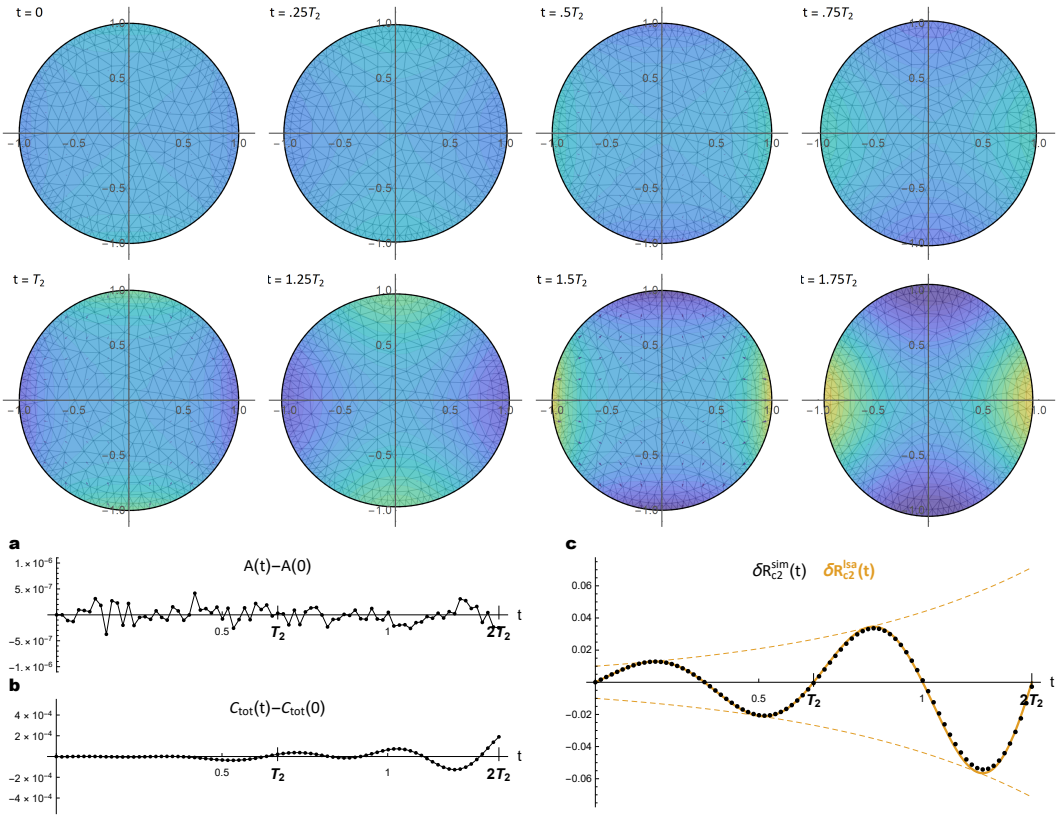

Fig. III.6 ***Growing shape-concentration standing wave (mode*** $m = 2$***):*** *We fixed* $\sigma = 1$, $a = 1$, $\chi = 1.8$, *set* $\delta R^0_{c2} = i\,0.02$ *in Eqs.* (III.27) – (III.28), *and chose* $\Delta t = 0.0005T_2$, *where* $T_2 = 2\pi/|\Im[s_2]| \simeq .6678$. *At the top we present simulation snapshots capturing the exponential growth of the coupled standing wave. The density plot in the bulk represents the solute concentration field* c *(from low in blue to high in yellow) and the vector field represents the fluid flow* $\mathbf{u}$. *a) Time series for the domain area* $A(t)$. *b) Time series for the total solute* $C_{tot}(t)$. *c) The predicted linear behaviour of the perturbed Fourier mode,* $\delta R^{lsa}_{c2}(t) = \Re\left[\delta R^0_{c2} e^{s_2 t}\right]$ *(orange line) vs. the simulation time series,* $\delta R^{sim}_{c2}(t)$ *(black, computed via Eq.* (III.26)*). We find that the fitted growth rate,* $s_2^N \simeq 0.4058$, *compares well with the predicted linear-stability growth rate,* $s_s \simeq 0.4067$ *(giving normalized deviation of* $(s_1^N - s_1)/s_1 \simeq -2 \times 10^{-3}$*).*

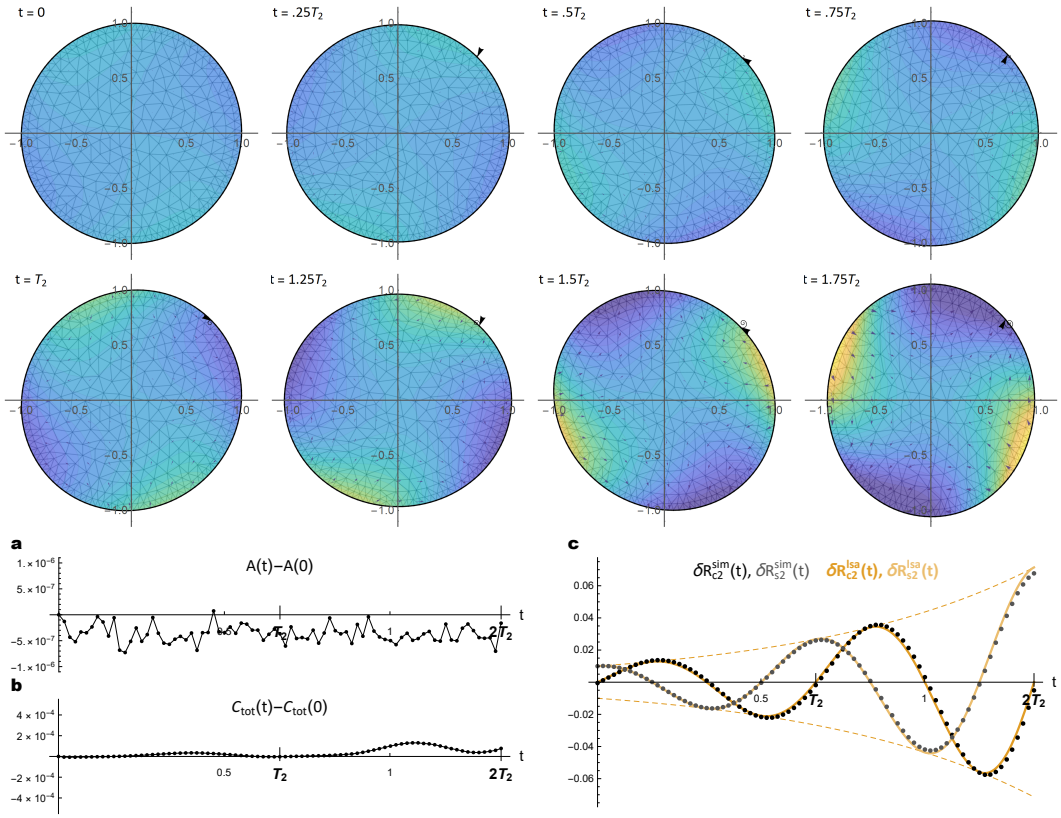

Fig. III.7 ***Growing shape-concentration traveling wave (mode*** $m = 2$***):*** *We fixed* $\sigma = 1$, $a = 1$, $\chi = 1.8$, *set* $\delta R^0_{c2} = i\,0.01$ *&* $\delta R^0_{s2} = 0.01$ *in Eqs.* (III.27) – (III.28), *and chose* $\Delta t = 0.0005 T_2$, *where* $T_2 = 2\pi/|\Im[s_2]| \simeq .6678$. *At the top we present simulation snapshots capturing the exponential growth of the coupled traveling wave. The density plot in the bulk represents the solute concentration field* c *(from low in blue to high in yellow) and the vector field represents the fluid flow* $\mathbf{u}$. *a) Time series for the domain area* $A(t)$. *b) Time series for the total solute* $C_{tot}(t)$. *c) The predicted linear behaviour of the perturbed Fourier modes,* $\delta R^{lsa}_{c2}(t) = \Re\left[\delta R^0_{c2} e^{s_2 t}\right]$ *&* $\delta R^{lsa}_{s2}(t) = \Re\left[\delta R^0_{s2} e^{s_2 t}\right]$ *(orange & light orange lines) vs. the simulation time series,* $\delta R^{sim}_{c2}(t)$ *&* $\delta R^{sim}_{s2}(t)$ *(black & gray, computed via Eq.* (III.26)*). We find that the fitted growth rates,* $s_2^N \simeq 0.4058$ *(for* $\delta R_{c2}(t)$*) &* $s_2^N \simeq 0.4058$ *(for* $\delta R_{s2}(t)$*), compare well with the predicted linear-stability growth rate,* $s_s \simeq 0.4067$ *(giving normalized deviations of* $(s_1^N - s_1)/s_1 \simeq -2 \times 10^{-3}$*).*

Remark III.2.4. *In our post-processing tool, the numerical growth rates of the coupled eigenmodes are obtained by fitting the time series of each shape Fourier component to the function* $\Re[\varepsilon e^{s_m^N t}]$ *(where* $\varepsilon, s_m^N \in \mathbb{C}$*). Being that the solute and shape components in the eigenmode share same growth rate* s*, there is no real need to decompose the Fourier-Bessel expansion of the numerical solute concentration.*

Results of three droplet-solute simulations are represented in Figs. III.5 – III.7. In Figs. III.5 and III.6 we introduced an initial shape-concentration perturbation strictly in one Fourier mode (cosine $m = 1$ and cosine $m = 2$, respectively), whereas in Fig. III.7 we introduced a superposition of two perturbations (cosine $m = 2$ and sine $m = 2$ with a temporal phase shift of a quarter oscillation period, i.e., $\delta R_{c2}^0 = i\,\delta R_{s2}^0$). For the time step and mesh density chosen, we find that the deviations in the droplet area and the total solute are small ($\sim 10^{-7}$ in A and $\sim 10^{-4}$ in C_{tot}). The fitted growth rates are also in good agreement with our linear stability predictions for both the real and imaginary parts of s_m (see details in figure captions).

Steadily-moving solutions

To test the performance of the FEM simulation at the nonlinear level, we insert our predicted steadily-moving solutions as initial states.

We recall that the reverse-engineered steady-state is defined by three numbers (u_1,p_1,c_1) and the curve $y^*(x)$ (a numerical ODE solution to Eq. (II.68) that defines the shape). We begin by selecting a solution of interest from the branches shown in Figs. II.5 – II.6. In the simulation, we set the matching parameter values and use u_1, c_1, and $y^*(x)$ to define the initial state.

The formula for the initial solute profile is granted:

$$c^0(x) = c_1 e^{-a u_1 x}.$$

The tricky part is to build the initial finite element domain over which c^0 (and also $\mathbf{u}^1$, p^1) will be defined. There are three practical problems with inputting $y^*(x)$ directly in the simulation: (i) this solution is resolved in Mathematica (TM) as a piece-wise interpolation function with no explicit formula given, (ii) approximating $y^*(x)$ as a Taylor or Fourier series for example is problematic because $y^{*\prime}(x)$ diverges at the two limit points (x_{L} & x_{R}, see Section II.5), and (iii) $y^*(x)$ is far from being an arc length parameterization of $\partial\Omega$, which is desired for a proper definition of Γ_h^0.

To address these issues, we look for an explicit counter-clockwise arc-length parameterization, $\gamma(l) = \{X(l), Y(l)\}$, of the boundary defined by $\pm y^*(x)$. Formally, $\gamma : (-L/2, L/2) \to \mathbb{R}^2$ and $|\gamma'(l)| = 1$, where $L := 2\int_{x_{\text{L}}}^{x_{\text{R}}} \sqrt{1 + (y^{*\prime}(x))^2}\,dx$ is the steady-state perimeter. The upper half of $\partial\Omega$ is parameterized as follows. For $l \in (0, L/2)$: $\gamma(l) = \{X(l), +y^*(X(l))\}$ such that $\gamma(0) = \{x_{\text{R}}, 0\}$ and $\gamma(L/2) = \{x_{\text{L}}, 0\}$. Using these boundary conditions and the criterion $|\gamma'(l)| = 1$ we obtain an ODE problem for $X(l)$:

$$X'(l) = -1/\sqrt{1 + y^{*\prime}(X(l))^2}\,; \quad X(0) = x_{\text{R}} \tag{III.29}$$

This problem is solved numerically in Mathematica (TM) over $l \in (0, L/2)$. To describe the reflected bottom half of $\partial\Omega$ continuously as a function of l, we now expand the

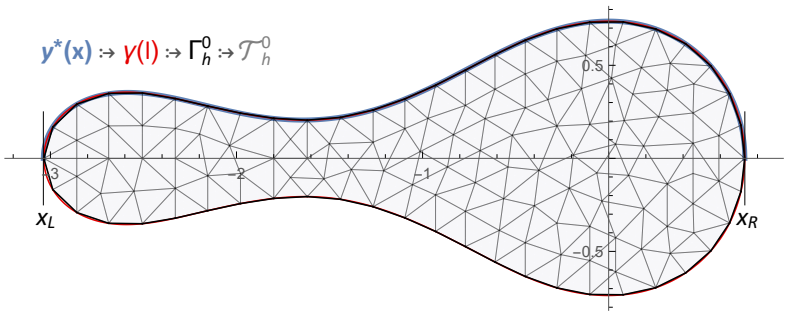

Fig. III.8 ***Building a finite element domain to match the steady-state shape.*** *In Mathematica (TM), the computational ODE solution $y^*(x)$ (blue) is used to define the arc-length parameterization $\gamma(l)$. The Fourier expansion of $\gamma(l)$ (red, Eq. (III.30)) is then used to define the affine approximation of the initial interface, Γ_h^0 (black). In turn, FreeFem++ uses Γ_h^0 to generate the internal triangulation mesh, $\mathcal{T}_h^0$ (gray).*

paramatrization such that for $l \in (-L/2, 0)$: $\gamma(l) = \{X(-l), -y^*((X(-l))\}$, where $X(l)$ is the solution to Eq. (III.29).

Unlike $y^*(x)$, the closed parameterization $\gamma(l)$ does not suffer from the problem (ii). It also defines $X(l)$ and $Y(l)$ as periodic functions which are even and odd, respectively. Hence, to bypass problem (i), it is natural to expand them in following Fourier series

$$\gamma(l) \simeq \left\{\frac{1}{2}X_0,\, 0\right\} + \sum_{k=1}^{k_{\max}} \left\{X_k \cos\frac{2\pi k l}{L},\, Y_k \sin\frac{2\pi k l}{L}\right\} \tag{III.30}$$

where

$$X_k = \frac{4}{L}\int_0^{L/2} X(l)\cos\frac{2\pi k l}{L}dl, \quad Y_k = \frac{4}{L}\int_0^{L/2} y^*(X(l))\sin\frac{2\pi k l}{L}dl$$

We choose some high $k_{\max}$ and take Eq. (III.30) as the explicit counter-clockwise definition the of initial interface (which then determines the internal triangulation mesh in FreeFem++). The procedure above of building $\mathcal{T}_h$ from $y^*(x)$—going through $\gamma(l)$ and Γ_h^0—is visualized in Fig. III.8.

In Fig. III.9, it is demonstrated up to small numerical deviations that the simulation sustains both the speed and shape of the initial condition (i.e., the predicted steadily-moving solution), while conserving the area A and the total solute C_{tot}. To this end, we did not fully investigate the source of error in the steady-state speed. However, it is sensible to consider that such an error is associated mostly with the spatial discretization of the domain, which produces deviations in both A and C_{tot}.

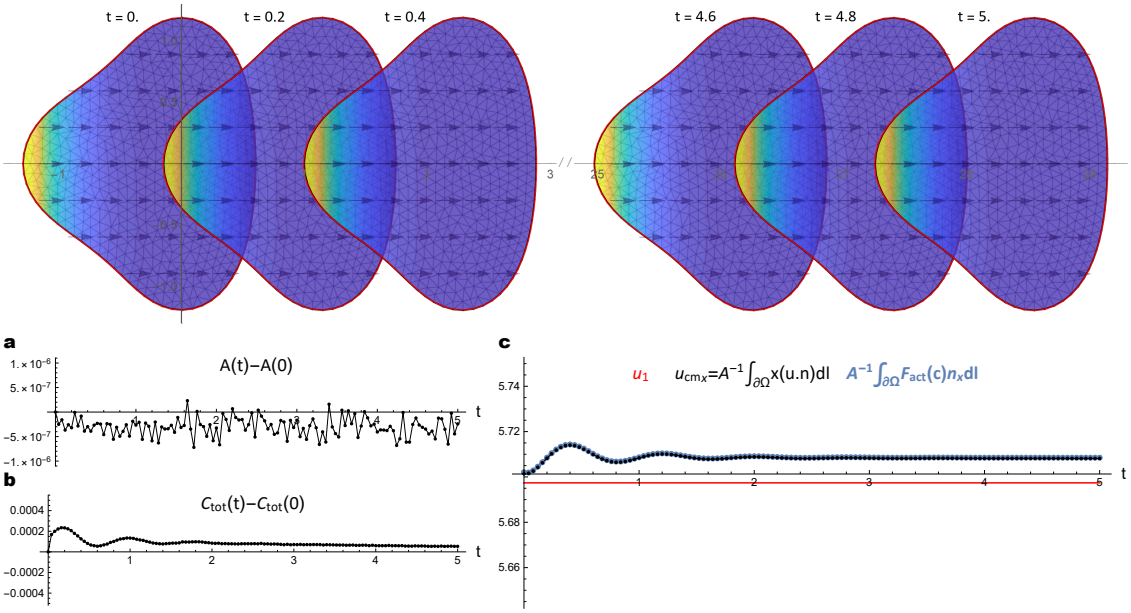

Fig. III.9 ***Stationarity of the steadily-moving state***: *We fixed* $\sigma = 1$, $a = 1$, $\chi = 0.75$, $c_s = 0.1$, *set* $c^0 = c_1 e^{-a u_1 x}$, *built the finite element domain to match the stable steadily-moving solution via* $\gamma(l)$ *(Eq.*(III.30)*), and chose* $\Delta t = 0.002$. *At the top we present simulation snapshots demonstrating the stationarity of the predicted solution. The density plot in the bulk represents the solute concentration field* c *(from low in blue to high in yellow), the vector plot represents the flow field* $\mathbf{u}$, *and the red outline represents the predicted steady-state shape. a) Time series for the domain area* $A(t)$. *b) Time series for the total solute* $C_{tot}(t)$. *c) The center of mass velocity* $\mathbf{u}_{cm}$ *(black), which also equals* $A^{-1} \oint_{\partial\Omega(t)} F_{act}(c)\mathbf{n}\,\mathrm{d}l$ *(blue), relaxes on the predicted* $u_1\hat{x}$ *(red).*

III.3 Limit behaviours of an isolated cell

In this section, we run a series of numerical experiments with the aim of exploring the nonlinear phase-space attractors of our droplet-solute model.

III.3.1 Selection of the steadily-moving state

By introducing a small symmetry-breaking perturbation of the unstable rest-state we find that the system robustly stabilizes on the predicted steadily-moving solution (if a stable solution exists, see blue branches in Figs. II.5 – II.6). This limit behaviour is demonstrated in Fig. III.10.

In fact, we observe that even when we do not include a transnational symmetry-breaking component in the initial state, the system still tends to find the stable traveling solution at the long time limit. This behaviour is demonstrated in Fig. III.11, where we introduced an initial perturbation of the unstable rest-state aimed strictly at triggering the shape-concentration wave in mode $m = 2$. Note here how the front-rear symmetry breaking occurs spontaneously (through numerical noise) at some point during the evolu-

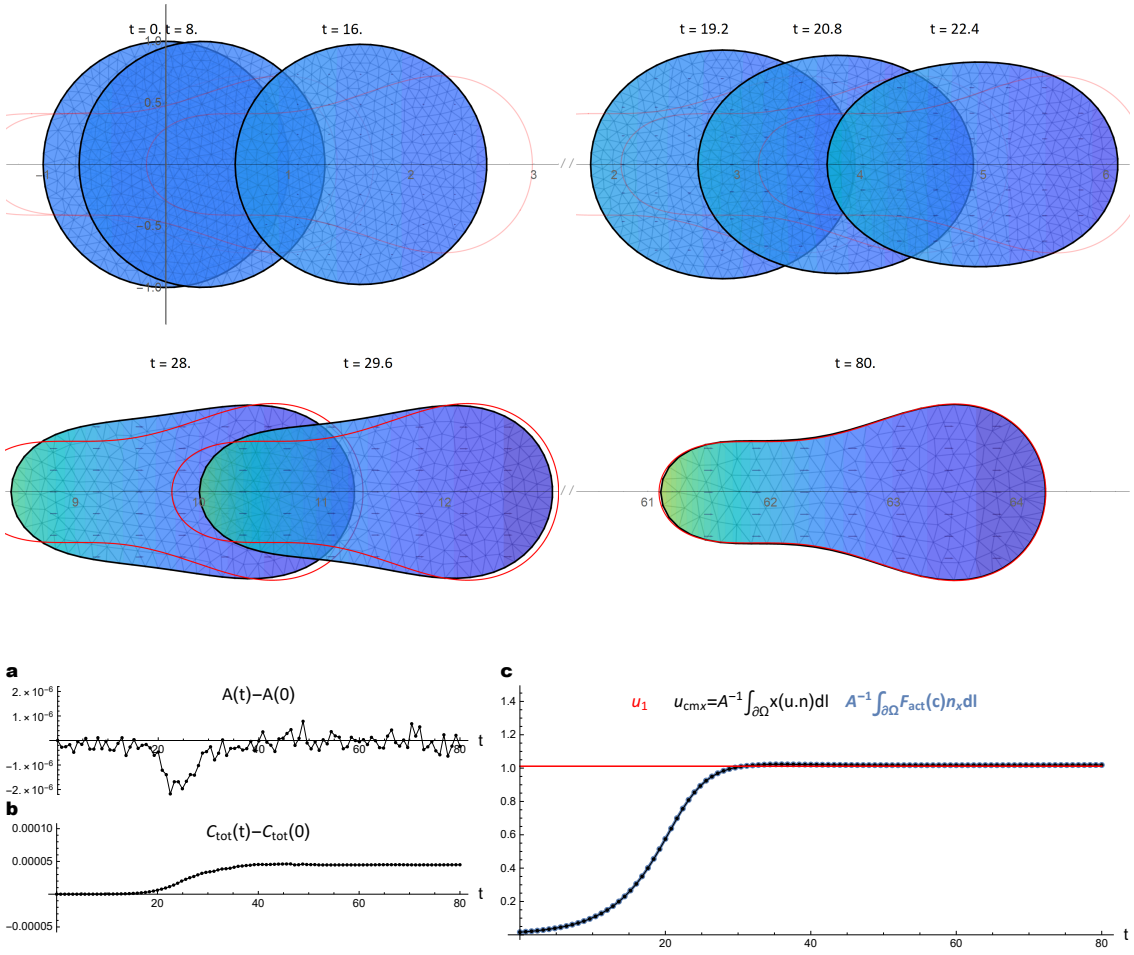

Fig. III.10 ***Attraction to the steadily-moving state**: We fixed $\sigma = .1$, $a = 1$, $\chi = 1.05$, $c_s = 0.5$, set $\delta R^0 = 0$, $\delta c^0 = -0.01x$, and chose $\Delta t = 0.02$. At the top we present simulation snapshots capturing the relaxation onto the predicted steadily-moving solution. The density plot in the bulk represents the solute concentration field c, the vector field represents the fluid flow $\mathbf{u}$, and the red outline represents the predicted steady-state shape. a) Time series for the domain area $A(t)$. b) Time series for the total solute $C_{tot}(t)$. c) The center of mass velocity $\mathbf{u}_{cm}$ (black), which always corresponds to $A^{-1}\oint_{\partial\Omega(t)} F_{act}(c)\mathbf{n}\,\mathrm{d}l$ (blue), relaxes on the predicted $u_1\hat{x}$ (red).*

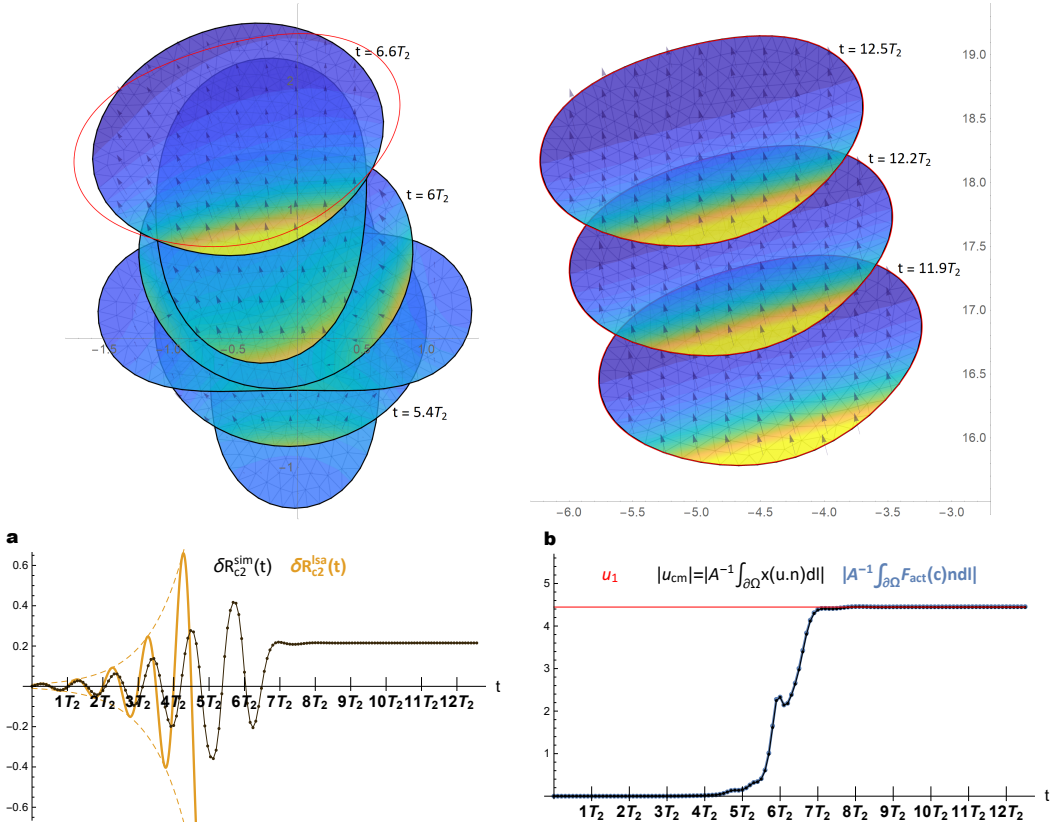

Fig. III.11 ***Spontaneous symmetry-breaking inhibits*** $m = 2$ ***standing wave and leads to the steadily-moving state***: *We fixed* $\sigma = 1$, $a = 1$, $\chi = 1.8$, $c_s = 1$, *set* $\delta R^0_{c2} = i\,0.01$ *in Eqs.* (III.27) – (III.28), *and chose* $\Delta t = 0.005T_2$, *where* $T_2 = 2\pi/|\Im[s_2]| \simeq .6678$. *At the top we present simulation snapshots capturing: (i) the system breaking the front-rear symmetry as the amplitude of the* $m = 2$ *shape-concentration wave grows, (ii) relaxation onto the predicted steadily-moving state at the long time limit. The density plot in the bulk represents the solute concentration field* c, *the vector field in the bulk represents the fluid flow* $\mathbf{u}$, *and the red outline represents the predicted steady-state shape. a) The predicted linear behaviour of the perturbed Fourier mode,* $\delta R^{lsa}_{c2}(t) = \Re\left[\delta R^0_{c2} e^{s_2 t}\right]$ *(orange line) vs. the simulation time series,* $\delta R^{sim}_{c2}(t)$ *(computed in the cell frame via Eq.* (III.26)*). b) The absolute center of mass velocity* $|\mathbf{u}_{cm}|$ *(black), which always corresponds to* $\left|A^{-1} \oint_{\partial\Omega(t)} F_{act}(c)\mathbf{n}\,\mathrm{d}l\right|$ *(blue), accelerates upon spontaneous symmetry-breaking, and relaxes on the predicted steady-state speed* u_1 *(red line) at the long time limit.*

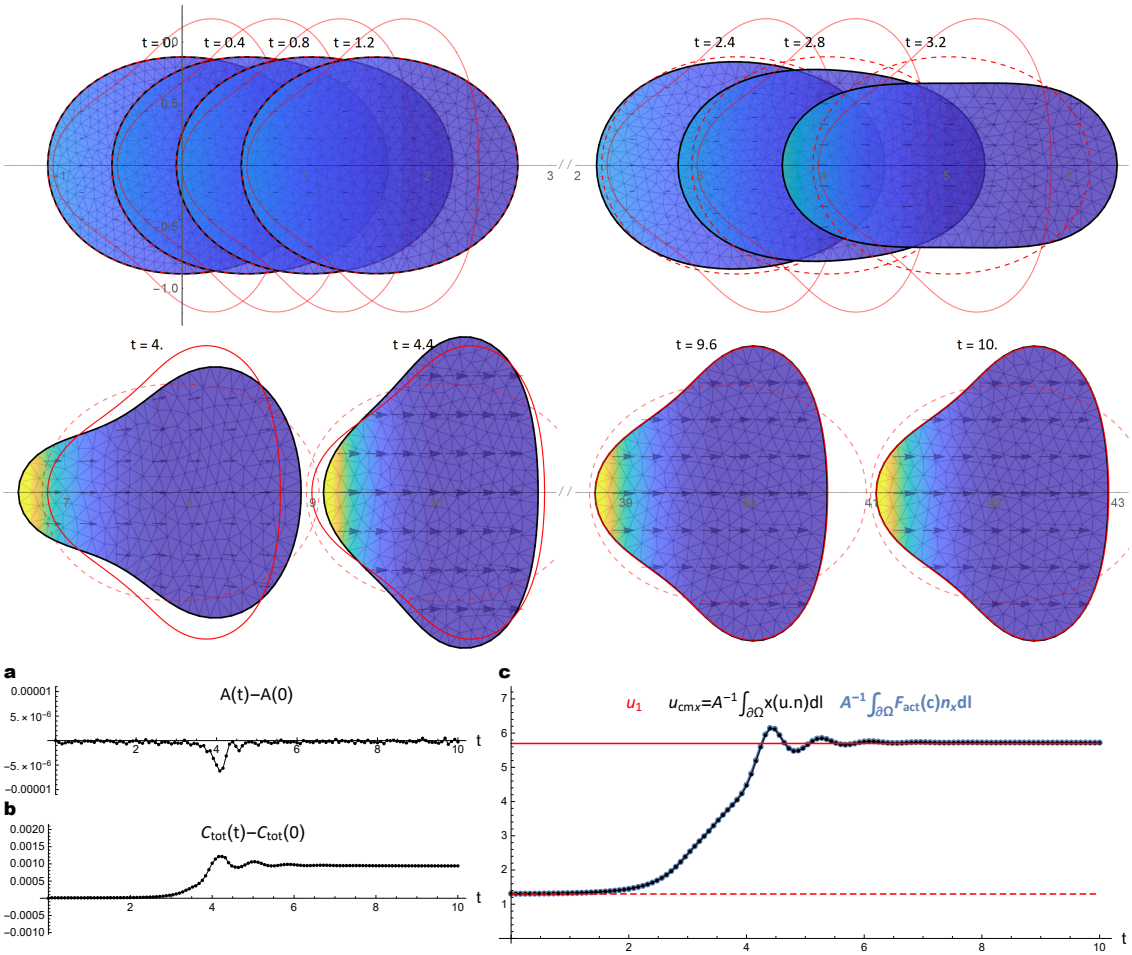

Fig. III.12 ***Evolution from the unstable to the stable steadily-moving state**: We fixed $\sigma = 1$, $a = 1$, $\chi = 0.75$, $c_s = 0.1$, set $c^0 = c_1 e^{-a u_1 x}$ (with c_1, u_1 corresponding to the unstable steady state), built the finite element domain to match the unstable steady shape via $\gamma(l)$ (Eq.(III.30)), and chose $\Delta t = 0.002$. At the top we present simulation snapshots capturing: (i) the system slowly pulling away from the unstable steady state, (ii) the phases of extension and contraction as the cell accelerates, and (iii) the final relaxation onto the predicted stable state. The density plot in the bulk represents the solute concentration field c, the blue vector field represents the fluid flow $\mathbf{u}$, and the red (dashed red) outline represents the predicted stable (unstable) steady-state shape. a) Time series for the domain area $A(t)$. b) Time series for the total solute $C_{tot}(t)$. c) The center of mass velocity $\mathbf{u}_{cm}$ (black), which always corresponds to $A^{-1} \oint_{\partial\Omega(t)} F_{act}(c)\mathbf{n}\, \mathrm{d}l$ (blue), pulls away from the initial unstable $u_1\hat{x}$ (dashed red line) and eventually relaxes on the predicted stable $u_1\hat{x}$ (red line).*

tion of the standing wave. Moreover, it is clear that as $m = 1$ "takes over" at the nonlinear level, the (linearly unstable) $m = 2$ oscillations are strongly damped. This behaviour can be seen as numerical evidence for the morphological stability of the steady traveling state.

The attraction to the stable steadily-moving state is further demonstrated by small perturbation of the unstable steadily-moving state, which exists in the bi-stable parametric regime, see Fig. III.12 (and Fig. II.5). Note how the cell in Fig. III.12 slowly pulls away from the (low-speed) unstable state before approaching the (high-speed) stable state. As the cell accelerates, it also morphs in a non-trivial fashion. Initially, the deformation tendency extends the cell elongation in direction of motion. At some point, the cell begins to contract towards the stable mushroom-like shape. In the final approach, we observe a damped oscillatory relaxation of the shape, the solute concentration and the speed. Note that this 'inertial-like' overshooting behaviour is associated with the mechanism of active-capillary (shape-concentration) waves that our model also captures at the linear perturbation level, see Section II.4.

Remark III.3.1. *For moderate values of c_s, χ, and σ, we find that the stabilization onto the stable steadily-moving solution is very robust, i.e., it is generally irrespective of the initial condition. However, by playing around with low and high values of c_s, high values of χ, and low surface tension σ, we tend to observe very strong and rapid deformation patterns that ultimately lead to simulation crashes (in the form of triangle element intersections or by failure of our Newtion method to converge). Frequent remeshing allows to go further into larger deformation limits, but generally it is not a 'fix-all' remedy. Indeed, in many scenarios one must work with denser meshes and much smaller values of Δt, which becomes computationally costly. Being that we have not yet fully explored the shape-concentration dynamics systematically for all parametric regimes where a stable steadily-moving solution exists, we cannot exclude at this point the co-existence of other stable attractors. Another possibility is the occurrence of a finite-time topological singularity, which would prevent our system from ever reaching the steady state.*

III.3.2 Approaching a topological singularity

We found that our system advances towards a pinching point under different regimes and conditions. Here, we discuss one example of particular interest motivated by our results in Section II.5.

We focus on the low-tension (and low c_s / high χ) regime, where the rest-state is unstable and we find no reverse-engineered steady states (see Fig. II.6). In the simulation shown in Fig. III.13, we set a force amplitude beyond the inverted saddle-node bifurcation that annihilates the stable solution branch. We introduced a small symmetry-breaking perturbation of the rest-state and observed that the system approached a topological singularity at finite time. That is, the narrowing rate of the cell neck (of width Δy_{neck}) does not appear to slow down in any significant way in the vicinity of the pinching point. Close to the singularity, our FEM simulation predictably crashes as the triangle lines tend to intersect.

Remark III.3.2. *The 2D model does not capture the true physical dynamics in the vicinity of the pinch-off. Indeed, when the width the of neck is at the order of the gap h between the surfaces, the problem becomes 3-dimensional. Moreover, in order to asses*

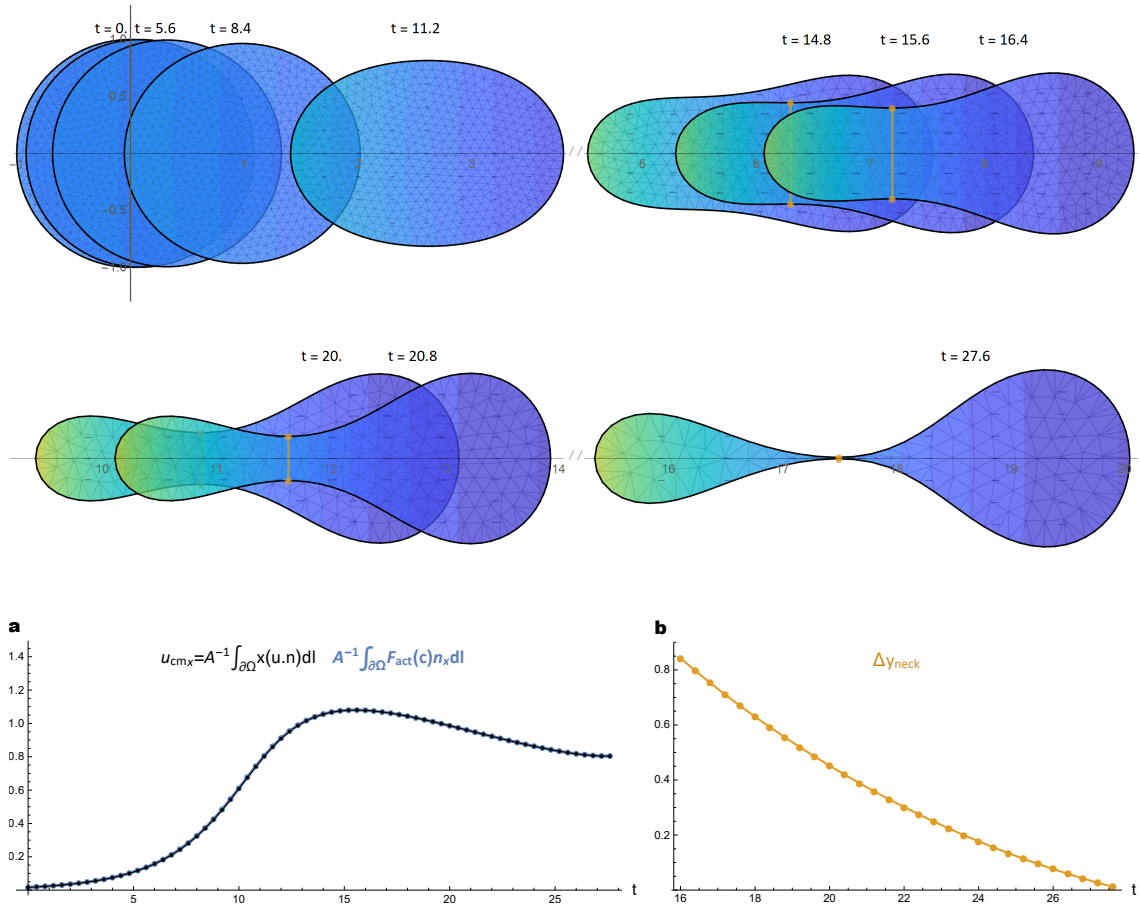

Fig. III.13 ***Finite time topological singularity (beyond the inverted saddle-node bifurcation)***: *We fixed* $\sigma = 0.1$, $a = 1$, $\chi = 1.1$, $c_s = 0.5$, *perturbed the circular homogeneous rest-state via* $\delta c^0 = -0.015x$, *and chose* $\Delta t = 0.02$. *At the top we present simulation snapshots capturing shape-concentration dynamics as system polarizes, deforms and ultimately approaches the pinching singularity. The density plot in the bulk represents the solute concentration field* c *and the blue vector field represents the fluid flow* $\mathbf{u}$. *a) The center of mass velocity* $\mathbf{u}_{cm}$ *(black), which always corresponds to* $A^{-1}\oint_{\partial\Omega(t)} F_{act}(c)\mathbf{n}\,\mathrm{d}l$ *(blue), accelerates until the cell begins to form the neck. b) We show the narrowing of the neck width* $(\Delta y_{neck}(t))$ *until the final frame at which the FEM simulation crashes.*

if pinching actually occurs, one must account for the microscopic physics underlying the phenomenon.

Remark III.3.3. *The non-monotonic behaviour of* $\mathbf{u}_{cm}$ *in Fig. III.13 is attributable to the deformation tendency of the cell. When the neck at the center begins to form, it effectively induces the active drag effect on the cell rear which leads to deceleration, as discussed in Section II.5.*

III.3.3 Shape-concentration limit cycles

By using the Hill-type force we found it difficult to observe stable limit-cycles, meaning shape-concentration waves of constant amplitude at the long time limit. Indeed, since $F''_{\rm act}(1) = 2\chi/(1+c_{\rm s}) \neq 0$, the Hopf bifurcations are generally not supercritical, meaning that even if a stable limit-cycle exists, its amplitude is not well controlled (it will not vanish at the bifurcation point). As we became more interested in nonlinear oscillatory attractors, we opted to modify the functional form of $F_{\rm act}(c)$ to a sigmoidal one, such that $F''_{\rm act}(1) = 0$ while $F'''_{\rm act}(1) > 0$ (i.e., the third derivative at $c = 1$ has the opposite sign to the first derivative, $F'_{\rm act}(1) = -\chi$). In this subsection, we use the following definition of the active force:

$$F_{\rm act}(c) = -\chi\delta c_{\rm s} \arctan\left(\frac{c-1}{\delta c_{\rm s}}\right) \tag{III.31}$$

where $\delta c_{\rm s}$ is a saturation parameter. The linear response of this force to deviations about the uniform solute concentration is still $F'(1) = -\chi$. At a qualitative level, Eq. (III.31) differs from the Hill-type force in that it reaches two plateaus: a first one for $c < 1 - \delta c_{\rm s}$ (where $F_{\rm act}(c) \simeq +\chi\delta c_{\rm s}\pi/2$), and a second one for $c > 1+\delta c_{\rm s}$ (where $F_{\rm act}(c) \simeq -\chi\delta c_{\rm s}\pi/2$). Recall that any uniform term added to $F_{\rm act}$ would merely offset the fluid pressure p by a constant.

To further facilitate the observation of limit-cycles, we also chose to artificially block the polarization-translation mode, which tends to dominate the limit behaviour (as highlighted previously). This is done in practice by introducing a uniform bulk force that directly cancels out the 1st moment, $\oint_{\partial\Omega} F_{\rm act}(c)\mathbf{n}\,{\rm d}l$. In each time step, after we solve for $(\mathbf{u}^{i+1},\, p^{i+1})$ and before solving for c^{i+1}, we compute $\mathbf{u}_{\rm cm} = A^{-1}\oint_{\partial\Omega} F_{\rm act}(c)\mathbf{n}\,{\rm d}l$ and redefine the bulk flow as $\mathbf{u}^{i+1} = \mathbf{u}^{i+1} - \mathbf{u}_{\rm cm}$. This operation essentially impedes the polarization-translation feedback loop ($m = 1$) with no additional effects on the multipolar modes, $m \geq 2$ (for which, in principle, $\oint_{\partial\Omega} F_{\rm act}(c)\mathbf{n}\,{\rm d}l = 0$).

With the steady-state attractor inaccessible, we find at the long time limit that the system relaxes spontaneously on a traveling wave limit-cycle in mode $m = 2$. This very robust behaviour is demonstrated in Fig. III.14. In this numerical experiment, we set parameter values in a regime where mode $m = 3$ is the most unstable at the linear level (i.e., $\Re[s_3] > \Re[s_2] > 0$) and we introduced a small perturbation of the rest-state triggering a superposition of standing waves in both $m = 2$ and $m = 3$. Although the $m = 3$ wave grows the fastest initially (as expected), it is clear that this mode saturates quickly at a low amplitude, while the slower mode ($m = 2$) reaches a higher amplitude. This has to do with the fact that the restoring capillary force, which balances $F_{\rm act}(c)$, is an increasing function of m. It is clear that the growing $m = 2$ oscillations lead to the strong damping of the $m = 3$ oscillations at the nonlinear level, similarly to the way in which the $m = 1$ mode (if enabled) tends to "take over" and dampen all the multi-polar modes. As the

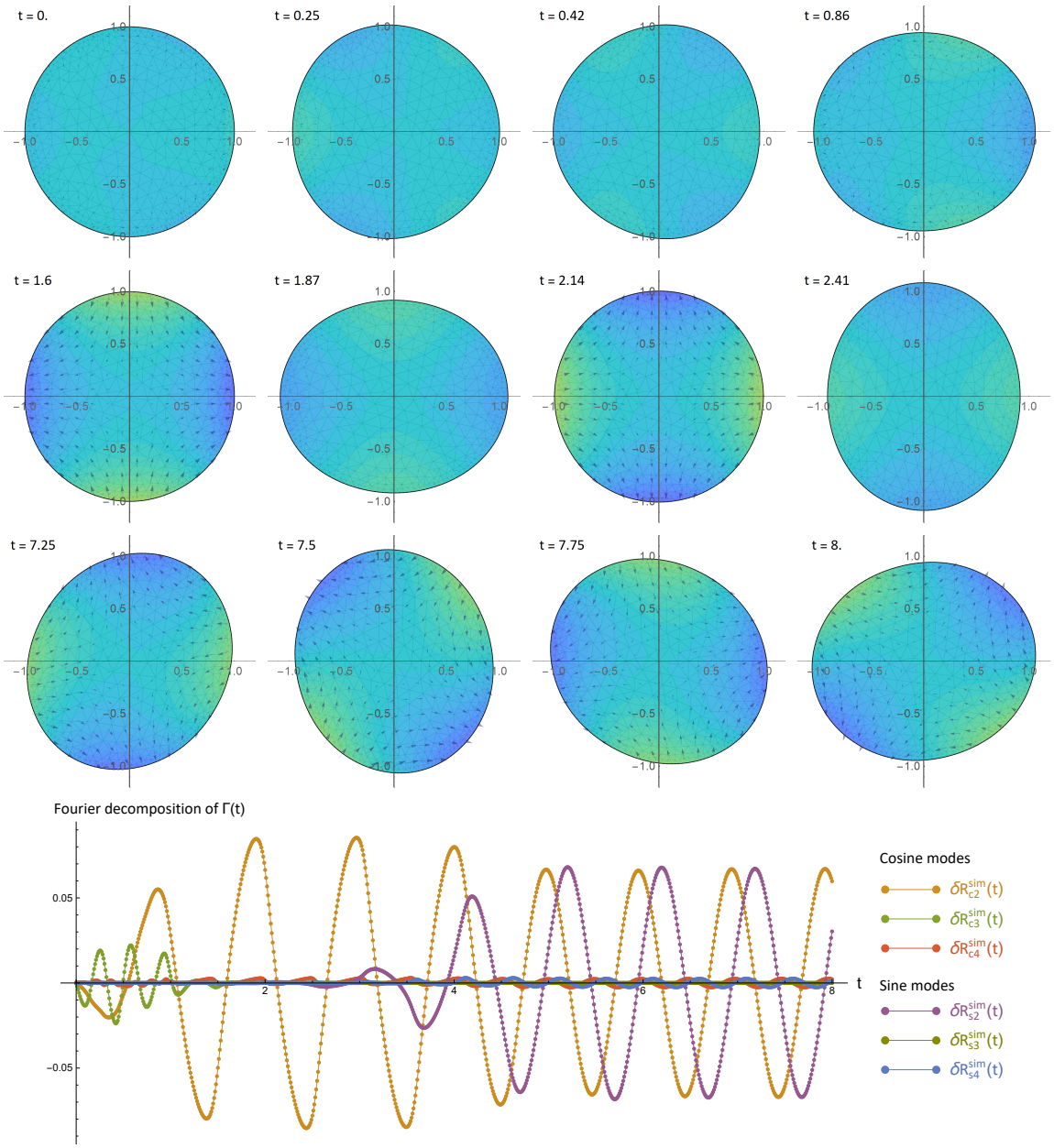

Fig. III.14 ***Shape-concentration waves at the long time limit (sigmoidal force with mode*** $m = 1$ ***blocked)****: We fixed* $\sigma = .5$, $a = 1$, $\chi = 2$, $\delta c_s = 0.1$, *set* $\delta R^0_{c2} = i\,0.01$ *and* $\delta R^0_{c3} = i\,0.01$ *in Eqs.* (III.27) – (III.28), *and chose* $\Delta t = 0.0002$. *At the top we present simulation snapshots capturing: (i) the initial growth and subsequent decay of the linearly most-unstable oscillatory mode* ($m = 3$), *(ii) the transient appearance of a high-amplitude standing wave in mode* $m = 2$, *and (iii) the final relaxation onto a stable traveling-wave limit-cycle (in* $m = 2$). *The density plot in the bulk represents the solute concentration field* c *and the vector field represents the fluid flow* $\mathbf{u}$. *Below, we show a decomposition of the normal Fourier components of the boundary line, computed via Eq.* (III.26).

$m = 2$ oscillations reach saturation, it appears as if the system finds a standing wave limit-cycle. However, at some point in time, the system spontaneously evolves into the $m = 2$ traveling wave. In other words, the standing wave is merely a transient attractor. The fact that the $\sin(2\theta)$ component is excited by some numerical noise after the $\cos(2\theta)$ wave has 'peaked', and since these orthogonal modes spontaneously lock amplitude and phase with each other (precisely at a quarter-period shift), suggests the existence of a strong nonlinear coupling between them. The selection of a stable traveling wave can be inferred from the Fourier decomposition at the bottom of Fig. III.14. Note that this graph also demonstrates the nonlinear coupling between $m = 2$ and an enslaved second harmonic (in $m = 4$).

III.4 Model extensions

In this section, we take advantage of our FEM tool to introduce various extensions of the isolated cell model. We choose to focus on repulsive interactions with external elements that are omnipresent in physiological situations and are known to significantly affect cell motility. We stress that the numerical experiments shown in this section serve primarily as 'proofs of concept', aimed at laying the ground work for future systematic studies. By simulating mechanical interactions of interest, we also managed to come by some nontrivial physical insights.

In the Hele-Shaw problem, we are free (in a mathematical sense) to introduce additional terms in the normal force balance (the Dirichlet condition). Such terms can represent external interaction forces on the cell boundary, e.g., forces derived from external potentials (projected on the normal to $\partial\Omega$). Formally, we introduce F_{pot} in the time-discrete Eq. (III.20),

$$p^{i+1}\mathbf{n}^i + F_{\text{act}}(c^i)\mathbf{n}^i + F^i_{\text{pot}}\mathbf{n}^i = \sigma\tilde{\mathbf{H}}^{i+1},$$

where

$$F^i_{\text{pot}} = -\nabla U \cdot \mathbf{n}^i,$$

and U is an external potential.

In our simulation, the Newton-like method is modified slightly such that Eq. (III.21) is now given by

$$\begin{aligned}\int_\Omega \mathbf{u}^{k+1}\cdot\mathbf{v}\,\mathrm{d}a - \int_\Omega p(\nabla\cdot\mathbf{v})\,\mathrm{d}a - \int_\Omega(\nabla\cdot\mathbf{u}^{k+1})q\,\mathrm{d}a + \sigma\oint_\Gamma \nabla\mathbf{v}\,\mathbf{t}\cdot T^k\,\mathrm{d}s \\ + \sigma\Delta t\oint_\Gamma \frac{(\nabla\delta\mathbf{u}^{k+1}\,\mathbf{t})\cdot(\nabla\mathbf{v}\,\mathbf{t})}{\mathrm{d}S^k}\,\mathrm{d}s - \oint_\Gamma\left(F_{\text{act}}(c^i)+F^i_{\text{pot}}\right)\mathbf{n}\cdot\mathbf{v}\,\mathrm{d}s = 0\end{aligned} \tag{III.32}$$

Remark III.4.1. *Like $F_{act}(c^i)$, the term F^i_{pot} is explicit, that is, it is calculated with respect to the current configuration Ω^i with no knowledge of the deformed configuration Ω^{i+1}. The explicit F^i_{pot} can be made sufficiently regular as to not cause numerical instabilities (associated, for example, with an explicit curvature term). That being said, performance could in principle be improved through more sophisticated implicit schemes (in the spirit of the implicit curvature treatment). Such alternatives to F^i_{pot} are left beyond the scope of the present study.*

Remark III.4.2. *Since the 2D momentum balance of the confined fluid is approximated by Darcy's law ($\mathbf{u} = -\nabla p$), which neglects in-plane viscous shear stresses, we do not have the freedom to balance external forces acting tangentially on $\partial\Omega$. Hence, in situations where such forces ought to be considered, one must reintroduce the planar deviatoric stress tensor (which would permit flow circulation). We leave this problem out of the scope of this study and allow only for normal interaction forces. In practice, this means that our simulated cell experiences frictionless interactions with the external 2D obstacles.*

III.4.1 Scattering from stationary walls and obstacles

To account for walls we chose a well-behaved power-law potential, such as

$$U = H(x - x_{\text{wall}}) \left(\frac{x - x_{\text{wall}}}{\Delta_{\text{wall}}} \right)^{\gamma}, \tag{III.33}$$

where H denotes the Heaviside step function, x_{wall} is the approximate wall coordinate, Δ_{wall} is a small width defining the prefactor of U, and γ is the potential exponent.

In Fig. III.15 we show two numerical experiments in which we introduced a small symmetry-breaking perturbation of the rest-state leading to polarization and motility of the cell towards a wall (defined via Eq.(III.33)). The snapshots in Fig. III.15a demonstrate a typical head-on collision. At first contact, the fluid at the leading edge of the cell experiences a sharp resistance from the external wall while the fluid at the cell rear continues to be pulled forward by the active boundary force (the polarization-translation feedback loop is still at play). In turn, the active pressing of the fluid against the wall flattens the cell—producing a strong counter force driven by both the tension and the wall. As a consequence, the cell stalls and the solute spreads out via diffusion, leading to a loss of internal polarity. During the capillary 'bounce' away from the wall, the solute accumulates on retracting edges. Hence, the cell establishes polarity (and motility) towards the opposite direction. In Fig. III.15b, we demonstrate cell scattering off a tilted wall. Unlike the head-on collision, this cell-wall interaction merely reorients the polarity axis of the cell (i.e, the cell does not completely 're-polarize'). Due to directional memory (persistence), the scattering angle is also narrower with respect to the symmetric angle characterizing classical elastic collisions.

In Fig. III.16, we demonstrate scattering of a highly deformable motile cell from a small circular obstacle. In this simulation, we initiated the cell with low tension at the steadily-moving state and directed it towards the obstacle with a fairly high impact parameter. Following the collision, which induces substantial fluid shearing in the (x, y) plane, the cell enters a strong deformation cascade that leads to a topological singularity (pinching point). Note how, in this case, the cell does not fall back to the motile steady-state even after fully clearing the obstacle. In fact, this means that the stable steady-state solution has a limited basin of attraction (at least in the low tension regime). In practical terms, we observe that a simple soft collision, such as the one shown in Fig. III.16, is sufficient to induce a marked change in the limit behaviour of the cell (inducing fragmentation as opposed to steady motility). Hence, in realistic physiological (as well as *in-vitro*) settings, our low-tension cell is likely to break up even when its parameters support a stable traveling state.

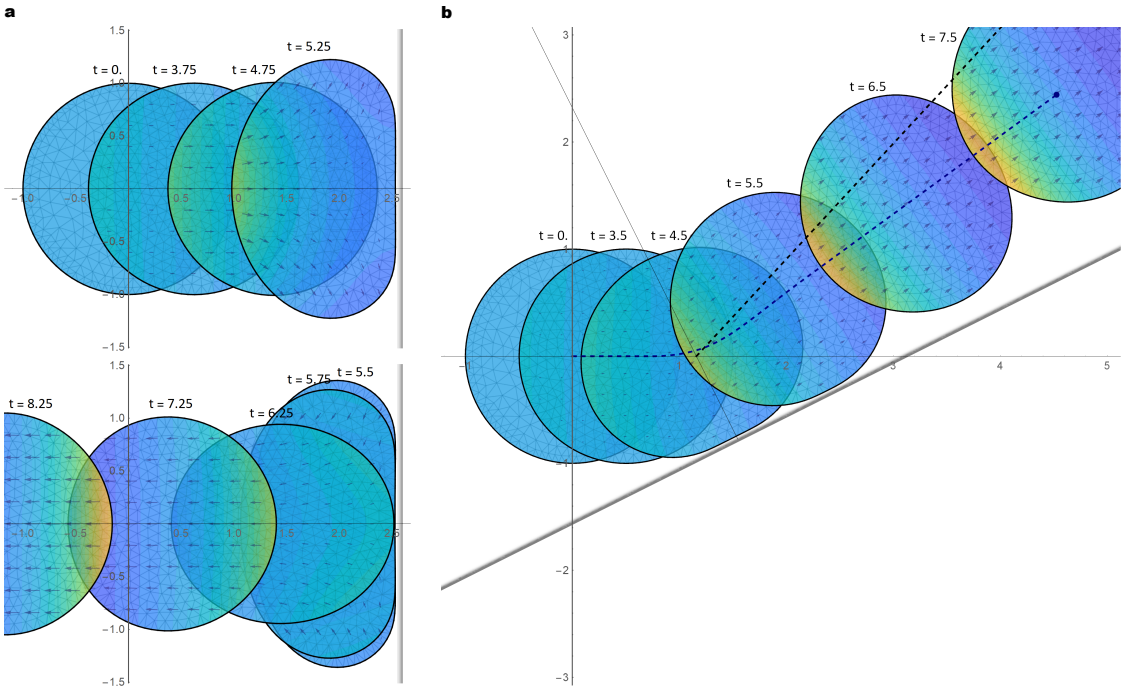

Fig. III.15 ***Cell-wall collisions**: Shown are two numerical experiments of a cell polarizing and colliding against a wall of varying slope. In both (a) and (b) we fixed $\sigma = .5$, $a = 1$, $\chi = 1.2$, $c_s = 1$, set $\delta R^0 = 0$ and $\delta c^0 = -0.02x$, and chose $\Delta t = 0.001$. The walls are defined via Eq. (III.33) with $\Delta_{wall} = 0.1$, $\gamma = 3$, $x_{wall} = 2.5$ (a) and $x_{wall} = 2y + 3$ (b). a) Simulation snapshots capturing (i) the initial cell collision with the perpendicular wall, and (ii) the consequent backwards 'bounce' leading to polarity inversion. b) Simulation snapshots capturing the scattering from from a tilted wall. The dashed blue curve marks the cell center of mass trajectory, revealing a scattering angle that differs from classical elastic collisions (dashed black line). The density plot in the bulk represents the solute concentration field c and the blue vector field represents the fluid flow $\mathbf{u}$.*

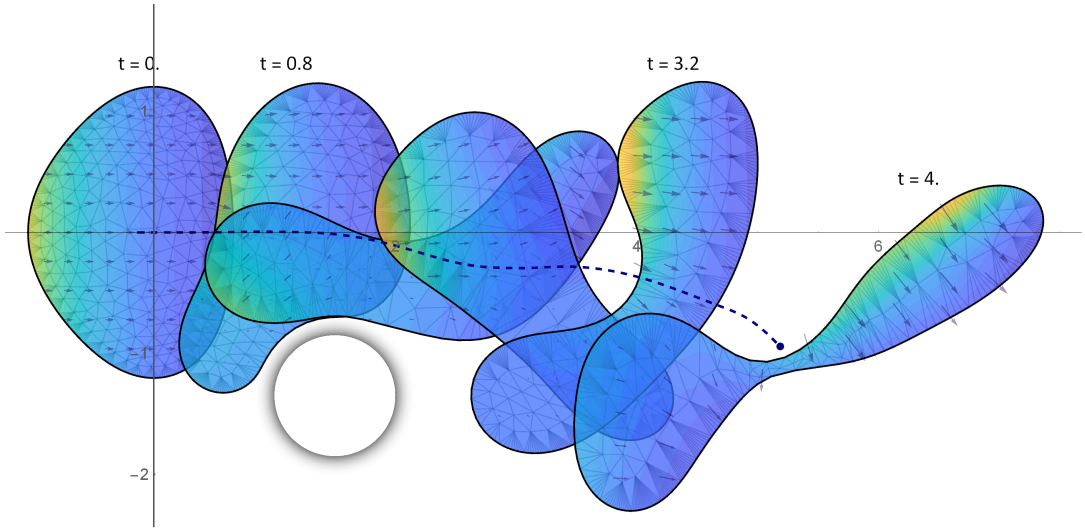

Fig. III.16 ***Scattering from a circular fragment (low tension regime)**: Shown are snapshots from a simulation in which a motile cell (at steady state) collides with a stationary fragment and proceeds towards a pinching singularity. We fixed $\sigma = .1$, $a = 1$, $\chi = 1.15$, $c_s = 1$, set $\delta c^0 = c_1 e^{-a u_1 x}$ (with c_1, u_1 corresponding to the stable steady state), built the finite element domain to match the stable steady shape via $\gamma(l)$ (Eq. (III.30)), and chose $\Delta t = 0.001$. The circular fragment is defined via a radial power-law potential, similarly to Eq. (III.33). The density plot in the bulk represents the solute concentration field c and the blue vector field represents the fluid flow $\mathbf{u}$. The dashed blue curve marks the center of mass trajectory.*

III.4.2 Migration through channels and constrictions

Here, we run numerical simulations motivated by the many recent studies of *in-vitro* cell migration through microfluidic channels and narrow constrictions (see, e.g., Heuzé et al (2011); Vargas et al (2014); Chabaud et al (2015); Lautscham et al (2015); Raab et al (2016); Sáez et al (2018)).

In Fig. III.17, we show a simulation of a motile cell (at the steadily-moving state) entering a channel, which we defined using a power-law potential (similarly to Fig. III.15). As expected, the cell experiences strong resistance upon contact with the geometric constraint. Nevertheless, owing to its persistence and deformability, the cell manages to squeeze itself through the entrance. In the external force balance (graph at the bottom of Fig. III.17), note the gap between the net active force applied (blue) and the net non-frictional force (orange) which includes $F_{\rm pot}$ (also corresponding to the cell speed (black)). When fully in the channel, the cell approaches a new (low speed) steady-state adapted to the imposed geometry. Note in addition that the exit from the channel is assisted by the opening itself (as also evident from the force balance). In fact, after the cell pulls away from the exterior potential, it overshoots the free steady-state speed (u_1) before exhibiting a damped relaxation (similarly to the cell in Fig. III.12).

In future work, it will be interesting to perform a systematic study to find the squeezed steady-state velocity in long linear channels ($u_1^{\rm chan}$) as a function of the channel width w. From what we gathered so far, it appears that this relationship is monotonic (i.e., narrower widths consistently produce slower speeds). Such a dependence could be understood intuitively from the net external force balance, $\mathbf{u}_{\rm cm} = A^{-1}\oint_{\partial\Omega}(F_{\rm act}(c)+F_{\rm pot})\mathbf{n}\,{\rm d}l$. Consider that the steady state is reached when $F_{\rm act}(c)$ at the cell rear saturates (regardless of the imposed shape). Due to symmetry, it is easy to see that the $\hat{y}$ component of the force balance vanishes in the channel. Since $c\propto e^{-au_1^{\rm chan}x}\to 0$ at the cell front (for sufficiently high speed), the negative contribution in the $\hat{x}$ direction coming from the free leading edge is negligible. Also, the $\hat{x}$ contribution from the flat top and bottom faces of the squeezed cell vanish because $n_x=0$. Hence, the speed is essentially determined by the integral $\int F_{\rm act}(c)n_x\,{\rm d}l$ evaluated strictly on the free trailing edge of the cell. Assume that $F_{\rm act}(c)\sim\beta$ $(=\chi(c_{\rm s}+1)^2/c_{\rm s})$ over this section, which may be approximated as a semicircle of radius $w/2$. With that, and with $A=\pi$, we obtain the estimate $u_1^{\rm chan}\sim w\beta/\pi$.

Another open question pertaining to microchannels is whether the imposed confinement in one additional dimension is capable of completely impeding migration in cells that are motile the "free" 2D environment (or vise versa). We propose to study this question in future work by using external walls that dynamically sandwich the cell.

In Fig III.18, we run simulations to examine the ability of our system to pass through a narrow constriction as a function of cell parameters. To ensure that the constriction imposes significant normal resistance to the advancing cell, we chose here to fix a relatively high $c_{\rm s}$ corresponding to high aspect-ratio shapes (narrow in the direction of motion). The cell in III.18a was initiated at steady state with high tension, on the one hand, and a high force amplitude, on the other hand, which allowed it to pass through. The cell in III.18b has a lower force amplitude with respect to (a) with the other parameters fixed. In this case, persistence is not strong enough to squeeze the cell past the constriction. As in Fig III.15a, this cell stalls at some point in time due to strong capillary resistance and then proceeds to polarize in the opposite direction. In Fig. III.18c we reduced

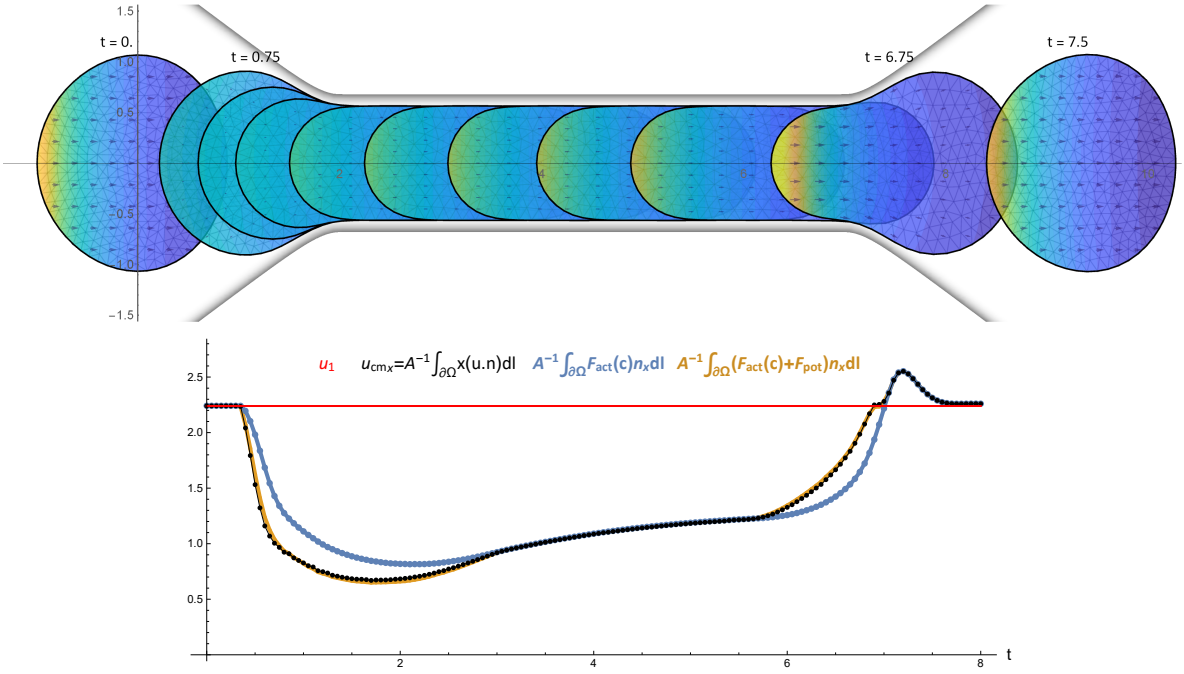

Fig. III.17 ***Migration through a linear channel***: *We fixed* $\sigma = 1$, $a = 1$, $\chi = 1.3$, $c_s = 1$, *set* $c^0 = c_1 e^{-a u_1 x}$ *(with* c_1, u_1 *corresponding to the stable steady state), built the finite element domain to match the stable steady shape via* $\gamma(l)$ *(Eq.* (III.30)*), and chose* $\Delta t = 0.001$. *The channel geometry is defined via a power-law potential (in the spirit of Eq.* (III.33)*). The simulation snapshots capture (i) the entrance to the channel, (ii) the movement in the channel, (iii) the accelerated exit from the channel, and (iv) the relaxation back onto the steady state (outside of the channel). Below, we show the center of mass velocity (black) compared to* $A^{-1} \oint_{\partial\Omega(t)} F_{act}\mathbf{n}\,\mathrm{d}l$ *(blue), the expected force-balance speed* $A^{-1} \oint_{\partial\Omega(t)} (F_{act} + F_{pot})\mathbf{n}\,\mathrm{d}l$ *(orange), and the predicted steady state speed* u_1 *(red).*

the tension significantly with respect to (b) while keeping the other parameters fixed. Interestingly, this cell pumps itself through the constriction utilizing the 'inertial-like' shape-concentration oscillations. This behavior allows the cell to deform appropriately as it moves a critical portion of its mass beyond the constriction opening. By the time the blob at the cell rear encounters the constriction again, the geometry assists in pushing the cell body forward.

In future work, it will be interesting to study the constriction passing capacity also as a function of the cell shape (via c_s), the angle of approach, and the specifics of the constriction geometry. In addition, it remains to be seen if a cell can trap itself within an array of such obstacles (as in Lautscham et al (2015)). Indeed, 'trapping' is entirely plausible as the cell may reach a slow, weakly-polarized state that will not suffice to the squeeze the cell through any available opening.

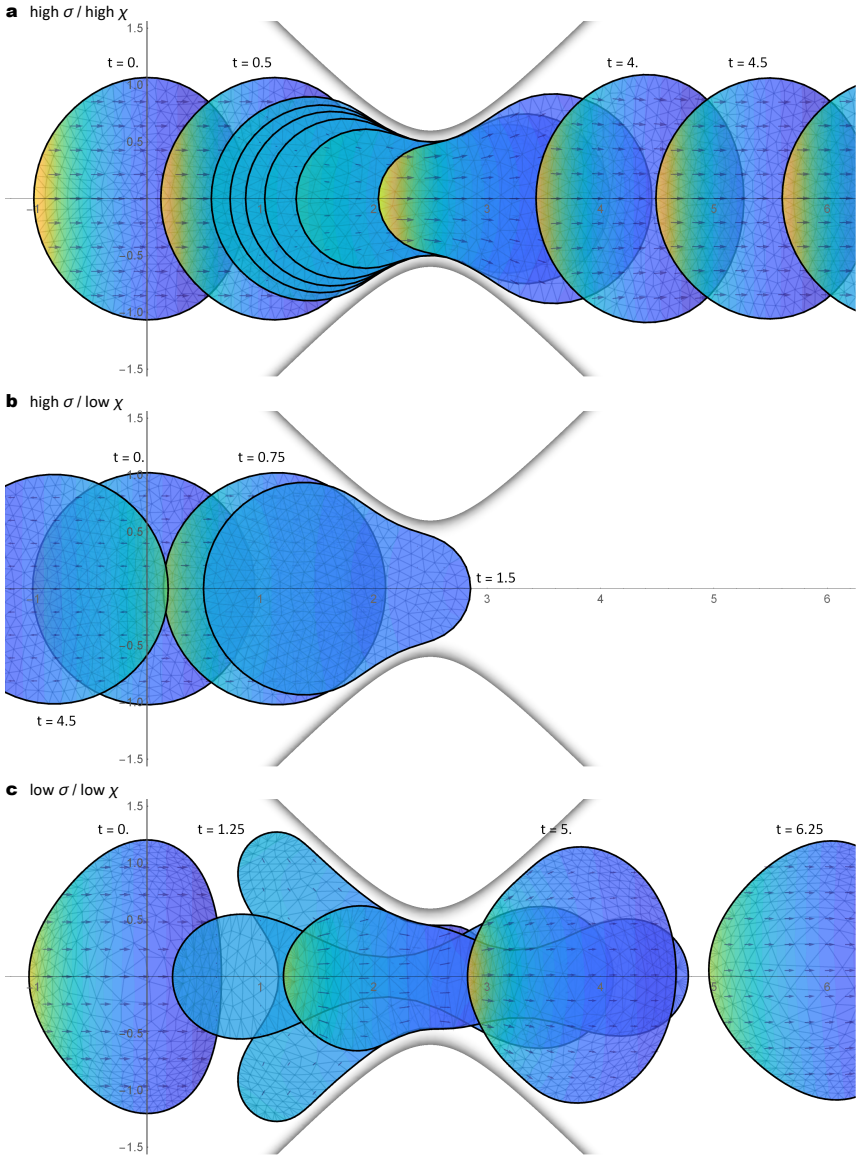

Fig. III.18 ***Passage through a constriction***: *Shown are three numerical experiments of a cell at steady state colliding with a narrow constriction. In (a) we set* $\chi = 1.3$ *and in (b),(c) we set* $\chi = 1.15$. *In (a),(b) we set* $\sigma = 1$ *and in (c) we set* $\sigma = 0.1$. *In all plots, we fixed* $a = 1$ *and* $c_s = 1$, *set* $\delta c^0 = c_1 e^{-a u_1 x}$ *(where* c_1, u_1 *correspond the stable steady state in each case), built the finite element domain to match the corresponding stable steady shape via* $\gamma(l)$ *(Eq.* (III.30)*), and chose* $\Delta t = 0.001$. *The constriction geometry is defined via a power-law potential (in the spirit of Eq.* (III.33)*). a) Simulation snapshots capturing the cell with high tension and high force amplitude squeezing through the constriction. b) Snapshots capturing the cell with high tension and low force amplitude stalling in the constriction and then polarizing toward the opposite direction. c) Snapshots capturing the cell with low tension and low force amplitude exhibiting shape-concentration waves as it passes through the constriction.*

III.4.3 Cell-cell collisions

To account for non-adhesive mechanical interactions between multiple cells exhibiting arbitrary migration and deformation dynamics, we incorporate a repulsive short-range force aimed strictly at inhibiting intersections of the curved interfaces. We stress that, like F_{pot}, the force used here is an effective phenomenological one, i.e., it does not faithfully represent a hydrodynamic interaction mediated by the surrounding fluid (which is not accounted for in this study). Note in this regard that modeling the exact hydrodynamic forces acting on two closely spaced droplets in a Hele-Shaw film (each of arbitrary shape and viscosity) remains an open theoretical challenge (with progress being made under certain symmetry considerations, see Chan et al (2010); Sarig et al (2016)).

In our simulation, we add $F^i_{\text{cell-cell}}\mathbf{n}$ to the boundary integral at the end of Eq. (III.32). This term represents an explicit normal force applied on Γ by the boundary of the second cell (Γ') in the current configuration of both cells,

$$F^i_{\text{cell-cell}}(\Gamma') = \mathbf{n} \cdot \oint_{\Gamma'} K(|\mathbf{x} - \mathbf{x}'|)\mathbf{n}' \, \mathrm{d}l' \tag{III.34}$$

where $\mathbf{x}$, $\mathbf{n}$ are the coordinate and normal vector pointing outward on Γ, and $\mathbf{x}'$, $\mathbf{n}'$, $\mathrm{d}l'$ are the coordinate, normal vector pointing outward and the length measure on Γ'. The kernel $K(x)$ is defined by

$$K(x) = H(r_0 - x)\, K_0(e^{-x/r_1} - e^{-r_0/r_1}), \tag{III.35}$$

where K_0 is a large number (compared to σ) scaling the max amplitude of the exclusionary force, r_1 is a short decay length, and r_0 ($> r_1$) is a cut-off distance beyond which $K(|\mathbf{x} - \mathbf{x}'|) = 0$ (introduced for computational efficiency).

Remark III.4.3. *For the cell-cell collision to be 'well-behaved' in our simulation, one must choose the parameters in Eq. (III.35) to be within a range that is compatible with the chosen Δt (or vise versa). To improve robustness, we are currently considering (i) adding a CFL condition for Δt (based on the current cell dynamics and the interaction parameters), and (ii) an implicit alternative to $F_{cell\text{-}cell}$ which would penalize intersections of the moved geometries in the next time iteration (Ω^{i+1}, Ω'^{i+1}).*

In Fig. III.19, we present a simulation demonstrating a typical collision between two motile cells. Note how $F_{\text{cell-cell}}$ acts in a sharp local manner to prevent contact between the curved boundaries. By doing so, it effectively transmits the external normal force exerted by one cell on the interface of the other. For finite (non vanishing) impact parameter (as in Fig. III.19), colliding cells tend to swirl and slide against each other through their soft frictionless interaction. This behaviour facilitates the cells ability to reorient their internal polarity towards a path of least resistance. After the scattering angle is chosen, the cells re-establish their polarity and speed as they stabilize on the steadily-moving solution.

Mechanical interactions such as cell-cell collisions become far more intriguing in the bistable parametric regime. Recall that, in this regime, the cell is expected to be locked either in the circular homogeneous rest-state (being that $a\chi < 1$) or in the stable high speed traveling state (as demonstrated in Fig. III.12). While we found one unstable steady state whose phase-space trajectory is sensitive to initial conditions, one wonders

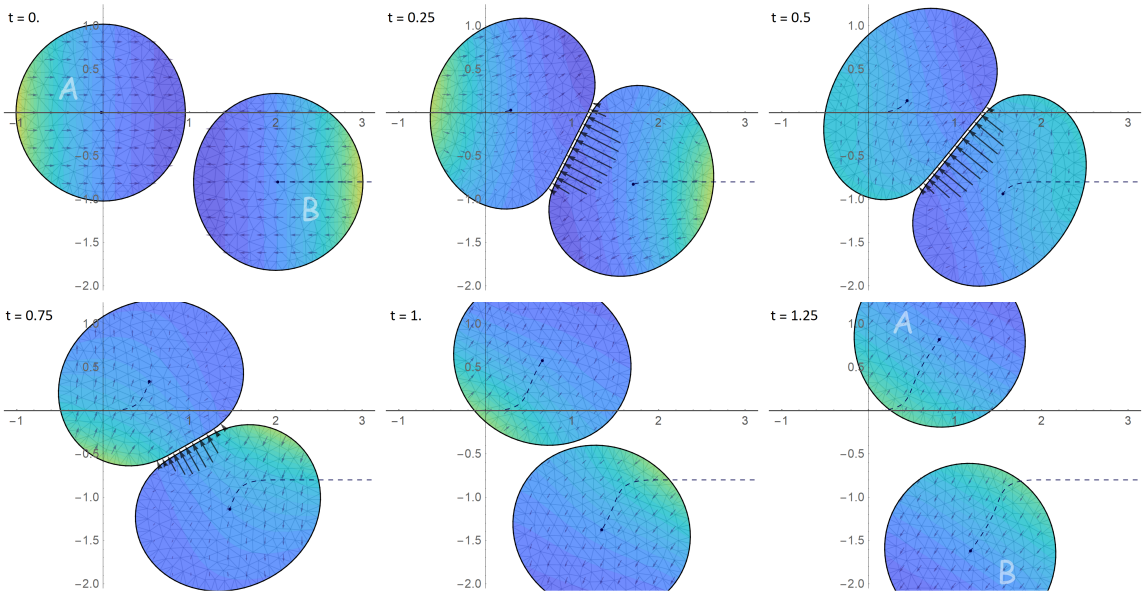

Fig. III.19 ***Cell-cell collision with impact parameter (traveling phase):*** *Shown are snapshots from a numerical experiment in which two motile cells collide against each other with an impact parameter ($b = 0.8$). Both cells have the same intrinsic parameters ($\sigma = 1$, $a = 1$, $\chi = 1.15$, and $c_s = 1$) and are initiated at the corresponding steady state facing opposite directions ($+\hat{x}$ and $-\hat{x}$). The time step was set at $\Delta t = 0.0005$. We denote the cell on the left by $\mathcal{A}$ and the cell on right by $\mathcal{B}$. The interaction force $F_{\text{cell-cell}}(\Gamma_B)\mathbf{n}$ applied on cell $\mathcal{A}$ by cell $\mathcal{B}$ is represented by the black arrows. Note that cell $\mathcal{A}$ applies the opposite normal force on cell $\mathcal{B}$ (not shown). Dashed blue curves mark the center of mass trajectories of both cells. The density plot in the bulk represent the solute concentration field c and the blue vector field represents the fluid flow* $\mathbf{u}$.

if naturally occurring interactions are sufficient to drive the cell out of one stable configuration and into the other. In this context, we ask specifically in Fig. III.20 if a cell in the stable motile state can—by mechanical means alone—induce self-sustained motility in a cell that is initially locked in the stable rest-state (or vise versa). Indeed, through the head-on collision presented in Fig. III.20, the motile cell (cell $\mathcal{A}$) pushes the 'resting' cell (cell $\mathcal{B}$) into the motile steady state. Initially, the final outcome is not obvious being that cell $\mathcal{B}$ is accelerated while cell $\mathcal{A}$ is decelerated. However, as cell $\mathcal{A}$ begins to slow down, it becomes clear that the net active force generated by this cell is actually amplified (due to the deformation tendency produced by the collision). This robust feedback mechanism, which opposes the backwards reaction force coming from cell $\mathcal{B}$, acts to sustain the persistence of the motile cell $\mathcal{A}$. It follows that cell $\mathcal{B}$ is driven forward until it too inevitably stabilizes on the predicted steadily-moving solution. Note in addition that the phase-space trajectory taken by cell $\mathcal{B}$ circumvents of the unstable steadily-moving solution (which was studied in Fig. III.12).

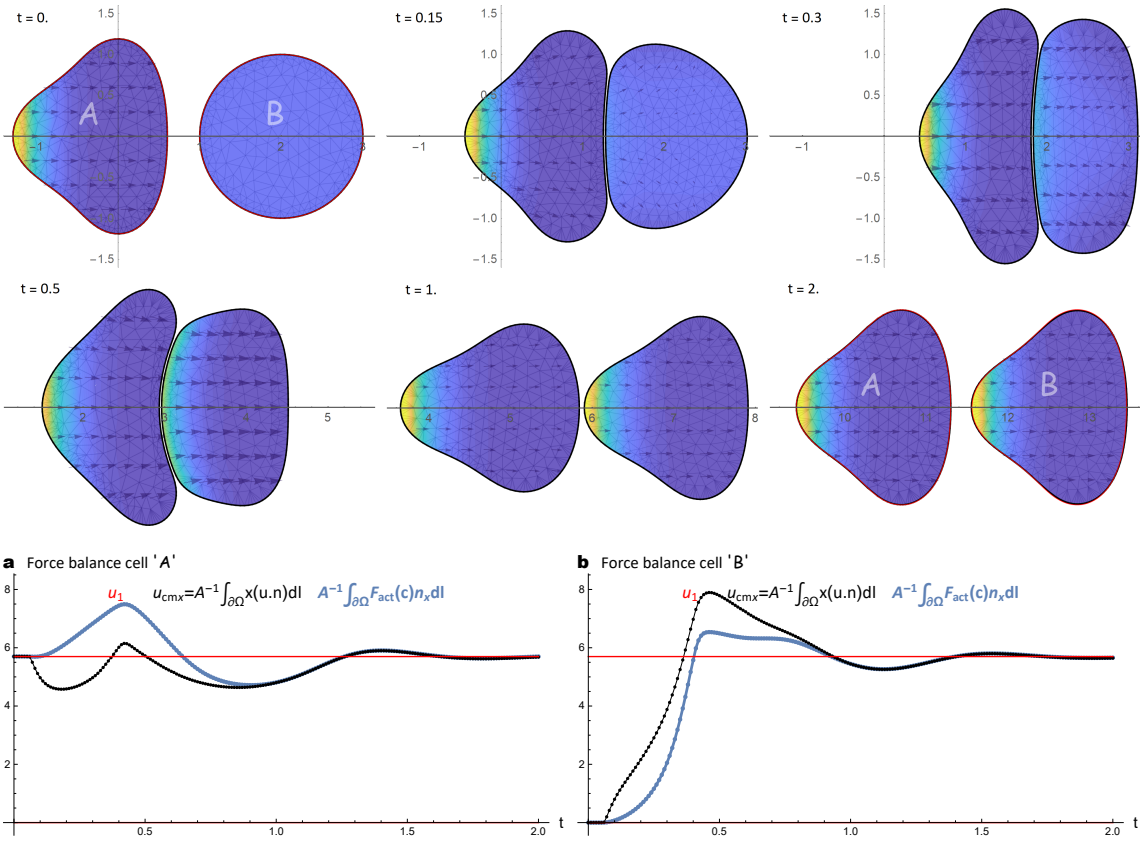

Fig. III.20 ***Activation of motility by cell-cell collision (bistable phase)**: Shown are snapshots from a numerical experiment in which a motile cell collides against a resting cell in the bistable regime. Both cells have the same intrinsic parameters ($\sigma = 1$, $a = 1$, $\chi = 0.75$, and $c_s = .1$). The time step was set at $\Delta t = 0.00025$. The cell on the left (denoted cell $\mathcal{A}$) was initiated at the stable traveling state pointing towards the cell on the right (denoted cell $\mathcal{B}$) which was initiated in the stable rest-state. Each cell interacts with the other via $F_{\text{cell-cell}}$, Eq. (III.34). The red mushroom-like outline represents the predicted shape of the stable traveling state (see Figs. II.5 and III.12). The red circle outlines the stable resting state. The density plot in the bulk represent the solute concentration field c and the blue vector field represents the fluid flow $\mathbf{u}$. a) Force balance corresponding to cell $\mathcal{A}$ showing the center of mass velocity (black) and the speed expected from the intrinsic active force (blue) (in the $\hat{x}$ direction) as well as the predicted steady-state speed of an isolated cell u_1 (red). b) same as (a) for cell $\mathcal{B}$.*

We expect the outcome of numerical experiments such the one presented in Fig. III.20 to depend on the choice of parameters. Closer to the subcritical pitchfork bifurcation (occurring at $a\chi = 1$ for $c_s < 0.5$, see Fig. II.5), it is clear that the stable motile state has a larger basin of attraction compared to the stable rest-state. However, closer to the saddle-node bifurcation (where $a\chi$ is lower and the stable/unstable solution branches approach each other), the stable rest-state should have the larger basin of attraction. The 'activation' (or 'deactivation') of motility by mechanical cell-cell interactions can lead to a highly consequential 'chain-reaction' effect when considering a population of multiple bistable cells occupying the same micro-environment. Hence, it will be interesting to perform a more computationally-taxing experiment in which a 'gas' of such cells are confined to a closed chamber (with walls defined as in Fig. III.15).

III.5 Conclusion and discussion

Our coupled FEM simulation (written and rendered in FreeFem++, anlalyzed and visualized using Mathematica (TM)) provides a high-performance numerical tool for investigating the full nonlinear dynamics of our droplet-solute model, defined originally in Section II.1. Our method solves a nonlinear implicit representation of the time-discrete system, whose variational formulation translates to a minimization problem. The simulation produces quantitative data that is consistent with analytical predictions derived for the PDE problem in Chapter II. Importantly, it allows us to observe and make sense of the shape-concentration dynamics in regimes that we were unable to access by analytic means. Moreover, this simulation is an efficient modular tool useful for (i) incorporating different external interactions with the isolated cell system, and (ii) potentially investigating a wider class of moving-boundary-value problems in which the hydrodynamics of confined viscous fluids are coupled to convection-diffusion-reaction fields.

By simulating the isolated cell system in different parametric regimes and with different initial conditions, we learned that it is robustly attracted to the stable steadily-moving solutions derived in Section II.5. It also became clear that there exists a parametric regime under which our system inevitably approaches a finite time topological singularity, suggesting a viscous fingering-like pathway for cell fragmentation Eggers (1997); Alvarez-Lacalle et al (2009). In addition, we found that shape-concentration limit cycles can be sustained by our model (albeit using a modified form of the active driving force). If the steadily-moving state is made inaccessible, we find that the $m = 2$ traveling wave is the dominant attractor. Interestingly, this type of wave is the most commonly observed in pulsating embryonic cells Maître et al (2015) (though these experiments were not set in confinement). Based on our current experimentation with the FEM tool, we arrive at the following empirical conclusion relating to the 'selection hierarchy' of modes in our dynamical system. Regardless of which mode m is the most unstable at the level of linear perturbations, and granted that a pinching point is never reached (due to saturation of $F_{\text{act}}(c)$), the system allows the lowest-order modes to grow to the largest amplitudes—thereby promoting their selection at the nonlinear level.

By introducing repulsive mechanical interactions between our droplet-solute system and stationary walls/obstacles, we observed more examples of nontrivial (and often 'inertial-like') deformation patterns. We attribute this behaviour to the intrinsic memory (or

persistence) of our system, associated with the diffusive transport of the active force-transducing solute. For instance, the simulation in Fig. III.16 shows a collision of a highly deformable motile cell against a small circular obstacle, leading to the self-driven pinch-off of the cell. In addition, motivated by *in-vitro* experimental studies, we defined specific micro-geometries such as channels and constrictions. The speed of the cell in the confining channel, as well as the ability of the cell to pass through a constriction, were shown to match intuitive physical expectations. Finally, we developed an effective scheme to simulate deformable cell-cell collisions. Such collisions are thought to play an important role in the development and organization of collective cell migration (as was demonstrated using phase-field modeling Löber et al (2015)). While we have yet to explore many of the possible scenarios, we have demonstrated in Fig. III.19 that cell-cell collisions—in the bistable parametric regime—are capable of activating motility in non migrating cells. In fact, this type of outcome was also reported experimentally Verkhovsky et al (1999).

Most importantly, the simulations presented in this chapter can be the basis for a systematic study of a wider range of scenarios. Our future goal is to use our FEM tool to explore new computational directions, as well as compare theoretical results to experimental observations. We discuss our proposals in the following chapter.

Chapter IV

Outlook

The summary and discussion of our results in Chapters II and III are given in Sections II.6 and III.5, respectively. This short chapter outlines the main directions that we believe are worth pursuing in future work. The ideas presented here, which are not fully developed, are motivated by the challenging questions we encountered, as well as the promising research opportunities that have been made accessible by our modular FEM tool.

IV.1 Connecting theory and experiments

A way to significantly elevate our work moving forward is by attempting to make semi-quantitative comparisons between our model predictions and experiments. To do so, one should look for reasonable numerical estimates of our model parameters. This task, which has the potential of connecting our model with observations, is very challenging for several reasons. One, in general, there exists a huge variability in cell parameters (between cell types and between individual cells). Two, it is very difficult to to perform independent measurements of each cell parameter—due to strong couplings that exist between different cell structures and components. Three, even with solid numerical estimates for physical parameters, such the membrane (or membrane + cortex) tension σ, the cytoplasmic viscosity μ, the effective diffusion coefficient D, and mean concentration $c_0 = C_{\text{tot}}/A$ of the suspected chemical, it would be another thing entirely to try to estimate our phenomenological parameters (β and c_{s}), as well as the binding/unbinding rates ($k_{\text{on}}, k_{\text{off}}$) that define the fraction a. Hence, one should try and fix as many parameters as possible, based on literature values, and use the remaining ones as fitting parameters.

As stated earlier (Section II.6), our model is intended to be a highly simplified representation of the biological cell. It would thus be more sensible to try and compare our results with simpler systems such as cytoplasts (enucleated cell fragments capable of migration), as in Euteneuer and Schliwa (1984); Verkhovsky et al (1999); Graham et al (2018), or reconstituted systems, as in Carvalho et al (2013); Simon et al (2018) (see Siton-Mendelson and Bernheim-Groswasser (2016) for a review).

IV.2 Augmenting the hydrodynamics

Accounting for an external fluid

Our current model assumes that pressure gradients in the surrounding fluid are negligible. By Darcy's law, the external fluid pressure is constant if the viscosity there goes to zero. Hence, our assumption is justified at the limit of high viscosity contrast, $C = 1$, where

$$C = \frac{\mu_1 - \mu_2}{\mu_1 + \mu_2},$$

with μ_1, μ_2 representing the fluid viscosities inside and outside of $\Omega(t)$, respectively.

At viscosity contrast $C \neq 1$, the fluids are coupled, that is, one must solve for both the internal and external pressure fields (p_1 and p_2, respectively). The normal force balance on $\partial\Omega(t)$ is consequently modified, and another boundary condition should hold, namely the continuity of the normal velocity.

$$\begin{aligned} p_1 - p_2 + F_{\text{act}}(c) &= \sigma\kappa && \text{on } \partial\Omega(t) \\ (\mathbf{u}_1 - \mathbf{u}_2) \cdot \mathbf{n} &= 0 && \text{on } \partial\Omega(t) \end{aligned}$$

where $\mathbf{u}_2 = -M_2 \nabla p_2$ represents the external fluid flow.

In future work, we suggest to incorporate the external fluid in our FEM simulation, implementing the boundary conditions above. We expect the main challenge to be the handling of a discontinuous tangential velocity, $(\mathbf{u}_1 - \mathbf{u}_2) \cdot \mathbf{t} \neq 0$ on $\partial\Omega(t)$. The numerical strategy could be the following:

- At $t = 0$, construct two triangulation meshes (an interior and exterior) that have a shared discretized interface Γ_h^0.
- At each time step, solve for p_1^{i+1}, u_1^{i+1}, and p_2^{i+1}, u_2^{i+1} together, in an extended variational formulation (computed in both domains and coupled on the interface). The implicit curvature term will be handled with our Newton-like method.
- Solve for c^{i+1} in Ω_1^i in the same exact manner (using the solution for u_1^{i+1}).
- Propagate all elements in Ω_1^i (including Γ^i) in the same exact manner, i.e., $\Omega_1^{i+1} = (\mathrm{Id} + \Delta t\, \mathbf{u}_1^{i+1})(\Omega_1^i)$. The interface Γ^{i+1} will then represent the cell boundary in the deformed configuration.
- Impose the same interface for the external fluid in the deformed configuration. That is, instead of propagating the external elements with $\mathbf{u}_2$, one could remesh (or redefine) this domain through Γ^{i+1}.

The manner in which low viscosity contrast modifies our results is an interesting open question. In classical viscous-fingering problems, it was shown that the nonlinear interface dynamics are highly sensitive to viscosity contrast, in particular in the vicinity of $C = 1$ Casademunt (2004). For instance, finite-time pinch-off could be promoted by having smaller viscosity contrast Alvarez-Lacalle et al (2009); Folch et al (2009).

A successful computational implementation of this problem will also open the door for investigating true hydrodynamic interactions between our cell and stationary wall-s/obstacles or other cells, as introduced in Chapter III in an effective phenomenological manner.

Adding the in-plane viscosity

Our current description of the cytoplasmic fluid is based on Darcy's law, $\mathbf{u} = -M\nabla p$, which neglects the in-plane viscous shearing stresses. We suggest to reintroduce the 2D deviatoric stress tensor of a viscous fluid on top of an effective friction ξ, i.e., to solve

$$-\xi\mathbf{u} + \mu\nabla^2\mathbf{u} - \nabla p = 0 \quad \text{in } \Omega(t) \tag{IV.1}$$

with the appropriate boundary conditions on $\partial\Omega(t)$ (representing normal and tangential force balance).

In such a problem, it is possible to balance arbitrary tangential forces induced by (i) gradients in surface tension (as in Marangoni droplets), controlled either by our solute c or some surfactant, and (ii) external interactions on $\partial\Omega(t)$ that can represent friction with the surrounding fluid, stationary obstacles, and/or other cells.

Remark IV.2.1. *Darcy's law can also be interpreted as friction being much larger than viscous forces in Eq.* (IV.1)*, as assumed in Callan-Jones et al (2008); Blanch-Mercader and Casademunt (2013).*

Adding the polarization field of the actin cytoskeleton

In future work, one could relax the assumption that the active cytoskeleton force, $F_{\text{act}}(c)$, is applied precisely in the direction normal to the free boundary. Indeed, such a force should depend on the average alignment of the polar actin filaments comprising the cortical cytoskeleton. In active gel theory, the polar symmetry of filaments is represented by an arbitrary polarization field $\mathbf{p}$ (with $|\mathbf{p}| < 1$), a non-conserved quantity that follows its own intricate dynamics in the bulk Kruse et al (2004, 2005); Joanny and Prost (2009); Marchetti et al (2013); Prost et al (2015).

Including $\mathbf{p}$ in our FEM tool would entail translating these dynamics into a variational formulation of an additional vector field defined in Ω. Assuming that this is manageable, we shall define the normal component of the applied cytoskeleton force as $F_{\text{act}}(\mathbf{p}, c) = f_{\text{act}}(c)\mathbf{p}\cdot\mathbf{n}$ on $\partial\Omega$. Note also that $\mathbf{p}$ may enter the convection-diffusion transport of c if our solute represents a molecular motor capable of walking along actin filaments (as was done, for instance, in Ziebert et al (2011)).

IV.3 Augmenting the biochemical complexity

Adding reactions

Many previous models have introduced a cubic reaction term in the bulk of the cell that effectively produces and sustains internal cell polarity (see, e.g., Mori et al (2008) and phase-field models reviewed in Ziebert and Aranson (2016)). Our study demonstrates that symmetry-breaking and motility can occur in a simple convection-diffusion-adsorption model that does not include such a phenomenological term. Notwithstanding, complex chemical interactions within the cell domain are worth exploring computationally because they are known to play crucial roles in the true biological system.

Using our FEM tool, one can easily introduce additional chemical species that interact with each other by known or conjectured reactions (as in Doubrovinski and Kruse (2011)).

When going down this path, it would be wise to design a systematic approach that will allow to isolate the effects of each kind of reaction on the overall behaviour of the cell.

Adding noise

For simplicity, our current model consists of completely deterministic equations of motion. However, the mechano-chemical processes driving motility in biological cells are highly stochastic. Noise is cased by multiple factors of both intrinsic and extrinsic origin. Intrinsic noise is chiefly traced to thermal fluctuations of biochemical reactions Tsimring (2014). To account for such fluctuations, we suggest to incorporate noise both in the transport equation of c, and directly in the active force term F_{act} (as to mimic the stochastic nature of the various molecular interactions generating the cytoskeleton-based force).

By incorporating noise in our simulation, we expect to obtain a phase diagram of cell trajectories that is similar to one predicted by the stochastic UCSP model Maiuri et al (2015), that is: diffusive migration, persistent migration, and intermittent migration, see Fig. I.8. Using our FEM tool for the deformable 2D cell, it will be possible to explore the characteristic shapes associated with the different migration phases. Moreover, it will be interesting to examine how cell trajectories are effected by spontaneously-induced 'active-capillary' waves. Having noise would also help to probe the local stability of our resolved steady state solutions.

IV.4 Constructing a FEM simulation of cell assemblies/ tissues

One could take advantage of our FEM-tool to investigate emergent self-organisation phenomena in large assemblies comprised of multiple active cells. In Figs. III.19 and III.20, we already demonstrated an effective contact-penalization scheme for simulating mechanical cell-cell interactions. In future work, our scheme should be further refined as to include attractive cell-cell forces (on top of short-range repulsion) that mimic adhesiveness between deforming active surfaces. A successful implementation of cell-cell adhesion would constitute an important step towards constructing a cell-based model of a compacted tissue. In addition, one could think of several ways in which cells in the assembly exchange chemical signals that affect intrinsic reactions and/or parameters. The combination of mechanical and chemical interactions between individual cells can lead to many fascinating outcomes, including collective cell migration, coordinated morphogenesis, synchronized shape-concentration waves, and the possible segregation and break-up of a tissue.

Appendix A

Appendix for Chapter II

A.1 Preliminaries

A.1.1 The lubrication approximation

For completeness, we present here a brief derivation of the classical thin-film lubrication approximation, leading to Eq. (II.1).

We consider a viscous fluid confined between two parallel plates and denote the 3-dimensional fluid flow by $\underline{u} = (u, v, w)$, where u, v have a typical scale U_0 and w has typical scale W_0. Let the gap h separating the plates be small in comparison to the scale L of deviations in the x, y directions. From incompressibility ($\nabla \cdot \underline{u} = 0$), it follows that $W_0/h \sim U_0/L$ (and thus $W_0 \ll U_0$).

The x, y components in the Navier-Stokes momentum equation are given by

$$\begin{cases} \rho(u_t + uu_x + vu_y + wu_z) &= -p_x + \mu(u_{xx} + u_{yy} + u_{zz}) \\ \rho(v_t + uv_x + vv_y + wv_z) &= -p_y + \mu(v_{xx} + v_{yy} + v_{zz}) \end{cases} \tag{A.1}$$

Here, the inertial terms (on the LHS) scale like $\rho U_0^2/L$, while the viscous shear terms, μu_{zz} and μv_{zz} (on the RHS), scale like $\mu U_0/h^2$. The lubrication approximation consists of taking the limit $\rho U_0^2/L \ll \mu U_0/h^2$, meaning that inertia is neglected.

As opposed to classical Stokes flow, in the Hele Shaw problem one further neglects the in-plane viscosity terms, $\mu(u_{xx} + u_{yy})$ and $\mu(v_{xx} + v_{yy})$, which supposedly scale like $\mu U_0/L^2 \ll \mu U_0/h^2$.

The system in Eq. (A.1) then reduces to

$$\begin{cases} 0 = -p_x + \mu u_{zz} \\ 0 = -p_y + \mu v_{zz} \end{cases} \tag{A.2}$$

From which it follows that

$$\begin{cases} u = -\frac{z(h-z)}{2\mu} p_x \\ v = -\frac{z(h-z)}{2\mu} p_y \end{cases} \tag{A.3}$$

where we integrated Eq. (A.2) and imposed no-slip conditions on $z = 0$ and $z = h$.

By averaging the parabolic flow profile, Eq. (A.3), along the vertical gap, one obtains

$$\mathbf{u} = \frac{1}{h}\int_0^h (u,\, v)dz = -\frac{h^2}{12\mu}(p_x, p_y)$$

Hence the result.

A.1.2 Convection-diffusion-adsorption problem

Here, we provide a short derivation of the solute transport equation given in Eq. (II.5).

Considering the adsorption of our solute on the top and bottom plates (Fig. II.1), we decompose the gap integrated concentration $c(t, x, y)$ into two sub-populations: molecules that adhere to the plates (c_p) and molecules that are free in the fluid (c_f). For the former, the fluid flow vanishes (owing to the no-slip conditions) and hence there is no convection. For the latter, we assume a convection speed that equals the gap-averaged flow, $\mathbf{u} = -M\nabla p$. Both populations are assumed to diffuse in the $(x,\, y)$ plane with coefficients D_p and D_f, respectively. The molecules have constant association and dissociation rates to the plates (k_on and k_off). The 2D transport dynamics of c_p and c_f are then given by

$$\begin{aligned} \partial_t c_\mathrm{p} - D_\mathrm{p}\Delta c_\mathrm{p} &= k_\mathrm{on}c_\mathrm{f} - k_\mathrm{off}c_\mathrm{p} && \text{in } \Omega(t) \\ \partial_t c_\mathrm{f} + \mathbf{u}\cdot\nabla c_\mathrm{f} - D_\mathrm{f}\Delta c_\mathrm{f} &= k_\mathrm{off}c_\mathrm{p} - k_\mathrm{on}c_\mathrm{f} && \text{in } \Omega(t) \end{aligned}$$

Assuming rapid rates ($k_\mathrm{on}, k_\mathrm{off} \gg D_\mathrm{p}/L^2, D_\mathrm{f}/L^2$), we consider a steady balance of the two populations that holds locally, i.e., $k_\mathrm{off}c_\mathrm{p} = k_\mathrm{on}c_\mathrm{f}$. The system can then be reduced to a single transport equation for the total concentration ($c = c_\mathrm{p} + c_\mathrm{f}$),

$$\partial_t c + (1-a)\mathrm{u}\cdot\nabla c - D\Delta c = 0 \qquad \text{in } \Omega(t)$$

where $a = k_\mathrm{on}/(k_\mathrm{on} + k_\mathrm{off})$ is the fraction of adsorbed molecules (meaning $c_\mathrm{p} = ac$), and $D = aD_\mathrm{p} + (1-a)D_\mathrm{f}$ is the effective diffusion coefficient.

A.2 Special cases for linear stability analysis

Here, we test the linearization of our model (about the circular homogeneous rest-state) by performing a series of sanity-checks on the contracted equations (Eqs. (II.40) – (II.42)). Specifically, we examine the dynamics of our linearized system in the special cases: $a = 0$, $\chi = 0$, and $\sigma = 0$. In these limits, one can easily square our results with a straightforward physical intuition.

First, it is clear that if the droplet-solute coupling is not closed (meaning $a\chi = 0$), the characteristic function in Eq. (II.42) gives the same eigenvalues that characterize the completely uncoupled system ($a = \chi = 0$). That is,

$$s_{m\sigma} = -\sigma m(m^2 - 1) \tag{A.4}$$

$$s_{m,n} = -\lambda_{m,n}^2 \tag{A.5}$$

where the eigenvalue $s_{m\sigma} \leq 0$ depicts the morphological stability of the Hele-Shaw droplet problem, and $s_{m,n} \leq 0$ are the infinitely-many eigenvalues corresponding to the decaying

solute diffusion modes (on a rigid unit disk with no-flux condition). In more detail, $\lambda_{m,n}$ represents the n^{th} real-positive root of $J'_m(\lambda) = \frac{1}{2}\left(J_{m-1}(\lambda) - J_{m+1}(\lambda)\right)$ (such that $\lambda_{m,n+1} > \lambda_{m,n}$).

We stress that even if $a\chi = 0$, our droplet-solute system may still be coupled via $\chi \neq 0$ or $a \neq 0$. To understand why the growth rates in Eqs. (A.4) – (A.5) remain unaffected by any one-way coupling, let us examine the eigenmodes associated with $s_{m\sigma}$ and $s_{m,n}$ in the two special cases; $a = 0$ and $\chi = 0$.

No solute adsorption

Substituting $a = 0$ in Eqs. (II.40) – (II.41), we find

$$v_{m\sigma}(r,\theta) = \begin{pmatrix} 1 \\ 0 \end{pmatrix} \cos(m\theta) \tag{A.6}$$

$$v_{m,n}(r,\theta) = \begin{pmatrix} \frac{\chi m J_m(\lambda_{m,n})}{\lambda_{m,n}^2 - \sigma m(m^2-1)} \\ J_m(\lambda_{m,n} r) \end{pmatrix} \cos(m\theta) \tag{A.7}$$

We first make sense of $v_{m\sigma}$, Eq. (A.6). Without adsorption on the plates, the solute is convected at the same speed of the fluid. This means that the moving boundary does not generate solute gradients, see Eq. (II.41). Hence, if the solute concentration is not perturbed ($\delta c = 0$), the active force on the boundary is kept uniform. It follows that the pure shape perturbation is stabilized by the tension alone (i.e., with $s_{m\sigma}$, Eq. (A.4)).

The modes $v_{m,n}$, Eq. (A.7), can be understood as follows. Since the solute diffusion problem is unaffected by any small motion of the boundary, we should recover the classical diffusion modes on a no-flux disk that decay with the growth rates $s_{m,n}$, Eq. (A.5). Notwithstanding, if $\chi \neq 0$ the small solute gradients still induce a nonuniform active force on the droplet boundary. This force transduction cannot change $s_{m,n}$ but it does generate the enslaved shape component in $v_{m,n}$. Note that in the special scenarios where $\sigma m(m^2-1) \simeq \lambda_{m,n}^2$, the mode $v_{m,n}$ effectively converges to the mode $v_{m\sigma}$, Eq. (A.6).

No force-transduction

Substituting $\chi = 0$ in Eqs. (II.40) – (II.41), we find

$$v_{m\sigma}(r,\theta) = \begin{pmatrix} 1 \\ \frac{a\sqrt{\sigma m(m^2-1)}}{J'_m\left(\sqrt{\sigma m(m^2-1)}\right)} J_m\left(\sqrt{\sigma m(m^2-1)}\, r\right) \end{pmatrix} \cos(m\theta) \tag{A.8}$$

$$v_{m,n}(r,\theta) = \begin{pmatrix} 0 \\ J_m(\lambda_{m,n} r) \end{pmatrix} \cos(m\theta) \tag{A.9}$$

We first consider $v_{m\sigma}$, Eq. (A.8). Since the active force on the boundary is kept uniform (independent of small solute deviations), any normal shape perturbation must decay with the growth rate $s_{m\sigma}$, Eq. (A.4). Assuming $a \neq 0$, the movement of the free boundary still feeds into solute transport problem via Eq. (II.41) (no-flux condition). On its own, this effect cannot change $s_{m\sigma}$ but it does generate the enslaved solute component

in $v_{m\sigma}$. Note that here, in the special scenarios where $\sigma m(m^2-1) \simeq \lambda_{m,n}^2$, the mode $v_{m\sigma}$ effectively converges to the mode $v_{m,n}$, Eq. (A.9).

The eigenmodes $v_{m,n}$, Eq. (A.9), are easier to understand. Since $\chi = 0$, the shape is unaffected by small solute deviations, Eq. (II.40). Hence, if the shape is not perturbed ($\delta R = 0$), we simply recover the decaying solute diffusion modes over the no-flux disk (associated with $s_{m,n}$, Eq. (A.5)).

Zero surface tension (ZST)

Here we consider $\sigma = 0$ and focus only the modes $m \geq 2$. Note that $m = 0$ and $m = 1$, which are independent of σ, are unique cases that we discuss separately Sections ??.

To find the eigenvalues, we begin by substituting $\sigma = 0$ in Eq. (II.42)

$$G_m^{\mathrm{zst}}(s) = -s\left(\frac{i\sqrt{s}}{2}\left(J_{m-1}(-i\sqrt{s}) - J_{m+1}(-i\sqrt{s})\right) + a\chi m J_m(-i\sqrt{s})\right) \tag{A.10}$$

It is clear that $s = 0$ is an eigenvalue for any $a\chi$. Substituting $\sigma = 0$ in Eqs. (II.40) – (II.41), we find that $s = 0$ is associated with the eigenmode

$$v_{m0}^{\mathrm{zst}}(r,\theta) = \begin{pmatrix} 1 \\ 0 \end{pmatrix} \cos(m\theta)$$

which describes the pure deformation of the droplet. With no surface tension, and with $\delta c = 0$, there is no nonuniform force acting on the boundary that can counter or amplify the curvature gradients represented by v_{m0}^{zst}. Hence, this perturbation must be marginally-stable (and thus $s = 0$).

Since $G_m^{\mathrm{zst}}(s)$ is highly nonlinear, we cannot find its additional roots analytically. As we are interested in instabilities, we expand Eq. (A.10) about $s = 0$

$$G_m^{\mathrm{zst}}(s) \simeq \frac{1}{m!}\left(-\frac{i\sqrt{s}}{2}\right)^m s\left(m(1-a\chi) + \frac{2+m(1-a\chi)}{4(m+1)}s\right)$$

This function has the additional real root $s_m^{\mathrm{zst}} \simeq \frac{4m(m+1)(a\chi-1)}{2+m(1-a\chi)}$, which changes sign from negative to positive as $a\chi$ exceeds the critical value of 1. We stress that s_m^{zst} is a valid approximation of a true root of $G_m^{\mathrm{zst}}(s)$ so long as it is is small (that is, for $a\chi \approx 1$). In which case, we may write $s_m^{\mathrm{zst}} \approx 2m(m+1)(a\chi-1)$. Its associated eigenmode is then given by

$$\begin{aligned} v_{ms_m}^{\mathrm{zst}}(r,\theta) = \begin{pmatrix} -\chi m J_m(-i\sqrt{s_m^{\mathrm{zst}}}) \\ s_m^{\mathrm{zst}} J_m(-i\sqrt{s_m^{\mathrm{zst}}}r) \end{pmatrix} \cos(m\theta) &\approx \left(-\frac{i\sqrt{s_m^{\mathrm{zst}}}}{2}\right)^m \begin{pmatrix} -\chi m \\ s_m^{\mathrm{zst}} r^m \end{pmatrix} \cos(m\theta) \\ &\sim \begin{pmatrix} \chi \\ 2(m+1)(1-a\chi)r^m \end{pmatrix} \cos(m\theta) \end{aligned}$$

where we expanded the Bessel functions for low s_m^{zst}. It is instructive to note that as $a\chi$ passes 1 (and hence $v_{ms_m}^{\mathrm{zst}}$ becomes unstable), the solute gradient component in the eigenmode also changes sign with respect to the shape component. The nature of this instability is analogous to the one obtained for $m = 1$, as explained in Section II.4.

Normal mode	$s_{m\sigma}$	$s_{m,1}$	$s_{m,2}$
$m=1$	0	-3.38996	-28.42428
$m=2$	-6σ	-9.32836	-44.97222
$m=3$	-24σ	-17.64999	-64.24402
$m=4$	-60σ	-28.27637	-86.16288
$m=5$	-120σ	-41.16013	-110.66747

Table A.1: Decoupled eigenvalues at $a\chi = 0$, see Eqs. (A.4) – (A.5) and Fig A.1.

A.3 Computational eigenvalues

Here, we aim to provide a more complete picture of our reduced linear system by studying the numerical roots of $G_m(s)$, Eq. (II.42). First, we explain an effective continuous-extension procedure for finding these roots as functions of the control parameters, σ and $a\chi$. Second, we describe our method for tracing the critical Hopf-bifurcation lines over the $a\chi$-σ diagram.

Continuous-extension of the eigenvalues

For any $m \geq 1$, we first set σ arbitrarily and compute the real-negative eigenvalues corresponding to $a\chi = 0$, see Eqs. (A.4) – (A.5) and Table A.1. Then, we examine how each one of these eigenvalues evolves as a continuous function of $a\chi$. To trace the numerical roots of $G_m(s)$, we increase $a\chi$ incrementally (starting from 0, where the roots are known). In each consecutive iteration of $a\chi$, we use the FindRoot function on $G_m(s)$, Eq. (II.42). This function implements a computational root-finding algorithm about an initial guess ($s^{\mathrm{g}} \in \mathbb{C}$). To facilitate convergence, and to prevent inadvertent confusion between the multiple roots of $G_m(s)$, we define s^{g} as the numerical root of interest obtained in the previous $a\chi$ iteration.

Let us demonstrate this analysis for the modes $m = 1$–5. As there are infinitely many roots for each m, we focus on the droplet eigenvalue ($s_{m\sigma} = -\sigma m(m^2-1)$) and the two least-negative diffusion eigenvalues ($s_{m,1}$ and $s_{m,2}$, given explicitly in Table A.1). The process of computing the numerical eigenvalues as functions of $a\chi$ is repeated for different values of σ, see Fig. A.1. The results shown in this figure essentially validate our main conclusions in Section II.4 regarding the linear stability of each mode m. Interestingly, Fig. A.1 also reveals that as $a\chi$ is increased from zero, the eigenvalue $s_{m\sigma}$ tends to merge with its closest neighboring $s_{m,n}$. Upon merger, these eigenvalues become a complex-conjugate pair, signifying a transition from a stable node to a stable focus. At high $a\chi$, after crossing the Hopf bifurcation, there is an additional point at which the complex-conjugates separate into two distinct real-positive eigenvalues, signifying a transition from an unstable focus to an unstable node. We stress that these transitions do not imply any qualitative change in the overall stability of each mode m, which is determined at the single Hopf bifurcation. Indeed, we find computationally that all other eigenvalues (those which do not merge with $s_{m\sigma}$) remain real-negative for any $a\chi$ and σ.

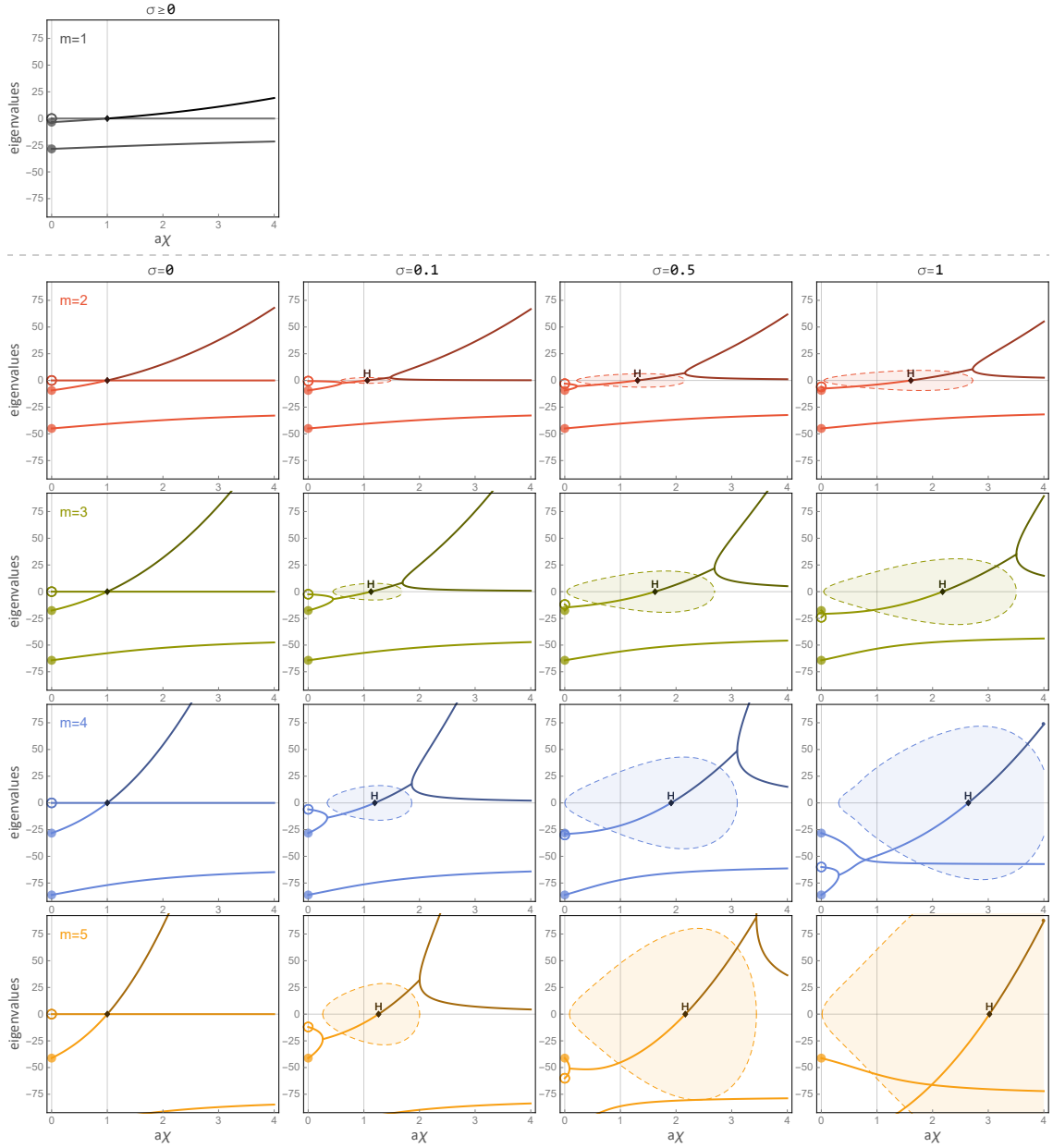

Fig. A.1 ***Numerical eigenvalues***. *For each mode $m = 1$–5, we plot three computational roots of $G_m(s)$ as functions of $a\chi$ (with σ fixed arbitrarily). At $a\chi = 0$, we mark the droplet eigenvalue $s_{m\sigma}$ (colored circle) and the two lest-negative diffusion eigenvalues, $s_{m,1}$, $s_{m,2}$ (colored disks), given explicitly in Table A.1. In each plot, full lines mark the real part of the eigenvalues while dashed lines mark the imaginary part. Bifurcations (marked by a dark diamond) correspond to a critical $a\chi$ at which the real part of at-least one eigenvalue turns from negative to positive. For $m = 1$ (and also for $m \geq 2$ if $\sigma = 0$) there exists one purely-real eigenvalue that changes sign precisely at $a\chi = 1$. For $m \geq 2$ (and $\sigma > 0$) there exist two complex-conjugate eigenvalues whose real part changes sign at a Hopf-bifurcation (marked with "H"). By numerical investigation, we find that for each m, the infinitely-many diffusion eigenvalues which do not merge with $s_{m\sigma}$ remain real-negative for any $a\chi$.*

Computing the critical lines on the stability phase diagram

For each $m \geq 2$, we look for the critical line that marks the Hopf-bifurcation over the $a\chi$–σ plane. On the bifurcation point, we know that $G_m(s)$ has two complex-conjugate roots whose real part crosses zero. Hence, one must solve two implicit equations, $\Re\left[G_m(i\omega)\right] = 0$ and $\Im\left[G_m(i\omega)\right] = 0$, in the variable $\omega \in \mathbb{R}$ and one of the control parameters (either $a\chi$ or σ).

We recall that in Section II.4 we addressed this problem using a Taylor expansion of $G_m(i\omega)$, Eq. (II.45). This allowed us to derive an explicit low-σ approximation for $a\chi^{\mathrm{c}}$ and ω at the critical point (see Eqs. (II.46) – (II.47)). Here, we approach the same problem numerically, without expansions, using the FindRoot function on Eq. (II.42). This function requires a good initial guess of the two variables in order to converge on the solution of interest. In practice, we work with small iterations of $a\chi$ (starting from $a\chi = 1$) and solve $\Re\left[G_m(i\omega)\right] = \Im\left[G_m(i\omega)\right] = 0$ in the variables ω and σ. About $a\chi = 1$, the critical tension σ and the frequency ω are both small, so we use Eqs. (II.46) – (II.47) to compute the initial guess: $\sigma^{\mathrm{g}} = \frac{4(m+2)(a\chi-1)}{3m^2+m-4}$ and $\omega^{\mathrm{g}} = m(m+1)\sqrt{2\sigma^{\mathrm{g}}(m-1)}$. At higher values of $a\chi$, the guess is computed by polynomial continuation of the previously registered numerical solutions.

The results of this method are presented in the linear-stability phase diagram in Fig. II.2 (colored lines). As expected, for each mode m, our explicit low-σ approximation, Eq. (II.46) (thin translucent lines in Fig. II.2), is tangent to the numerical branch at the critical point $(a\chi, \sigma) = (1, 0)$.

A.4 Rectangular chamber model

Here, we aim explore the behaviours of our fluid-solute system in a geometry that is different from the circular droplet one. Our objective is to demonstrate the robustness of the physical instability leading to 'active-capillary' (shape-concentration) waves. For brevity, the model is directly formulated in dimensionless form.

A.4.1 Dimensionless formulation

Let $\Omega(t)$ be the planar domain enclosed by the periodic side walls ($x = 0$, $x = L$), the rigid no-flux floor ($y = 0$), and the free boundary defined by the graph $y = Y(t, x)$, see Fig. A.2. Note that the scaling of variables and parameters is similar to our droplet model (Section II.3), except that here the length scale R_0 refers to the equilibrium width of the domain (along the y-axis) and $A = R_0 L$ would be the dimensional area of the domain. Hence, in this dimensionless model, the equilibrium state is defined by $Y = 1$ and $c = 1$.

In the bulk, the equations governing the fluid flow are as in Eqs. (II.12) – (II.13),

$$\mathbf{u} = -\nabla p \qquad \text{in } \Omega(t) \tag{A.11}$$

$$\nabla \cdot \mathbf{u} = 0 \qquad \text{in } \Omega(t) \tag{A.12}$$

On the free boundary $Y(t, x)$, the force balance and kinematic conditions are as in Eqs.

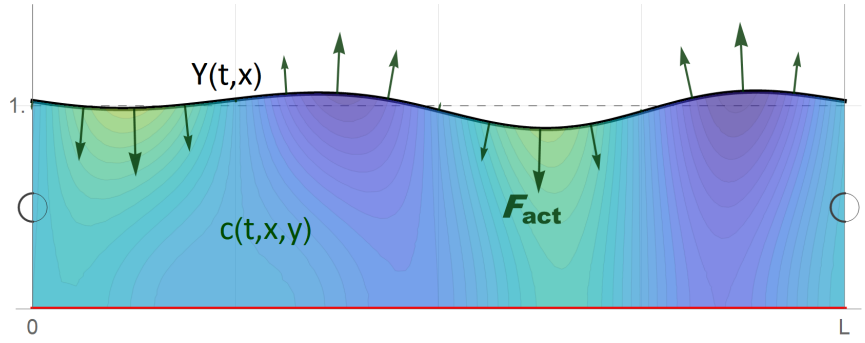

Fig. A.2 ***Rectangular chamber model.*** *The graph $Y(x)$ (black) depicts the free boundary of the domain $\Omega(t)$. The side walls ($x = 0$, $x = L$) are periodic. The rigid bottom wall $y = 0$ (red) has no flux conditions. The density plot in the bulk represents the solute concentration field c, which controls the active normal force F_{act} (dark green arrows).*

(II.14) – (II.15),

$$p + F_{\text{act}}(c) = \sigma\kappa \qquad \text{on } Y(t,x) \tag{A.13}$$
$$V_{\text{n}} = \mathbf{u}\cdot\mathbf{n} \qquad \text{on } Y(t,x) \tag{A.14}$$

The boundary conditions for the fluid on the periodic sides ($x = 0$, $x = L$) are

$$Y(t,0) = Y(t,L), \quad \partial_x Y(t,0) = \partial_x Y(t,L) \tag{A.15}$$
$$p(t,0,y) = p(t,L,y), \quad \partial_x p(t,0,y) = \partial_x p(t,L,y) \tag{A.16}$$

and on the no-flux floor ($y = 0$),

$$\partial_y p(t,x,0) = 0 \tag{A.17}$$

As for the solute, the transport dynamics in the bulk are defined as in Eq. (II.16),

$$\partial_t c + (1-a)\mathbf{u}\cdot\nabla c - \Delta c = 0 \qquad \text{in } \Omega(t) \tag{A.18}$$

The no-flux condition on the free boundary $Y(t,x)$ is defined as in Eq. (II.17),

$$\nabla c\cdot\mathbf{n} + aV_{\text{n}}c = 0 \qquad \text{on } Y(t,x) \tag{A.19}$$

On the periodic sides ($x = 0$, $x = L$),

$$c(t,0,y) = c(t,L,y), \quad \partial_x c(t,0,y) = \partial_x c(t,L,y) \tag{A.20}$$

and on the no-flux floor ($y = 0$),

$$\partial_y c(t,x,0) = 0 \tag{A.21}$$

The linear response of the active force is given by $F'_{\text{act}}(1) = -\chi$, and the (dimensionless) area and total solute are $A = C_{\text{tot}} = L$.

A.4.2 Linear stability analysis

Let us consider the rectangular rest-state solution, where the free-boundary is given by $Y = 1$ and the solute concentration is $c = 1$. In this state, the curvature along Y is simply $\kappa = 0$ and the resulting pressure is constant ($p = -F_{\text{act}}(1)$ in Ω), meaning that $\mathbf{u} = -\nabla p = 0$. We now perturb both the edge of the domain and the solute concentration such that $Y(t,x) = 1 + \delta Y(t,x)$ and $c(t,x,y) = 1 + \delta c(t,x,y)$. To satisfy the periodic conditions, Eqs. (A.15) and (A.20), we expand the perturbations in the following Fourier series

$$\delta Y(t,x) = \sum_{m=0}^{\infty} \left(\delta Y_{\text{cm}}(t)\cos(k_m x) + \delta Y_{\text{sm}}(t)\sin(k_m x)\right) \tag{A.22}$$

$$\delta c(t,x,y) = \sum_{m=0}^{\infty} \left(\delta c_{\text{cm}}(t,y)\cos(k_m x) + \delta c_{\text{sm}}(t,y)\sin(k_m x)\right) \tag{A.23}$$

where $|\delta Y_{\text{cm}}|, |\delta Y_{\text{sm}}|, |\delta c_{\text{cm}}|, |\delta c_{\text{sm}}| \ll 1$ and $k_m := 2\pi m/L$ with m being an integer.

Similarly, we expand the resulting variation in the pressure. It follows from Eqs. (A.11) – (A.12) that $\Delta\delta p = 0$ and thus

$$\delta p(t,x,y) = \sum_{m=1}^{\infty} \cosh(k_m y)\left(A_m(t)\cos(k_m x) + B_m(t)\sin(k_m x)\right) \tag{A.24}$$

where we considered Eq. (A.16) and resolved Eq. (A.17) by discarding solutions proportional to $\sinh(k_m y)$.

On the free boundary, it follows from the force-balance, Eq. (A.13), that $\delta p = \sigma\kappa - \delta F_{\text{act}}$, where $\delta F_{\text{act}} = F'(1)\delta c = -\chi\delta c$. To first order in the perturbations, the boundary deviations in pressure and solute are

$$\delta p \simeq \delta p(y=1) = \sum_{m=1}^{\infty} \cosh(k_m)\left(A_m(t)\cos(k_m x) + B_m(t)\sin(k_m x)\right) \tag{A.25}$$

$$\delta c \simeq \delta c(y=1) = \sum_{m=1}^{\infty} \left(\delta c_{\text{cm}}(t,1)\cos(k_m x) + \delta c_{\text{sm}}(t,1)\sin(k_m x)\right) \tag{A.26}$$

where we used Eqs. (A.24) and (A.23), respectively.

The curvature is (to first order in $Y_{\text{cm}}, Y_{\text{sm}}$)

$$\begin{aligned}\kappa = \frac{-Y_{xx}}{(1+Y_x^2)^{3/2}} &\simeq -\partial_{xx}\delta Y(t,x) \\ &= \sum_m k_m^2 \left(\delta Y_{\text{cm}}(t)\cos(k_m x) + \delta Y_{\text{sm}}(t)\sin(k_m x)\right)\end{aligned} \tag{A.27}$$

Substituting Eqs. (A.25), (A.26), and (A.27) in the force-balance, we obtain the pressure amplitudes

$$A_m(t) = \operatorname{sech}(k_m)\left(\sigma k_m^2 \delta Y_{\text{cm}}(t) + \chi\delta c_{\text{cm}}(t,1)\right) \tag{A.28}$$

$$B_m(t) = \operatorname{sech}(k_m)\left(\sigma k_m^2 \delta Y_{\text{sm}}(t) + \chi\delta c_{\text{sm}}(t,1)\right) \tag{A.29}$$

The normal fluid flow on the free boundary is

$$\mathbf{u}\cdot\mathbf{n} \simeq -\partial_y p(y=1) = -\sum_{m=1}^{\infty} k_m \sinh(k_m)\left(A_m \cos(k_m x) + B_m \sin(k_m x)\right) \tag{A.30}$$

where we used Eq. (A.24).

The normal velocity of the sharp interface is

$$V_\mathrm{n} \simeq \partial_t \delta Y(t,x) = \sum_m \left(\delta\dot{Y}_{cm}(t)\cos(k_m x) + \delta\dot{Y}_{sm}(t)\sin(k_m x)\right) \tag{A.31}$$

where we used Eq. (A.22).

By substituting Eqs. (A.30) – (A.31) in the kinematic condition, Eq. (A.14), it follows that

$$\delta\dot{Y}_{cm}(t) = -k_m \sinh(k_m) A_m \tag{A.32}$$
$$\delta\dot{Y}_{sm}(t) = -k_m \sinh(k_m) B_m \tag{A.33}$$

Substituting the pressure amplitudes, Eqs. (A.28) – (A.29), in Eqs. (A.32) – (A.33)

$$\delta\dot{Y}_{cm}(t) = -\tanh(k_m)\left(\sigma k_m^3 \delta Y_{cm}(t) + \chi k_m \delta c_{cm}(t,1)\right) \tag{A.34}$$
$$\delta\dot{Y}_{sm}(t) = -\tanh(k_m)\left(\sigma k_m^3 \delta Y_{sm}(t) + \chi k_m \delta c_{sm}(t,1)\right) \tag{A.35}$$

Note that in these linearized equations for the shape evolution, the cosine and sine perturbations are uncoupled (δY_{cm} couples only with δc_{cm} and δY_{sm} with δc_{sm}).

Next, we linearize the solute transport problem, Eqs. (A.18) – (A.19). In the bulk, we neglect the quadratic convection term ($\mathbf{u}\cdot\nabla c = -\nabla\delta p\cdot\nabla\delta c$), which leaves the diffusion equation $\partial_t \delta c = \Delta\delta c$. Substituting the expansion, Eq. (A.23), we obtain

$$\partial_t \delta c_{cm}(y,t) = \left[\partial_{yy} - k_m^2\right]\delta c_{cm}(y,t) \tag{A.36}$$
$$\partial_t \delta c_{sm}(y,t) = \left[\partial_{yy} - k_m^2\right]\delta c_{sm}(y,t) \tag{A.37}$$

From the no-flux condition on $y=0$, Eq. (A.21), it follows that

$$\partial_y \delta c_{cm}(t,0) = 0 \tag{A.38}$$
$$\partial_y \delta c_{sm}(t,0) = 0 \tag{A.39}$$

The no-flux condition on the free boundary, Eq. (A.19), translates to $\nabla\delta c\cdot\mathbf{n} = -aV_\mathrm{n}$ (to first order in δc). With $\nabla c\cdot\mathbf{n} \simeq \partial_y \delta c(y=1)$, and with V_n given in Eq. (A.31), we obtain

$$\partial_y \delta c_{cm}(t,1) = -a\delta\dot{Y}_{cm}(t) \tag{A.40}$$
$$\partial_y \delta c_{sm}(t,1) = -a\delta\dot{Y}_{sm}(t) \tag{A.41}$$

Like Eqs. (A.34) – (A.35), our linearized solute transport problem, Eqs. (A.36) – (A.41), only couples δc_{cm} with δY_{cm} (and δc_{sm} with δY_{sm}). Thus, Eqs. (A.34), (A.36),

(A.38), and (A.40) describe a closed dynamical system for the pair of cosine perturbations, $\delta Y_{cm}(t) \ll 1$ and $\delta c_{cm}(r,t) \ll 1$. The pair of sine perturbations are governed an equivalent system, Eqs. (A.35), (A.37), (A.39), and (A.41). Without loss of generality, we focus only on the cosine system hereinafter.

The kernels of Eq. (A.36) satisfying the boundary condition Eq. (A.38) are given by $\cos\left(-i\sqrt{s+k_m^2}y\right)e^{st}$, where the growth rate s is an eigenvalue (constrained by the remaining boundary condition and normally real-negative for pure diffusion problems). We search for coupled shape-concentration eigenmodes of our fluid-solute system by imposing a shared eigenvalue for both degrees of freedom, i.e.,

$$\delta Y_{cm}(t) = \alpha_{ms}e^{st}, \quad \delta c_{cm}(y,t) = \beta_{ms}\cos\left(-i\sqrt{s+k_m^2}y\right)e^{st} \tag{A.42}$$

where $s, \alpha_{ms}, \beta_{ms} \in \mathbb{C}$ and $\delta c_{cm}(y,t)$ is chosen to solve Eqs. (A.36) and (A.38).

Substituting the ansatz, Eq. (A.42), back in Eqs. (A.34) and (A.40) constitutes the final reduction of our linearized system

$$\left(\coth(k_m)s + \sigma k_m^3\right)\alpha_{ms} = -\chi k_m \cos\left(-i\sqrt{s+k_m^2}\right)\beta_{ms} \tag{A.43}$$

$$i\sqrt{s+k_m^2}\sin\left(-i\sqrt{s+k_m^2}\right)\beta_{ms} = -as\alpha_{ms} \tag{A.44}$$

We find the eigenvalues of this system by computing the roots of the complex characteristic function

$$G_k(s) = \left(\coth(k)s + \sigma k^3\right) i\sqrt{s+k^2}\sin\left(-i\sqrt{s+k^2}\right) - a\chi sk\cos\left(-i\sqrt{s+k^2}\right) \tag{A.45}$$

where we omitted the subscript m for brevity.

We stress that for any k, $G_k(s)$ has an infinite set of roots. Each root s is then associated with the eigenmode

$$v_{ks}(x,y) = \begin{pmatrix} \alpha_{ks} \\ \beta_{ks}\cos\left(-i\sqrt{s+k^2}\,y\right) \end{pmatrix}\cos(kx)$$

where here α_{ks}, β_{ks} represent a solution to Eqs. (A.43) – (A.44) for a given s.

To clarify, $v_{ks}(x,y)$ represents a coupled shape-concentration perturbation of the rectangular homogeneous rest-state that evolves with the growth rate s. Hence, if the real part of s is negative (or positive) then the associated eigenmode is stable (or unstable). Like our droplet-solute system, we find that Eq. (A.45), which determines s and thus governs stability, depends only on σ and $a\chi$.

Zero surface tension

Let us first consider the special case of zero surface tension (ZST). Substituting $\sigma = 0$ in Eq. (A.45) gives

$$G_k^{\text{zst}}(s) = i\coth(k)s\sqrt{s+k^2}\sin\left(-i\sqrt{s+k^2}\right) - a\chi sk\cos\left(-i\sqrt{s+k^2}\right) \tag{A.46}$$

We find computationally that this function admits only purely-real roots. As we are interested in instabilities, we look for a root s of Eq. (A.46) that continuously crosses zero as a function of $a\chi$. Expanding the Taylor series of $G_k^{\text{zst}}(s)$ up to order 2 in s gives

$$G_k^{\text{zst}}(s) \simeq (1-a\chi)k\cosh(k)s + \frac{\cosh(k)(1+k\coth(k)) - a\chi k\sinh(k)}{2k}s^2 + O(s^3)$$

This expansion has two real roots

$$s=0, \quad s_k^{\text{zst}} = \frac{2(a\chi-1)k^2\cosh(k)}{\cosh(k)(1+k\coth(k)) - a\chi k\sinh(k)} \tag{A.47}$$

Substituting $\sigma = 0$ in Eqs. (A.43) – (A.44), we find that $s = 0$ is associated with the eigenmode

$$v_{k0}^{\text{zst}}(x,y) = \begin{pmatrix} 1 \\ 0 \end{pmatrix}\cos(kx)$$

which describes the pure deformation of the free interface. With no surface tension, and with $\delta c = 0$, there is no nonuniform force acting on the boundary that can counter or amplify the curvature gradients represented by v_{k0}^{zst}. Hence, this perturbation must be marginally-stable (and thus $s = 0$).

The additional real root s_k^{zst} changes sign from negative to positive as $a\chi$ exceeds the critical value of 1. We stress that s_m^{zst} is a valid approximation of a true root of $G_k^{\text{zst}}(s)$ so long as it is is small (that is, for $a\chi \approx 1$). In which case, we may write $s_k^{\text{zst}} \approx \frac{2(a\chi-1)k^2\cosh(k)}{\cosh(k)+k\,\text{csch}(k)}$. Its associated eigenmode is then given by

$$\begin{aligned} v_{ks_k}^{\text{zst}}(x,y) &= \begin{pmatrix} -\chi k\cos\left(-i\sqrt{s_k^{\text{zst}}+k^2}\right) \\ \coth(k)s_k^{\text{zst}}\cos\left(-i\sqrt{s_k^{\text{zst}}+k^2}\,y\right) \end{pmatrix}\cos(kx) \\ &\approx \begin{pmatrix} -\chi k\cosh(k) \\ \coth(k)s_k^{\text{zst}}\cosh(ky) \end{pmatrix}\cos(kx) \sim \begin{pmatrix} \chi \\ \frac{2(1-a\chi)k\coth(k)}{\cosh(k)+k\,\text{csch}(k)}\cosh(ky) \end{pmatrix}\cos(kx) \end{aligned}$$

where we expanded terms to leading order in s_m^{zst}, substituted $s_k^{\text{zst}} \approx \frac{2(a\chi-1)k^2\cosh(k)}{\cosh(k)+k\,\text{csch}(k)}$ and omitted global prefactors. Note that as $a\chi$ passes 1 (and $v_{ms_m}^{\text{zst}}$ becomes unstable), the solute gradient component in the eigenmode also changes sign with respect to the shape component. The nature of this steady instability is analogous to the one discussed in Section II.4.

Generic case

With $\sigma > 0$, we look for an eigenvalue s^* (complex root of $G_k(s)$) whose real part changes sign from negative to positive as a function of the destabilizing control parameter $a\chi$. At the critical point, denoted $a\chi^{\text{c}}$, the real part of s^* is zero and thus $s^* = i\omega$ (where $\omega \in \mathbb{R}$ represents an oscillation frequency). By solving $\Re[G_k(i\omega)] = \Im[G_k(i\omega)] = 0$, we may compute both ω and $a\chi^{\text{c}}$ as functions of k and σ. Assuming small frequency, let us expand $G_k(i\omega)$, Eq. (A.45), to up to 3rd-order in ω

$$G_k(i\omega) \simeq F_k(\omega^2) + \left(\frac{i\omega}{2}\right)H_k(\omega^2) + O(\omega^4)$$

where $F_k(\omega^2)$, $H_k(\omega^2)$ are the real-valued functions

$$\begin{aligned}
F_k(\omega^2) &= \sigma k^4 \sinh(k) \\
&\quad + \frac{\omega^2}{8k}\left(k\sinh(k)\left(4a\chi + \sigma(1-k^2)\right) - \cosh(k)\left(4(k\coth(k)+1) + \sigma k^2\right)\right) \\
H_k(\omega^2) &= k\left(\cosh(k)\left(2(1-a\chi) + \sigma k^2\right) + \sigma k \sinh(k)\right) \\
&\quad - \frac{\omega^2}{24k^3}\Big(\cosh(k)\left(k^2\left(6(1-a\chi) + \sigma\left(k^2-3\right)\right) + 6\left(k\coth(k)-1\right)\right) \\
&\quad\quad + 3k\sinh(k)(2a\chi+\sigma)\Big)
\end{aligned}$$

Since we need to solve $G_k(i\omega) = 0$, it follows that $F_k(\omega^2) \simeq 0$ and $H_k(\omega^2) \simeq 0$. This system of two implicit equations can be solved in the variables ω^2 and $a\chi$. Using Mathematica (TM), we find one explicit solution that gives $\omega \to 0$ and $a\chi^{\mathrm{c}} \to 1$ at the limit $\sigma \to 0$, agreeing with our result for zero surface tension (see Eq. (A.47)). We stress that this solution can be considered a valid approximation of the bifurcation point so long as ω is small. Hence, we expand it here up to leading order in σ

$$a\chi^{\mathrm{c}} \simeq 1 + \left(\frac{k^3}{\sinh(2k)+2k} + \frac{3}{4}k\tanh(k)\right)\sigma \tag{A.48}$$

$$\omega_{\pm} \simeq \pm 2k^2 \sinh(k)\sqrt{\frac{\sigma k}{(\sinh(2k)+2k)}} \tag{A.49}$$

To recapitulate, for $\sigma > 0$, we find a pair of complex-conjugate eigenvalues whose real part crosses 0 as $a\chi$ exceeds the critical point $a\chi^{\mathrm{c}}$, approximated by Eq. (A.48). At this Hopf-bifurcation point, the frequency ω is approximated by Eq. (A.49). Using Eq. (A.43), we can express the coupled eigenmode associated with the eigenvalue $s^* = i\omega$. This eigenmode represents a shape-concentration standing wave.

$$\begin{aligned}
v_{ki\omega}(x,y) &= \begin{pmatrix} -\chi k \cos\left(-i\sqrt{i\omega+k^2}\right) \\ \left(\coth(k)i\omega + \sigma k^3\right)\cos\left(-i\sqrt{i\omega+k^2}\,y\right)\end{pmatrix}\cos(x) \\
&\approx \begin{pmatrix} -\chi\left(k\cosh(k) + \frac{1}{2}\sinh(k)i\omega\right) \\ \sigma k^3\cosh(ky) + \left(\coth(k)\cosh(ky) + \frac{1}{2}k^2\sigma y\sinh(ky)\right)i\omega\end{pmatrix}\cos(x)
\end{aligned}$$

where we expanded terms to first order in ω.

The fact that standing waves are enabled also means that traveling waves can be constructed in a straightforward manner by superimposing two orthogonal standing waves, $\cos(kx)$ and $\sin(kx)$, evolving at the same amplitude and frequency with a temporal phase-shift of a quarter period.

Indeed, at the linear perturbation level, our fluid-solute system in the rectangular chamber is almost entirely analogous to our droplet-solute model. This serves to show that the Hopf instability is not of geometric origin, but rather attributable to the active interface itself. The only essential difference with respect to the droplet is that the rectangular mode $m = 1$ represents a deformation wave (similarly to all $m > 1$ modes) and no longer depicts a 'polarization-translation' (motility) mode. Note that the absence of such a mode has to do with the fact that we impose no fluid flux on $y = 0$.

A.5 Movie legends

Movie II.1. Shape-concentration normal waves corresponding to $m = 2$. Parameters are set on the Hopf-bifurcation point ($\mathrm{Re}[s_2] = 0$), matching in this case to $\sigma = 1$ and $a\chi \simeq 1.61$. a)–Standing $\cos(2\theta)$ wave. b)–Standing $\sin(2\theta)$ wave evolving at a temporal phase-shift of a quarter period with respect to (a). c)–Traveling $m = 2$ wave resulting from a superposition of (a) and (b). In all panels, the color density map in the bulk represents δc (negative in blue to positive in light green). The color coded boundary represents $\delta\kappa$ (negative in dark red to positive in yellow). The blue vector field in the bulk represent the instantaneous fluid flow, $\mathbf{u} = -\nabla\delta p$. On the boundary of the traveling wave (c), we also trace several fluid path-lines over time.

Movie II.2. Shape-concentration normal waves corresponding to $m = 3$. Parameters are set on the Hopf-bifurcation point ($\mathrm{Re}[s_3] = 0$), matching in this case to $\sigma = 1$ and $a\chi \simeq 2.18$. a)–Standing $\cos(3\theta)$ wave. b)–Standing $\sin(3\theta)$ wave evolving at a temporal phase-shift of a quarter period with respect to (a). c)–Traveling $m = 3$ wave resulting from a superposition of (a) and (b). In all panels, the color density map in the bulk represents δc (negative in blue to positive in light green). The color coded boundary represents $\delta\kappa$ (negative in dark red to positive in yellow). The blue vector field in the bulk represent the instantaneous fluid flow, $\mathbf{u} = -\nabla\delta p$. On the boundary of the traveling wave (c), we also trace several fluid path-lines over time.

Appendix B

Appendix for Chapter III

B.1 Preliminaries

In this section, we present a brief introduction to the variational formulation and the finite element method (FEM). For a more comprehensive guide, see Le Dret and Lucquin (2016).

B.1.1 Variational formulation

A variational formulation is an integral representation of the boundary value problem, such as Eq. (III.1). This representation is obtained by multiplying the PDE with a smooth test function and then integrating it over the domain in which the PDE is defined. The boundary value problem is then transformed into an entirely different kind of problem that allows the use of an existence and uniqueness theory, as well as the definition of approximation methods. The variational approach is quite simple and well suited for a whole class of approximation methods, which are used to obtain quantitative information about the PDE solution when there is no closed formula for it. Note that even though we limit ourselves to variational approximation methods, there are other approximation methods that are not variational.

We demonstrate the variational formulation through the Laplace equation in 2D. The strong form of the Laplace (or Poisson) equation with the Neumann boundary condition is given by

$$-\Delta p = f \quad \text{in } \Omega \tag{B.1}$$

$$\frac{\partial p}{\partial n} = g \quad \text{on } \partial\Omega \tag{B.2}$$

Multiplying Eq. (B.1) by an arbitrary smooth test function q and integrating over the domain Ω gives

$$-\int_\Omega \operatorname{div}(\nabla p) q \,\mathrm{d}a = \int_\Omega f q \,\mathrm{d}a$$

Integrating the LHS by parts, we obtain the integral representation of Eq. (B.1)

$$\int_\Omega \nabla p \cdot \nabla q \,\mathrm{d}a - \oint_{\partial\Omega} \frac{\partial p}{\partial n} q \,\mathrm{d}l = \int_\Omega f q \,\mathrm{d}a$$

where $\mathrm{d}l$ is a measure defined on the boundary $\partial\Omega$. We now insert the boundary condition, Eq. (B.2),

$$\int_\Omega \nabla p \cdot \nabla q \,\mathrm{d}a = \oint_{\partial\Omega} gq \,\mathrm{d}l + \int_\Omega fq \,\mathrm{d}a$$

The trick above of multiplying the equation by some well-chosen functions (test functions) and integrating the result by parts will be the core of the existence and uniqueness theory using variational formulations. It will be also the basis of variational approximation methods such as the finite element method that we employ in our simulation.

Intuitively, the test functions make it possible to extract information about the PDE solution via the integral representation. The variational formulation provides a convenient way of encompassing the conditions that a function must satisfy to be a solution of the PDE. Any particular test function, in its support (i.e., where the function is non-zero), provides a very small amount of information on the PDE solution. Therefore, one must use all the possible test functions in order to reveal the entire solution.

The next step to obtain the variational formulation of Eqs. (B.1) – (B.2) requires the use of some function spaces. The first space required is the Lebesgue space designated by $L^2(\Omega)$, which is the space of all the functions whose squares are integrable (on the domain Ω) in the sense of Lebesgue:

$$L^2(\Omega) = \left\{ f \text{ measurable}; \int_\Omega |f|^2 \,\mathrm{d}a < \infty \right\}$$

In this definition, f is not strictly speaking a function, but an equivalence class of functions that are equal almost everywhere with respect to the Lebesgue measure. However, in practice and outside of very specific circumstances, we can think of f as just a function, not an equivalence class.

When equipped with the norm

$$\|f\|_{L^2(\Omega)} = \left(\int_\Omega |f|^2 \,\mathrm{d}a \right)^{\frac{1}{2}}$$

it is a Hilbert space for the scalar product

$$(f|g)_{L^2(\Omega)} = \int_\Omega fg \,\mathrm{d}a$$

It turns out that functions that are differentiable in the classical sense are typically not enough to work with for solving PDEs. A more general concept is needed, called weak derivation. Unlike the usual derivation, it can be applied to functions that may not be point-wise differentiable with their derivatives existing only in the Lebesgue sense. This is useful from a theoretical and practical viewpoint, because it gives freedom in approximating the true solution of the PDE. Here we will consider the case of functions whose weak derivative φ also are functions, even though they may not be differentiable in the classical sense.

The function f of $L^2(\Omega)$ is said to admit a weak derivative φ if for any smooth function g with compact support in Ω one has

$$\int_\Omega \varphi g \,\mathrm{d}a = -\int_\Omega f g' \,\mathrm{d}a$$

where g' is the usual derivative of g.

Let us now introduce the definition of the Sobolev space H^1:

$$H^1(\Omega) = \left\{ p \in L^2(\Omega), \nabla p \in \left(L^2(\Omega) \right)^2 \right\}$$

where $\left(L^2(\Omega)\right)^2$ is the set of 2d vector functions, whose individual components are in $L^2(\Omega)$. Functions in H^1 are said to be "weakly" differentiable. In dimension one these functions are necessarily continuous, but this is no longer true in dimensions 2 and higher. Notwithstanding, in 2D PDE problems we typically need continuous boundary values in order to write Dirichlet or Neumann conditions. The definition of a good boundary value for functions that belong to H^1 is done by means of a mapping called the trace mapping. This mapping is the unique continuous extension to $H^1(\Omega)$ with values in $L^2(\partial\Omega)$. This allows to extend the integration by parts formula(s) to elements of Sobolev spaces H^1. Let Ω be a Lipschitz open set and $f, g \in H^1(\Omega)$. Then we have

$$\int_\Omega \frac{\partial f(x)}{\partial x_i} g(x)\, \mathrm{d}a = -\int_\Omega f(x) \frac{\partial g(x)}{\partial x_i}\, \mathrm{d}a + \oint_{\partial\Omega} \gamma_0(f)(y)\gamma_0(g)(y) n_i\, \mathrm{d}l$$

where γ_0 is the trace mapping. The image of H^1 by γ_0 is called $H^{1/2}(\partial\Omega)$, which is a strict dense subspace of $L^2(\partial\Omega)$. For simplicity we will write the last integral as $\oint_{\partial\Omega} f(y)g(y)n_i\, \mathrm{d}l$.

The variational formulation of Eqs. (B.1) – (B.2) is now given by the following statement: find a solution $p \in H^1(\Omega)$ such that

$$\int_\Omega \nabla p \cdot \nabla q\, \mathrm{d}a = \oint_{\partial\Omega} gq\, \mathrm{d}l + \int_\Omega fq\, \mathrm{d}a, \qquad \text{for all } q \in H^1(\Omega) \tag{B.3}$$

where f is in the dual space of $H^1(\Omega)$ and g is in the dual space of $H^{1/2}(\partial\Omega)$. The space H^1 was chosen because it is the largest function space for which the integral $\int_\Omega \nabla p \cdot \nabla q\, \mathrm{d}a$ makes sense. Note that the solution p is not required to be twice differentiable, as it is in the boundary value problem, Eqs. (B.1) – (B.2). For this reason, Eq. (B.3) is also called a weak formulation.

Finding a solution to Eq. (B.3) can be done by writing p and q as linear combinations of basis functions that span all of $H^1(\Omega)$ (i.e., the Galerkin method). This would lead to a set of equations for computing the coefficients of the basis functions. However, the basis functions are not easily obtainable when Ω is an arbitrary domain. Therefore, an alternative method consists of replacing the space $H^1(\Omega)$ by a finite dimensional subspace, as done in the finite element method.

B.1.2 Finite element method

The finite element method (FEM) is a powerful numerical method for approximating PDE solutions to boundary value problems. In essence, the FEM consists of partitioning the PDE domain into a finite number of simple elements. The equations which describe these elements are then assembled into a larger system of equations that encompass the entire problem. The calculus used to approximate the solution is based on the variational formulation.

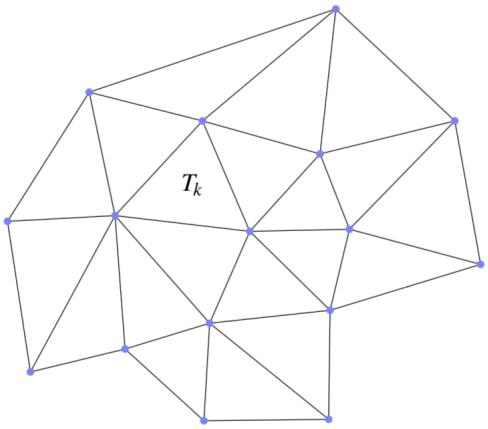

Fig. B.1 ***Triangular mesh***. *A domain Ω has been partitioned into a coarse trianglulation $\mathcal{T} = \{T_k\}$. Figure taken from Le Dret and Lucquin (2016).*

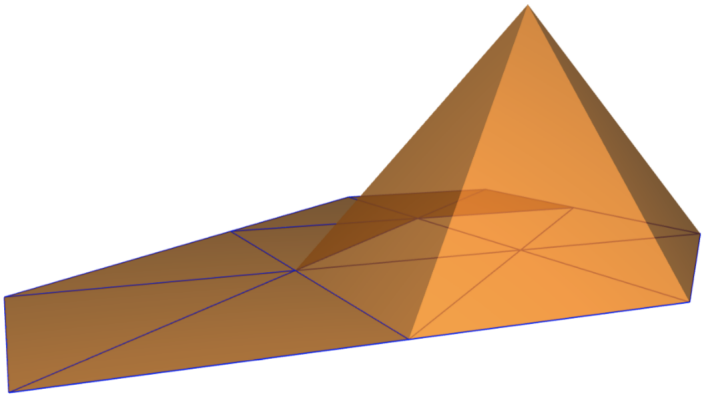

Fig. B.2 ***Hat function***. *A local "hat" function is shown over a sub-domain of Ω. There is one hat function for each vertex in the triangulation. Figure taken from Le Dret and Lucquin (2016).*

In more detail, the idea is to cover Ω (an open subset in $\mathbb{R}^2$) with a finite number of disjoint sets T_k of simple shape, called the elements, $\Omega = \cup_{k=1}^{N_\mathcal{T}} T_k$, with $\mathcal{T} = \{T_k\}$ and $N_\mathcal{T} = \text{card}\mathcal{T}$. Note that this decomposition will be used to convert integrals into sums and therefore $(T_k \cap T_{k'}) = 0$ for $k \neq k'$. Then, we define a set of functions which are subordinate to the partitioning. In the case of a triangulation (Fig. B.1), one can take a set of basis functions, $Q \subset H^1(\Omega)$, to be piecewise "hat" functions that are linear over each triangle and continuous at the edges of the triangles (see Fig. B.2). With respect to the infinite-dimensional Eq. (B.3), this procedure defines a finite dimensional formulation: find a solution $p \in Q$ such that

$$\int_\Omega \nabla p \cdot \nabla q \, \mathrm{d}a = \oint_{\partial\Omega} gq \, \mathrm{d}l + \int_\Omega fq \, \mathrm{d}a, \qquad \text{for all } q \in Q \tag{B.4}$$

The well-posedness of this problem is directly inherited from the generic case of Eq. (B.3). The problem defined in Eq. (B.4) leads to a sparse linear system of equations that can be solved by standard techniques for solving matrix equations.

B.2 Shape derivative of the deformed perimeter

Lemma B.2.1. *The shape derivative of the deformed perimeter is given by*

$$d\mathcal{P}((\mathrm{Id}+\Delta t\,\mathbf{u}^{i+1})(\Omega^i);\mathbf{v}) = -\Delta t \oint_{\Gamma^i} \tilde{\mathbf{H}}^{i+1}\cdot\mathbf{v}\,\mathrm{d}s$$

Proof. Let us first omit the superscript i to simplify the notations. The perimeter of the moved domain is given by

$$\mathcal{P}((\mathrm{Id}+\Delta t\,\mathbf{u})(\Omega)) = \oint_{\Gamma} |(\mathrm{I}+\Delta t\nabla\mathbf{u})\mathbf{t}|\,\mathrm{d}s$$

where $\mathrm{d}s$, $\mathbf{t}$ are respectively the unit length and the tangent vector on Γ.

In order to compute the shape derivative $d\mathcal{P}((\mathrm{Id}+\Delta t\,\mathbf{u})(\Omega);\mathbf{v})$, we perform an asymptotic expansion of order one of $\mathcal{P}((\mathrm{Id}+\Delta t(\mathbf{u}+\delta\mathbf{u}))(\Omega))$ with respect to $\delta\mathbf{u}$.

We first find that

$$|(\mathrm{I}+\Delta t\,\nabla(\mathbf{u}+\delta\mathbf{u}))\mathbf{t}|^2 = |(\mathrm{I}+\Delta t\,\nabla\mathbf{u})\mathbf{t}|^2 + 2\Delta t\nabla\delta\mathbf{u}\,\mathbf{t}\cdot(\mathbf{t}+\Delta t\,\nabla\mathbf{u}\,\mathbf{t}) + O(||\nabla\delta\mathbf{u}||^2)$$

Using the Taylor expansion of $\sqrt{\mathrm{d}S^2+x}$ (where $\mathrm{d}S = |(\mathrm{I}+\Delta t\,\nabla\mathbf{u})\mathbf{t}|$) we obtain

$$|(\mathrm{I}+\Delta t\,\nabla(\mathbf{u}+\delta\mathbf{u}))\mathbf{t}| = |(\mathrm{I}+\Delta t\nabla\mathbf{u})\mathbf{t}| + \Delta t\nabla\delta\mathbf{u}\,\mathbf{t}\cdot T + O(||\nabla\delta\mathbf{u}||^2)$$

where

$$T = \frac{(\mathrm{I}+\Delta t\nabla\mathbf{u})\mathbf{t}}{|(\mathrm{I}+\Delta t\nabla\mathbf{u})\mathbf{t}|}$$

and thus

$$\mathcal{P}((\mathrm{Id}+\Delta t\,\mathbf{u}+\Delta t\delta\mathbf{u})(\Omega)) = \mathcal{P}((\mathrm{Id}+\Delta t\,\mathbf{u})(\Omega)) + \Delta t\oint_{\Gamma}\nabla\delta\mathbf{u}\,\mathbf{t}\cdot T\,\mathrm{d}s + O(||\nabla\delta\mathbf{u}||^2)$$

Consequently, for $\mathbf{v}:\Gamma\to\mathbb{R}^2$ one has

$$d\mathcal{P}((\mathrm{Id}+\Delta t\,\mathbf{u})(\Omega);\mathbf{v}) = \Delta t\oint_{\Gamma}\nabla\mathbf{v}\,\mathbf{t}\cdot T\,\mathrm{d}s \tag{B.5}$$

With s being the arc length coordinate of Γ, it follows that $\nabla\mathbf{v}\,\mathbf{t} = \frac{\mathrm{d}\mathbf{v}}{\mathrm{d}s}$. Then, integrating Eq. (B.2) by parts one obtains

$$d\mathcal{P}((\mathrm{Id}+\Delta t\,\mathbf{u})(\Omega);\mathbf{v}) = -\Delta t\oint_{\Gamma}\mathbf{v}\cdot\frac{\mathrm{d}T}{\mathrm{d}s}\,\mathrm{d}s$$

Finally, since $\tilde{\mathbf{H}} = -\frac{\mathrm{d}T}{\mathrm{d}s}$ we deduce the result. □

B.3 Second order expansion of the deformed perimeter

Lemma B.3.1. *The second order Taylor expansion of the deformed perimeter functional F at $\mathbf{u}$ is given by*

$$\begin{aligned} F(\mathbf{u}+\delta\mathbf{u}) &= F(\mathbf{u}) + \Delta t \int_\Gamma \nabla\delta\mathbf{u}\,\mathbf{t}\cdot T\,\mathrm{d}s \\ &\quad + \frac{\Delta t^2}{2}\int_\Gamma \frac{(\nabla\delta\mathbf{u}\,\mathbf{t}\cdot\mathbf{N})^2}{\mathrm{d}S}\,\mathrm{d}s + O(||\nabla\delta\mathbf{u}||^3) \end{aligned}$$

where $\mathrm{d}s$, $\mathbf{t}$ *and* $\mathbf{n}$ *are respectively the unit length, the tangent and the outward pointing unit normal vectors in the current configuration* Ω. *In addition,* $\mathrm{d}S$, T *and* $\mathbf{N}$ *are respectively the unit length, the tangent and the outward pointing unit normal vectors in the deformed configuration* $(\mathrm{Id}+\Delta t\,\mathbf{u})(\Omega)$ *"pulled back" in the coordinate system of the current configuration.*

Proof. We perform the asymptotic expansion of order two with respect to $\delta\mathbf{u}$ of the perimeter of the deformed configuration $(\mathrm{Id}+\Delta t\,\mathbf{u})(\Omega)$.

$$F(\mathbf{u}+\delta\mathbf{u}) = \mathcal{P}((\mathrm{Id}+\Delta t(\mathbf{u}+\delta\mathbf{u}))(\Omega)) = \oint_\Gamma |(\mathrm{I}+\Delta t\,\nabla(\mathbf{u}+\delta\mathbf{u}))\mathbf{t}|\,\mathrm{d}s$$

We first develop the square of the integrand

$$|(\mathrm{I}+\Delta t\,\nabla(\mathbf{u}+\delta\mathbf{u})|^2 = |(\mathrm{I}+\Delta t\,\nabla\mathbf{u})\mathbf{t}|^2 + 2\Delta t\nabla\delta\mathbf{u}\,\mathbf{t}\cdot(\mathbf{t}+\Delta t\,\nabla\mathbf{u}\,\mathbf{t}) + \Delta t^2|\nabla\delta\mathbf{u}\,\mathbf{t}|^2$$

Using the Taylor expansion of $\sqrt{\mathrm{d}S^2+x}$ (where $\mathrm{d}S = |(\mathrm{I}+\Delta t\nabla\mathbf{u})\mathbf{t}|$) we obtain

$$\begin{aligned} |\,(\mathrm{I}+\Delta t\,(\nabla\mathbf{u}+\nabla\delta\mathbf{u}))\,\mathbf{t}| &= |(\mathrm{I}+\Delta t\,\nabla\mathbf{u})\mathbf{t}| + \Delta t\,\nabla\delta\mathbf{u}\,\mathbf{t}\cdot T - \frac{\Delta t^2(\nabla\delta\mathbf{u}\,\mathbf{t}\cdot T)^2}{2|(\mathrm{I}+\Delta t\,\nabla\mathbf{u})\mathbf{t}|} \\ &\quad + \frac{\Delta t^2|\nabla\delta\mathbf{u}\,\mathbf{t}|^2}{2|(\mathrm{I}+\Delta t\,\nabla\mathbf{u})\mathbf{t}|} + O(||\nabla\delta\mathbf{u}||^3)\,, \end{aligned}$$

where

$$T = \frac{(\mathrm{I}+\Delta t\,\nabla)\mathbf{t}}{|(\mathrm{I}+\Delta t\,\nabla)\mathbf{t}|}$$

Since $N = T^\perp$, one has

$$|\delta\mathbf{u}\,\mathbf{t}|^2 - (\delta\mathbf{u}\,\mathbf{t}\cdot T)^2 = (\delta\mathbf{u}\,\mathbf{t}\cdot\mathbf{N})^2$$

Substituting this relation and $\mathrm{d}S = |(\mathrm{I}+\Delta t\,\nabla\mathbf{u})\mathbf{t}|$ in the second order terms of the expansion above gives

$$-\frac{\Delta t^2(\nabla\delta\mathbf{u}\,\mathbf{t}\cdot T)^2}{2|(\mathrm{I}+\Delta t\,\nabla\mathbf{u})\mathbf{t}|} + \frac{\Delta t^2|\nabla\delta\mathbf{u}\,\mathbf{t}|^2}{2|(\mathrm{I}+\Delta t\,\nabla\mathbf{u})\mathbf{t}|} = \frac{\Delta t^2\,(\nabla\delta\mathbf{u}\,\mathbf{t}\cdot\mathbf{N})^2}{2\,\mathrm{d}S}$$

hence the result. □

Appendix C

Coupling membrane blebs and invaginations

Here, we attach our paper on the coupling between blebs and membrane invaginations Lavi et al (2019a). Formatting changes have been made from the preprint version in order to fit this thesis.

C.1 Title and authors

Cellular blebs and membrane invaginations are coupled through membrane tension buffering

Ido Lavi[1,*], Mohammad Goudarzi[2], Erez Raz[2], Nir S. Gov[3], Raphael Voituriez[1], Pierre Sens[4]

[1] Laboratoire Jean Perrin, UMR 8237 CNRS, Sorbonne University, 4 place Jussieu, 75005 Paris, France

[2] Institute for Cell Biology, ZMBE, Von-Esmarch-Strasse 56, 48149 Münster, Germany

[3] Department of Chemical Physics, Weizmann Institute of Science, Herzl St 234, Rehovot 76100, Israel

[4] Institut Curie, PSL Research University, CNRS, UMR 168, 26 rue d'Ulm, 75005 Paris, France

[*] Correspondence: ido.lavi@etu.upmc.fr

C.2 Abstract

Bleb-type cellular protrusions play key roles in a range of biological processes. It was recently found that bleb growth is facilitated by a local supply of membrane from tubular invaginations, but the interplay between the expanding bleb and the membrane tubes remains poorly understood. On the one hand, the membrane area stored in tubes may serve as a reservoir for bleb expansion. On the other hand, the sequestering of excess membrane in stabilized invaginations may effectively increase the cell membrane tension, which suppresses spontaneous protrusions. Here, we investigate this duality through physical modeling and *in-vivo* experiments. In agreement with observations, our model describes the transition into a tube-flattening mode of bleb expansion, while also predicting that the blebbing rate is impaired by elevating the concentration of the curved membrane

proteins that form the tubes. We show both theoretically and experimentally that the stabilizing effect of tubes could be counterbalanced by the cortical myosin contractility. Our results largely suggest that proteins able to induce membrane tubulation, such as those containing N-BAR domains, can buffer the effective membrane tension — a master regulator of all cell deformations.

C.3 Introduction

Cellular blebs are protruding hemispherical bulges that form rapidly following local uncoupling of the plasma membrane from the cortical cytoskeleton Albrecht-Buehler (1982); Cunningham (1995); Charras et al (2005). Protrusions of this type are instrumental in cellular processes such as apoptosis, mitosis, and motility. The formation of blebs is driven by the intracellular hydrostatic pressure generated by actomyosin contractility Keller and Eggli (1998); Paluch et al (2005); Pullarkat (2006); Paluch and Raz (2013). Theoretical models of bleb initiation have thus far considered the membrane-cortex adhesion and the membrane tension as the forces that act against the detachment and deformation of the bulging membrane Charras et al (2008); Norman et al (2010); Spangler et al (2011); Strychalski and Guy (2013); Alert and Casademunt (2016); Fang et al (2017). While these parameters are indeed important, the common description of the membrane as a flat interface fails to represent the seemingly more complex expansion mechanism. Given that stretching a flat plasma membrane is limited to just 2%–3% before rupture Kleinschmidt (2006); Kwok and Evans (1981), and that this extension requires a force that cells cannot generate Sheetz et al (2006), bleb expansion was suggested to depend on a local supply of membrane Erickson and Trinkaus (1976); Schmid-Schonbein et al (1980); Dai et al (1998); Sheetz et al (2006). Such area exchange affects the stress-strain relationship of the plasma membrane in a manner that remains poorly understood. This stress-strain (or tension-expansion) relationship is an important aspect of bleb formation Young and Mitran (2010) and of all other cellular processes where plasma membrane mechanics play a crucial role.

In a recent study Goudarzi et al (2017), some of us investigated the *in-vivo* motility of primordial germ cells (PGCs) in the Zebrafish Embryo. These cells migrate towards their target, the developing gonad, employing blebs as forward protrusions Blaser et al (2006); Goudarzi et al (2012); Paksa and Raz (2015); Barton et al (2016). We found that the rapid membrane expansion associated with blebs relies on the local flattening of inwards-pointing tubular invaginations (or tubes) of the plasma membrane. Previous works suggest that cell membrane tubes may be formed and stabilized via a scaffolding mechanism involving crescent-shaped BAR domain proteins Takei et al (1999); Lee et al (2002); Peter et al (2004); Masuda et al (2006) (for reviews see McMahon and Gallop (2005); Itoh and De Camilli (2006); Baumgart et al (2011); Simunovic et al (2015)). Depending on their concentration, N-BAR proteins were shown to act both as membrane curvature sensors as well as curvature inducers Peter et al (2004); Bhatia et al (2009). Accordingly, in our experiments Goudarzi et al (2017), we were able to track the membrane tubes by expressing the YFP-labeled N-BAR domain of Amphiphysin. At low concentration, N-BAR served purely as a tubes-sensor and had no effect on the blebbing capacity nor the motility of PGCs. At high concentrations of N-BAR, an increase in tubular mem-

brane invaginations and thus an increase in membrane area sequestered within them was observed. Strikingly, this manipulation also resulted in impaired blebbing and defective migration. Whereas the apparent membrane reservoir for bleb expansion increased, the blebbing activity markedly decreased.

Motivated by this puzzle, we propose in this paper a simplified physical description of membrane tubulation by curved proteins, coupled to the thermodynamics of bleb formation. In our model, we formulate the free energy of the membrane and the bound proteins that form scaffolds for membrane tubes. Discarding dynamics, we minimize this energy sequentially on a timescale hierarchy. Through this minimization, we calculate analytically both the folded membrane area and the effective membrane tension. We then show quantitatively how these properties control the expansion mechanism and the probability of bleb initiation. Our model yields a parametric regime under which cells could, in principle, regulate their blebbing activity through the expression of tube-forming proteins (such as N-BAR). A qualitative comparison with previous observations suggests that this regime is likely relevant to wild type (WT) PGCs in the embryo. The model further provides another experimentally-accessible prediction, namely, that blebbing could be rescued post-N-BAR over-expression by elevating the myosin contractility. We were able to verify this prediction qualitatively in new *in-vivo* experiments.

C.4 Model

C.4.1 Membrane tubes and expanding bleb are coupled by membrane tension

We begin by introducing our central hypothesis that couples the tubular invaginations with the protruding bleb. This coupling is based on the area dependence of the membrane tension σ. In simple membrane systems such as giant vesicles, the membrane tension is primarily of entropic origin, and is non-linearly (exponentially) related to the "excess area", broadly defined as the relative difference between the true membrane area (related to the number of lipid molecules) and the "apparent area": the surface area of the average vesicle's shape, which excludes thermal fluctuations Evans and Rawicz (1990). Conditions that increase the apparent area under constant true area, such as an hypo-osmotic shock, increase the membrane tension by flattening out thermal fluctuations. Such simple relationship does not exist for cells, where the membrane interacts with the cytoskeleton and experiences active fluctuations in addition to the thermal ones Sens and Plastino (2015). One may nevertheless expect that processes that increase the apparent cell membrane area, such as membrane tubulation and bleb formation, should also lead to an increase of membrane tension. To capture this at the phenomenological level, we postulate the following relationship between the cell membrane tension σ, the area held in tubes S_t and the increase of (apparent) cell membrane area associated to bleb formation ΔS_b:

$$\sigma = \sigma_0 + k_\sigma \frac{S_\mathrm{t} + \Delta S_\mathrm{b}}{A} \tag{C.1}$$

where σ_0 is the tension in a reference state with neither tubes nor a bleb, k_σ is an effective stretching modulus, and A is the area over which tension may be considered uniform. If tension equilibrates fast, A is the entire cell area. However, it has recently been shown that the cell membrane resists flow, possibly due to its tight interaction with the cytoskeleton

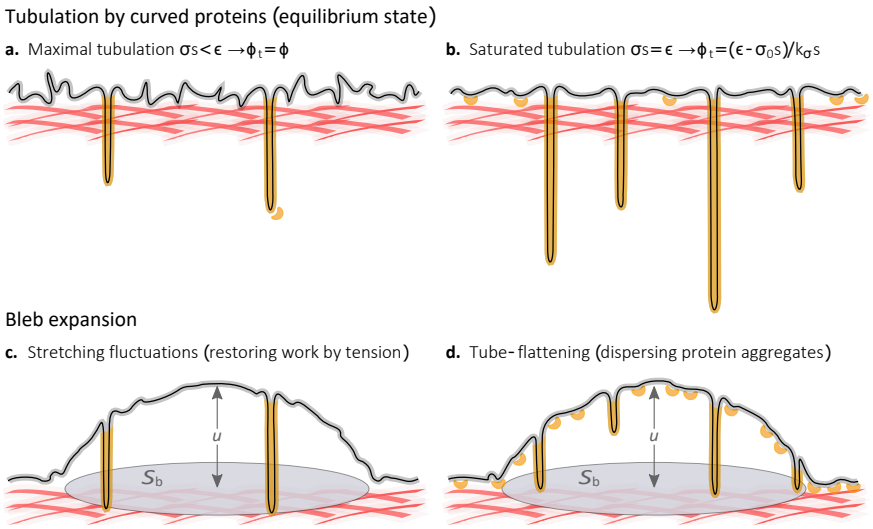

Fig. C.1 **System illustration.** *The equilibrium state of the membrane under the regimes of low and high protein surface fraction is illustrated in figures (a) and (b) respectively. Figures (c) and (d) illustrate the initial expansion of the bleb, which bulges out of the equilibrium states (a) and (b) respectively. The gray-highlighted curve represents the "true" membrane area, including the thermal and active membrane fluctuations. The orange-highlighted curve represents S_t, the membrane area held in tubes. The small banana-shaped components (orange) depict N-BAR proteins. The red mesh represents the underlying actin cortex. The increase of apparent area due to bleb formation is $\Delta S_b = \pi u^2$.*

Shi et al (2018), so that A could be restricted to the cortex-detached region underneath an expanding bleb. The phenomenological relationship is chosen to be linear for simplicity. Taking into account possible non-linearities associated to large variations of the apparent cell membrane area, *e.g.* during the expansion of large blebs, would require introducing additional phenomenological parameters. We stress that many factors could plausibly affect σ_0 and k_σ, including the linkage of the membrane to the cytoskeleton Gov and Safran (2004). In our model we treat both as constant parameters.

At equilibrium, meaning the stabilized folded state with no bleb, the membrane tension is an increasing function of the folded area, S_t, which is induced by the curved proteins (see Fig. C.1a). When the bleb does form, following the local membrane-cortex detachment, this heightened tension is the restoring force that acts against the deformation of the membrane (see Fig. C.1c). Thus, the bleb's energy should be expected to grow as a function of the concentration of the curved protein. Notwithstanding, membrane area can be merely converted from the inward pointing tubules to the expanding bleb, such that no restoring work would be done by the membrane tension (see Figs. C.1b,d). Nevertheless, this expansion by means of unfolding (or tube-flattening) presents its own free-energy cost associated with dispersing the curved protein scaffolds that form the tubules. To accommodate the initial expansion of the bleb, the system minimizes its total free energy by paying with one energetic currency or another, or possibly an optimized fraction of both stretching the membrane (that is, seizing area from fluctuations), and unfolding the

membrane (releasing the area held in stabilized invaginations). Our model incorporates both of these processes, which are physically coupled through the area dependence of the membrane tension, Eq. (C.1).

C.4.2 Tubulation by curved membrane proteins

Although the cell membrane is clearly an out-of-equilibrium system, models based on equilibrium thermodynamics have proven valuable to understand aspects of membrane proteins self-aggregation of high physiological relevance Sens et al (2008). In this section, we propose such a model to determine the configuration of the membrane-bound curved proteins and the area stored in tubes at equilibrium and throughout the expansion of the bleb. We stress that our minimal aggregation model doesn't deal with the specifics of the N-BAR-membrane interaction. We thus refer the reader to previous theoretical models, e.g. Kabaso et al (2011); Lipowsky (2013); Schweitzer and Kozlov (2015), and molecular-dynamics simulations Blood and Voth (2006); Ayton et al (2007, 2009); Arkhipov et al (2009); Yin et al (2009); Simunovic et al (2013); Noguchi (2016) that describe this process at the molecular level. Here, our aim is to provide a simplified coarse-grained description of the equilibrated state of the membrane and to highlight the effect of tension buffering by tubulating proteins. Thus, our approach also differs from previous continuum models that have either focused solely on the onset of spontaneous tubulation Shi and Baumgart (2015) or described the enrichment of curved proteins on preexistent (mechanically pulled) membrane tubes Sorre et al (2012).

There exist direct experimental evidence that, at high concentration, N-BAR proteins such as amphiphysin Sorre et al (2012) and endophilin Chen et al (2016) can form protruding tubes on reconstituted membranes (giant vesicles). These tubes are enriched in N-BAR proteins and coexist with (almost) flat membrane regions. Similarly, in PGCs we have observed membrane tubes pointing inwards from relatively flat regions (see figure 3A and movie S3 in Goudarzi et al (2017)). Thus, in our model, we consider membrane-bound proteins that can be either isolated on a flat membrane or aggregated on dense scaffolds that form stable membrane tubes. Note that this assumption naturally breaks down in several cases, e.g., in the limit of high temperature (as explained in SI), or high tension and small system sizes that would not permit co-existence of tubes and flat membrane Gallop et al (2006). The number of isolated proteins is given by $n_1 = \rho_1 A$ and the number of p-sized aggregates (tubes) is given by $n_p = \rho_p A$ (where ρ_1 and ρ_p are uniform coarse-grained densities). We assume that the folded area held in each p-sized tube is ps, where s is the folded membrane area per protein. We also fix the protein surface fraction on tubes to unity to reduce the number of parameters. Accordingly, the tubes hold a total area of $S_\mathrm{t} = A \sum_{p \geq p_\mathrm{c}} \rho_p ps$ (where p_c is a critical protein number for forming a tube cap), and the number of translational sites is A/s. In Eq. (C.2), we present the free energy associated with the curved proteins and the membrane tubes, including the work done by the membrane tension against the formation of the tubes and the expansion of the bleb. Note that the energy associated with membrane-cortex binding and the work done by the hydrostatic pressure will be considered later on in the analysis of the complete bleb

Description	Symbol	Estimate	Units	Refs/Comments
N-BAR surface area on membrane	s	30-50	nm^2	Adam et al (2015); Peter et al (2004)
Membrane tension (without tubes)	σ_0	10^{-4}-1	pN/nm	Evans and Rawicz (1990); Lieber et al (2013); Sens and Plastino (2015)
Effective membrane stretching modulus	k_σ	0.1-10	pN/nm	This phenomenological parameter is expected to be much smaller than the stretching modulus of pure lipid bilayer in the elastic regime ($\simeq$ 100 pN/nm) due to thermal and active fluctuations Evans and Rawicz (1990); Brückner and Janshoff (2015)
N-BAR affinity to tubes	ϵ	10-100	k_BT	As a rough estimate, we consider the gain in the elastic energy of the membrane associated with clustering isolated N-BAR scaffolds Schweitzer and Kozlov (2015); Schweitzer et al (2015)
Energy of tube cap	E_{cap}	100-600	k_BT	As a rough estimate, we consider the bending energy of a hemisphere, $4\pi K_c$, where K_c ~10-50 k_BT is the bending stiffness Nagle et al (2015); Picas et al (2012)

Table C.1: Quantitative estimates of our tubulation model parameters. With $k_BT \simeq 4$ pN.nm, we obtain $\sigma_0 s \approx 10^{-3}$-10 k_BT, $k_\sigma s \approx$ 1-100 k_BT.

energy.

$$\begin{aligned} F_t =& A\left(\rho_1 \log\frac{\rho_1 s}{e} + \sum_{p\geq p_c}\rho_p \log\frac{\rho_p s}{e}\right) + A\sum_{p\geq p_c}\rho_p\left(E_{cap}-\epsilon p\right) \\ &+ \int_0^{S_t+\Delta S_b}\left(\sigma_0 + \frac{k_\sigma S}{A}\right)dS + \mu A\left(\rho_1 + \sum_{p\geq p_c}\rho_p p\right) \end{aligned} \tag{C.2}$$

This formulation of F_t contains four essential contributions, given in units of k_BT. The first term comes from the translational entropy of all surface species, i.e., isolated proteins and tubes (to lowest order in $\rho_1 s$ and $\rho_p s$). The second term accounts for the energy cost of forming the tube caps (E_{cap} per tube of any size) as well as the energy gain of aggregating proteins onto the tubular scaffolds (ϵ per recruited protein, accounting for any per-protein difference in the protein binding/ membrane bending energy). The third term accounts for the restoring work done by varying the membrane tension against the extension of the tubes and the bleb (see Eq. (C.1)). In effect, due to total membrane conservation (which is represented phenomenologically by Eq. (C.1)), the area $S_t + \Delta S_b$ is drawn from thermal and active membrane fluctuations. Lastly, in the fourth term, μ denotes a Lagrange multiplier that fixes the total number of membrane-bound proteins. The parameters of this model ($s, \sigma_0, k_\sigma, \epsilon, E_{cap}$) are estimated in Table C.1.

We first minimize F_t with respect to the densities of isolated proteins and tubes (assuming ρ_1 and ρ_p are fast variables compared to the bleb expansion ΔS_b)

$$0 = \frac{\partial F_t}{\partial \rho_1} \rightarrow \rho_1 = \frac{1}{s}e^{-\mu}, \qquad 0 = \frac{\partial F_t}{\partial \rho_p} \rightarrow \rho_p = \frac{1}{s}e^{-E_{cap}-(-\epsilon+\sigma s+\mu)p} \tag{C.3}$$

where $\sigma = \sigma_0 + k_\sigma(\phi_t + \Delta S_b/A)$, and $\phi_t = S_t/A$ is the surface fraction of proteins belonging to tubes, see SI for detailed derivation.

The conservation of the total protein number is given by

$$\begin{aligned} \phi = \phi_1 + \phi_t =& s\rho_1 + s\sum_{p\geq p_c}\rho_p p \\ =& e^{-\mu} + e^{-E_{cap}}\frac{e^{(1-p_c)(-\epsilon+\sigma s+\mu)}\left(1+(e^{-\epsilon+\sigma s+\mu}-1)p_c\right)}{\left(e^{-\epsilon+\sigma s+\mu}-1\right)^2} \end{aligned} \tag{C.4}$$

where ϕ is the total protein surface fraction and ϕ_1 denotes the surface fraction of isolated proteins.

The conservation condition, Eq. (C.4), defines the Lagrange multiplier μ as a function of ϕ, with the closed nonlinear relationship obtained by substituting $\phi_t = \phi - e^{-\mu}$ back in σ. Unfortunately, we cannot extract μ explicitly from this implicit equation. Yet, in the limit $E_{cap} \gg 1$ —which is in agreement with our estimation in Table C.1—we find numerically that $\mu(\phi)$ exhibits a sharp transition between two solvable asymptotic cases, namely: (i) at low ϕ, the surface fraction of isolated proteins ϕ_1 dominates over the surface fraction of proteins belonging to tubes ϕ_t, and (ii) at higher ϕ, the fraction ϕ_t (last term on the RHS) will start to dominate. The mathematical treatment, detailed in SI, further reveals that when E_{cap} is the largest energy scale (as we indeed estimate), μ practically loses a quantitative dependency on both E_{cap} and p_c. Ultimately, we obtain an explicit pieace-wise approximation of ϕ_t:

$$\phi_t = \phi - e^{-\mu(\phi)} \simeq \begin{cases} 0 & \phi < \phi^* \\ \phi - \frac{1}{k_\sigma s} W\left(k_\sigma s e^{-k_\sigma s\left(\frac{\epsilon-\sigma_0 s}{k_\sigma s} - \frac{\Delta S_b}{A} - \phi\right)}\right) & \phi > \phi^* \end{cases} \tag{C.5}$$

where $W(x)$ denotes the product-log (Lambert function) and the crossover point of the two asymptotic limits (i.e., the point at which $\mu_{\phi\simeq\phi_1} = \mu_{\phi\simeq\phi_t}$) is, in this $E_{cap} \gg 1$ approximation,

$$\phi^* = e^{-(\epsilon-\sigma_0 s - k_\sigma s \Delta S_b/A)} \tag{C.6}$$

It is clear from Eq. (C.5) that ϕ^* represents a critical protein surface fraction for the onset of tubulation (corresponding to a critical density of proteins ϕ^*/s). Note that this result is reminiscent of the "critical budding concentration" of the membrane proteins that induce caveolae, which are a spherical type of membrane invaginations Sens and Turner (2004). Also note that Eqs. (C.5) – (C.6) in essence depend only on three contracted parameters: $(\epsilon - \sigma_0 s)$, $k_\sigma s$, and ϕ, as well as one additional variable: $\Delta S_b/A$.

C.5 Results

C.5.1 Tubulation

Using Eqs. (C.5) – (C.6), we can compute the total folded area, $S_t = A\phi_t$, as well as the membrane tension, $\sigma = \sigma_0 + k_\sigma(\phi_t + \Delta S_b/A)$, for any set of parameters and any given bleb expansion. We first interpret the equilibrium result and then analyze how it is altered by the expanding bleb.

The equilibrium (pre-bleb) state

We focus on ϕ_t^{eq}, the surface fraction of proteins belonging to tubes at equilibrium, i.e., with $\Delta S_b = 0$. To gain insight into Eq. (C.5), we briefly examine the limits $(\epsilon - \sigma_0 s) \gg 1$ and $k_\sigma s \gg 1$ (completely negligible entropy). First, we find that $\phi^* \to 0$ and thus

$$\phi_t^{eq} \approx \phi - \lim_{k_\sigma s\to\infty} \frac{1}{k_\sigma s} W\left(k_\sigma s e^{-k_\sigma s\left(\frac{\epsilon-\sigma_0 s}{k_\sigma s} - \phi\right)}\right) = \begin{cases} \phi & \phi < \frac{\epsilon-\sigma_0 s}{k_\sigma s} \\ \frac{\epsilon-\sigma_0 s}{k_\sigma s} & \phi > \frac{\epsilon-\sigma_0 s}{k_\sigma s} \end{cases} \tag{C.7}$$

This result is expected and could be understood as follows. At low protein surface fraction ($\phi < (\epsilon - \sigma_0 s)/k_\sigma s$), the energetic gain of protein aggregation onto a few established tubes (of size $p > E_{cap}/(\epsilon - \sigma_0 s)$) dominates over the work that is done by the

membrane tension against the per-protein extension of tubes ($\epsilon > \sigma s$). Since all added proteins are recruited to the tubes, we find that $\phi_t \simeq \phi$ in this limit (see Eq. (C.7) and Fig. C.1a). However, as the amount of tube-forming proteins is increased so does the folded area ($S_t = A\phi_t$), which increases the membrane tension in accordance with our underlying assumption, Eq. (C.1). When this tension balances out the protein aggregation energy (i.e. when $\sigma s \simeq \epsilon$, corresponding to $\phi_t \simeq (\epsilon - \sigma_0 s)/k_\sigma s$), any additional protein aggregation will not be energetically preferable (see Eq. (C.7) and Fig. C.1b). Thus, the equilibrated ϕ_t and the membrane tension σ tend to saturate as a function of ϕ. The transition between the regimes of maximal tubulation ($\phi_t = \phi$) and saturated tubulation ($\phi_t = (\epsilon - \sigma_0 s)/k_\sigma s$) is smoothed out when increasing the relative weight of entropy (decreasing $(\epsilon - \sigma_0 s)$ and $k_\sigma s$ proportionally), as that enhances the tendency to mix the distinguishable densities (isolated proteins and tubes of all sizes) at high protein concentration. At low protein concentration, the translational entropy favors isolated proteins over those clustered into large tubules. Thus, a decrease in $(\epsilon - \sigma_0 s)$ increases the critical density ϕ^* for the onset of tubulation. All of these effects can be inferred from Fig. C.2, where the black curves represent $\phi_t^{eq} = \phi_t(\Delta S_b = 0)$ using Eq. (C.5).

Using the numerical estimates of the parameters given in Table C.1, we find that the aggregation of proteins into membrane tubes can increase the cell membrane tension up to a maximal value $\epsilon/s \simeq 1 - 10$pN/nm, corresponding to the saturation regime. This is a high value which can exceed the membrane rupture tension. The saturation regime can be reached if the surface fraction of protein exceeds a value of order $\epsilon/(k_\sigma s)$, which can be as low as 10%. For lower composition, the system is in the regime of maximal tubulation, increasing the protein density by an amount $\Delta\phi$ leads to an increase of the membrane tension by $k_\sigma \Delta\phi$, which reach 1pN/nm for $\Delta\phi = 10\%$. We reiterate that these value should be considered as crude estimates due to the large uncertainty regarding the value of the effective stretching modulus k_σ. Nevertheless, they show the the effect of tube-forming proteins on the cell membrane tension can be highly physiologically significant.

The bleb state

The bleb expansion effectively increases the tension, Eq. (C.1), making the extension of tubes more costly. Therefore, we find that ϕ_t decreases as a function of ΔS_b (see orange curves in Fig. C.2). Specifically, the limit at which the tension balances out the aggregation energy ($\sigma s \simeq \epsilon$) corresponds to a lower saturation threshold for ϕ_t (see Figs. C.2a1,a2). The change in the total folded area, $\Delta S_t = A(\phi_t^{eq} - \phi_t)$, is the tube-flattened area that accounts for a fraction of ΔS_b (proportional to the orange vertical gaps in Fig. C.2). The remaining expansion area, $\Delta S_b - \Delta S_t = A\left(\frac{\Delta S_b}{A} + \phi_t - \phi_t^{eq}\right)$, is drawn from fluctuations (membrane stretching, proportional to the blue vertical gaps in Fig. C.2). Given $\phi > \phi^*$, we may approximate, to first order in ΔS_b, the tube-flattened area and the stretched area

$$\Delta S_t \approx -A \left.\frac{d\phi_t}{d\Delta S_b}\right|_{\Delta S_b=0} \Delta S_b = \frac{k_\sigma s \phi_1^{eq}}{k_\sigma s \phi_1^{eq} + 1} \Delta S_b, \qquad \Delta S_b - \Delta S_t \approx \frac{1}{k_\sigma s \phi_1^{eq} + 1} \Delta S_b$$

where $\phi_1^{eq} = \phi - \phi_t^{eq} \approx \frac{1}{k_\sigma s} W\left(k_\sigma s e^{-k_\sigma s\left(\frac{\epsilon - \sigma_0 s}{k_\sigma s} - \phi\right)}\right)$ is the surface fraction of isolated proteins at equilibrium. We find that there is a sharp transition in the mechanism of the

initial bleb expansion: from stretching out fluctuations to flattening the tubes (illustrated in Figs. C.1c,d). This transition occurs at $\phi \simeq \frac{\epsilon - \sigma_0 s}{k_\sigma s}$, the limit at which the protein surface fraction belonging to tubes ($\phi_{\rm t}^{\rm eq}$) and the membrane tension ($\sigma^{\rm eq} = \sigma_0 + k_\sigma \phi_{\rm t}^{\rm eq}$) saturate (see Eq. (C.7) and Fig. C.2a). As expected, an increase in the stiffness modulus k_σ, which increases the energetic cost of stretching out fluctuations, results in favoring the expansion via tube-flattening. The effect of increasing $(\epsilon - \sigma_0 s)$ is precisely the opposite, since a higher energetic gain for protein aggregation stabilizes the membrane tubules.

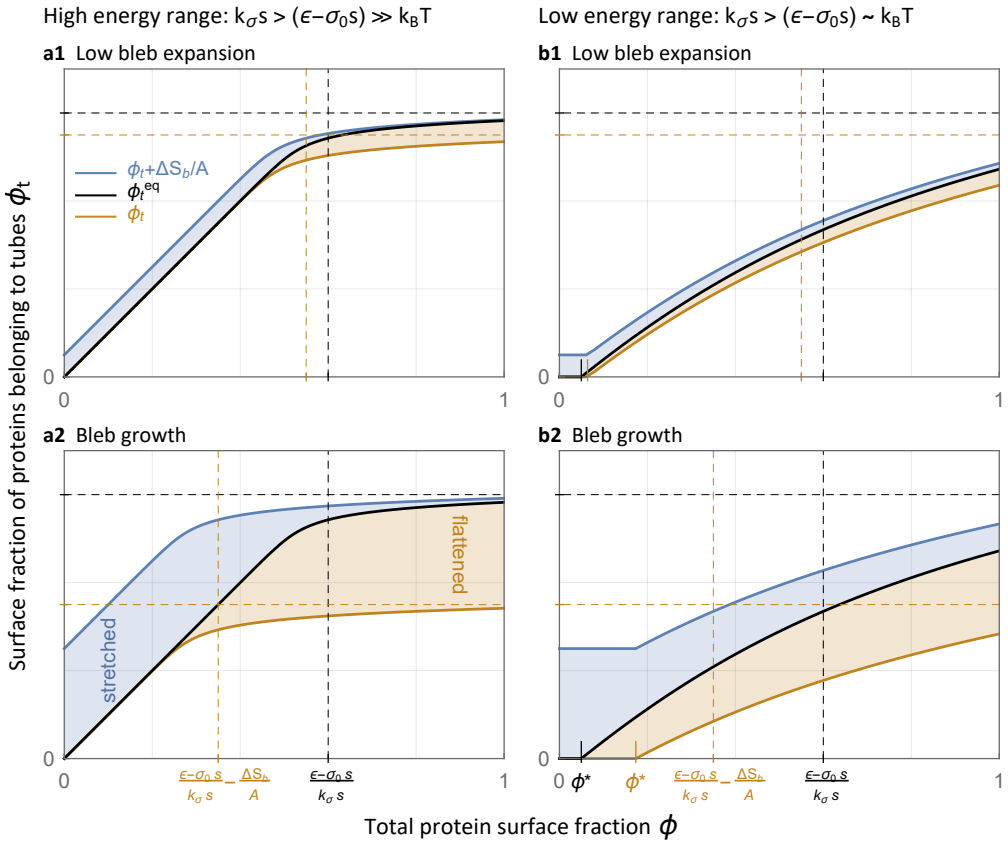

Fig. C.2 **Tubulation by curved proteins and the bleb-tubes-fluctuations area exchange.** *All plots are for $E_{cap} \gg 1$, as in Eqs. (C.5) – (C.6). In each plot, we present ϕ_t^{eq} (black line), ϕ_t in the bleb state (orange line), and $\phi_t + \Delta S_b/A$ (blue line, also proportional to the tension, $\sigma = \sigma_0 + k_\sigma(\phi_t + \Delta S_b/A)$) as functions of ϕ (see Eq. (C.5)). The vertical gap between the black and orange curves (light-orange region) is proportional to the tube-flattened area, and the vertical gap between the blue and black curves (light-blue region) is proportional to the stretched area (seized from membrane fluctuations). The dependence on $(\epsilon - \sigma_0 s)$ and on $k_\sigma s$ is indicated by the dashed grid-lines (saturation limits), and the ticks that mark the critical density for tubulation, ϕ^* (Eq. (C.6)), at equilibrium (black), and in the bleb state (orange). The entropic effects that arise from increasing the temperature (or decreasing all energy parameters proportionally) can be inferred from the different plots. In plots (a1) and (a2), the entropic effects are negligible since $(\epsilon - \sigma_0 s) \gg 1$ (specifically, $(\epsilon - \sigma_0 s) = 30$ and $k_\sigma s = 50$, well within our estimations in Table C.1). In plots (b1) and (b2), where $(\epsilon - \sigma_0 s) \sim 1$ (specifically, $(\epsilon - \sigma_0 s) = 3$ and $k_\sigma s = 5$), one may notice a finite critical density for tubulation, $\phi^* > 0$, as well as a smoother transition into saturation. The dependence on bleb growth can be inferred from plots (a2) and (b2), where $\Delta S_b/A$ is increased to 25% from 5% in plots (a1) and (b1).*

C.5.2 The bleb nucleation energy

In this section, we first present the complete energy of a bleb that bulges out from the equilibrium state (folded membrane adhered to the cortex, see Figs. C.1a,b). We then use this expression to derive the energy barrier that limits the nucleation of blebs.

A compelling depiction of bleb formation as a nucleation process was first suggested in Charras et al (2008). In their treatment, Charras et al. began by minimizing the bleb energy with respect to curvature — ensuring normal force-balance on the detached membrane (the Young-Laplace condition). They then found that the minimized bleb energy exhibits a non-monotonic dependency on the cortex-detached area: the energy first increases with the membrane detachment and beyond some critical size it decreases, making it energetically preferable to form the macroscopic bleb. The maximal energy which corresponds to the critical detachment is thus interpreted as the energetic barrier for bleb nucleation. Here, we extend this fundamental description by coupling it directly to the total free energy associated with the membrane tubes and the curving proteins, Eq. (C.2).

The total energy difference between the bleb state and the equilibrium (pre-bleb) state is given by

$$E_{\mathrm{b}} = -PV_{\mathrm{b}} + JS_{\mathrm{b}} + \Delta F_{\mathrm{t}} \tag{C.8}$$

where P is the hydrostatic pressure driven by actomyosin contractility, V_{b} is the inflated bleb volume, J is the membrane-cortex adhesion strength, S_{b} is the cortex-detached area (the base of the bleb, see Fig. C.1), and ΔF_{t} is the difference in the free energy of the membrane and the curved proteins that results from the bleb expansion. It is calculated from the variation of the free energy F_{t} in Eq. (C.2) upon variation of the bleb expansion area from zero to ΔS_{b}. We assume that the tubular proteins equilibrate fast compared to the dynamics of bleb expansion, so that the densities ρ_1 and ρ_p are given by Eq. (C.3). As we are interested in bleb nucleation, we consider the shallow bleb limit ($u^2/S_{\mathrm{b}} \ll 1$, where u is the maximal height of the bleb, see Figs. C.1), for which $\Delta S_{\mathrm{b}} \simeq \pi u^2$ and $V_{\mathrm{b}} \simeq S_{\mathrm{b}} u/2$. Assuming $S_{\mathrm{b}} > K_{\mathrm{c}}/\sigma$ (where K_{c} is the bending rigidity), we neglected in Eq. (C.8) the bending energy induced by the bleb deformation. Lastly, assuming that the change in tension is negligible during the nucleation stage of the bleb, we will also neglect contributions to ΔF_{t} that are quadratic in ΔS_{b} (quartic in u).

For a given ΔS_{b}, the minimized F_{t} can be expressed in terms of $\phi_1, \phi_{\mathrm{t}}$ (see Supplementary Eq. (C.22)). As shown in SI, we use this expression to derive

$$\left.\frac{dF_{\mathrm{t}}}{d\Delta S_{\mathrm{b}}}\right|_{\Delta S_{\mathrm{b}}=0} \approx \begin{cases} \sigma_0 & \phi < \phi^* \\ \sigma_0 + k_\sigma \phi_{\mathrm{t}}^{\mathrm{eq}} & \phi > \phi^* \end{cases} = \sigma^{\mathrm{eq}} \tag{C.9}$$

This result entails important physical meaning regarding the stress-strain relationship of the cell membrane. In the regime of low protein surface fraction (meaning $\phi < (\epsilon - \sigma_0 s)/k_\sigma s$), the free-energy cost of bleb expansion increases with ϕ ($\Delta F_{\mathrm{t}} \simeq \sigma^{\mathrm{eq}} \Delta S_{\mathrm{b}} = (\sigma_0 + k_\sigma \phi)\Delta S_{\mathrm{b}}$). This is because the tubulating proteins effectively stiffen the membrane tension, which then works against the initial bleb expansion. In the regime of high protein surface fraction ($\phi > (\epsilon - \sigma_0 s)/k_\sigma s$), the cost of bleb expansion is given by $\Delta F_{\mathrm{t}} \simeq (\epsilon/s)\Delta S_{\mathrm{b}}$. In essence, this cost is attributed to unfolding the tubes (dispersing $\Delta S_{\mathrm{b}}/s$

proteins from tubular aggregates at the cost of ϵ per-protein). In other words, Eq. (C.9) concisely accounts for the transition between the two possible expansion mechanisms.

Substituting $\Delta F_{\mathrm{t}} = \sigma^{\mathrm{eq}} \Delta S_{\mathrm{b}}$ back in Eq. (C.8)

$$E_{\mathrm{b}} = -PS_{\mathrm{b}}u/2 + JS_{\mathrm{b}} + \sigma^{\mathrm{eq}}\pi u^2$$

Following Charras et al (2008), we proceed by minimizing E_{b} with respect to the bleb height u (assuming that the detached area S_{b} is the slowest variable). It follows that $u = \frac{PS_{\mathrm{b}}}{4\pi\sigma^{\mathrm{eq}}}$ and $E_{\mathrm{b}} = -\frac{P^2 S_{\mathrm{b}}^2}{16\pi\sigma^{\mathrm{eq}}} + JS_{\mathrm{b}}$. The u-minimized bleb energy has a maximum at $S_{\mathrm{b}}^{\mathrm{nuc}} = 8\pi\sigma^{\mathrm{eq}} J/P^2$. This maximum corresponds to an energy barrier which we call the bleb nucleation energy

$$E_{\mathrm{b}}^{\mathrm{nuc}} = 4\pi\sigma^{\mathrm{eq}} J^2/P^2 \tag{C.10}$$

Note that $u^{\mathrm{nuc}} = 2J/P$ and $\Delta S_{\mathrm{b}}^{\mathrm{nuc}} = 4\pi J^2/P^2$ are the bleb height and the bleb expansion area at the nucleation point. The result given in Eq. (C.10) is valid so long as our simplifying assumptions (shallow deformation, negligible bending energy of the bleb, and negligible change in tension) are met throughout the nucleation stage (see range of validity in SI).

Large bleb expansion might eventually lead to the complete flattening of all tubes, if ΔS_{b} is so large that $\phi < \phi^*(\Delta S_{\mathrm{b}})$ (see Eq. (C.6)). We assume that this limit is not reached during the nucleation stage, which is valid provided that:

$$\Delta S_{\mathrm{b}}^{\mathrm{nuc}} < \Delta S_{\mathrm{b}}^{*} \equiv A\frac{\log\phi + \epsilon - \sigma_0 s}{k_\sigma s} \quad \rightarrow J < PR_{\mathrm{cell}}\sqrt{\frac{\log\phi + \epsilon - \sigma_0 s}{k_\sigma s}} \tag{C.11}$$

where here we considered that the area A is roughly $4\pi R_{\mathrm{cell}}^2$.

C.5.3 Model vs Experiments

In this section, we discuss the relevance of our theory to the experiments. First, we infer which is the theoretical regime that bares the most qualitative resemblance to our previous observations. Second, we use the model to predict the consequences of performing two competing manipulations sequentially. We then verify this prediction in new *in-vivo* experiments.

Comparison with previous observations

Let us first recall two major findings from our previous experimental study Goudarzi et al (2017), namely that the folded area held in tubes increases with N-BAR expression, and that the blebbing frequency decreases with N-BAR expression. These observed responses are supported theoretically by the model if both $S_{\mathrm{t}}^{\mathrm{eq}}$ (the equilibrium folded area) and $E_{\mathrm{b}}^{\mathrm{nuc}}$ (the bleb nucleation energy) are increasing functions of the total protein density. Since $S_{\mathrm{t}}^{\mathrm{eq}} = A\phi_{\mathrm{t}}^{\mathrm{eq}}$ and $E_{\mathrm{b}}^{\mathrm{nuc}} = \frac{4\pi J^2}{P^2}(\sigma_0 + k_\sigma \phi_{\mathrm{t}}^{\mathrm{eq}})$, these two requirements are met so long as $\phi_{\mathrm{t}}^{\mathrm{eq}}$ is not saturated as a function of ϕ (see black curves in Fig. C.2). Assuming that entropic effects are negligible (that is, $(\epsilon - \sigma_0 s) \gg 1$ and $k_\sigma s \gg 1$), this condition corresponds to $\phi < (\epsilon - \sigma_0 s)/k_\sigma s$. We thus infer that PGCs naturally express relatively low levels of tube-forming proteins. This regime seems favorable from an evolutionary standpoint

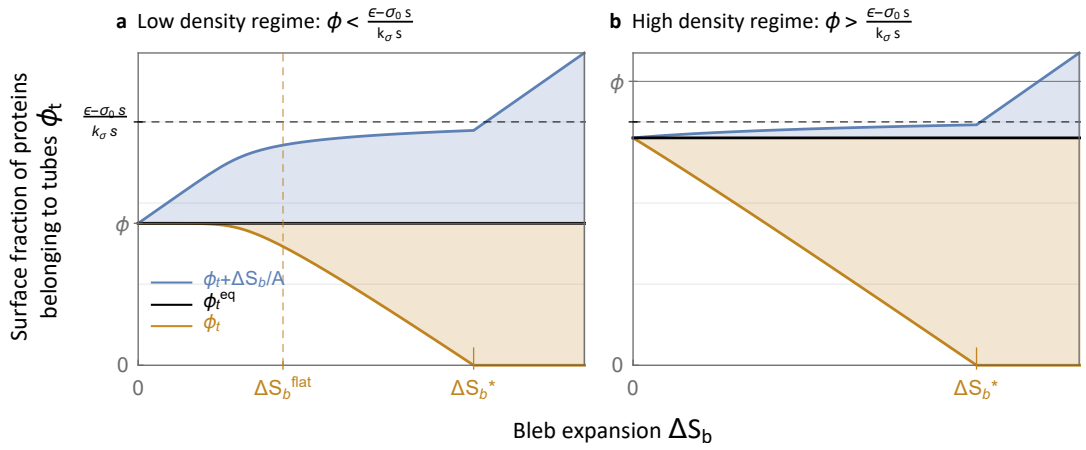

Fig. C.3 **Area exchange during bleb expansion.** *In each plot, we present* ϕ_t^{eq} *(black line),* ϕ_t *in the bleb state (orange line), and* $\phi_t + \Delta S_b/A$ *(blue line, also proportional to the tension,* $\sigma = \sigma_0 + k_\sigma(\phi_t + \Delta S_b/A)$*) as functions of* ΔS_b *(see Eq. (C.5)). The vertical gap between the black and orange curves (light-orange region) is proportional to the tube-flattened area, and the vertical gap between the blue and black curves (light-blue region) is proportional to the stretched area (seized from membrane fluctuations). The dependence on parameters is indicated by the black dashed grid-line (saturation limit of tubulation), the orange dashed grid-line (*ΔS_b^{flat}*, given in Eq. (C.12), beyond which the bleb expansion induces tube-flattening), the horizontal gray line (marking the total protein surface fraction* ϕ*), and the orange tick which marks the critical bleb expansion,* ΔS_b^**, Eq. (C.11), beyond which* $\phi_t \simeq 0$*. We vary the protein surface fraction* ϕ*, such that the equilibrium tubulation is maximal in plot (a) (*$\phi_t^{eq} \simeq \phi$*), and saturated in plot (b) (*$\phi_t^{eq} \simeq (\epsilon - \sigma_0 s)/k_\sigma s$*). We set* $(\epsilon - \sigma_0 s) = 30$ *and* $k_\sigma s = 50$ *as in Fig. C.2a1,a2.*

as it allows for PGCs to regulate their blebbing activity (and consequent motility) by modulating their N-BAR expression.

In the low ϕ regime, our model attributes at least a part of the initial bleb expansion to membrane stretching (seizing area from membrane fluctuations rather than from stabilized tubes, see Figs. C.2a1,a2 and Fig. C.1c). That being said, our experiments have suggested that bleb growth is concomitant with the local flattening of the membrane tubes Goudarzi et al (2017). Yet, since the blebs form very rapidly, and the spatio-temporal resolution of our imaging is limited, one cannot conclude from these observations that the mere onset of the bleb must rely strictly on tube-flattening. Our model suggests that, even if the bleb expands purely via stretching throughout the initial nucleation stage, it should enter a tube-flattening mode very quickly after nucleation. This is because the tension increases with bleb expansion (see Eq. (C.1)), and when $\sigma s \simeq \epsilon$ it becomes energetically preferable to draw area from the tubular reservoir. Tube flattening is triggered by bleb expansion when the expansion area reaches:

$$\Delta S_{\rm b} \approx \Delta S_{\rm b}^{\rm flat} \equiv A\left(\frac{\epsilon - \sigma_0 s}{k_\sigma s} - \phi\right) \simeq 4\pi R_{\rm cell}^2\left(\frac{\epsilon - \sigma_0 s}{k_\sigma s} - \phi\right) \tag{C.12}$$

Note that our assumption is $\Delta S_{\mathrm{b}}^{\mathrm{nuc}} < \Delta S_{\mathrm{b}}^{\mathrm{flat}}$, which translates into $J < PR_{\mathrm{cell}}\sqrt{\frac{\epsilon-\sigma_0 s}{k_\sigma s} - \phi}$.

For high protein surface fraction, $\phi > (\epsilon - \sigma_0 s)/k_\sigma s$, our model predicts that the expansion via tube-flattening (rather than stretching fluctuations) will ensue immediately following membrane-cortex detachment (see Fig. C.3b and Fig. C.1d). Thus, the very inception of the bleb would necessarily correlate with the flattening of membrane tubes. As discussed above, this regime cannot corresponds to the WT experimental case, because it is inconsistent with the fact that N-BAR over-expression increases the number of tubes and the membrane tension. Nonetheless, cells with over-expressed N-BAR may be in this regime.

Prediction and new supporting experiments

For all parameter regimes, the minimized bleb energy has a maximum as a function of S_{b}. This maximum corresponds to a finite bleb nucleation energy, $E_{\mathrm{b}}^{\mathrm{nuc}}$ (given in Eq. (C.10)), which tends to saturate as a function of ϕ, but is always proportional to $1/P^2$. In other words, the stabilizing effect of the tubulating proteins is limited while the destabilizing effect of the hydrostatic pressure is not. We may conclude then, that regardless of ϕ, one can continuously increase the probability of bleb formation (proportional to $e^{-E_{\mathrm{b}}^{\mathrm{nuc}}}$), by gradually increasing P (see Fig. C.4a).

To test this prediction, we conducted a complementary study using Zebrasfish PGCs as an *in-vivo* model. The experimental methods are similar to those reported in Goudarzi et al (2017), see SI for details. In these new experiments, we first inhibited the blebbing activity by over-expressing the N-BAR domain of Amphiphysin (Amph-N-BAR) specifically in the PGCs. We then expressed in these embryos varying concentrations of CA-MLCK (constitutively active myosin light-chain kinase), the enzyme which enhances myosin II contraction. Since the myosin contraction is known to increase the hydrostatic pressure, we expected to first rescue blebbing, and then to increase the blebbing frequency as a function of the CA-MLCK concentration. Indeed, although we were not able to measure the pressure directly, our results show the expected trend (see Fig. C.4b). Following this manipulation, the blebbing frequency of cells overexpressing Amph-N-BAR recovered to WT levels. Furthermore, by overexpressing the CA-MLCK protein, we were able to increase the blebbing activity beyond that observed in wild-type cells, which is also qualitatively consistent with the model. The recovery of blebbing in Amph-N-BAR PGCs by CA-MLCK overexpression is demonstrated in Fig. C.4c and Movie C.1. Here, two PGCs expressing elevated levels of Amph-N-BAR are presented (Yellow label). One of the PGCs was engineered to express CA-MLCK (cell expressing mCherry in its nucleus) and this cell produces blebs (marked by asterisks).

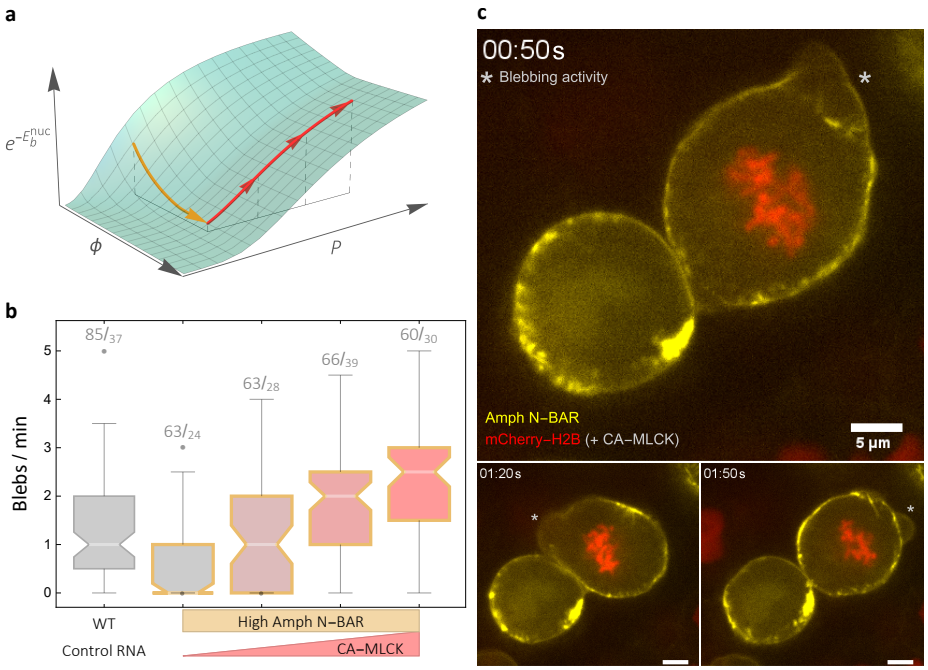

Fig. C.4 **Blebbing recovery in Amph N-BAR PGCs through CA-MLCK expression.** *(a) Plot of the theoretical probability of bleb formation, proportional to* $e^{-E_b^{nuc}}$*, as a function of the protein surface fraction* ϕ *and the hydrostatic pressure* P *(see Eq. (C.10)). The arrows indicate the qualitative direction of the theoretically-motivated manipulations. (b) Box-whisker plot (with outliers) summarizing the in-vivo blebbing frequency of WT and manipulated PGCs. White lines denote medians (with notched confidence interval) and each box extends from the 25% to the 75% quantile. Boxes with orange edges indicate datasets of cells expressing 250pg of N-BAR domain of Amphiphysin (Amph-N-BAR), and the red-level fillings indicates the increasing levels of CA-MLCK (from 0 to 40pg). Numbers indicate the number of cells quantified over the number of manipulated embryos. (c) Snapshots from Movie C.1, showing a mosaic of cells that are overexpressing N-BAR (yellow). In contrast to the stable cell on the left, the blebbing cell on the right also expresses CA-MLCK. Blebbing activity is marked with asterisks and the nuclear marker (mCherry-H2B) was used to tag cells that co-express both N-BAR and CA-MLCK.*

C.6 Discussion

Our derivation of $E_{\mathrm{b}}^{\mathrm{nuc}}$ (see Eq. (C.10)) shows how the bleb initiation probability scales with physical parameters including the intracellular hydrostatic pressure (driven by actomyosin contractility), the membrane-cortex adhesion strength, and the fluctuations-driven membrane tension Charras et al (2008). We claim that bleb nucleation is controlled by the curved membrane proteins (N-BAR domains) through their capacity to control membrane tension by sequestering membrane area into tubular invaginations. Although a quantitative comparison with experiments remains limited, mostly due to the lack of precise independent measurements of our model parameters for this cell type, our theoretical results do provide a qualitative explanation of the observed responses of PGCs to manipulations in the level of the N-BAR domain of Amphiphysin and in the activity of the MLCK enzyme that induces actomyosin contraction. Indeed, increasing MLCK activity in wildtype somatic cells that do not normally bleb led to bleb formation in these cells Goudarzi et al (2012). It would thus be interesting to examine this option in different cell types, at different steps such as at the initiation of migration, during migration and at the stage when the cells stop migration.

For simplicity, we have discarded possible couplings between the membrane-cortex adhesion strength, J, the density of the curved proteins, ϕ/s, and their aggregation energy, ϵ. However, a complex co-dependence between these factors is likely to arise since the tubes were observed to penetrate the cortex. Moreover, we found experimentally that tube-flattening was mostly confined to the cortex-detached region of the expanding bleb (that is, tubes in distant parts of the membrane remained intact). This phenomenon could result from a possible stabilization of membrane tubes over the cortex-bound membrane through their interaction with cytoskeleton components. This could be taken into account in the model by assigning a larger value of the energy ϵ for tubes embedded in the cortex. Another possibility is that the increase of membrane tension following bleb expansion fails to propagate over the entire cell membrane due to friction with the cytoskeleton, as was recently observed in HeLa cells Shi et al (2018). Such dynamical effects may be crudely accounted for in our equilibrium theory through the area A over which the tension is assumed to be uniform. If tension equilibrates fast compared to bleb expansion, A is the total cell area, as was assumed in Eqs. (C.11) and (C.12). If friction over the cytoskeleton effectively prevents tension equilibration away from the growing bleb, A is equivalent to the cortex-detached area S_{b}. The only relevant parameters that depends on this area are the tension increase during bleb expansion: $\Delta\sigma_{\mathrm{bleb}} = k_\sigma \frac{\Delta S_{\mathrm{b}}}{A}$ (see Eq. (C.1)), and the total area stored in tubes $S_{\mathrm{t}} = A\phi$. Restricting tension propagation to the cortex-detached bleb membrane thus has two consequences; the bleb membrane tension increases much faster during bleb expansion and is more likely to reach the threshold tension at which tubes flatten, and tube flattening is restricted to the bleb membrane. Both consequences are in agreement with our observations.

Due to the fairly high uncertainty of the parameter values, precise quantitative predictions are beyond the scope of our model. We may nevertheless propose a realistic scenario based on our experimental evidence. In the context of our model, the inhibitory effect of N-BAR over-expression on bleb formation is evidence that WT PGCs are in the maximal tubulation regime, Fig. C.1a. Membrane tension is thus below a threshold set by the affinity of N-BAR proteins to tubular structures and the protein size: $\sigma_{\mathrm{WT}} < \frac{\epsilon}{s} \sim 1\mathrm{pN/nm}$

(with $\epsilon = 10 k_B T$ and $s = 50 nm^2$, see Table C.1). In this regime, increasing the protein density by an amount $\Delta\phi$ leads to a relative increase of tension $\frac{\Delta\sigma}{\sigma} = \frac{k_\sigma}{\sigma}\Delta\phi$. Since N-BAR over-expression strongly decreases the blebbing rate, we may expect that it leads to a large variation of the bleb nucleation energy (Eq. (C.10)) $\frac{\Delta E_b^{nuc}}{E_b^{nuc}} = \frac{\Delta\sigma}{\sigma} \sim 1$. As we don't expect the protein surface fraction to be much larger than $\Delta\phi \sim 0.1$, this requires that k_σ is one order of magnitude larger than σ, which is consistent with our estimates (Table C.1). We have shown that increasing acto-myosin contractility can compensate the effect of N-BAR over-expression on blebbing. According to Eq. (C.10), this requires that $\frac{\Delta P}{P} \sim \frac{\Delta\sigma}{2\sigma} \sim \frac{1}{2}$. An increase of contractility by 50% is indeed a reasonable outcome of CA-MLCK over-expression.

C.7 Conclusion

Together, we have presented a comprehensive coarse-grained theory of bleb initiation and membrane tubulation by curved proteins, such as N-BAR domains. In this theory, the tubes control the rate of bleb formation by increasing the cell membrane tension. When the blebbing rate is sensitive to N-BAR expression, as in the case of WT PGCs, we infer from our model that the membrane reservoir contained in the tubes remains mostly folded during the nucleation stage of the bleb. We propose that the flattening of tubes is prompted when the energetic cost of stretching out fluctuations exceeds the free-energy cost of dispersing the dense protein scaffolds that form the tubes. This unfolding mode is likely triggered at a later stage of bleb growth, since the bleb expansion itself also increases the membrane tension. The results obtained in our description of the tubes at rest (that is, without a bleb) shed light on a more generic regulatory role for the curved membrane proteins. We suggest that these proteins significantly impact the tension by folding the cell membrane, and could thus influence any cellular process in which membrane mechanics plays an important role. The relevance of our findings is thus particularly broad, as membrane tension is increasingly being regarded as a master regulator of important cellular process such as cell motility Keren (2011); Sens and Plastino (2015); Diz-Muñoz et al (2013) and cell spreading Raucher and Sheetz (2000); Gauthier et al (2011).

C.8 Supporting Information

Minimization of F_t

We derive main Eq. (C.2) with respect to the densities of isolated proteins and tubes

$$\partial_{\rho_1} F_t = A\left(\log \rho_1 s + \mu\right) + \partial_{\rho_1} I_\sigma, \qquad \partial_{\rho_p} F_t = A\left(\log \rho_p s + E_{cap} - \epsilon p + \mu p\right) + \partial_{\rho_p} I_\sigma \quad \text{(C.13)}$$

where I_σ denotes the tension integral in Eq. (C.2):

$$I_\sigma = \int_0^{S_t + \Delta S_b} \left(\sigma_0 + k_\sigma \frac{S}{A}\right) dS = \sigma_0 \left(S_t + \Delta S_b\right) + k_\sigma \frac{\left(S_t + \Delta S_b\right)^2}{2A}$$

Since $S_t = A \sum_{p \geq p_c} \rho_p p s$, we find that:

$$\partial_{\rho_1} I_\sigma = 0, \qquad \partial_{\rho_p} I_\sigma = \left(\sigma_0 + k_\sigma \frac{S_t + \Delta S_b}{A}\right) A p s = A \sigma p s \quad \text{(C.14)}$$

where we used Eq. (C.1).

We obtain Eq. (C.3) by inserting Eq. (C.14) back in Eq. (C.13) and solving $0 = \partial_{\rho_1} F_\mathrm{t}$, $0 = \partial_{\rho_p} F_\mathrm{t}$.

High E_cap limit

We begin by restating main Eq. (C.4): the conservation of the total protein number

$$\phi = \phi_1 + \phi_\mathrm{t} = e^{-\mu} + e^{-E_\mathrm{cap}} \frac{e^{(1-p_\mathrm{c})(-\epsilon+\sigma s+\mu)} \left(1 + (e^{-\epsilon+\sigma s+\mu} - 1)p_\mathrm{c}\right)}{\left(e^{-\epsilon+\sigma s+\mu} - 1\right)^2}$$

where $\sigma = \sigma_0 + k_\sigma \left(\phi - e^{-\mu}\right) + k_\sigma \Delta S_\mathrm{b}/A$.

In the limit $E_\mathrm{cap} \gg 1$, the total protein surface fraction is dominated either by the fraction of isolated proteins ($\phi \simeq \phi_1$) or the fraction of proteins in tubes ($\phi \simeq \phi_\mathrm{t}$). In these asymptotic limits, we obtain

$$\begin{aligned} \mu_{\phi\simeq\phi_1} &= -\log\phi \\ \mu_{\phi\simeq\phi_\mathrm{t}} &= \epsilon - \sigma_0 s - k_\sigma s \Delta S_\mathrm{b}/A - k_\sigma s\phi + \log x_{p_\mathrm{c}} \\ &\quad + W\left(k_\sigma s\, x_{p_\mathrm{c}}^{-1} e^{-\epsilon+\sigma_0 s+k_\sigma s\Delta S_\mathrm{b}/A+k_\sigma s\phi}\right) \end{aligned} \tag{C.15}$$

where x_{p_c} is the largest real root of

$$f_{p_\mathrm{c}}(x) = p_\mathrm{c} - 1 - p_\mathrm{c} x + \phi e^{E_\mathrm{cap}} x^{p_\mathrm{c}-1}(1 - 2x + x^2) \tag{C.16}$$

The protein surface fraction belonging to tubes is then

$$\phi_\mathrm{t} = \phi - e^{-\mu} \simeq \begin{cases} 0 & \phi < \phi^* \\ \phi - \frac{1}{k_\sigma s} W\left(k_\sigma s\, x_{p_\mathrm{c}}^{-1} e^{-k_\sigma s\left(\frac{\epsilon-\sigma_0 s}{k_\sigma s} - \frac{\Delta S_\mathrm{b}}{A} - \phi\right)}\right) & \phi > \phi^* \end{cases} \tag{C.17}$$

where ϕ^* marks the crossover point between the two asymptotic limits, defined implicitly by $\mu_{\phi\simeq\phi_1} = \mu_{\phi\simeq\phi_\mathrm{t}}$.

We can infer from Eq. (C.16) that $x_{p_\mathrm{c}} \to 1$ when $\phi e^{E_\mathrm{cap}} \gg 1$. Substituting $x_{p_\mathrm{c}} = 1$ back in Eq. (C.15), we obtain the following approximation of the crossover point ϕ^*

$$\phi^* \simeq e^{-(\epsilon-\sigma_0 s-k_\sigma s\Delta S_\mathrm{b}/A)} \tag{C.18}$$

With E_cap being larger than ϵ in our estimation (Table C.1), it is clear that $\phi^* e^{E_\mathrm{cap}}$ can be quite large. Hence, for $\phi > \phi^*$ (the second asymptotic limit in Eq. (C.17)), we also infer that ϕe^{E_cap} is large enough to justify our approximation of $x_{p_\mathrm{c}} \approx 1$ and ϕ^*, Eq. (C.18). We present this reduced approximation in Eqs. (C.5) – (C.6) of the main text.

Note that, in the simple case $p_\mathrm{c} = 1$ we can derive x_1 and the corresponding ϕ^* analytically:

$$x_1 = \frac{1 + 2\phi^{E_\mathrm{cap}} + \sqrt{4\phi^{E_\mathrm{cap}} + 1}}{2\phi^{E_\mathrm{cap}}}, \quad \phi^* = e^{-(\epsilon-\sigma_0 s-k_\sigma s\Delta S_\mathrm{b}/A)} - e^{-(E_\mathrm{cap}+\epsilon-\sigma_0 s-k_\sigma s\Delta S_\mathrm{b}/A)/2}$$

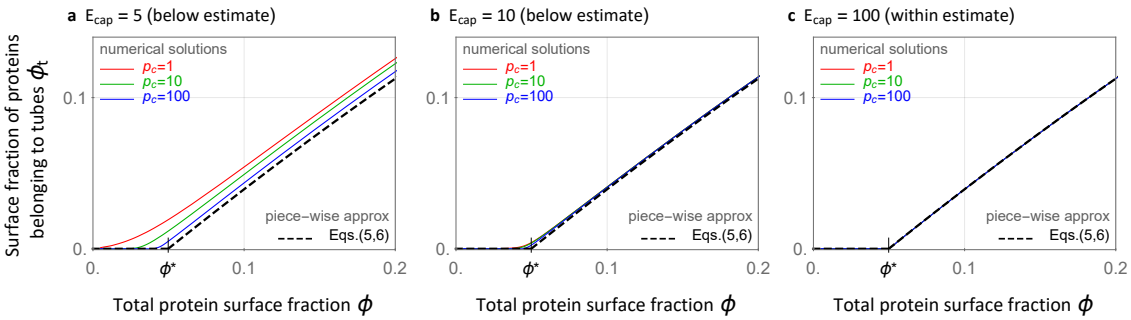

Fig. C.5 **Numerical solutions vs piecewise approximation (convergence at high E_{cap}).** *Colored plots mark numerical solutions for the protein surface fraction belonging to tubes, $\phi_t = \phi - e^{-\mu_N(\phi)}$, where $\mu_N(\phi)$ denotes the numerical solution to main Eq. (C.4) for the specified E_{cap} and p_c. Dashed black plot represents the explicit piecewise approximation (independent of E_{cap}, p_c) given in main Eq. (C.5), with ϕ^* denoting the critical protein surface fraction for the onset of tubulation, Eq. (C.6). In all plots, we set $(\epsilon - \sigma_0 s) = 3$ and $k_\sigma s = 5$, as in main Fig. C.2b1. Note the convergence to our explicit approximation as E_{cap} falls within the estimated range for this paramater (see Table C.1). Also note that when $(\epsilon - \sigma_0 s) \gg 1$ and thus $\phi^* \to 0$ (as in main Fig. C.2a1), the approximation is even more precise, i.e., numerical solutions directly fall behind Eq. (C.5).*

As expected, this result converges to $x_1 \to 1$ and Eq. (C.18) when $E_{\mathrm{cap}} \gg 1$.

To further test the validity of our explicit approximation, we contrast it in Fig. C.5 with direct numerical solutions of Eq. (C.4) at different values of E_{cap} and p_c. These plots consistently show convergence to our reduced piecewise approximation as we increase E_{cap}.

High temperature limit

For $\epsilon \to 0$, $\sigma_0 s \to 0$, $k_\sigma s \to 0$ and $E_{\mathrm{cap}} \to 0$ we find that Eq. (C.4) reduces to

$$\phi = e^{-\mu} + \frac{e^{(1-p_c)\mu}\left(1 + (e^{\mu} - 1)p_c\right)}{(e^{\mu} - 1)^2}$$

and thus $\mu = \log y_{p_c}$, where y_{p_c} is the largest real root of

$$g_{p_c}(y) = p_c - 1 - p_c y - y^{p_c - 2} + (2 + \phi) y^{p_c - 1} - (1 + 2\phi) y^{p_c} + \phi y^{p_c + 1}. \tag{C.19}$$

In Fig. C.6, we plot $\phi_t = \phi - e^{-\mu} = \phi - y_{p_c}^{-1}$ for different values of p_c. Here, ϕ_t is the surface fraction of proteins belonging to tubes that maximizes the entropy, $-A\left(\rho_1 \log \frac{\rho_1 s}{e} + \sum_{p \geq p_c} \rho_p \log \frac{\rho_p s}{e}\right)$, under the constraint of a fixed total number of membrane-bound proteins. For $p_c = 1$ (red line in Fig. C.6), we find that $\phi_t \geq \phi/2$ because tubes of size $p = 1$ already have the same entropic weight as that of isolated proteins. For $p_c > 1$, and given low ϕ, the translational entropy favors isolated proteins over those clustered in tubular aggregates. However, since the entropy dependence on ρ_1 and ρ_p is concave, entropy could be gained, at high ϕ, by converting p_c isolated proteins into a single tube

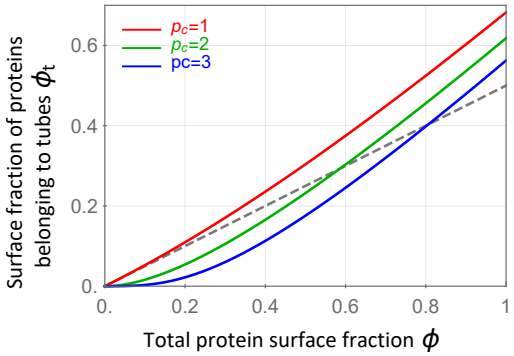

Fig. C.6 **High temperature limit (non-physical, entropy-driven tubulation).** *We plot the protein surface fraction belonging to tubes, $\phi_t = \phi - e^{-\mu} = \phi - y_{p_c}^{-1}$ (finding the roots of Eq. (C.19)), as a function of ϕ for different values of p_c. This calculation of ϕ_t maximizes the total translational entropy of isolated proteins and tubes while conserving the total number of membrane-bound proteins. Colored lines represent ϕ_t while the gray dashed line represents $\phi_t = \phi/2$ for reference.*

(a gain associated to mixing distinguishable densities). The larger p_c, the higher is the protein concentration required for such aggregation to increase the entropy (see green and blue lines in Fig. C.6). In our simplified model, such entropy-driven clustering also produces tubes. In effect, this is a non-physical result that follows from our assumption that all protein aggregates necessarily produce tubes, an assumption that should break down at the high T limit. We stress that in the main text we focus only on the physical regime in which tubulation is driven by ϵ (the binding/bending energy gained per curved protein recruited to a tube).

Simplifying the minimized free energy

Let us consider F_t, Eq. (C.2), minimized with respect to ρ_1, ρ_p (which are then given by Eq. (C.3))

$$\begin{aligned} F_t =& A\rho_1 \log\frac{\rho_1 s}{e} + A\sum_p \rho_p \left(\log\frac{\rho_p s}{e} + E_{cap}\right) + A\sum_p \rho_p p(-\epsilon + \sigma_0 s) + \sigma_0 \Delta S_b \\ &+ A\frac{k_\sigma}{2}\left(\sum_p \rho_p p s + \frac{\Delta S_b}{A}\right)^2 \end{aligned} \tag{C.20}$$

where we omitted the Lagrange multiplier term in Eq. (C.2), which does not contribute to the real free energy.

We prefer to express F_t in terms of the protein surface fractions ϕ_1, ϕ_t, which we already characterized as simpler explicit functions of ΔS_b in Eq. (C.5). Since $\phi_1 = \rho_1 s$ and $\phi_t = \sum_p \rho_p p s$, it is easy to find that Eq. (C.20) translates to

$$F_t = \frac{A}{s}\left(\phi_1 \log\frac{\phi_1}{e} + \sum_p \rho_p s \left(\log\frac{\rho_p s}{e} + E_{cap}\right) + (-\epsilon + \sigma_0 s)\phi_t + \sigma_0 s\frac{\Delta S_b}{A} + \frac{k_\sigma s}{2}\left(\phi_t + \frac{\Delta S_b}{A}\right)^2\right) \tag{C.21}$$

The remaining sum over ρ_p in Eq. (C.21) accounts for terms that contribute solely to the free energy of tubes (rather than the energy of proteins). We recall that ρ_p is given in Eq. (C.3) by $\rho_p = \frac{1}{s} e^{-E_{\rm cap}-(-\epsilon+\sigma s+\mu)p}$, and thus

$$\sum_p \rho_p s \left(\log \frac{\rho_p s}{e} + E_{\rm cap}\right) = \sum_p \rho_p s \left((\epsilon - \sigma s - \mu)p - 1\right) = (\epsilon - \sigma s - \mu)\phi_{\rm t} - \frac{e^{-E_{\rm cap}}}{e^{-\epsilon+\sigma s+\mu} - 1}$$

$$= (\epsilon - \sigma_0 s - k_\sigma s\,(\phi_{\rm t} + \Delta S_{\rm b}/A) + \log\phi_1)\phi_{\rm t} - \frac{\phi_1 e^{-E_{\rm cap}}}{e^{-\epsilon+\sigma_0 s+k_\sigma s(\phi_{\rm t}+\Delta S_{\rm b}/A)} - \phi_1}$$

where we substituted $\sigma = \sigma_0 + k_\sigma\,(\phi_{\rm t} + \Delta S_{\rm b}/A)$ and $\mu = -\log\phi_1$. Eq. (C.21) then amounts to

$$F_{\rm t} = \frac{A}{s}\left(\phi\log\phi_1 - \phi_1 + \sigma_0 s\frac{\Delta S_{\rm b}}{A} + \frac{k_\sigma s}{2}\left(\frac{\Delta S_{\rm b}^2}{A^2} - \phi_{\rm t}^2\right) - \frac{\phi_1 e^{-E_{\rm cap}}}{e^{-\epsilon+\sigma_0 s+k_\sigma s(\phi_{\rm t}+\Delta S_{\rm b}/A)} - \phi_1}\right) \tag{C.22}$$

Since $\phi_{\rm t} = \phi - \phi_1$, we calculate $dF_{\rm t}/d\Delta S_{\rm b}$ as follows

$$\frac{dF_{\rm t}}{d\Delta S_{\rm b}} = \frac{\partial F_{\rm t}}{\partial \Delta S_{\rm b}} + \left(\frac{\partial F_{\rm t}}{\partial \phi_1} - \frac{\partial F_{\rm t}}{\partial \phi_{\rm t}}\right)\frac{d\phi_1}{d\Delta S_{\rm b}} \tag{C.23}$$

where

$$\frac{\partial F_{\rm t}}{\partial \Delta S_{\rm b}} = \sigma_0 + k_\sigma\frac{\Delta S_{\rm b}}{A} + k_\sigma\phi_1\frac{e^{-E_{\rm cap}-\epsilon+\sigma_0 s+k_\sigma s(\phi_{\rm t}+\Delta S_{\rm b}/A)}}{\left(e^{-\epsilon+\sigma_0 s+k_\sigma s(\phi_{\rm t}+\Delta S_{\rm b}/A)} - \phi_1\right)^2} \tag{C.24}$$

$$\left(\frac{\partial F_{\rm t}}{\partial \phi_1} - \frac{\partial F_{\rm t}}{\partial \phi_{\rm t}}\right) = \frac{A}{s}(k_\sigma s\phi_1 + 1)\left(\frac{\phi_{\rm t}}{\phi_1} - \frac{e^{-E_{\rm cap}-\epsilon+\sigma_0 s+k_\sigma s(\phi_{\rm t}+\Delta S_{\rm b}/A)}}{\left(e^{-\epsilon+\sigma_0 s+k_\sigma s(\phi_{\rm t}+\Delta S_{\rm b}/A)} - \phi_1\right)^2}\right)$$

Recalling that $\phi_1 \simeq \phi$ for $\phi < \phi^*$, and $\phi_1 \simeq \frac{1}{k_\sigma s} W\left(k_\sigma s e^{-k_\sigma s\left(\frac{\epsilon-\sigma_0 s}{k_\sigma s} - \frac{\Delta S_{\rm b}}{A} - \phi\right)}\right)$ for $\phi > \phi^*$ (see Eq. (C.5)), we find

$$\frac{d\phi_1}{d\Delta S_{\rm b}} \approx \begin{cases} 0 & \phi < \phi^* \\ \frac{1}{A}\left(\frac{k_\sigma s\phi_1}{k_\sigma s\phi_1 + 1}\right) & \phi > \phi^* \end{cases} \tag{C.25}$$

Substituting Eqs. (C.24) – (C.25) in Eq. (C.23) yields

$$\frac{dF_{\rm t}}{d\Delta S_{\rm b}} \approx \begin{cases} \sigma_0 + k_\sigma\frac{\Delta S_{\rm b}}{A} + k_\sigma\phi\frac{e^{-E_{\rm cap}-\epsilon+\sigma_0 s+k_\sigma s\Delta S_{\rm b}/A}}{\left(e^{-\epsilon+\sigma_0 s+k_\sigma s\Delta S_{\rm b}/A} - \phi\right)^2} & \phi < \phi^* \\ \sigma_0 + k_\sigma\left(\phi_{\rm t} + \frac{\Delta S_{\rm b}}{A}\right) & \phi > \phi^* \end{cases},$$

$$\approx \begin{cases} \sigma_0 + k_\sigma\frac{\Delta S_{\rm b}}{A} & \phi < \phi^* \\ \sigma_0 + k_\sigma\left(\phi_{\rm t} + \frac{\Delta S_{\rm b}}{A}\right) & \phi > \phi^* \end{cases}$$

which, evaluated at $\Delta S_{\rm b} = 0$, gives

$$\left.\frac{dF_{\rm t}}{d\Delta S_{\rm b}}\right|_{\Delta S_{\rm b}=0} \approx \begin{cases} \sigma_0 & \phi < \phi^* \\ \sigma_0 + k_\sigma\phi_{\rm t}^{\rm eq} & \phi > \phi^* \end{cases} = \sigma^{\rm eq}$$

Defining the range of validity

We recall that in our formulation of the bleb energy, Eq. (C.8), we assumed the shallow bleb limit, negligible bending energy induced by the bleb, and negligible change in tension during the bleb's nucleation stage. Given our results for the nucleation point, $S_{\mathrm{b}}^{\mathrm{nuc}} = 8\pi\sigma^{\mathrm{eq}}J/P^2$ and $\Delta S_{\mathrm{b}}^{\mathrm{nuc}} = 4\pi J^2/P^2$, we find that these assumptions correspond to Eqs. (C.26), (C.27), and (C.28), respectively.

$$\frac{\Delta S_{\mathrm{b}}^{\mathrm{nuc}}}{S_{\mathrm{b}}^{\mathrm{nuc}}} \ll 1 \quad \rightarrow J \ll 2(\sigma_0 + k_\sigma \phi_{\mathrm{t}}^{\mathrm{eq}}) \tag{C.26}$$

$$S_{\mathrm{b}}^{\mathrm{nuc}} > \frac{K_{\mathrm{c}}}{\sigma^{\mathrm{eq}}} \quad \rightarrow J > \frac{K_{\mathrm{c}}P^2}{8\pi(\sigma_0 + k_\sigma \phi_{\mathrm{t}}^{\mathrm{eq}})^2} \tag{C.27}$$

$$k_\sigma \left(\frac{\Delta S_{\mathrm{b}}^{\mathrm{nuc}}}{A}\right)^2 \ll \sigma^{\mathrm{eq}} \quad \rightarrow J^4 \ll P^4 R_{\mathrm{cell}}^4 \left(\frac{\sigma_0}{k_\sigma} + \phi_{\mathrm{t}}^{\mathrm{eq}}\right) \tag{C.28}$$

where $\phi_{\mathrm{t}}^{\mathrm{eq}}$ is approximated in Eq. (C.7).

We stress that the range given in Eqs. (C.26) – (C.28) confers validity to the approximations used in the text to simplify the calculation of $E_{\mathrm{b}}^{\mathrm{nuc}}$, Eq. (C.10), but does not restrict the validity of our main conclusion. The contribution of the membrane bending energy is to disfavor small blebs, but it does not change the nucleation-and-growth nature of bleb formation. If tension increases in a sizable fashion during bleb growth, this could stall bleb formation for a particular bleb size in the absence of membrane tubes. In their presence, tension would increase only up to the value at which tubes flatten, and bleb nucleation would proceed under the conditions discussed in the main text.

Experimental Methods

Zebrafish work

Zebrafish (Danio rerio) of the AB background and transgenic fish carrying the Tg(kop:mCherry-f-UTRnanos3) expressing mCherry on the membrane of PGCs Meyen et al (2015) were used as the wild type. The fish were maintained on a 14-hour light/10-hour dark cycle, and fertilized eggs were collected and the embryos were raised at 25C, 28C or 32C in 0.3x Danieau's solution [17.4mM NaCl, 0.21mM KCl, 0.12mM MgSO4.7H2O, 0.18mM Ca(NO3)2, 1.5mM HEPES (pH 7.6)]. The embryos used were of early developmental stages prior to sex determination. The maintenance of the fish was done according to the regulations of the LANUV NRW and was supervised by the veterinarian office of the city of Muenster.

Spinning Disk (SD) microscopy

Embryos were imaged using Carl Zeiss Axio imager Z1 microscope equipped with Yokogawa CSU X.1 spinning disk unit. Samples were maintained at 28C using heated stage (PECON, TempController 2000-2). Imaging was performed using 63x NA=1.0 water immersion objective, Hamamatsu Orca flash 4.0 camera and Visitron Systems acquisition software (Visi-View2007-2011).

RNA Expression and bleb frequency measurement

mRNA was synthesized using the mMessage Machine kit (Ambion). RNAs were injected into the yolk of one-cell stage and then then into one of the eight blastomeres of the 8-cell stage embryos. Injection of Amph-n-bar-yfp mRNA at one-cell stage leads to the expression of Amph-N-BAR-YFP in all primordial germ cells (the mRNA will be degraded in somatic cells but will be preserved and translated in primordial germ cells due to the presence of the nanos 3' untranslated region Köprunner et al (2001)). Subsequent injection of the RNA into one cell at the 8-cell stage of the same embryos, resulted in the expression of RNAs encoding for CA-MLCK (0-10-20 and 40pg respectively) and mCherry-H2B in a sub population of PGCs. The experimental and control embryos were from same clutch of eggs (same parents). For the data presented in Fig.4b, Embryos from Tg(kop:mCherry-f-UTRnanos3) transgenic line were injected at one cell stage with 250pg of the Amph-n-bar-yfp mRNA and increasing amounts of mRNA encoding for CA-MLCK (0-10-20 and 40pg respectively).The PGCs were imaged in 18hpf embryos using a spinning disk microscope for 2 minutes, with 5 sec time intervals between time-points. Bleb frequency was measured manually using Fiji (ImageJ) software. The cell and embryo count from cumulative data of three independent experiments are as follow: WT (wildtype siblings: 85 cells from 37 embryos, 250pg Amph-n-bar-yfp mRNA (0pg Ca-mlck mRNA): 63 cells from 24 embryos, 250pg Amph-n-bar-yfp mRNA (10pg Ca-mlck mRNA): 63 cells from 28 embryos, 250pg Amph-n-bar-yfp mRNA (20pg Ca-mlck mRNA): 66 cells from 39 embryos, 250pg Amph-n-bar-yfp mRNA (40pg Ca-mlck mRNA): 60 cells from 30 embryos. For the Fig.4c and Movie C.1 embryos of AB background were injected with 250pg mRNA encoding got Amph-N-BAR-YFP at the one cell stage. At the 8 cells stage, one of the distal blastomeres was co-injected with 100pg of mRNA encoding for CA-MLCK and 50pg of mRNA encoding for mCherry-H2B Paksa et al (2016). The expression of mCherry-H2B in nuclei allowed the identification of cells that received also the ca-mlck mRNA. Imaging of the mosaic embryos was performed at 18hpf for 2minutes, with 5sec interval between the consecutive images.

Statistical visualization

Statistical test and visualization in Fig.4b was performed using the BoxWhiskerChart function in Mathematica (TM). Default options where used: in each box, the median is marked by the white horizontal line, notched edges extend the median confidence interval, box edges extend from the 25% quantile up to the 75% quantile, top and bottom fences extend the data range excluding outliers.

Movie Legend

Movie C.1. Video showing two manipulated PGCs in the Zebrafish embryo. The stabilized non-blebbing cell on the left expresses high levels of the Amph-N-BAR protein (yellow), and no added CA-MLCK. The unstable blebbing cell on the right, identified via a nuclear marker (mCherry-H2B in red), expresses the same level of the N-BAR protein and also the constitutively active MLCK protein (CA-MLCK). See Methods for more details.

Bibliography

Abercrombie M, Heaysman JE, Pegrum SM (1971) The locomotion of fibroblasts in culture: Iv. electron microscopy of the leading lamella. Experimental cell research 67(2):359–367 6

Adam J, Basnet N, Mizuno N (2015) Structural insights into the cooperative remodeling of membranes by amphiphysin/bin1. Scientific reports 5:15,452 124

Alberts B, Bray D, Lewis J, Raff M, Roberts K, Watson J (2002) Molecular Biology of the Cell, 4th edn. Garland 2, 3, 4

Albrecht-Buehler G (1982) Does blebbing reveal the convulsive flow of liquid and solutes through the cytoplasmic meshwork? In: Cold Spring Harbor symposia on quantitative biology, Cold Spring Harbor Laboratory Press, vol 46, pp 45–49 120

Alert R, Casademunt J (2016) Bleb nucleation through membrane peeling. Physical review letters 116(6):068,101 120

Álvarez-Lacalle E, Ortín J, Casademunt J (2004) Nonlinear saffman-taylor instability. Physical review letters 92(5):054,501 49

Alvarez-Lacalle E, Casademunt J, Eggers J (2009) Pinch-off singularities in rotating hele-shaw flows at high viscosity contrast. Physical Review E 80(5):056,306 93, 96

Ananthakrishnan R, Ehrlicher A (2007) The forces behind cell movement. International journal of biological sciences 3(5):303 6, 7

Arkhipov A, Yin Y, Schulten K (2009) Membrane-bending mechanism of amphiphysin n-bar domains. Biophysical journal 97(10):2727–2735 123

Ayton GS, Blood PD, Voth GA (2007) Membrane remodeling from n-bar domain interactions: insights from multi-scale simulation. Biophysical journal 92(10):3595–3602 123

Ayton GS, Lyman E, Krishna V, Swenson RD, Mim C, Unger VM, Voth GA (2009) New insights into bar domain-induced membrane remodeling. Biophysical journal 97(6):1616–1625 123

Balzer EM, Tong Z, Paul CD, Hung WC, Stroka KM, Boggs AE, Martin SS, Konstantopoulos K (2012) Physical confinement alters tumor cell adhesion and migration phenotypes. The FASEB Journal 26(10):4045–4056 10

Barton LJ, LeBlanc MG, Lehmann R (2016) Finding their way: themes in germ cell migration. Current opinion in cell biology 42:128–137 120

Baumgart T, Capraro BR, Zhu C, Das SL (2011) Thermodynamics and mechanics of membrane curvature generation and sensing by proteins and lipids. Annual review of physical chemistry 62:483–506 120

Bensimon D, Kadanoff LP, Liang S, Shraiman BI, Tang C (1986) Viscous flows in two dimensions. Reviews of Modern Physics 58(4):977 17, 18, 53

Bergert M, Chandradoss SD, Desai RA, Paluch E (2012) Cell mechanics control rapid transitions between blebs and lamellipodia during migration. Proceedings of the National Academy of Sciences 109(36):14,434–14,439 10

Bergert M, Erzberger A, Desai RA, Aspalter IM, Oates AC, Charras G, Salbreux G, Paluch EK (2015) Force transmission during adhesion-independent migration. Nature cell biology 17(4):524 9, 10, 50

Betapudi V (2014) Life without double-headed non-muscle myosin ii motor proteins. Frontiers in chemistry 2:45 4

Bhatia VK, Madsen KL, Bolinger PY, Kunding A, Hedegård P, Gether U, Stamou D (2009) Amphipathic motifs in bar domains are essential for membrane curvature sensing. The EMBO journal 28(21):3303–3314 120

Bibbo M, Wilbur D (2014) Comprehensive Cytopathology E-Book. Elsevier Health Sciences 2

Blanch-Mercader C, Casademunt J (2013) Spontaneous motility of actin lamellar fragments. Physical review letters 110(7):078,102 10, 17, 18, 19, 24, 97

Blanchoin L, Boujemaa-Paterski R, Sykes C, Plastino J (2014) Actin dynamics, architecture, and mechanics in cell motility. Physiological reviews 94(1):235–263 3

Blaser H, Reichman-Fried M, Castanon I, Dumstrei K, Marlow FL, Kawakami K, Solnica-Krezel L, Heisenberg CP, Raz E (2006) Migration of zebrafish primordial germ cells: a role for myosin contraction and cytoplasmic flow. Developmental cell 11(5):613–627 120

Blood PD, Voth GA (2006) Direct observation of bin/amphiphysin/rvs (bar) domain-induced membrane curvature by means of molecular dynamics simulations. Proceedings of the National Academy of Sciences 103(41):15,068–15,072 123

Bottino DC, Fauci LJ (1998) A computational model of ameboid deformation and locomotion. European Biophysics Journal 27(5):532–539 53

Brückner BR, Janshoff A (2015) Elastic properties of epithelial cells probed by atomic force microscopy. Biochimica et Biophysica Acta (BBA)-Molecular Cell Research 1853(11):3075–3082 124

Callan-Jones A, Voituriez R (2013) Active gel model of amoeboid cell motility. New Journal of Physics 15(2):025,022 10

Callan-Jones A, Joanny JF, Prost J (2008) Viscous-fingering-like instability of cell fragments. Physical review letters 100(25):258,106 10, 17, 18, 19, 27, 97

Camley BA, Zhao Y, Li B, Levine H, Rappel WJ (2013) Periodic migration in a physical model of cells on micropatterns. Physical review letters 111(15):158,102 6, 10, 53

Camley BA, Zhao Y, Li B, Levine H, Rappel WJ (2017) Crawling and turning in a minimal reaction-diffusion cell motility model: Coupling cell shape and biochemistry. Physical Review E 95(1):012,401 10, 53

Carlsson A (2011) Mechanisms of cell propulsion by active stresses. New journal of physics 13(7):073,009 10, 14

Carvalho K, Lemière J, Faqir F, Manzi J, Blanchoin L, Plastino J, Betz T, Sykes C (2013) Actin polymerization or myosin contraction: two ways to build up cortical tension for symmetry breaking. Philosophical Transactions of the Royal Society B: Biological Sciences 368(1629):20130,005 95

Casademunt J (2004) Viscous fingering as a paradigm of interfacial pattern formation: Recent results and new challenges. Chaos: An Interdisciplinary Journal of Nonlinear Science 14(3):809–824 17, 96

Chabaud M, Heuzé ML, Bretou M, Vargas P, Maiuri P, Solanes P, Maurin M, Terriac E, Le Berre M, Lankar D, et al (2015) Cell migration and antigen capture are antagonistic processes coupled by myosin ii in dendritic cells. Nature communications 6:7526 11, 12, 87

Chan DY, Klaseboer E, Manica R (2010) Dynamic interactions between deformable drops in the hele–shaw geometry. Soft Matter 6(8):1809–1815 90

Charras G, Paluch E (2008) Blebs lead the way: how to migrate without lamellipodia. Nature reviews Molecular cell biology 9(9):730 6

Charras GT, Yarrow JC, Horton MA, Mahadevan L, Mitchison T (2005) Non-equilibration of hydrostatic pressure in blebbing cells. Nature 435(7040):365 120

Charras GT, Coughlin M, Mitchison TJ, Mahadevan L (2008) Life and times of a cellular bleb. Biophysical journal 94(5):1836–1853 120, 129, 130, 134

Chen Z, Zhu C, Kuo CJ, Robustelli J, Baumgart T (2016) The n-terminal amphipathic helix of endophilin does not contribute to its molecular curvature generation capacity. Journal of the American Chemical Society 138(44):14,616–14,622 123

Cunningham CC (1995) Actin polymerization and intracellular solvent flow in cell surface blebbing. The Journal of Cell Biology 129(6):1589–1599 120

Dai J, Sheetz MP, Wan X, Morris CE (1998) Membrane tension in swelling and shrinking molluscan neurons. Journal of Neuroscience 18(17):6681–6692 120

Dallaston MC (2013) Mathematical models of bubble evolution in a hele-shaw cell. PhD thesis, Queensland University of Technology 53

Danuser G, Allard J, Mogilner A (2013) Mathematical modeling of eukaryotic cell migration: insights beyond experiments. Annual review of cell and developmental biology 29:501–528 10

Dawes AT, Ermentrout GB, Cytrynbaum EN, Edelstein-Keshet L (2006) Actin filament branching and protrusion velocity in a simple 1d model of a motile cell. Journal of theoretical biology 242(2):265–279 10

DiMilla P, Barbee K, Lauffenburger D (1991) Mathematical model for the effects of adhesion and mechanics on cell migration speed. Biophysical journal 60(1):15–37 9, 10

Diz-Muñoz A, Fletcher DA, Weiner OD (2013) Use the force: membrane tension as an organizer of cell shape and motility. Trends in cell biology 23(2):47–53 135

Doostmohammadi A, Ignés-Mullol J, Yeomans JM, Sagués F (2018) Active nematics. Nature communications 9(1):1–13 5

Doubrovinski K, Kruse K (2011) Cell motility resulting from spontaneous polymerization waves. Physical review letters 107(25):258,103 10, 97

Dreher A, Aranson IS, Kruse K (2014) Spiral actin-polymerization waves can generate amoeboidal cell crawling. New Journal of Physics 16(5):055,007 10

Driscoll MK, McCann C, Kopace R, Homan T, Fourkas JT, Parent C, Losert W (2012) Cell shape dynamics: from waves to migration. PLoS computational biology 8(3):e1002,392 51

Eggers J (1997) Nonlinear dynamics and breakup of free-surface flows. Reviews of modern physics 69(3):865 93

Erickson C, Trinkaus J (1976) Microvilli and blebs as sources of reserve surface membrane during cell spreading. Experimental cell research 99(2):375–384 120

Etienne-Manneville S (2008) Polarity proteins in migration and invasion. Oncogene 27(55):6970 7

Euteneuer U, Schliwa M (1984) Persistent, directional motility of cells and cytoplasmic fragments in the absence of microtubules. Nature 310(5972):58 95

Evans E, Rawicz W (1990) Entropy-driven tension and bending elasticity in condensed-fluid membranes. Physical Review Letters 64(17):2094 121, 124

Fang C, Hui T, Wei X, Shao X, Lin Y (2017) A combined experimental and theoretical investigation on cellular blebbing. Scientific reports 7(1):16,666 120

Farutin A, Rafaï S, Dysthe DK, Duperray A, Peyla P, Misbah C (2013) Amoeboid swimming: A generic self-propulsion of cells in fluids by means of membrane deformations. Physical review letters 111(22):228,102 10

Farutin A, Etienne J, Misbah C, Recho P (2019) Crawling in a fluid. arXiv preprint arXiv:190201730 5

Fischer RS, Fowler VM (2015) Thematic minireview series: the state of the cytoskeleton in 2015. Journal of Biological Chemistry 290(28):17,133–17,136 3

Folch R, Alvarez-Lacalle E, Ortín J, Casademunt J (2009) Pattern formation and interface pinch-off in rotating hele-shaw flows: A phase-field approach. Physical Review E 80(5):056,305 96

Friedl P, Gilmour D (2009) Collective cell migration in morphogenesis, regeneration and cancer. Nature reviews Molecular cell biology 10(7):445 2

Friedl P, Wolf K (2010) Plasticity of cell migration: a multiscale tuning model. The Journal of cell biology 188(1):11–19 2, 7, 9

Gallinato O, Ohta M, Poignard C, Suzuki T (2017) Free boundary problem for cell protrusion formations: theoretical and numerical aspects. Journal of mathematical biology 75(2):263–307 53

Gallop JL, Jao CC, Kent HM, Butler PJG, Evans PR, Langen R, McMahon HT (2006) Mechanism of endophilin n-bar domain-mediated membrane curvature. The EMBO Journal 25(12):2898–2910 123

Gauthier NC, Fardin MA, Roca-Cusachs P, Sheetz MP (2011) Temporary increase in plasma membrane tension coordinates the activation of exocytosis and contraction during cell spreading. Proceedings of the National Academy of Sciences 108(35):14,467–14,472 135

Goudarzi M, Banisch TU, Mobin MB, Maghelli N, Tarbashevich K, Strate I, van den Berg J, Blaser H, Bandemer S, Paluch E, et al (2012) Identification and regulation of a molecular module for bleb-based cell motility. Developmental cell 23(1):210–218 120, 134

Goudarzi M, Tarbashevich K, Mildner K, Begemann I, Garcia J, Paksa A, Reichman-Fried M, Mahabaleshwar H, Blaser H, Hartwig J, et al (2017) Bleb expansion in migrating cells depends on supply of membrane from cell surface invaginations. Developmental cell 43(5):577–587 120, 123, 130, 131, 132

Gov N, Safran S (2004) Pinning of fluid membranes by periodic harmonic potentials. Physical Review E 69(1):011,101 122

Gracheva ME, Othmer HG (2004) A continuum model of motility in ameboid cells. Bulletin of mathematical biology 66(1):167–193 10

Graham DM, Andersen T, Sharek L, Uzer G, Rothenberg K, Hoffman BD, Rubin J, Balland M, Bear JE, Burridge K (2018) Enucleated cells reveal differential roles of the nucleus in cell migration, polarity, and mechanotransduction. J Cell Biol 217(3):895–914 95

Hawkins RJ, Piel M, Faure-Andre G, Lennon-Dumenil A, Joanny J, Prost J, Voituriez R (2009) Pushing off the walls: a mechanism of cell motility in confinement. Physical review letters 102(5):058,103 10, 14, 15, 17, 19

Hawkins RJ, Poincloux R, Bénichou O, Piel M, Chavrier P, Voituriez R (2011) Spontaneous contractility-mediated cortical flow generates cell migration in three-dimensional environments. Biophysical journal 101(5):1041–1045 10

Hecht F, Le Hyaric A, Pironneau O, Ohtsuka K (2008) Freefem++. second edition, version 2.22-2-2 63

Helfrich W (1973) Elastic properties of lipid bilayers: theory and possible experiments. Zeitschrift für Naturforschung C 28(11-12):693–703 3

Heuzé ML, Collin O, Terriac E, Lennon-Duménil AM, Piel M (2011) Cell migration in confinement: a micro-channel-based assay. In: Cell Migration, Springer, pp 415–434 87

Hirt CW, Nichols BD (1981) Volume of fluid (vof) method for the dynamics of free boundaries. Journal of computational physics 39(1):201–225 53

Holmes WR, Edelstein-Keshet L (2012) A comparison of computational models for eukaryotic cell shape and motility. PLoS computational biology 8(12):e1002,793 10

Houk AR, Jilkine A, Mejean CO, Boltyanskiy R, Dufresne ER, Angenent SB, Altschuler SJ, Wu LF, Weiner OD (2012) Membrane tension maintains cell polarity by confining signals to the leading edge during neutrophil migration. Cell 148(1-2):175–188 5

Howard J, et al (2001) Mechanics of motor proteins and the cytoskeleton 3

Itoh T, De Camilli P (2006) Bar, f-bar (efc) and enth/anth domains in the regulation of membrane–cytosol interfaces and membrane curvature. Biochimica et Biophysica Acta (BBA)-Molecular and Cell Biology of Lipids 1761(8):897–912 120

Joanny JF, Prost J (2009) Active gels as a description of the actin-myosin cytoskeleton. HFSP journal 3(2):94–104 5, 97

Jurado C, Haserick JR, Lee J (2005) Slipping or gripping? fluorescent speckle microscopy in fish keratocytes reveals two different mechanisms for generating a retrograde flow of actin. Molecular biology of the cell 16(2):507–518 11

Kabaso D, Gongadze E, Elter P, Van Rienen U, Gimsa J, Kralj-Iglic V, Iglic A (2011) Attachment of rod-like (bar) proteins and membrane shape. Mini reviews in medicinal chemistry 11(4):272–282 123

Keller H, Eggli P (1998) Protrusive activity, cytoplasmic compartmentalization, and restriction rings in locomoting blebbing walker carcinosarcoma cells are related to detachment of cortical actin from the plasma membrane. Cell motility and the cytoskeleton 41(2):181–193 120

Keren K (2011) Cell motility: the integrating role of the plasma membrane. European Biophysics Journal 40(9):1013 135

Keren K, Pincus Z, Allen GM, Barnhart EL, Marriott G, Mogilner A, Theriot JA (2008) Mechanism of shape determination in motile cells. Nature 453(7194):475 50

Keren K, Yam PT, Kinkhabwala A, Mogilner A, Theriot JA (2009) Intracellular fluid flow in rapidly moving cells. Nature cell biology 11(10):1219 5

Kleinschmidt JH (2006) Folding kinetics of the outer membrane proteins ompa and foma into phospholipid bilayers. Chemistry and physics of lipids 141(1):30–47 120

Klughammer N, Bischof J, Schnellbächer ND, Callegari A, Lénárt P, Schwarz US (2018) Cytoplasmic flows in starfish oocytes are fully determined by cortical contractions. PLoS computational biology 14(11):e1006,588 5

Köprunner M, Thisse C, Thisse B, Raz E (2001) A zebrafish nanos-related gene is essential for the development of primordial germ cells. Genes & development 15(21):2877–2885 141

Koslover EF, Chan CK, Theriot JA (2017) Cytoplasmic flow and mixing due to deformation of motile cells. Biophysical journal 113(9):2077–2087 3, 5

Kosmalska AJ, Casares L, Elosegui-Artola A, Thottacherry JJ, Moreno-Vicente R, González-Tarragó V, Del Pozo MÁ, Mayor S, Arroyo M, Navajas D, et al (2015) Physical principles of membrane remodelling during cell mechanoadaptation. Nature communications 6:7292 3

Kozlov MM, Mogilner A (2007) Model of polarization and bistability of cell fragments. Biophysical journal 93(11):3811–3819 6, 10

Kruse K, Joanny JF, Jülicher F, Prost J, Sekimoto K (2004) Asters, vortices, and rotating spirals in active gels of polar filaments. Physical review letters 92(7):078,101 4, 5, 16, 97

Kruse K, Joanny JF, Jülicher F, Prost J, Sekimoto K (2005) Generic theory of active polar gels: a paradigm for cytoskeletal dynamics. The European Physical Journal E 16(1):5–16 5, 97

Kruse K, Joanny J, Jülicher F, Prost J (2006) Contractility and retrograde flow in lamellipodium motion. Physical biology 3(2):130 6, 10

Kwok R, Evans E (1981) Thermoelasticity of large lecithin bilayer vesicles. Biophysical journal 35(3):637–652 120

Ladoux B, Mège RM (2017) Mechanobiology of collective cell behaviours. Nature Reviews Molecular Cell Biology 18(12):743 2

Ladoux B, Mège RM, Trepat X (2016) Front–rear polarization by mechanical cues: From single cells to tissues. Trends in cell biology 26(6):420–433 6

Lämmermann T, Bader BL, Monkley SJ, Worbs T, Wedlich-Söldner R, Hirsch K, Keller M, Förster R, Critchley DR, Fässler R, et al (2008) Rapid leukocyte migration by integrin-independent flowing and squeezing. Nature 453(7191):51 10

Lauffenburger D (1989) A simple model for the effects of receptor-mediated cell—substratum adhesion on cell migration. Chemical Engineering Science 44(9):1903–1914 10

Lautscham LA, Kämmerer C, Lange JR, Kolb T, Mark C, Schilling A, Strissel PL, Strick R, Gluth C, Rowat AC, et al (2015) Migration in confined 3d environments is determined by a combination of adhesiveness, nuclear volume, contractility, and cell stiffness. Biophysical journal 109(5):900–913 87, 88

Lavi I, Piel M, Lennon-Duménil AM, Voituriez R, Gov NS (2016) Deterministic patterns in cell motility. Nature Physics 12(12):1146 10, 11, 12, 36, 41

Lavi I, Goudarzi M, Raz E, Gov NS, Voituriez R, Sens P (2019a) Cellular blebs and membrane invaginations are coupled through membrane tension buffering. Biophysical journal 119

Lavi I, Meunier N, Pantz O (2019b) A mathematical model for cell crawling migration. in redaction 54

Le Clainche C, Carlier MF (2008) Regulation of actin assembly associated with protrusion and adhesion in cell migration. Physiological reviews 88(2):489–513 4

Le Dret H, Lucquin B (2016) Partial differential equations: modeling, analysis and numerical approximation, vol 168. Springer 113, 116

Lee E, Marcucci M, Daniell L, Pypaert M, Weisz OA, Ochoa GC, Farsad K, Wenk MR, De Camilli P (2002) Amphiphysin 2 (bin1) and t-tubule biogenesis in muscle. Science 297(5584):1193–1196 120

Lewis OL, Zhang S, Guy RD, Del Alamo JC (2015) Coordination of contractility, adhesion and flow in migrating physarum amoebae. Journal of The Royal Society Interface 12(106):20141,359 5, 10

Lieber AD, Yehudai-Resheff S, Barnhart EL, Theriot JA, Keren K (2013) Membrane tension in rapidly moving cells is determined by cytoskeletal forces. Current biology 23(15):1409–1417 124

Lipowsky R (2013) Spontaneous tubulation of membranes and vesicles reveals membrane tension generated by spontaneous curvature. Faraday discussions 161:305–331 123

Litschel T, Ramm B, Maas R, Heymann M, Schwille P (2018) Beating vesicles: encapsulated protein oscillations cause dynamic membrane deformations. Angewandte Chemie International Edition 57(50):16,286–16,290 51

Liu YJ, Le Berre M, Lautenschlaeger F, Maiuri P, Callan-Jones A, Heuzé M, Takaki T, Voituriez R, Piel M (2015) Confinement and low adhesion induce fast amoeboid migration of slow mesenchymal cells. Cell 160(4):659–672 9, 10, 50

Löber J, Ziebert F, Aranson IS (2014) Modeling crawling cell movement on soft engineered substrates. Soft matter 10(9):1365–1373 10

Löber J, Ziebert F, Aranson IS (2015) Collisions of deformable cells lead to collective migration. Scientific reports 5:9172 94

Lodish H, Berk A, Zipursky SL, Matsudaira P, Baltimore D, Darnell J (2000) Molecular cell biology 4th edition. National Center for Biotechnology Information, Bookshelf 5

Maitre E, Misbah C, Peyla P, Raoult A (2012) Comparison between advected-field and level-set methods in the study of vesicle dynamics. Physica D: Nonlinear Phenomena 241(13):1146–1157 53

Maître JL, Niwayama R, Turlier H, Nédélec F, Hiiragi T (2015) Pulsatile cell-autonomous contractility drives compaction in the mouse embryo. Nature cell biology 17(7):849 51, 93

Maiuri P, Terriac E, Paul-Gilloteaux P, Vignaud T, McNally K, Onuffer J, Thorn K, Nguyen PA, Georgoulia N, Soong D, et al (2012) The first world cell race. Current Biology 22(17):R673–R675 11, 14

Maiuri P, Rupprecht JF, Wieser S, Ruprecht V, Bénichou O, Carpi N, Coppey M, De Beco S, Gov N, Heisenberg CP, et al (2015) Actin flows mediate a universal coupling between cell speed and cell persistence. Cell 161(2):374–386 6, 10, 11, 12, 13, 14, 19, 36, 41, 50, 98

Marchetti MC, Joanny JF, Ramaswamy S, Liverpool TB, Prost J, Rao M, Simha RA (2013) Hydrodynamics of soft active matter. Reviews of Modern Physics 85(3):1143 5, 10, 97

Masuda M, Takeda S, Sone M, Ohki T, Mori H, Kamioka Y, Mochizuki N (2006) Endophilin bar domain drives membrane curvature by two newly identified structure-based mechanisms. The EMBO journal 25(12):2889–2897 120

Maugis B, Brugués J, Nassoy P, Guillen N, Sens P, Amblard F (2010) Dynamic instability of the intracellular pressure drives bleb-based motility. J Cell Sci 123(22):3884–3892 6

McMahon HT, Gallop JL (2005) Membrane curvature and mechanisms of dynamic cell membrane remodelling. Nature 438(7068):590 120

Meyen D, Tarbashevich K, Banisch TU, Wittwer C, Reichman-Fried M, Maugis B, Grimaldi C, Messerschmidt EM, Raz E (2015) Dynamic filopodia are required for chemokine-dependent intracellular polarization during guided cell migration in vivo. Elife 4 140

Mietke A, Jülicher F, Sbalzarini IF (2019) Self-organized shape dynamics of active surfaces. Proceedings of the National Academy of Sciences 116(1):29–34 5

Mittasch M, Gross P, Nestler M, Fritsch AW, Iserman C, Kar M, Munder M, Voigt A, Alberti S, Grill SW, et al (2018) Non-invasive perturbations of intracellular flow reveal physical principles of cell organization. Nature Cell Biology 20(3):344 5

Mogilner A, Oster G (1996) Cell motility driven by actin polymerization. Biophysical journal 71(6):3030–3045 10, 11

Mogilner A, Marland E, Bottino D (2001) A minimal model of locomotion applied to the steady gliding movement of fish keratocyte cells. In: Mathematical Models for Biological Pattern Formation, Springer, pp 269–293 10

Mori Y, Jilkine A, Edelstein-Keshet L (2008) Wave-pinning and cell polarity from a bistable reaction-diffusion system. Biophysical journal 94(9):3684–3697 6, 10, 97

Mseka T, Coughlin M, Cramer LP (2009) Graded actin filament polarity is the organization of oriented actomyosin ii filament bundles required for fibroblast polarization. Cell motility and the cytoskeleton 66(9):743–753 5

Nagle JF, Jablin MS, Tristram-Nagle S, Akabori K (2015) What are the true values of the bending modulus of simple lipid bilayers? Chemistry and physics of lipids 185:3–10 124

Noguchi H (2016) Membrane tubule formation by banana-shaped proteins with or without transient network structure. Scientific reports 6:20,935 123

Norman LL, Brugés J, Sengupta K, Sens P, Aranda-Espinoza H (2010) Cell blebbing and membrane area homeostasis in spreading and retracting cells. Biophysical journal 99(6):1726–1733 120

Ohta T, Tarama M, Sano M (2016) Simple model of cell crawling. Physica D: Nonlinear Phenomena 318:3–11 10

Ortega JM, Rheinboldt WC (1970) Iterative solution of nonlinear equations in several variables, vol 30. Siam 59

Paksa A, Raz E (2015) Zebrafish germ cells: motility and guided migration. Current opinion in cell biology 36:80–85 120

Paksa A, Bandemer J, Hoeckendorf B, Razin N, Tarbashevich K, Minina S, Meyen D, Biundo A, Leidel SA, Peyrieras N, et al (2016) Repulsive cues combined with physical barriers and cell–cell adhesion determine progenitor cell positioning during organogenesis. Nature communications 7:11,288 141

Palecek SP, Loftus JC, Ginsberg MH, Lauffenburger DA, Horwitz AF, et al (1997) Integrin-ligand binding properties govern cell migration speed through cell-substratum adhesiveness. Nature 385(6616):537–540 9

Paluch E, Piel M, Prost J, Bornens M, Sykes C (2005) Cortical actomyosin breakage triggers shape oscillations in cells and cell fragments. Biophysical journal 89(1):724–733 120

Paluch EK, Raz E (2013) The role and regulation of blebs in cell migration. Current opinion in cell biology 25(5):582–590 120

Paluch EK, Aspalter IM, Sixt M (2016) Focal adhesion–independent cell migration. Annual review of cell and developmental biology 32:469–490 7, 8, 9

Paňková K, Rösel D, Novotnỳ M, Brábek J (2010) The molecular mechanisms of transition between mesenchymal and amoeboid invasiveness in tumor cells. Cellular and molecular life sciences 67(1):63–71 7, 8, 9

Pérez-González C, Alert R, Blanch-Mercader C, Gómez-González M, Kolodziej T, Bazellieres E, Casademunt J, Trepat X (2019) Active wetting of epithelial tissues. Nature Physics 15(1):79 5

Peskin CS (2002) The immersed boundary method. Acta numerica 11:479–517 53

Peter BJ, Kent HM, Mills IG, Vallis Y, Butler PJG, Evans PR, McMahon HT (2004) Bar domains as sensors of membrane curvature: the amphiphysin bar structure. Science 303(5657):495–499 120, 124

Picas L, Rico F, Scheuring S (2012) Direct measurement of the mechanical properties of lipid phases in supported bilayers. Biophysical journal 102(1):L01–L03 124

Pollard TD, Borisy GG (2003) Cellular motility driven by assembly and disassembly of actin filaments. Cell 112(4):453–465 4

Prost J, Jülicher F, Joanny JF (2015) Active gel physics. Nature Physics 11(2):111 5, 10, 97

Pullarkat PA (2006) Loss of cell-substrate adhesion leads to periodic shape oscillations in fibroblasts. arXiv preprint physics/0612156 51, 120

Raab M, Gentili M, de Belly H, Thiam HR, Vargas P, Jimenez AJ, Lautenschlaeger F, Voituriez R, Lennon-Duménil AM, Manel N, et al (2016) Escrt iii repairs nuclear envelope ruptures during cell migration to limit dna damage and cell death. Science 352(6283):359–362 87

Raucher D, Sheetz MP (2000) Cell spreading and lamellipodial extension rate is regulated by membrane tension. J Cell Biol 148(1):127–136 135

Recho P, Putelat T, Truskinovsky L (2013) Contraction-driven cell motility. Physical review letters 111(10):108,102 10, 14

Reig G, Pulgar E, Concha ML (2014) Cell migration: from tissue culture to embryos. Development 141(10):1999–2013 7

Ruprecht V, Wieser S, Callan-Jones A, Smutny M, Morita H, Sako K, Barone V, Ritsch-Marte M, Sixt M, Voituriez R, et al (2015) Cortical contractility triggers a stochastic switch to fast amoeboid cell motility. Cell 160(4):673–685 6, 9, 10, 50

Sáez PJ, Barbier L, Attia R, Thiam HR, Piel M, Vargas P (2018) Leukocyte migration and deformation in collagen gels and microfabricated constrictions. In: Cell Migration, Springer, pp 361–373 87

Salbreux G, Joanny JF, Prost J, Pullarkat P (2007) Shape oscillations of non-adhering fibroblast cells. Physical biology 4(4):268 51

Salbreux G, Charras G, Paluch E (2012) Actin cortex mechanics and cellular morphogenesis. Trends in cell biology 22(10):536–545 3

Sarig I, Starosvetsky Y, Gat AD (2016) Interaction forces between microfluidic droplets in a hele-shaw cell. Journal of Fluid Mechanics 800:264–277 90

Schmid-Schonbein G, Shih YY, Chien S (1980) Morphometry of human leukocytes. Blood 56(5):866–875 120

Schweitzer Y, Kozlov MM (2015) Membrane-mediated interaction between strongly anisotropic protein scaffolds. PLoS computational biology 11(2):e1004,054 123, 124

Schweitzer Y, Shemesh T, Kozlov MM (2015) A model for shaping membrane sheets by protein scaffolds. Biophysical journal 109(3):564–573 124

Sens P, Plastino J (2015) Membrane tension and cytoskeleton organization in cell motility. Journal of Physics: Condensed Matter 27(27):273,103 3, 5, 121, 124, 135

Sens P, Turner MS (2004) Theoretical model for the formation of caveolae and similar membrane invaginations. Biophysical journal 86(4):2049–2057 125

Sens P, Johannes L, Bassereau P (2008) Biophysical approaches to protein-induced membrane deformations in trafficking. Current Opinion in Cell Biology 20(4):476 – 482 123

Serrador JM, Nieto M, Sánchez-Madrid F (1999) Cytoskeletal rearrangement during migration and activation of t lymphocytes. Trends in cell biology 9(6):228–233 15

Shao D, Rappel WJ, Levine H (2010) Computational model for cell morphodynamics. Physical review letters 105(10):108,104 10, 53

Shao D, Levine H, Rappel WJ (2012) Coupling actin flow, adhesion, and morphology in a computational cell motility model. Proceedings of the National Academy of Sciences 109(18):6851–6856 6, 10, 53

Sheetz MP, Sable JE, Döbereiner HG (2006) Continuous membrane-cytoskeleton adhesion requires continuous accommodation to lipid and cytoskeleton dynamics. Annu Rev Biophys Biomol Struct 35:417–434 120

Shepherd VA (2006) The cytomatrix as a cooperative system of macromolecular and water networks. Current topics in developmental biology 75:171–223 2

Shi Z, Baumgart T (2015) Membrane tension and peripheral protein density mediate membrane shape transitions. Nature communications 6:5974 123

Shi Z, Graber ZT, Baumgart T, Stone HA, Cohen AE (2018) Cell membranes resist flow. Cell 175(7):1769–1779 122, 134

Simon C, Caorsi V, Campillo C, Sykes C (2018) Interplay between membrane tension and the actin cytoskeleton determines shape changes. Physical biology 15(6):065,004 95

Simunovic M, Srivastava A, Voth GA (2013) Linear aggregation of proteins on the membrane as a prelude to membrane remodeling. Proceedings of the National Academy of Sciences 110(51):20,396–20,401 123

Simunovic M, Voth GA, Callan-Jones A, Bassereau P (2015) When physics takes over: Bar proteins and membrane curvature. Trends in cell biology 25(12):780–792 120

Singer SJ, Nicolson GL (1972) The fluid mosaic model of the structure of cell membranes. Science 175(4023):720–731 3

Siton-Mendelson O, Bernheim-Groswasser A (2016) Toward the reconstitution of synthetic cell motility. Cell adhesion & migration 10(5):461–474 95

Sorre B, Callan-Jones A, Manzi J, Goud B, Prost J, Bassereau P, Roux A (2012) Nature of curvature coupling of amphiphysin with membranes depends on its bound density. Proceedings of the National Academy of Sciences 109(1):173–178 123

Spangler EJ, Harvey CW, Revalee JD, Kumar PS, Laradji M (2011) Computer simulation of cytoskeleton-induced blebbing in lipid membranes. Physical Review E 84(5):051,906 120

Street CA, Bryan BA (2011) Rho kinase proteins—pleiotropic modulators of cell survival and apoptosis. Anticancer research 31(11):3645–3657 4

Strychalski W, Guy RD (2013) A computational model of bleb formation. Mathematical medicine and biology: a journal of the IMA 30(2):115–130 120

Svitkina TM, Verkhovsky AB, McQuade KM, Borisy GG (1997) Analysis of the actin–myosin ii system in fish epidermal keratocytes: mechanism of cell body translocation. The Journal of cell biology 139(2):397–415 11

Takei K, Slepnev VI, Haucke V, De Camilli P (1999) Functional partnership between amphiphysin and dynamin in clathrin-mediated endocytosis. Nature cell biology 1(1):33 120

Tjhung E, Marenduzzo D, Cates ME (2012) Spontaneous symmetry breaking in active droplets provides a generic route to motility. Proceedings of the National Academy of Sciences 109(31):12,381–12,386 10

Tjhung E, Tiribocchi A, Marenduzzo D, Cates M (2015) A minimal physical model captures the shapes of crawling cells. Nature communications 6:5420 10, 53

Tsimring LS (2014) Noise in biology. Reports on Progress in Physics 77(2):026,601 98

Tsukita S, Yonemura S, Tsukita S (1997) Erm proteins: head-to-tail regulation of actin-plasma membrane interaction. Trends in biochemical sciences 22(2):53–58 3

Vargas P, Terriac E, Lennon-Duménil AM, Piel M (2014) Study of cell migration in microfabricated channels. JoVE (Journal of Visualized Experiments) (84):e51,099 87

Verkhovsky AB, Svitkina TM, Borisy GG (1999) Self-polarization and directional motility of cytoplasm. Current Biology 9(1):11–S1 6, 50, 94, 95

Voituriez R, Joanny J, Prost J (2006) Generic phase diagram of active polar films. Physical review letters 96(2):028,102 5

Welch MD (2015) Cell migration, freshly squeezed. Cell 160(4):581–582 9

Whitfield CA, Hawkins RJ (2016) Immersed boundary simulations of active fluid droplets. PloS one 11(9):e0162,474 53

Wu H, Thiébaud M, Hu WF, Farutin A, Rafai S, Lai MC, Peyla P, Misbah C (2015) Amoeboid motion in confined geometry. Physical Review E 92(5):050,701 10

Yang TD, Park K, Park JS, Lee JH, Choi E, Lee J, Choi W, Choi Y, Lee KJ (2019) Two distinct actin waves correlated with turns-and-runs of crawling microglia. PloS one 14(8):e0220,810 10, 51

Yin Y, Arkhipov A, Schulten K (2009) Simulations of membrane tubulation by lattices of amphiphysin n-bar domains. Structure 17(6):882–892 123

Young J, Mitran S (2010) A numerical model of cellular blebbing: a volume-conserving, fluid–structure interaction model of the entire cell. Journal of biomechanics 43(2):210–220 120

Ziebert F, Aranson IS (2016) Computational approaches to substrate-based cell motility. npj Computational Materials 2:16,019 10, 53, 97

Ziebert F, Swaminathan S, Aranson IS (2011) Model for self-polarization and motility of keratocyte fragments. Journal of The Royal Society Interface 9(70):1084–1092 53, 97

Ziebert F, Swaminathan S, Aranson IS (2012) Model for self-polarization and motility of keratocyte fragments. Journal of The Royal Society Interface 9(70):1084–1092 10